Development of cementitious materials from the magnesium silicate minerals

Nan Yang

A thesis submitted in partial fulfilment of the requirements for the degree of

DOCTOR OF PHILOSOPHY IN CIVIL ENGINEERING

University of Canterbury

September 2020

Abstract

Concrete is the second most-consumed items in the world after water. Although cement only accounts for 10-20% of the concrete's weight, it attributes up to 95% of the total carbon emission. Because of the large amount consumed every year, it emitted around 8% of the total carbon emission. Many solutions were proposed or already in place to reduce the carbon footprint during the manufacturing, design, use and end of life stages. Among these initiatives, using MgO-based cement is one of the most promising approaches. However, the availability of the MgO is limited compared to the raw material to prepare Portland cement. Especially in New Zealand, there is no production for MgO, thus it has to be imported from overseas. On the other hand, New Zealand is rich in magnesium-rich silicates rocks, such as olivine and serpentine. Therefore, this research conducted a feasibility study on the magnesia and silica extraction from these magnesium silicates minerals and then used them as a binder system.

The dissolution properties of the olivine under different conditions were first investigated. It was highlighted that the dissolution rate was in a good relationship with the pH value, and mechanical grinding also improved its dissolution rate. As a result, acid digestion was proposed to process the fine mineral particles. The magnesia (MgO) was successfully recovered from the olivine after digestion, separation, evaporation and thermal decomposition. However, it was identified that the recovered products only contained 52.1% MgO while the SiO_2 impurity took up 27.9%. The reactivity of the recovered MgO

is lower than MgO from a commercial source. In terms of silica(SiO_2) extraction, acid digestion was also used on serpentine. To systematically investigate the reactivity of the recovered silica, seven different characterisation techniques were used and compared with other silica sources. It concluded that the recovered silica contains a certain proportion of amorphous silica phase, and it was pozzolanic active.

The recovered MgO was then mixed with the extracted SiO_2. The sample mixed with recovered products demonstrated higher strength than it mixed with commercial MgO and silica fume. It was also noted that the strength of the sample containing recovered MgO was constantly higher than it with commercial MgO source. This was caused by the presence of amorphous silica in the recovered MgO. The amorphous silica reacted with the MgO and formed the magnesium silicate hydrate gel, contributing to the strength gain. However, the recovered silica did not show any comparable reactivity to the silica fume.

Lastly, since hydrochloride acid (HCl) was used for acid digestion, it generates a considerable amount of waste acid. The magnesia was then proposed to neutralise the waste acid and to develop the MgO-HCl binder system. The mix of MgO with waste acid showed superior mechanical properties, especially at early ages. It reached more than 40 MPa at 3 days which was more than doubled of the mix with $MgO+H_2O$. The hydration products of the MgO +waste acid were found to be brucite, magnesium carbonates and $3MgO\text{-}MgCl_2\text{-}8H_2O$ (phase 3). These products were similar to the Sorel cement/magnesium oxychloride cement.

To conclude, this research proved the feasibility of extracting magnesia and silica from ultramafic minerals and developed the prototypes of the $MgO+SiO_2+H_2O$ and MgO-HCl binder systems.

Contents

Abstract 2

List of Figures 11

List of Tables 17

1 Introduction 19

1.1 Background 19

1.2 Cement production process 20

1.3 Strategies for low-carbon cement industry 21

1.4 Research significance and motivations 22

1.5 Objectives and scope 24

1.5.1 Specific objectives 24

1.5.2 Scope of the research 25

1.6 Outline of the thesis 25

2 Literature review 29

2.1 Introduction 29

2.2 Magnesium silicate minerals 30

2.2.1 Olivine 30

2.2.2 Serpentine 31

2.3 Mineral processing 31

2.3.1 Thermal activation 31

2.3.2 Magnesium dissolution 34

2.3.3 Silica recovery 38

2.4 Properties of MgO and SiO_2 40

2.4.1 Magnesium oxide 40

2.4.2 Silica....47
2.4.3 Amorphous silica....47
2.4.4 Pozzolanic activity assessment....48
2.5 Magnesia based cement....55
2.5.1 Magnesium silica cement....57
2.5.2 Magnesium oxychloride cement system....58
2.5.3 Magnesium oxysulfide cement system....59
2.5.4 Magnesium phosphate cement system....60
2.5.5 Reactive magnesia cement....61
2.6 Mineral based cement....62
2.6.1 Formation of magnesium silicates....62
2.6.2 Use of magnesium silicates as cement....63
2.6.3 Use of magnesium silicates as a silica source....64
2.7 Summary and conclusion....66
3 Raw material and experimental methodology....68
3.1 Introduction....68
3.2 Raw Materials....70
3.2.1 Magnesium silicates minerals....70
3.2.2 Magnesia....74
3.2.3 Silica fume....76
3.2.4 Quartz....78
3.2.5 Acids and bases....80
3.3 Experiment methods and techniques....80

3.3.1 Sampling method....81
3.3.2 Grinding....81
3.3.3 Calcination....82
3.3.4 Filtration....83
3.3.5 pH monitoring....84
3.3.6 Ion concentration measurement....85
3.3.7 Conductivity test....87
3.3.8 Cement sample preparation and curing....87
3.3.9 Sample hydration arrestment and storage....88
3.3.10 Compressive strength....88
3.3.11 Mortar workability test....89
3.3.12 X-ray powder diffraction and X-ray fluorescence....90
3.3.13 Thermogravimetric analysis....90
3.3.14 Scanning Electron microscopy (SEM)....91
3.3.15 Particle analysis....93
3.3.16 Hydration Heat Measurement....94
4 Study on olivine solubility for magnesium extraction....96
4.1 Introduction....96
4.2 Material and methods....99
4.3 Results and Discussion....99
4.3.1 Effect of mechanical activation....99
4.3.2 Effect of pH....105
4.3.3 Effect of acid type....107

4.3.4 Effect of acid concentration 110
4.3.5 Effect of CO_2 content 111
4.3.6 Effect of CO_2 pressure.....114
4.3.7 Effect of reaction duration.....115
4.3.8 Characterisation of the recovered magnesium composite116
4.3.9 Olivine dissolution: Thermodynamics, kinetics and mechanisms.....120
4.4 Summary and conclusion.....125
5 Investigation on the magnesium composites extracted from olivine.....127
5.1 Introduction.....127
5.2 Raw material and processing method 129
5.2.1 Acid reaction 130
5.2.2 Filtration.....130
5.2.3 Evaporation 131
5.2.4 Thermal decomposition.....131
5.2.5 Characterisation methods 132
5.3 Results and discussion 133
5.3.1 Olivine residue after acid digestion.....134
5.3.2 Magnesium acetate recovered (R-MgAc) from the reaction solution.....137
5.3.3 Magnesia obtained from the calcination of the recovered MgAc 143
5.4 Summary and conclusion.....151

6 Pozzolan reactivity assessment of the silica recovered from magnesium silicates.....153
6.1 Introduction.....153
6.2 Material and methods.....156
6.2.1 Materials.....156
6.2.2 Silica extraction process.....156
6.2.3 Pozzolan reactivity test.....157
6.3 Results and Discussion.....161
6.3.1 The silica extracted from serpentine.....161
6.3.2 Chemical composition and phase identification.....165
6.3.3 Particle size and surface area analysis.....167
6.3.4 Conductivity Test.....170
6.3.5 Ion concentration test.....172
6.3.6 Microstructure observation.....173
6.3.7 Thermogravimetric analysis.....177
6.3.8 Strength activity test.....178
6.3.9 Discussion.....180
6.4 Summary and conclusion.....187
7 The cementitious properties of the recovered products from olivine and serpentine.....189
7.1 Introduction.....189
7.2 Material and method.....190
7.3 $MgO + SiO_2 + H_2O$ binder system.....191

7.3.1 Compressive strength 192
7.3.2 Reaction products 194
7.3.3 Microstructure 195
7.3.4 Comparison of the recovered silica with silica fume 198
7.3.5 Comparison of the recovered MgO with commercial MgO 199
7.4 Recovered MgO + H_2O binder system 204
7.4.1 Compressive strength 205
7.4.2 Reaction products 206
7.4.3 Comparison of the recovered MgO with water and with silica fume. 208
7.5 Summary and conclusion 210
8 Investigation on the cementitious properties of a binder derived from the reaction of MgO with waste acid 212
8.1 Introduction 212
8.1.1 Waste acid management 212
8.1.2 Magnesium oxychloride cement 213
8.2 Materials and Method 214
8.3 Results and discussion 215
8.3.1 Waste acid solution characterization 215
8.3.2 Hydration temperature profile 219
8.3.3 Mechanical properties 220
8.3.4 Reaction mechanism and hydration products 224

8.3.5 Material identification 229
8.4 Summary and conclusion 230
9 Conclusions and recommendations 232
9.1 Main findings 232
9.1.1 Extraction of the magnesia and silica from magnesium silicates 232
9.1.2 Characterisation the activity of the recovered products 233
9.1.3 Development of a cementitious material from the recovered products 234
9.1.4 Utilisation of the material waste to produce cementitious systems 235
9.2 Recommendation for future work. 236
9.2.1 Improve the mineral dissolution 237
9.2.2 Increase the purity of the recovered product. 238
9.2.3 Full utilization of the reaction products 239
9.2.4 Investigate the effect of seawater and waste acid on magnesia binder 240
9.2.5 Study on the durability of this binder 240
10 Reference 241

List of Figures

Figure 1-1 Global cement and fossil energy production[4, 5] 20

Figure1-2. Simplified process of the cement production[8] 21

Figure 1-3 Comparison of the alternative binders being developed[6]. 23

Figure 1-4.The world map distribution of the ultramafic rocks[19]. 24

Figure 1-5 The illustration of the main chapters 28

Figure 2-1. XRD of the natural and calcined olivine at 1400°C [48]. 32

Figure 2-2. The relationship of pH with logarithm of the measured specific dissolution rate of olivine log(*r*) at different temperature. 35

Figure2-3. Flowchart for the production of a $Mg(OH)_2$ powder from serpentine [61] ... 37

Figure2-4. Illustration of serpentine processing to separate magnesia and silica [70] 39

Figure 2-5. Surface of MgO under different calcination temperature[74] 43

Figure 2-6. Micrograph of the magnesia hydration product at different temperatures [80]. 44

Figure 2-7 Relationship between specific surface area and agglomeration ratio with magnesia reactivity [89] 46

Figure 2-8. Relationship between strength and fineness of the natural pozzolan [125] ... 53

Figure 2-9. Compassion of the strength development of M-S-H and Portland Cement [170] 58

Figure 2-10. Schematic illustration of the formation of M-S-H gel.[208] 63

Figure 2-11. Pozzolanic consumption of CH in lime - silica mixtures determined by DTA/TG [213] 65

Figure 2-12. Strength comparison of the recovered silica from olivine with silica fume [213] 66

Figure3-1. The particle size distribution of raw olivine sand 71
Figure3-2. The particle size distribution of raw serpentine sand 71
Figure3-3. XRD analysis of the olivine and serpentine sand 72
Figure3-4. The TG and DTG curve of olivine and serpentine sand 73
Figure3-5. Microscopy of the olivine particle 74
Figure3-6. Microscopy of the serpentine particle 74
Figure3-7. The particle size distribution of raw magnesia 75
Figure3-8. Microscopy of the magnesia particle 76
Figure3-9. The particle size distribution of the silica fume 77
Figure3-10. Microscopy of the silica fume particle 78
Figure3-11. XRD pattern of the silica fume [215] 78
Figure3-12. The particle size distribution of the quartz sand 79
Figure3-13. Microscopy of the quartz sand particle 79
Figure 3-14. XRD of the quartz 80
Figure3-15. Illustration of the cone and quartering method[217] 81
Figure3-16. The Ring and puck mill 82
Figure3-17 The box furnace 83
Figure3-18. The filtration setup 84
Figure 3-19 The conductivity test setup 85
Figure3-20. The compressive strength setup 89
Figure 3-21. Electron-matter interaction volume[222]. 92
Figure 3-22. The calorimeter used for this study. 95
Figure 4-1. The particle size distribution of olivine samples with different grinding times. 101

Figure 4-2. Electron microscopy analysis of the sample after grinding. 102

Figure 4-3. The pH and conductivity profile of the olivine with different grinding times. 104

Figure 4-4. The Mg^{2+}(aq) concentration of olivine in water with different grinding times. 105

Figure 4-5. The pH changes of olivine mixed with different solutions. 107

Figure 4-6. The pH profile of olivine in different acids..... 109

Figure 4-7. The $Mg^{2+}_{(aq)}$ concentration of olivine with different acids at different time intervals. 109

Figure 4-8. Mg^{2+}(aq) released from olivine under different nitric acid concentrations...111

Figure 4-9. pH profile of olivine mixed with various CO_2 content solution. 113

Figure 4-10. Magnesium concentration of olivine with different CO_2 content solution. 113

Figure 4-11. Effect of CO_2 pressure on olivine solubility after 2 hours. 114

Figure 4-12. $Mg^{2+}_{(aq)}$ concentration and reaction rate with different reaction times. 116

Figure 4-13. TG/DTG curves of references and composites recovered from olivine.....117

Figure 4-14. XRD analysis of the recovered products from olivine solution. 118

Figure 4-15. Microscopy of Mg-composite recovered from olivine with CO_2 bubbled water. 119

Figure 4-16 The linear relation between pH and log *(r)*. 124

Figure 5-1. Different factors that influencing the MgO hydration in cement materials[276]. 128

Figure 5-2 The simplified processing diagram of olivine..... 129

Figure 5-3. The evaporation and condensation process..... 131

Figure 5-4. Experimental setup of the accelerated reactivity test: *(a) pH meter; (b) probe; (c) plastic beaker; (d) plastic lid; (e) aqueous solution of magnesium oxide and acid; (f) magnet; (g) stirrer.* [88] 133

Figure 5-5. The olivine processing and its products 134
Figure 5-6 The XRD comparison of olivine before and after reaction 136
Figure 5-7. Microscopy of the olivine before and after digestion 137
Figure 5-8 Thermogravimetric analysis of the recovered product 138
Figure 5-9 The thermal degradation analysis of the recovered products 140
Figure 5-10 X-ray diffraction results of the recovered product 141
Figure 5-11. The microscopy of the olivine and the MgAc recovered from olivine 142
Figure 5-12. The element mapping of the recovered MgAc 143
Figure 5-13 The XRD pattern of the recovered MgO from Olivine 145
Figure 5-14. The microscopy and the EDS of the recovered magnesia from olivine 147
Figure 5-15. The pH profile of the MgO activity test 149
Figure 5-16. Microscopy of the hydration products from different sources of magnesia 150
Figure 5-17. The TG curves of different hydration products from olivine and magnesia 151
Figure 6-1. The illustration of the serpentine process. 157
Figure 6-3. The XRD pattern of the serpentine before and after leaching 163
Figure 6-4. Microscopy and the EDS results of the serpentines 164
Figure 6-5. XRD pattern of different silica sources 166
Figure 6-6. Particle size analysis of the silica materials. 168
Figure 6-7. The surface area and pore volume analysis of the silica materials 170
Figure 6-8. The conductivity test of the different silica materials mixed with lime water 171
Figure 6-9. The ion concentration change of calcium in different silica solutions 173
Figure 6-10. The microscopy of different silica materials mixed with CH at 28 days ... 176

Figure 6-11. The microscopy of recovered silica mixed with CH at 28 days 176

Figure 6-12. TG curves of the silica sources mixed with CH powder at different ages. 178

Figure 6-13. Strength activity index of the silica materials 180

Figure 6-14. The comparison of silica reactivity of different materials using various techniques. *(inside ring: the least reactive, outside ring: most reactive)* 181

Figure 6-15. The settled silica precipitation from leached serpentine solution. 186

Figure 6-16. XRD pattern of the precipitated silica from leached serpentine solution. . 187

Figure 7-1. Strength development of the samples mixed from different magnesia and silica sources..... 193

Figure 7-2. The TG curves of different MgO + SiO_2 samples at the age of 28 days..... 194

Figure 7-3. The microscopy of the mixture of MgO and SiO_2 at 3 days 197

Figure 7-4. The microscopy of the mixture of MgO and SiO_2 at 28 days 198

Figure 7-5. Heat flow of different magnesia mixed with silica fume 200

Figure 7-6. The quantified mass loss of CMSF and RMSF at different ages. 202

Figure 7-7. XRD results of the CMSF and RMSF at the age of 28 days. （B：Brucite ⋆: Quartz ☆: M-S-H gel） 203

Figure 7-8. XRD results of the RMSF at different ages. （☆: M-S-H gel; P: Periclase; B: Brucite） 204

Figure 7-9. Strength comparison of the sample with different MgO sources..... 206

Figure 7-10. The microscopy of the magnesia mixture at the age of 28 days. 206

Figure 7-11. Comparison of the TG curves of different MgO sources with water..... 208

Figure 7-12. Heat evolution of the reactions with R-MgO with water and silica fume . 209

Figure 7-13. XRD results of the RMSF and RMDW at the age of 28 days. （☆: M-S-H gel; P: Periclase; B: Brucite） 210

Figure 8-1. The pH profile with the addition of MgO to water and waste acid..... 217

Figure 8-2. Colour change of the waste acid before and after the addition of MgO. 218

Figure 8-3. XRD results of the precipitates from the waste acid solution 219

Figure 8-4. The hydration temperature profile of the MgO mixtures with water and waste acid and their comparison with OPC 220

Figure 8-5. The strength development of different solutions mixed with MgO 221

Figure 9-1. The proposed processing chart for olivine 238

List of Tables

Table 2-1. Chemical Composition of the serpentine before and after HCl leaching [71] 40

Table 2-2. Different grades of MgO based on calcination temperature. 41

Table 2-3. Methods for pozzolanic activity assessment..... 48

Table 2-4. Different types of MgO-based cement..... 56

Table 3-1. Material and methods used in different chapters 69

Table 3-2. Chemical composition of olivine sand and serpentine 72

Table 3-3. Chemical composition of magnesia..... 75

Table 4-1. The particle size distribution of the olivine after different grinding time..... 100

Table 4-2. The magnesium ion concentration in different pH solutions..... 107

Table 4-3. The pH and CO_2 solubility under various CO_2 partial pressure 114

Table 4-4. The Mg and Si concentration from olivine mixed with D.I. water and CO_2 water 119

Table 4-5. Thermodynamic analysis during olivine dissolution (at 1 atm, 298.5K) [264] 121

Table 5-1. The chemical composition of the olivine residue after acid leaching..... 135

Table 5-2. Quantification of the magnesium acetate produced from olivine acid dissolution 139

Table 5-3. The element analysis of the recovered MgAc from olivine dissolution..... 143

Table 5-4. Chemical composition of the recovered and commercial MgO 144

Table 6-1.The mixing design of the strength activity index test..... 160

Table 6-2. The particle size of the serpentine under different grinding durations. 161

Table 6-3. The chemical composition of the serpentine before and after HCl leaching. 162

Table 6-4. The comparison of the EDS results of different serpentines. 164

Table 6-5. Chemical composition of the silica sources..... 166

Table 6-6. The comparison of the surface area between serpentine and silica fume. 169

Table 6-7. The calcium ion concentration of the CH solution mixed with different silica sources..... 172

Table 6-8. The residual CH content of the CH + SiO_2 mixture at different ages 178

Table 6-9. The compressive strength of the sample mixed with different silica materials. 179

Table 7-1. Chemical composition of the raw materials 190

Table 7-2. The mixing ratio of the magnesia with silica for strength test..... 191

Table 8-1. Mixing proportion of the MgO-$MgCl_2$-H_2O system 215

Table 8-2. The ion concentrations of waste acid and seawater samples. 215

Table 8-3. The pH value of different solutions used for the MgO mixing..... 216

1 Introduction

1.1 Background

Concrete is the most widely used construction material for buildings and infrastructure, and it is the second most-consumed substance in the world after water. It is a mixture of aggregate, water and cement. Cement is the crucial ingredient in concrete as it reacts with water to bind the aggregate together. Although cement makes up only 10%~20% of concrete by weight, it counts for 95% of the total carbon footprint.

Global cement production, as shown in Figure 1-1, has increased more than 30-fold since 1950 and almost 4-fold since 1990, with much more rapid growth than global fossil fuel energy production in the last two decades[1]. In 2019, approximately 4.2 billion metric tons of cement were produced globally[2], and this attributed to 8% of the world CO_2 emission[3].

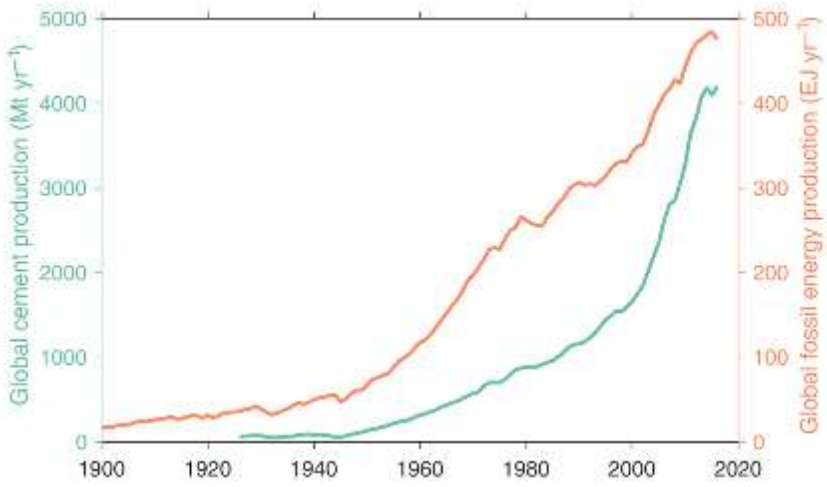

Figure 1-1 Global cement and fossil energy production[4, 5]

1.2 Cement production process

In the early 19th century, Joseph Aspdin laid the foundation for the Portland cement by heating powdered limestone and clay. The recipes used to produce modern cement have been refined over time, but the process, as demonstrated in Figure1-2, has not experienced any significant changes for the last 200 years.

During the production of cement, CO_2 is emitted through two ways: approximately 60% are the unavoidable results of the breakdown of the limestone during the calcination, and the remaining 40% is emitted by fossil fuel combustion[6]. The global cement production is expected to be 4.83 billion tons in 2030 and further increase to 5.5 billion tons in 2050[7]. The business-as-usual practices in the cement industry would lead to an undesirable CO_2 level if no actions were taken.

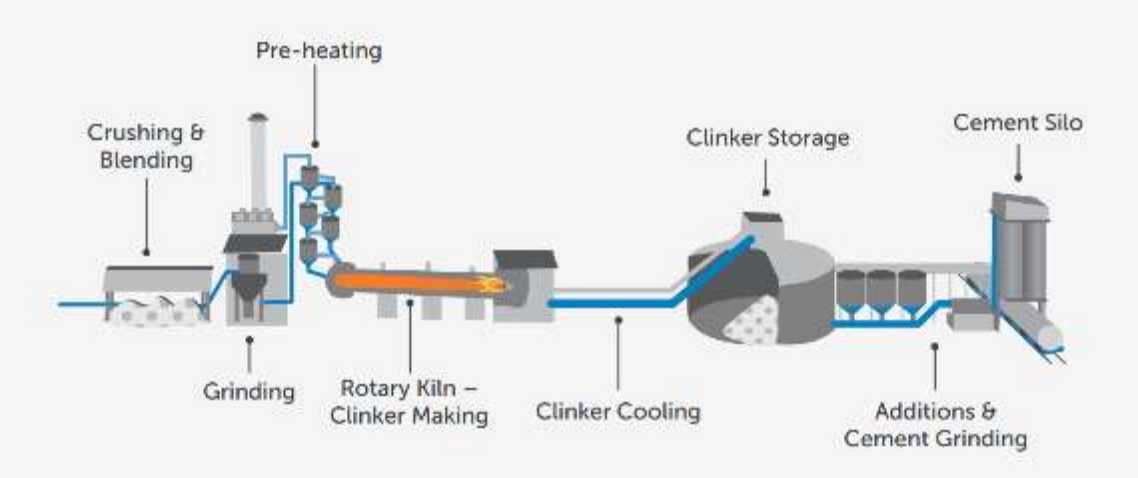

Figure1-2. Simplified process of the cement production[8]

1.3 Strategies for low-carbon cement industry

To achieve the carbon emission target by 2050, many organisations and thinktanks proposed roadmaps combined with technology and policy solutions[6, 8-11]. The potentially feasible solutions for carbon emission reduction in the cement industry can be summarised into the following categories.

- **Improving kilns energy efficiency**: deploying the latest technologies to improve energy performance levels in cement kilns, such as waste heat recovery and preheating.
- **Using alternative fuels for calcination**: promoting the use of biofuels and waste materials as fuels in cement kilns to offset the consumption of fossil fuels.
- **Electrification of the heating process**: switching to plasma, microwave energy, hydrogen or other technologies for heating.
- **Substitution of clinker:** Using other cementitious materials and decreasing the clinker to cement ratio.

- **Carbon capture, storage and utilisation**: Capturing and storing CO_2 from for other industrial processes or using concrete as a carbon sink.
- **Cement replacement**: increasing the potential of supplementary cementitious material and exploring other new sources.
- **Development of alternative binders and novel cements:** searching for new cement chemistries and further investigating the life-cycle assessment.

1.4 Research significance and motivations

The primary motivation behind this investigation is to develop a low-carbon emission binder, from widely available silicate minerals, in New Zealand and around the world.

The most prominent alternative binders and novel types of cement currently being developed have been summarised and compared according to UN Environment and ETH reports[10, 11]. As can be seen in Figure 1-3, most alternative cements do not reduce process emission intensity significantly, while those with the highest potential to cut emission are the least available. Magnesium-based silicate cement has the potential to eliminate the whole carbon footprint as a carbon-neutral binder. However, the magnesium silicate minerals are much more localised compared to limestone and typically occur deeper in the Earth's crust. This limits the development and potential of the magnesium silicate-based cement.

On the other side, both olivine ($(Mg,Fe)_2SiO_4$) and serpentine ($Mg_3Si_2O_5(OH)_4$) minerals are abundant in magnesium and silicates. In New Zealand, Olivine, an ultramafic igneous rock, is estimated to have billion tonnes of deposit around the Dun Mountain

Ophiolite Belt [12] while serpentine minerals are also commonly found in basaltic rocks that are particularly abundant in New Zealand. These ultramafic rocks are rich in magnesium and silicates (<50%wt) with its global distribution shown in Figure 1-4.

Olivine can sequester CO_2 by forming a stable carbonate, which makes it one of the most promising minerals for carbon capture and storage [13-16]. However, a limited number of studies have been found on recovering the magnesia and silica[17] or developing a cementitious binder from these minerals [18].

Therefore, there is a significant research gap for the feasibility study of using these magnesium silicates minerals to produce a cementitious system.

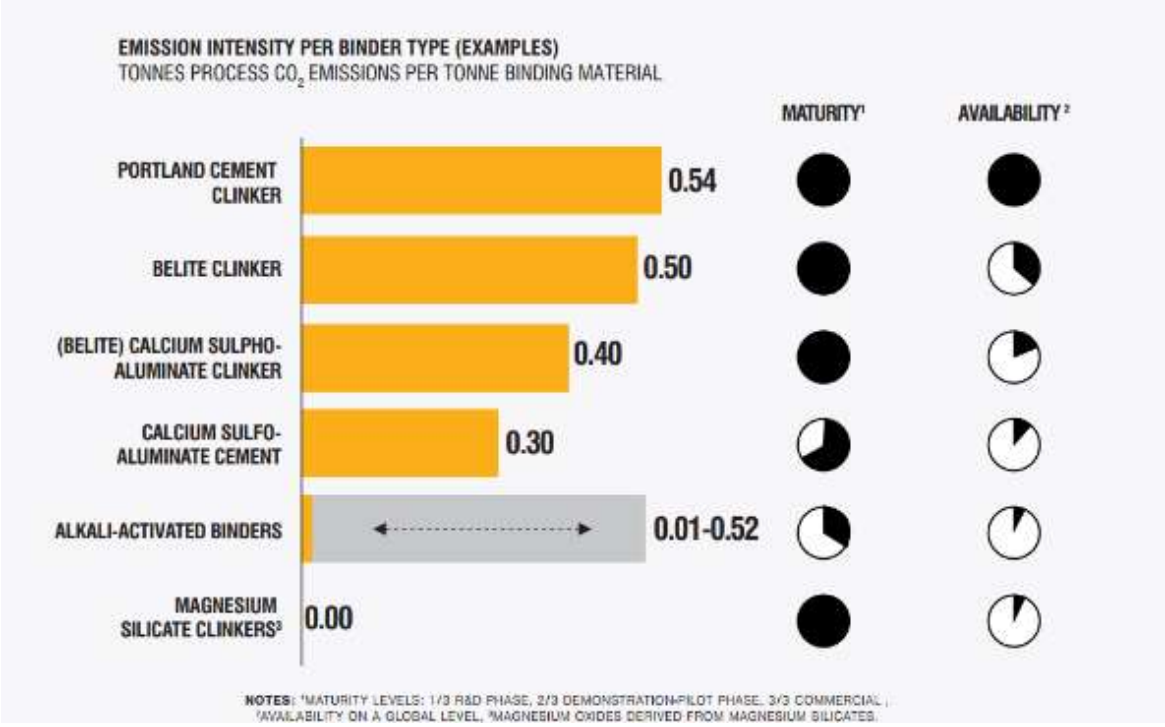

Figure 1-3 Comparison of the alternative binders being developed[6].

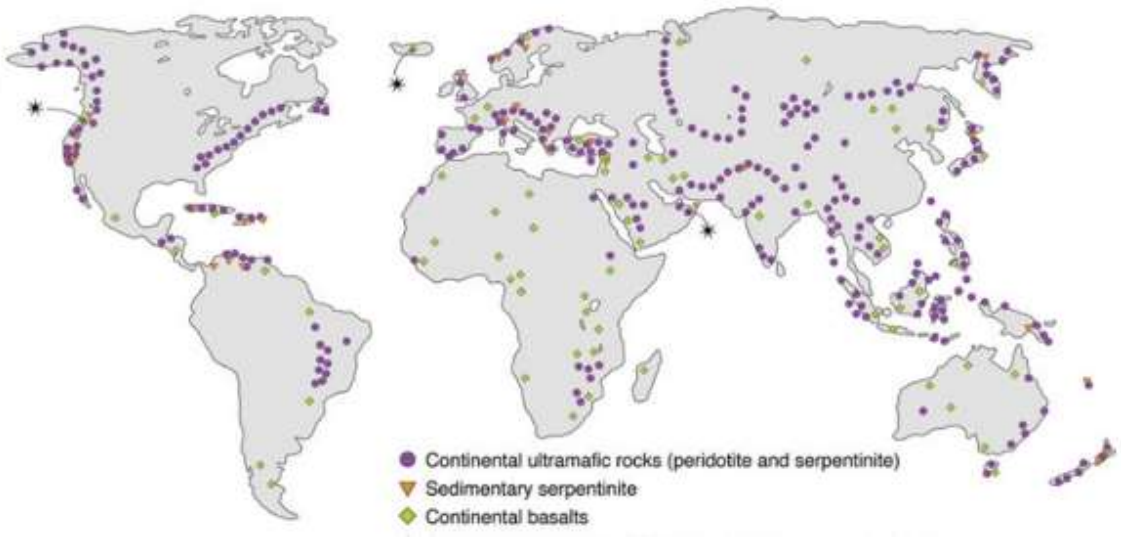

Figure 1-4.The world map distribution of the ultramafic rocks[19].

1.5 Objectives and scope

The principal objectives of this study are to develop a low carbon processing method for extracting the magnesium/silica from magnesium silicate minerals and to examine the feasibility of using them to produce cementitious binder systems.

1.5.1 Specific objectives

- To study the dissolution properties of the minerals, such as olivine and serpentine, under various environmental conditions.
- To extract magnesium oxide and silica from the raw materials and characterise their reactivities, especially MgO reactivity and silica pozzolanic reactivity.
- To investigate the possible cementitious reaction between these recovered products.
- To examine the hydration mechanism and mechanical properties of the novel binder system.

1.5.2 Scope of the research

- This research aims to use relatively low energy processing methods with readily available materials. High temperature/pressure, extensive calcination or grinding, and complex multi-stage process are not used although they are considered beneficial for the production.
- The study focusses on the dissolution and recovery of the magnesium and silica from minerals. The recovery of metal ions, such as iron, or hydrogen gas are outside the scope of the project.
- This is a *proof-of-concept* study of using the recovered products for an alternative binder. The optimization of the mixing proportion for better performance will not be examined.
- The hydration reaction, microstructure properties and mechanical strength development of the novel binders will be investigated at the paste/mortar level. Due to the limited quantity of the recovered products, concrete samples will not be produced while the material durability is also out of the scope.

1.6 Outline of the thesis

Chapter 1 provides an introduction of the proposed research in terms of background and objectives. It points out the significant environmental impact caused by the cement production but there has been lacking innovation since its invention. Future trends for developing the low-carbon cement are summarised, and the niche market for this project was identified. This chapter also establishes the expectation for the final finding and how the thesis is structured.

Chapter 2 summarises the existing knowledge regarding this topic and sets the starting point of this research. To avoid repeating what had been already investigated or re-inventing the wheel, it focuses on reviewing the current situation of magnesia-based cements, mineral processing for ultramafic minerals and the feasibility of developing cementitious materials from these minerals. Based on the objectives set in Chapter 1, this chapter identifies the knowledge gap between what we know and what we do not know.

Chapter 3 gives a detailed account of the materials used in this study and also the procedures and the methods that were followed in completing the experiments. The experiment methodologies cover sampling, processing, and analysing. This chapter also describes the sources and properties of the raw materials.

Chapter 4 starts the exploration on the magnesium-silicate material: olivine. Different factors affecting the magnesium dissolution from the olivine, such as particle size, solution pH, CO_2, temperature and pressure, are investigated. By summarising the ion concentration data, this section explains the thermodynamics, kinetics and the mechanisms of its dissolution.

Chapter 5 focuses on the recovery of the magnesium composites from olivine, based on the optimum dissolution conditions outlined by Chapter 4. It establishes a *digestion- filtration- evaporation- decomposition* recovery process. The intermediate products between each stage and the final product (recovered MgO) are characterised using various techniques.

Chapter 6 provides information on the extraction of silica from another widely distributed magnesium-silicate mineral: serpentine. It proposes the silica recovery process from this mineral. The recovered product is comprehensively analysed and compared with

commonly used natural pozzolans (rice husk ash, micro silica) and an industrial by-product (silica fume). The pozzolanic reactivity assessment methods including conductivity test, thermogravimetric analysis, strength activity index, microstructure observation and phase identification.

Chapter 7 investigates the hydration and mechanical properties of the binder system produced from the reaction of the recovered product from the magnesium-silicate minerals. The MgO recovered from olivine is mixed with the SiO_2 extracted from serpentine. It also compares the binders mixed with commercial source and the recovered products, respectively.

Chapter 8 further explores the possibility of reusing the waste acid solution after the silica extraction from Chapter 7. This chapter first characterises the composition of the waste solution and investigates its hydration reaction with the magnesia product. The mechanical property and the reaction products are studied in this section.

Chapter 9 is the conclusion part of the thesis. It highlights the main findings of the research work and provides alternatives to the identified challenges faced by the cement industry. It also aims to fill the knowledge gap outlined in the introduction sections. However, due to the limitation of this research, recommendations for future investigation are provided.

To further clarify the and relations of experiment chapters, i.e.: Chapter 4~8, a visualised structure is illustrated below in Figure 1-5.

Chapter 4 and 5 are both based on olivine studies. However, Chapter 4 focuses on the magnesium dissolution from the olivine while Chapter 5 investigates the recovery and the characterisation of the recovered magnesia. Similarly, Chapter 6 presents the

dissolution, recovery and the property characterisation of the silica, but from another magnesium -rich mineral: serpentine.

Chapter 7 and 8 demonstrate the *proof-of-concept* of developing cementitious materials from olivine and serpentine. The recovered MgO is mixed with the extracted SiO_2 to produce the magnesium-silicate binder, and it is investigated in Chapter 7. The by-product from the silica extraction: waste acid solution, is used to react with commercial MgO to test its feasibility of developing a magnesium oxychloride binder.

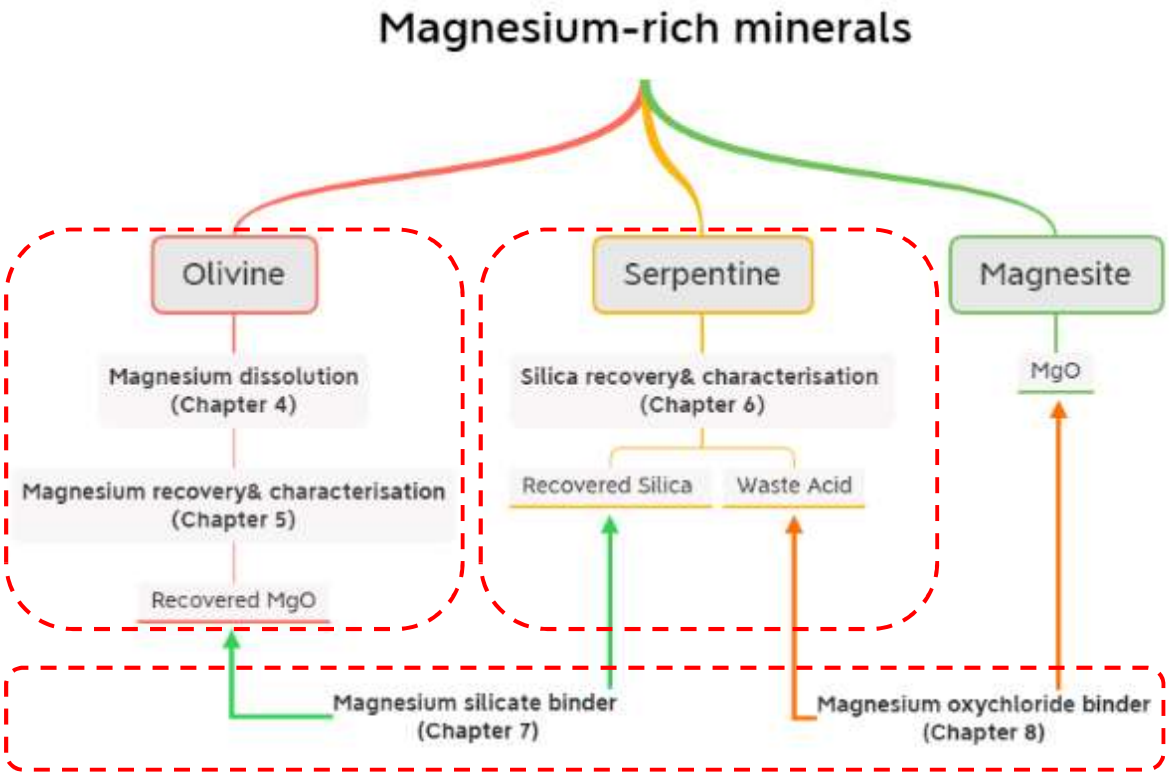

Figure 1-5 The illustration of the main chapters

2 Literature review

2.1 Introduction

The previous chapter has identified the current challenges for the cement industry and outlined the future strategies for a low-carbon cement economy. Among these viable options, this research focuses on the development of an alternative magnesium-based binder from world available minerals. This chapter aims to summarise the relevant information which lays the foundation for this research.

The literature review first examines the general information on the magnesium silicate minerals: their composition and other properties. It also reviews the current processing methods of these minerals for their application. Previous investigation on their potential for magnesium and silica recovery are summarised.

To better understand the property of the materials, this chapter outlines the source and the properties of the magnesium oxide and silica. Particularly, it focuses on the methods to measure and improve the material reactivities, as these methods and properties are critical for the recovered products from the minerals.

Since this project is proposing a magnesium-based binder, it presents information on the reaction mechanism and hydration properties of the five different types of Mg-based

cements from past studies. Previous efforts on developing the binder system from these magnesium silicate minerals are also summarised.

2.2 Magnesium silicate minerals

2.2.1 Olivine

Olivine is a nesosilicate, or orthosilicate, mineral with the general formula $(Mg,Fe)_2SiO_4$. The olivine group is a solid solution set existing between forsterite (Mg_2SiO_4) and fayalite (Fe_2SiO_4). Olivine is relatively reactive in comparison to other silicate minerals and has a simple mineral structure that contains isolated silica tetrahedra[20-24].

Ultramafic rocks are igneous rocks with high magnesium oxide (generally >18%) and silica content typically around 45% or less. The most common magnesium silicate minerals are olivine and serpentine[25, 26]. These two minerals have been commonly investigated for mineral carbonation as they give the highest capacity and longest storage time of the currently known carbon dioxide capture and storage options[27, 28].

At Earth's surface temperatures, olivine dissolution usually occurs stoichiometrically and few weathering products are formed. The reactions (see Equation 2-1 and Equation 2-2) typically occur in natural environments over a range of temperatures and pressures in what is commonly thought to take thousands of years. However, it is proposed that if the olivine was ground into very fine particles, for example, less than approximately 100 μm, the reaction can be rapid even at ambient temperature[29-31].

$$2Mg_2SiO_{4s}\ (Olivine\ forsterite)+3H_2O \rightarrow Mg_3Si_2O_5(OH)_4(Serpentine)+Mg(OH)_2 \qquad \text{Equation 2-1}$$

$$3Fe_2SiO_4\ (Olivine\ fayalite)\ +2H_2O \rightarrow 2Fe_3O_4+3SiO_2+2H_2 \qquad \text{Equation 2-2}$$

Weathering of olivine is sometimes called serpentinization due to the formation of serpentine minerals as alteration products[32].

2.2.2 Serpentine

Serpentine is a rock which consists predominantly of one or more serpentine group minerals: antigorite, chrysotile, and lizardite. It commonly contains 32–38% MgO and 35–40% SiO_2 with minor amounts of Fe, Al, Ca, Cr, and Ni.

Currently, serpentines are mainly used in industry as railway ballasts, building materials and thermal or electrical insulations.[33-35]. Apart from these traditional applications, large serpentine reserves have the potential for being also used also in more sophisticated non-traditional fields.

Serpentine is also used as a potential source of nickel [36-38] or as a raw material in the production of metallic magnesium and/or pure magnesium compounds [39-41].

2.3 Mineral processing

2.3.1 Thermal activation

In order to improve the activity of the mineral, calcination of the minerals usually takes place before any further processing.

The calcined olivine is an active material that can be employed as an in-situ catalyst in a fluidised bed[42-44]. It also can be added into the blast furnace burden to improve slag stability and fluidity[45]. However, the phase transformation of olivine during calcination is not well understood, with only a few studies reported in the literature[46, 47].

Mitchel et al. [48] did a comprehensive investigation on the phase transformations of olivine. According to the XRD data shown in Figure 2-1, the main phase in natural olivine (mined at the Åheim Plant in Norway) was forsterite (Mg_2SiO_4) while the secondary crystalline phases were enstatite ($MgSiO_3$), serpentine ($Mg_3Si_2O_5(OH)_4$) and α-quartz (SiO_2). After calcination (1400 °C), no peaks of the hydrated serpentine phase ($Mg_3Si_2O_5(OH)_4$) or α-quartz SiO_2 were detected, and a new spinel phase appeared.

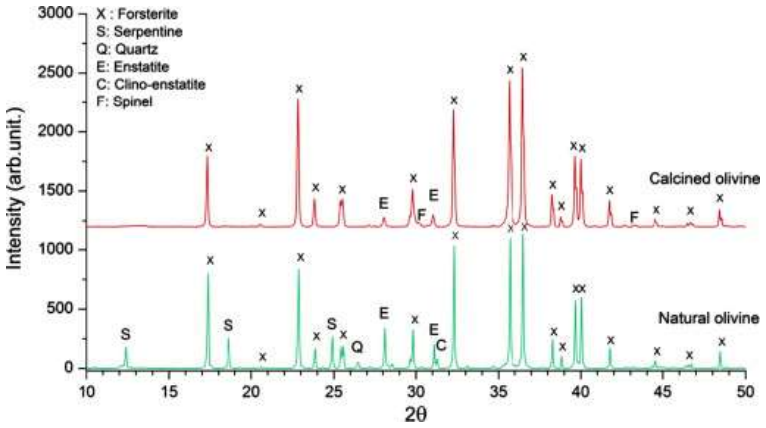

Figure 2-1. XRD of the natural and calcined olivine at 1400°C [48].

By calcining the olivine at varying temperatures in air, XRD analysis highlighted the structural transformations consisting of the dehydration of serpentine below 600 °C, the disappearance of the quartz phase at 1030 °C, and the formation of iron oxide phases.

Among silicate minerals, olivine is susceptible to mechanical and chemical breakdown, while the common products of these reactions are serpentine phases [49].

During the calcination of serpentine, water is released according to Equation 2-3. The water loss leads the compact, double-layered structure of serpentine to become disordered. The intermediate $Mg_3Si_2O_7$(s), defined as dehydroxylate I, is therefore expected to be more reactive than the raw (un-calcined) serpentine, thus displaying faster magnesium dissolution in acidic solutions. The calculated equilibrium temperature for the thermal decomposition of serpentine is 539 °C [50]. At temperatures above 800 °C, dehydroxylate I is converted into forsterite (Equation 2-4). Conversion of serpentine to forsterite as a primary product, accompanied by amorphous silica, at temperatures between 800 °C and 1000 °C is described by Equation 2-5.

$$Mg_3Si_2O_5(OH)_4\ (s) \rightarrow Mg_3Si_2O_7\ (s) + 2H_2O\ (g) \qquad \textit{Equation 2-3}$$

$$2Mg_3Si_2O_7\ (s) \rightarrow 3Mg_2SiO_4\ (s) + SiO_2\ (s) \qquad \textit{Equation 2-4}$$

$$2Mg_3Si_2O_5(OH)_4\ (s) \rightarrow 3Mg_2SiO_4\ (s) + SiO_2\ (s) + 4H_2O \qquad \textit{Equation 2-5}$$

The Differential thermal analysis (DTA) and the X-ray Diffraction (XRD) result drawn by Midgley[51] demonstrated the serpentine rock was mainly composed of lizardite, $3MgO \cdot SiO_2 \cdot 2H_2O$. By calcination, the lizardite can be replaced by the crystalline $2MgO \cdot SiO_2$ (olivine) and amorphous magnesium silicate. The amorphous magnesium silicate can react with water, and according to Midgley, was believed to form a material akin to saponite, $3MgO \cdot 4SiO_2 \cdot H_2O$.

Hršak[50] proposed that the optimum thermal treatment for serpentine is heating the specimens at a temperature of 660 °C for 3 hours. By using this parameter, the original crystal lattice was broken down, and an amorphous mixture of free oxides, magnesium oxide and silica was obtained with the lowest energy consumption. However, the XRD test failed to identify the types of mixtures due to their amorphous phase.

Based on another XRD result conducted by Nemie and Hršak [52] in 2005, it indicated the main component of serpentine is antigorite, while no significant characteristic peaks occur on the sample after calcination. It concluded that thermal treatment of antigorite, $(Mg,Fe)_3Si_2O_5(OH)_4$, destroyed the original crystal lattice and resulted in amorphous mixtures.

2.3.2 Magnesium dissolution

To utilise the magnesium silicate minerals (olivine or serpentine) for carbon sequestration, the extraction of magnesium is the essential step for the subsequent carbonation to form the stable magnesium carbonate.

Oelkers et al. [53] did a critical review on the olivine dissolution rates and summarised four major significant factors influencing forsteritic olivine dissolution rates: a) pH, b) water activity, c) temperature, and d) mineral-fluid interfacial surface area.

Prigiobbe et al. [54] further explored the effect of temperature, pH, CO_2 pressure and salinity on the olivine dissolution kinetics. The pH was found to be the most important factor, and it was found to have a linear relation with the logarithm of the measured specific dissolution rate, *log(r)*, as shown in Figure 2-2.

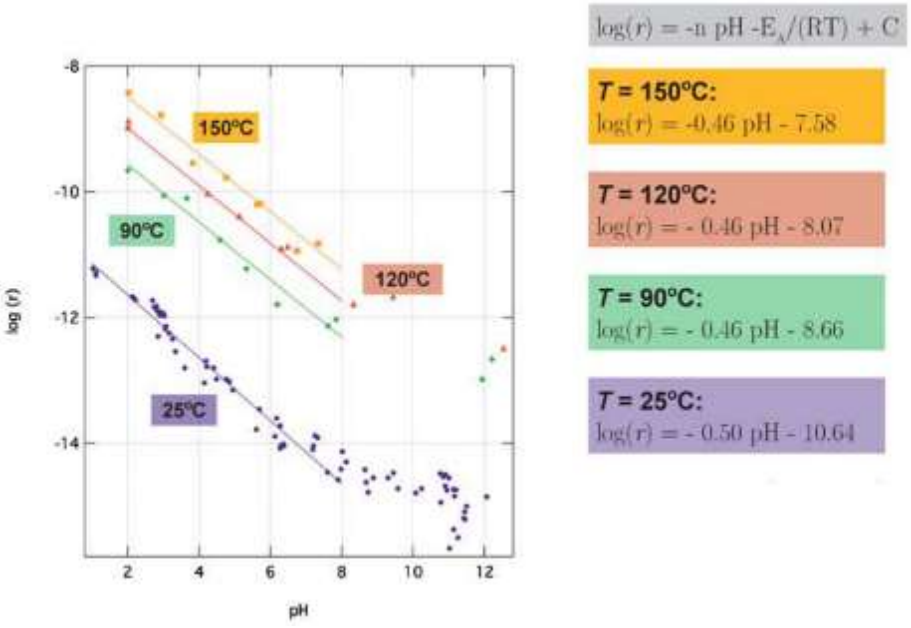

Figure 2-2. The relationship of pH with logarithm of the measured specific dissolution rate of olivine log(*r*) at different temperature[54].

Wogelius and Walther [55] measured the dissolution rates of olivine in aqueous solutions over the pH range 2 ~ 12.4 at 25 °C, and found the following relationship between the reaction rate with the concentration of active hydrogen ion at low partial pressure of CO_2.

$$R=9.07 \times 10^{-12} (a_{H^+})^{0.54} +5.25 \times 10^{-15} +2.33 \times 10^{-17} (a_{H^+})^{-0.31} \quad \text{Equation 2-6}$$

Where R is the rate of olivine dissolution (mol/cm^2/s), and a_{H^+} is the activity of H^+ in solution. However, in basic solutions, olivine dissolution rates are nearly pH-independent throughout the pH range 6 ~ 12. Chen[56] confirmed this relation between pH 2 and 5 using a batch reactor at a temperature of 65 °C and derived the simplified dissolution rate (R) law, as shown in the equation

$$R=10^{-8.54} \times (a_{H^+})^{0.70} \qquad \text{Equation 2-7}$$

Consequently, acid digestion/leaching is usually the first stage of the overall dissolution process. The leaching generates a soluble magnesium salt, which builds up in solution. The solution was then separated from the insoluble residue, and later refined. Commonly used lixiviants are hydrochloric acid and other inorganic and organic acids.

$$Mg_2SiO_4\ (Olivine) + 4H^+\ (aq) \rightarrow 2Mg^{2+}\ (aq) + SiO_2(s) + 2H_2O \qquad \textit{Equation 2-8}$$

$$Mg_3Si_2O_5(OH)_4(Serpentine) + 6H^+(aq) \rightarrow 3Mg^{2+}(aq) + 2SiO_2(s) + 5H_2O \qquad \textit{Equation 2-9}$$

Teir and Revitzer[57] compared the dissolution of natural serpentinite in different acids, and showed that H_2SO_4 was the most efficient at extracting magnesium from serpentinite, followed by HCl, HNO_3, HCOOH and CH_3COOH. They also proposed that the dissolution rate may be limited by formation of a diffusion layer around serpentinite particles with a size distribution of 74 ~ 125 μm.

Yoo et al. [33] studied the dissolution of magnesium from serpentine minerals in H_2SO_4 solution under different concentration, dissolution temperature and agitation speed. Complete dissolution of Mg from natural serpentine was achieved in 30 min at a temperature of 90 °C in 0.5 M H_2SO_4. In 2015, Zhao et al.[58] further investigated this and suggested the leaching efficiency was limited by the produced layer with the layer thickness being influenced by agitation and ultrasonication. In this study, about 84% of Mg was recovered.

Gabra[59] proposed an alternative approach of utilizing SO_2 gas as a leaching agent for serpentine, which leads to the formation of soluble magnesium hydrogen sulphite. High purity magnesium oxide (99.5%) was prepared from the crystalline magnesium sulphite through decomposition in an inert atmosphere such as nitrogen at 700 °C.

In 2008, Lin [60] extracted magnesium hydroxide from serpentine using HCl digestion and then NaOH titration, as shown in Figure2-3. The extracted $Mg(OH)_2$ powder had a mean crystal domain size as small as 12 nm and an apparent surface area of 54 m^2/g, compared to commercially available $Mg(OH)_2$ of 33 nm and 3.5 m^2/g, respectively.

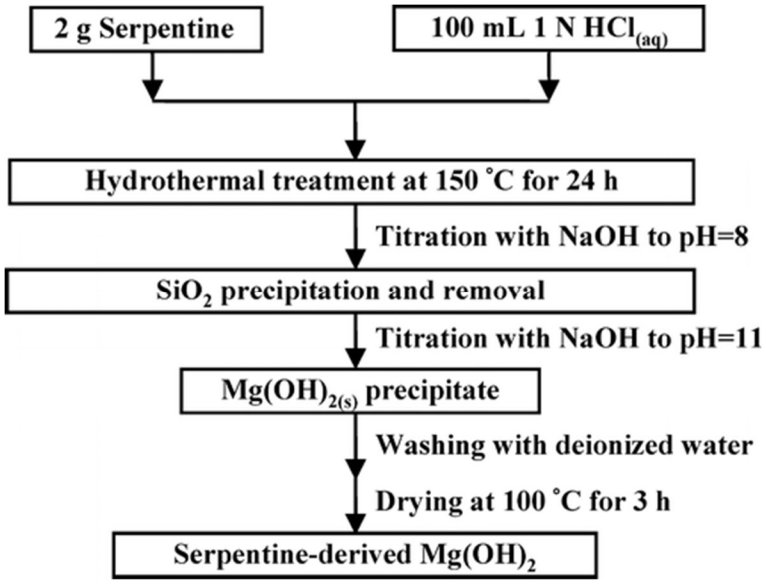

Figure2-3. Flowchart for the production of a $Mg(OH)_2$ powder from serpentine [60]

A research group in Åbo Akademi University, Finland [61-66] investigated the use of magnesium silicates minerals, especially serpentine, to capture and store CO_2. An optimum range of reaction conditions for the extraction stage (Mg extraction) and precipitation stages (production of valuable products) of the process were identified:

- Mg extraction is achieved by reacting pulverized serpentine or olivine rocks with ammonium sulphate salt at temperatures 270 ~ 600 °C.
- The study found the serpentine reacted significantly quicker than olivine.
- Higher Mg/Fe ratio, surface area and porosity led to higher reaction rate.

- It was suggested that reaction temperatures 400~480 °C and time 30~60 min was sufficient for 65% of Mg extraction from the serpentinite rocks tested.

Teir and Kuusik [67] developed an approach to capture and storage of CO_2 by precipitation of magnesium carbonate in the dissolved serpentine solution. CO_2 gas was bubbled through to react with the magnesium in solution and 94% of magnesium ions and 37% carbon dioxide were observed to convert to carbonate. However, this process consumed a large amount of NaOH (2.4 tonnes per tonne CO_2 stored) and acid (2~4 tonne per tonne CO_2 stored).

To sum up, the typical treatment for magnesium silicate minerals for magnesium dissolution is the digestion in strong acids. Elevated reaction temperatures and extended reaction durations have commonly been used. After the Mg dissolution, NaOH or another basic solution was added to increase the pH of the solution to allow the Mg to precipitate. Alternatively, CO_2 was bubbled directly through the solution to react with the Mg^{2+} and to produce geologically stable magnesium carbonates ($MgCO_3$). However, at the current stage, this is more a proof of concept study, as the energy intensity for achieving the reaction conditions and the chemical consumption are not economically viable for carbon sequestration.

2.3.3 Silica recovery

Compared to preparing magnesium compounds from magnesium silicate minerals, little attention has been devoted to the processing of insoluble residue (SiO_2) into products tailored for applications in industry or environmental protection. High purity amorphous

silica is prepared in relatively expensive ways, such as hydrolysis of tetraethoxysilane . All silica gels and precipitated silica of primary commercial importance are currently derived from sodium silicate[68].

In 2004, Pietrikova et al. [69] investigated the mechanism of the leaching process of serpentine to produce SiO_2, as demonstrated in Figure2-4. The acid concentration and the reaction temperature along with duration are crucial factors. The highest reaction efficiency was using 25% HCl with the solid to liquid ratio of 1:4. The temperature was above 105 °C and 1 hour was the most cost-effective reaction time. Increasing the leaching time above 2 hours did not increase the reaction efficiency. The final product after processing was a powder with the content of SiO_2 up to 99%.

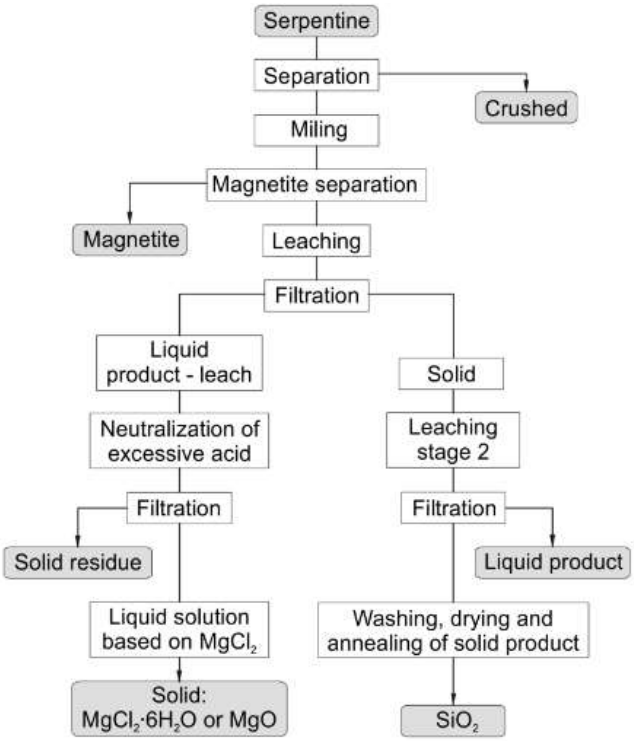

Figure2-4. Illustration of serpentine processing to separate magnesia and silica [69]

Fedoročková et al.[70] examined the effect of precipitating agents (HCl, CO_2 and $(NH_4)_2CO_3$) on the surface area of the recovered silica powders after hydrochloric acid leaching. The study concluded that the surface area of the resulting silica powders depends on the pH and the composition of the silicate solution. A microporous xerogel with a high specific surface area (541 m^2/g) was formed in a highly acidic solution. The high surface area of the product makes it an active amorphous silica. The following table demonstrates(Table 2-1) a comparison of the chemical composition of the sample of serpentine before and after acid leaching. The purity of the SiO_2 in the serpentine residue was 87.2% according to the XRF result.

Table 2-1. Chemical Composition of the serpentine before and after HCl leaching [70]

	Chemical composition (wt.%)							
	MgO	CaO	SiO_2	Fe_2O_3	Al_2O_3	NiO	Cr_2O_3	L.O.I.
Serpentine	38.2	1.2	37.3	5.7	1.4	0.1	0.3	14.1
Serpentine Residue	1.54	0.08	87.2	0.4	0.8	0.02	0.04	9.2

2.4 Properties of MgO and SiO_2

It is now acknowledged that extracting the magnesium and silica from these minerals is the first step, no matter whether the mineral is used for carbon storage or cement development. Therefore, the properties of the extracted material need to be examined and compared with the ones from commercial sources. This section provides information on the properties and characterisation methods for the conventionally used MgO and SiO_2.

2.4.1 Magnesium oxide

2.4.1.1 Production

Magnesium oxide has to be obtained from other commercially available materials as it does not exist in nature. There are different sources from which it can be derived. The first source is from calcination of mined magnesite deposits with the identified world resource of 12 billion tons[71]. The main reaction is

$$MgCO_3 + Heat\ (>600\ °C) \rightarrow MgO + CO_2 \qquad \text{Equation 2-10}$$

Another commercial way of producing magnesia is synthetic processing from seawater, inland brines, or salt deposits. Adding a strong base to the seawater or brine can raise the pH to 10.5 and leads to $Mg(OH)_2$ precipitation. The average Mg^{2+} concentration in seawater is approximately 1.29~1.35 g/L[72]; thus, this source is huge and almost limitless.

Magnesium oxide can also be obtained from the mining and calcination of brucite precipitated from various Mg-compounds.

Based on the different calcination temperatures, magnesia is generally classified into several grades (shown in Table 2-2). In the temperature range of 500 ºC to 1000 ºC, the magnesium carbonate ($MgCO_3$) transforms to magnesia (MgO) gradually followed by surface reorganization with less defects occurs between 1000 ºC to 1500 ºC. When above 1500 ºC, the magnesia particles are molten and agglomerate. The magnesia produced above the fusion point is perfectly reorganized and chemically stable. Among them, the light burned magnesia, i.e. the reactive magnesia, is the main raw material for the most types of magnesia based cement system, expect for magnesium phosphate cement which uses the dead burned MgO.

Table 2-2. Different grades of MgO based on calcination temperature.

Grades	Light Burned	Hard burned	Dead burned	Fused

Calcination temperature	700 ~ 1000ºC	1000 ~ 1500ºC	1500 ~ 2000ºC	> 2800ºC
Reactivity	High	Low	Lower	Very little
Applications	Agricultural, catalysts.	Abrasives, building products, ceramics.	Refractory applications.	Refractory / electrical insulating.

It can be seen from the Table 2-2 that by increasing calcination temperature, the reactivity decreases. It can be attributed to the reduction of the specific surface area (SSA) and the increase of the particle size. The microstructure of the magnesia surface in different calcination temperatures is shown in Figure 2-5.

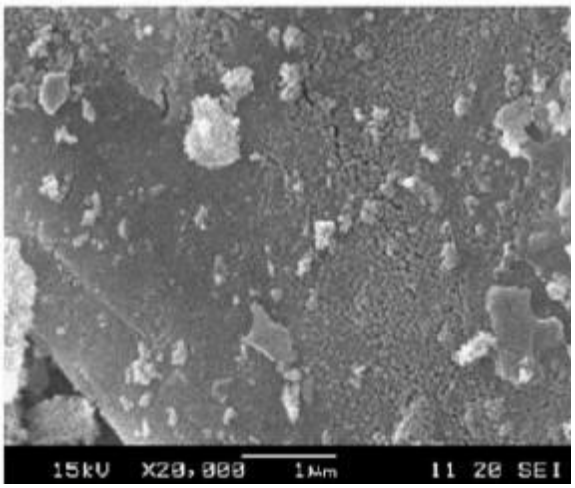

(a) 900 ºC for 1 hour

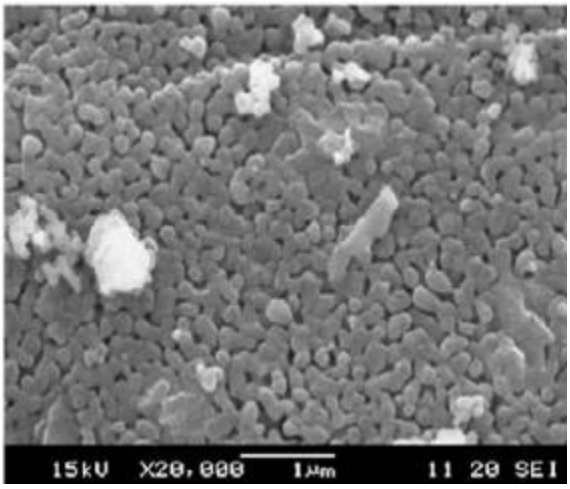

(b) 1100 ºC for 1 hour

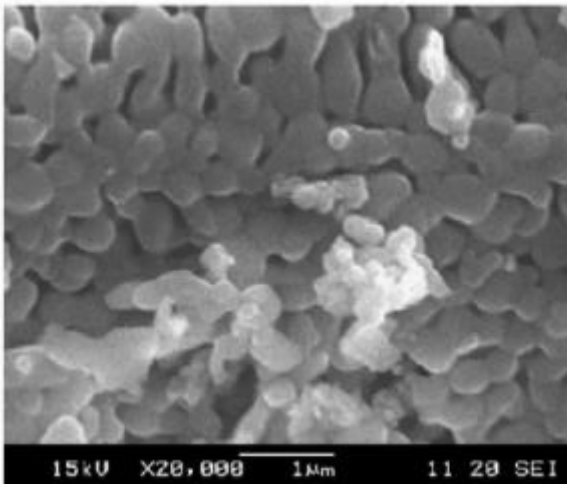

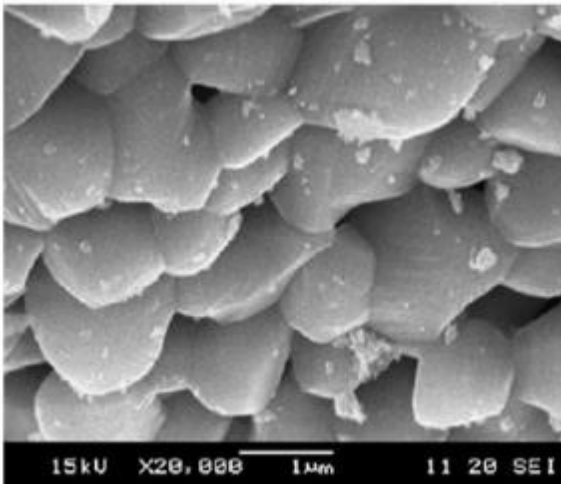

(c) 1100 ℃ for 1.5 hour *(d) 1300 ℃ for 1h*

Figure 2-5. Surface of MgO under different calcination temperature[73]

There is limited number of reports on obtaining magnesia from other materials as decomposition of magnesium salts was considered to be the easiest approach to obtain MgO. However, the surface morphology and particle size are difficult to control using this methods. In order to control the morphology of the particle, Pradita el al. [74] synthesised magnesium oxide particles from two magnesium sources using ultrasonic spray pyrolysis. It pointed out that by using this method, MgO particles from magnesium acetate ($Mg(CH_3COO)_2 \cdot 4H_2O$) precursor has hollow irregular shape and hollow spherical shape particle was resulted from the magnesium nitrate ($Mg(NO_3)_2 \cdot 6H_2O$) precursor. The purity and the hydration property of the obtained MgO was out of the scope of their study.

2.4.1.2 MgO Hydration

The hydration of magnesia occurs when it comes into contact with water, water vapours, or moist conditions. The MgO particle dissolves in water and when it reaches the maximum solubility of its main hydration product, magnesium hydroxide, $Mg(OH)_2$, begins to precipitate. There are serveral explanations for the hydration of MgO according to literature [75-78].

The commonly accepted mechanism of the hydration of the magnesia can be divided into two steps. First, the water is absorbed at the surface and diffuses into the porous MgO particles. Then it begins to hydrate at the grain boundaries and forms a brucite ($Mg(OH)_2$) layer around the particle. At this stage, the reaction rate of magnesia with water is governed by the oxide dissolution. As the reaction proceeds, the magnesia particles are

coated by the hydrates both over the surface and in pores. Thus, the porosity is reduced, and the water diffusion is hindered inside particles. It becomes diffusion controlled and the overall reaction rate is then decreased. The second mechanism is based on the hydration process of magnesia at temperatures lower than 90 ˚C. At lower temperatures, the hydration is purely kinetically controlled (the oxide dissolution) as the conversion is relatively slow.

The microstructures of the hydration products of magnesia at different temperatures is shown in Figure 2-6. As can be seen at low temperature, the magnesium hydroxide is porous while the particles became more compact at high temperatures.

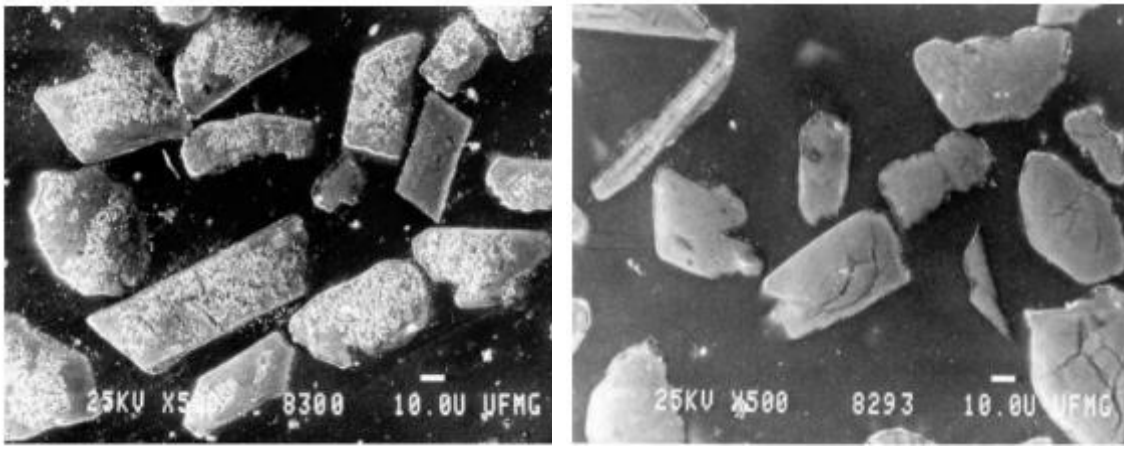

a. At low temperature (35 ˚C) *b. At high temperature (90 ˚C)*

Figure 2-6. Micrograph of the magnesia hydration product at different temperatures [79].

There are many factors that significantly influence the hydration rate and degree, which includes the reactivity, specific surface area and particle size. Besides, the environmental conditions such as pH, pressure and temperature, ion concentration are also relevant. According to the literature [80-83], the high chemical reactivity directly leads to the high conversion rate to brucite while increasing the temperature and pressure can

improve the hydration rate as well. Some researchers [84-86] also indicated that the hydration rate and degree can be improved by adding a hydration agent such as magnesium acetate, acetic acid or hydrochloric acid, which decrease the pH value thus increase the solubility of MgO . It lead to the increase the Mg ion concentration which influences the hydration degree.

2.4.1.3 Reactivity of MgO

Due to the variation of the magnesia source and production process, the characteristics, hydration properties, and impurities of the magnesium oxide may have significant differences. It is important to understand what factors affect the reactivity of the magnesium product and to compare the commercial products with the one recovered from minerals.

In 2008, Chau and Li [87] proposed a simple but effective method for evaluating the reactivity of MgO. The reactivity (R) of the MgO was expressed by the time required to neutralise an acetic acid solution (1 mol/L, 100 mL) by the MgO particles (5 g). Based on their experimental results of the reactivity (R), they further classified the light burnt MgO into four different classes: $R<90s$, $90s<R<180s$, $180s< R< 240s$ and $R> 240s$.

To study the relationship between their properties with reactivity, pH, surface specific area and hydration behaviour, Jin [88] compared 14 products of commercial reactive grade magnesium oxide. Their research stated that synthetic magnesia generally demonstrated higher reactivity with less impurities, larger surface area with smaller crystallite size.

It was found that the reactivity of the magnesia increases with the increase of specific surface area until 60 m^2/g and formed a linear relationship with the agglomeration ratio, as shown in Figure 2-7.

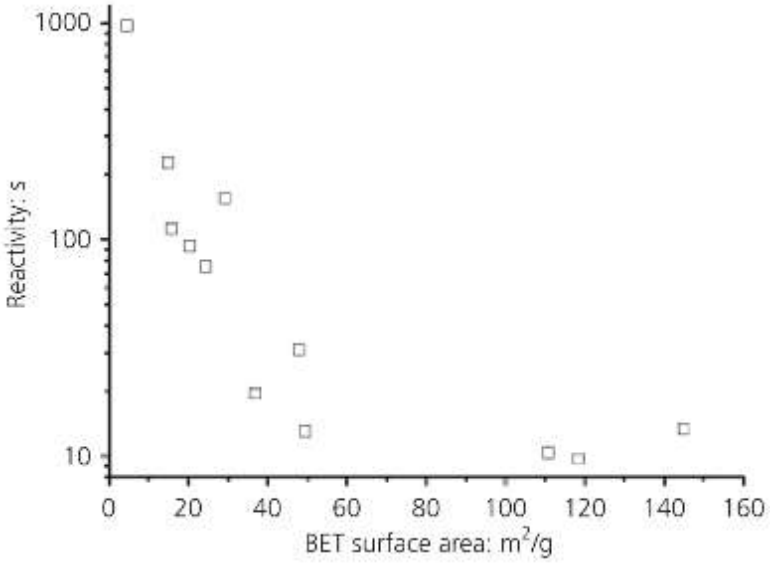

(a). Relationship between specific surface area and reactivity

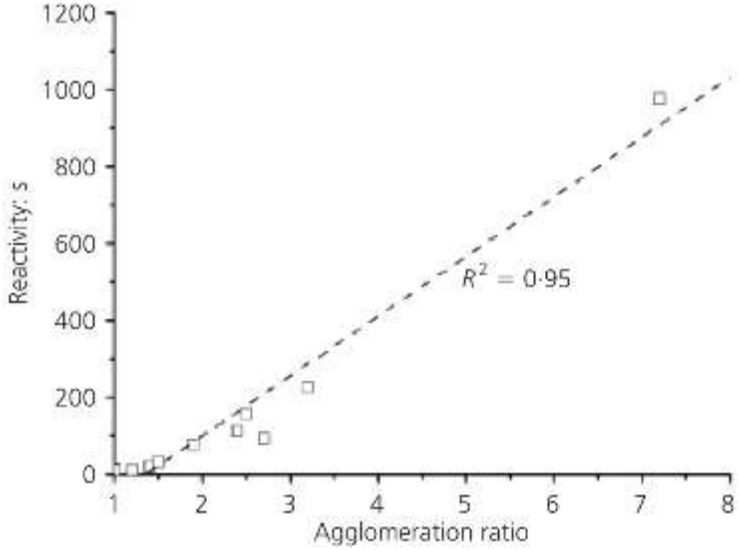

(b). Relationship between agglomeration ratio and reactivity

Figure 2-7 Relationship between specific surface area and agglomeration ratio with magnesia reactivity [88]

2.4.2 Silica

Silica, also known as silicon dioxide, is the major component of the Earth's crust and by far the most common crystalline form is quartz. However, other forms can be produced under certain natural or laboratory conditions. These forms can be classified into the following types [89-92]:

- anhydrous crystalline SiO_2.
- hydrated crystalline $SiO_2 \cdot xH_2O$.
- anhydrous amorphous silica of microporous anisotropic form such as fibres or sheets.
- anhydrous and hydrous amorphous silica of colloidally subdivided or microporous isotropic form such as sols, gels and fine powders.
- massive dense amorphous silica glass.

Among these, the amorphous silica exhibits extensive external and internal surfaces and have been used in the cement construction to improve its performance.

2.4.3 Amorphous silica

Amorphous silica does not have a crystalline structure and shows no intensity peaks in X-ray diffraction measurement. The amorphous silica can be found in various materials:

- in naturally occurring minerals associated with volcanic activity and geothermal deposits, such as pumice and perlite.
- the by-product from industrial process, e.g.: silica fume, fly ash and blast furnace slag.

- after the processing of waste materials, such as rice husk ash, incinerated sewage sludge.

These amorphous silicas are also known as pozzolanic materials. Pozzolan, according to ASTM C125 [93], is defined as

> *"a siliceous and aluminous material which, in itself, possesses little or no cementitious value but which will, in finely divided form in the presence of moisture, react chemically with calcium hydroxide at ordinary temperature to form compounds possessing cementitious properties"*

The ability of amorphous silica to react with calcium hydroxide (CH) to form cementitious materials is defined as pozzolanic activity.

2.4.4 Pozzolanic activity assessment

For assessing and comparing the pozzolanic activity of different materials, many test methods have been proposed. According to Donatello et al. [94], they can be categorised into the following types as shown in Table 2-3.

Besides these quantitative techniques, other methods like observing the microstructure of the hydration products using Scanning Electron Microscopy (SEM) [95] could be useful. In addition, the particle size analysis and specific surface area [96, 97] are commonly used as indicators.

Table 2-3. Methods for pozzolanic activity assessment

	Methods	Techniques	Reference
Direct measure of the CH consumption with time	Analytical	*X-ray diffraction*	[98, 99]
		Thermogravimetric analysis	[100, 101]
	Chemical	*Frattini titration test*	[102, 103]
		Saturated lime titration test	[104, 105]

Indirect measurement using other indicators	Mechanical	*Compressive strength active index*	[106, 107]
	Electrical	*Conductivity change*	[108, 109]
	Thermal	*Hydration Heat evolution*	[96, 110]

2.4.4.1 Supplementary Cementitious Materials

Amorphous silica materials are commonly used in the cement/concrete industry as supplementary cementitious materials (SCMs) owing their ability to react with the $Ca(OH)_2$ in cement to produce a cementitious binder. They can partially replace cement while still providing comparable strength and improved durability.

Some siliceous materials sourced from industrial by-products or natural products are also known as pozzolan materials.

- **Silica fume** is a by-product from the production of the silicon metal or ferrosilicon alloys. It primarily consists of very fine particle size of amorphous SiO_2 (>95%) with high silica reactivity. Adding the silica fume into concrete improves its mechanical properties and durability owing to the three effects[111, 112]:

    i. Pore-size refinement and matrix densification due to the extreme fineness of the particles, where it acts as filler.
    ii. Reaction with calcium hydroxide(CH). Additional reactive silica reacts with the CH in cement and produces calcium silicate hydrate (C-S-H) gel which contributes to the increase of the strength and reduction of porosity.
    iii. Interfacial transition zone refinement. The addition of silica fume helps to reduce the interfacial transition zone thickness between cement paste and aggregate, thus improving its performance.

  However, the availability of silica fume is quite limited. For Australia and New Zealand, most silica fume is imported[113]. Due to its high price, silica fume is generally used in high strength or specially purposed concrete.

- **Metakaolin** is produced by the calcination and dehydroxylation of kaolinitic clay at temperatures between 650 °C ~ 900 °C. After the thermal activation, the metakaolin is further ground to a specific particle size and surface area. Simila to silica fume, the metakaolin enhances the strength and long term properties through three actions[114, 115]: (i) filler effect, (ii) reaction with CH and (iii) the acceleration of cement hydration.

  The downside of the metakaolin is that during its production process, the temperature needs to be precisely controlled, and it needs both mechanical and thermal treatment which is relatively energy intensive. Besides, the addition of the metakaolin has a significant effect on the rheological property of the concrete[116]: the workability of the fresh concrete decreased with the increased replacement level of metakaolin.

- **Rice husk ash** (RHA) is produced when rice husks are burned under controlled conditions between 550~ 700 °C. The surface area of the rice husk ash is generally quite high due to its porous structure nature. Ganesan's study [117] indicates that up to 30% of RHA could be advantageously blended with cement without adversely affecting the strength and permeability properties of concrete.

  Uncontrolled burning below 500 °C of the RHA can lead to the unburnt carbon, which has an adverse effect on the silica reactivity. This limits the practice of producing the product in many areas, especially in under-developed countries.

- **Volcanic deposits** also demonstrated high silica reactivity due to its hydrous nature, high silica and alumina content. The small particles of pulverised volcanic rock and glass were initially used by the Romans to make concrete.

In 1959, the Department of Scientific and Industrial Research of New Zealand made a major investigation[118] into the volcanic deposits. Twenty-two samples were collected across New Zealand to determine whether they were sufficiently reactive for cement replacement. The two outstanding materials were found to be diatomite and pumicite.

Ghafari [119] evaluated the feasibility of incorporating perlite, pumice, and zeolite in concrete and concluded that these three materials might be used to replace class C fly ash in concrete.

The most significant advantage of using these volcanic materials is that most of them do not require heat treatment and demonstrate significant silica reactivity with minimal processing. On the other side, the distribution of this material is quite localised, and properties vary by origins.

2.4.4.2 Reactivity activation

The addition of the pozzolan materials generally reduces the early strength of the cement, and some natural pozzolans need to be activated to demonstrate silica reactivity. Different attempts have been made to improve pozzolanic activity and they can be classified into three types: mechanical, thermal, and chemical treatment.

- **Mechanical Activation.**

  Prolonged grinding of the material into fine particle size increases the specific surface area, which leads to a faster reaction rate. The pozzolan material can have a nucleation effect based on its particle size [120]. The smaller particles act as a nucleation site and accelerate early hydration rate [121, 122]. For example, quartz,

which is not an active pozzolan, demonstrated high reactivity when ground to ultra-fine powders [123].

A study [124] showed the strength of the natural pozzolan mixed with the hydrated lime sample were in a linear relation with the pozzolan's Blaine fineness, as shown in Figure 2-8, but the effect is more evident in early stages. An investigation[125] on twenty-two pozzolans showed no general correlation between the long-term (28 and 60 days) compressive strength with the surface area. It should be noted, that further grinding or continued increase in the surface area does not contribute to the performance of the pozzolanic activity. This statement was also mentioned in the previous section on MgO activity, as dissolution and hydration reaction are observed to occur simultaneously: the reaction products (C-S-H or $Mg(OH)_2$) have covered the particles thus reducing its further dissolution.

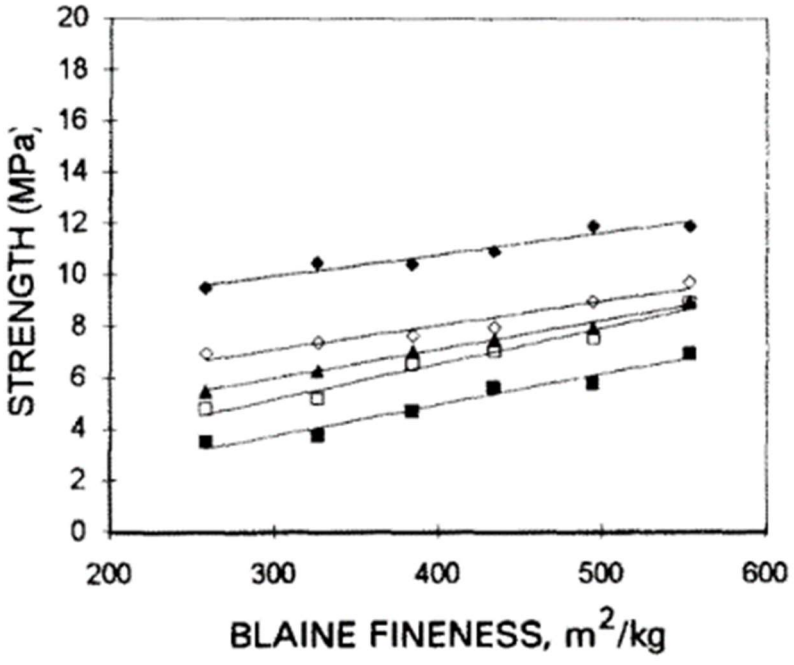

Figure 2-8. Relationship between strength and fineness of the natural pozzolan [124]

Grinding also increases the number of imperfection centres. Previous studies demonstrate that the number of active centres given a positive relationship with its pozzolan activity[126-128].

However, the effects of the grinding on different minerals are not the same, and thus their influence on cement hydration needs to be individually assessed.

- **Thermal activation.**

  Calcining pozzolanic materials and using elevated temperature for curing are two common methods for thermal activation.

  Calcination is a thermal treatment process that heats the mineral to a temperature below its melting point. The transformations during calcination includes dehydration, dehydroxylation, mineral collapse, and neo-formation [129]. The natural pozzolans after calcination are classified as Class N, according to the ASTM C 618 standard [130]. ACI 232.2 further classified calcined pozzolans as metakaolin, calcined clays, and calcined shale [131]. Calcination conditions (temperature and residence duration) affect the pozzolan activity in a combined two effects: an activation depending on the reactivity of the raw material and a reduction owing to the decrease of the surface area, soluble fraction and the increase of crystalline fraction[132, 133]. For example, the calcination temperature for metakaolin should be carefully controlled to avoid the formation of inert phases such as mullite.

Elevated temperature curing can increase the reaction activation energy, and thus improve the reaction rate. High-temperature curing is especially beneficial for the early age hydration and strength development. This compensates the 'dilution' effect due to the addition of the mineral admixtures, as the pozzolan reaction typically takes place after 7 days. However, statistical analysis from Shi[134] indicated that the ultimate strength of the pastes decreased with curing temperature. Other studies also showed similar results[135-137].

- **Chemical treatment**

The chemical treatment can be further divided into three methods: acid digestion, alkali activation and using other chemical activators.

Acid digestion can increase the reactivity of a pozzolan material by dissolving the basic oxide. Natural pozzolan minerals are most often acidic oxides that can react with basic calcium hydroxide formed during cement hydration, producing calcium silicate hydrates. Acid treatment can have two positive effects on a mineral: a) dissolution of the metal oxide which leads to a porous structure and an increased surface area; b) reducing the impurities thus improving the reaction performance per unit mass. In 1955, Alexander [138] investigated the activation of pozzolanic materials by treatment with acid and found that this method is more effective than mechanical activation. The degree of activation depends on the acid concentration while raising the reaction temperature or reaction duration showed no further improvement.

Nevertheless, it should be noted that acid treatment should not be used for high calcium pozzolans such as fly ash. The calcium will also be dissolved in the acid, thus reducing the overall reactivity.

Alkali activation is a chemical process that transforms glassy structures (partially or totally amorphous and/or metastable) into very compact well-cemented composites[139]. Alkali activation has been extensively studied, and alkali-activated cement was developed based on this theory[140-143]. The activated material can be coal fly ash, metakaolin, blast furnace slag, steel slag or other slags, municipal solid waste incinerator ash, or other alumina-rich materials. The alkali used as the activator tends to be an alkali silicate solution such as sodium silicate (water glass) but can also be sodium hydroxide solution, or a combination of the two, or other sources of alkali (such as lime).

Beside alkaline solutions, other **chemical activators** are NaCl, $CaCl_2$, $AlCl_3$, Na_2CO_3 and Na_2SO_4. Shi [144-146] did a series of study on the effect of Na_2SO_4 and $CaCl_2$ on different types of fly ashes (low and high calcium content). Results showed the pozzolanic reactivity of both types can be increased by the addition of a small amounts (3~5%). Other researches also confirmed this [147-149]. However, the detailed mechanism has not been fully understood yet.

2.5 Magnesia based cement

Different types of MgO-based cements that have attracted the most attention are summarised in Table 2-4.

Table 2-4. Different types of MgO-based cement

	Magnesium Oxy-Chloride Cement	**Magnesium Oxy-Sulphate Cement**	**Magnesium Phosphate Cement**	**Magnesium Silica Cement**
Raw Materials	$MgO+MgCl_2$	$MgO+MgSO_4$	$MgO+NH_4H_2PO_4$/ KH_2PO_4	$MgO+SiO_2$
Cementitious compounds	$3Mg(OH)_2 \cdot MgCl_2 \cdot 8H_2O$, $5Mg(OH)_2 \cdot MgCl_2 \cdot 8H_2O$.	$3Mg(OH)_2 \cdot 3MgSO_4 \cdot 8H_2O$, $5Mg(OH)_2 \cdot MgSO_4 \cdot 2H_2O$.	$NH_4MgPO_4 \cdot 6H_2O$/ $KMgPO_4 \cdot 6H_2O$	$Mg(OH)_2$, $3MgO \cdot 2SiO_2 \cdot 2H_2O$
Pros and cons	Favourable fire and abrasion resistance, Low thermal conductivity. Poor water stability		Quick setting and high early strength, Good bonding. Poor water resistance	High temperature resistance, low pH and good surface gloss
Reference	[150-155]		[156-163]	[164-171]

Magnesium oxychloride cement (MOC), also as known as Sorel cement, is derived from the reaction of the light burnt magnesia (calcined around 700~900 ˚C) with magnesium chloride ($MgCl_2$) and water; while magnesium oxy-sulphate cement (MOS) is produced from the mixture of magnesia and magnesium sulphate ($MgSO_4$). They have superior properties to ordinary Portland cement, such as higher early compressive strength, no need for water curing, as well as high fire and abrasion resistance. However, their use of products remains limited due to their poor water resistance.

In terms of the magnesium phosphate cement (MPC) which is derived from reactions between phosphate and dead burnt (above 1400 ˚C) magnesium oxide, it can be used as a rapid repair material due to its quick setting, excellent bonding properties with old concrete and high early strength.

The magnesium silicate hydrate cement (M-S-H) is produced from the reaction between magnesium oxide and a source of highly reactive silica. Nevertheless, there are hardly any reports on the commercial application of magnesium silicate hydrate cement and limited studies on its hydration and mechanical properties, nor its long-term durability. However, the moderate pH of M-S-H cement and its special hydration reaction make it an ideal immobilizing agent for the disposal of heavy metal wastes.

2.5.1 Magnesium silica cement

Magnesium-silicate-hydrate (M-S-H) gel was first observed in concrete in the later stages of sulphate attack, mainly on the deteriorated surface and it was generally considered to have little cementitious properties or strength [172-175]. However, later research on the synthesis of M-S-H proved it to have favourable strength compared to ordinary Portland cement [176-180].

In the magnesium silicate hydrate (M-S-H) system, brucite is formed in the hydration reaction between reactive magnesia and water and then reacts with pozzolanic materials to form magnesium silicate hydrate gel. The formation process of M-S-H can be influenced by factors including ratio and characteristics of the precursors, temperature and the pH value of the system [165, 177-179].

In 2006, Wei et al [165] first studied the compressive and flexural strength of mortar with a M-S-H binder, which had comparable strength with Portland cement. The highest compressive strength of the M-S-H cement, prepared with the magnesia to silica fume ratio 7:3, reached 57.4 MPa after 28 days of curing at room temperature. According to Zhang et al.'s research [169], shown in Figure 2-9, it compared the M-S-H with the cement system

mixed with Portland cement and blast furnace slag (1:3). The water to binder ratios were 0.55 and 0.35, respectively. The compressive strength of the M-S-H mortar at the early age of 7 days was lower than the Portland cement control, but after that point, the strength increased, reaching higher values than the cement mortar.

The strength of hardened M-S-H-based materials is mainly dependent on the M-S-H gel phase, which is considered to have a more substantial bonding effect than brucite itself and potentially can be used for concrete material to achieve adequate strength for structural applications.

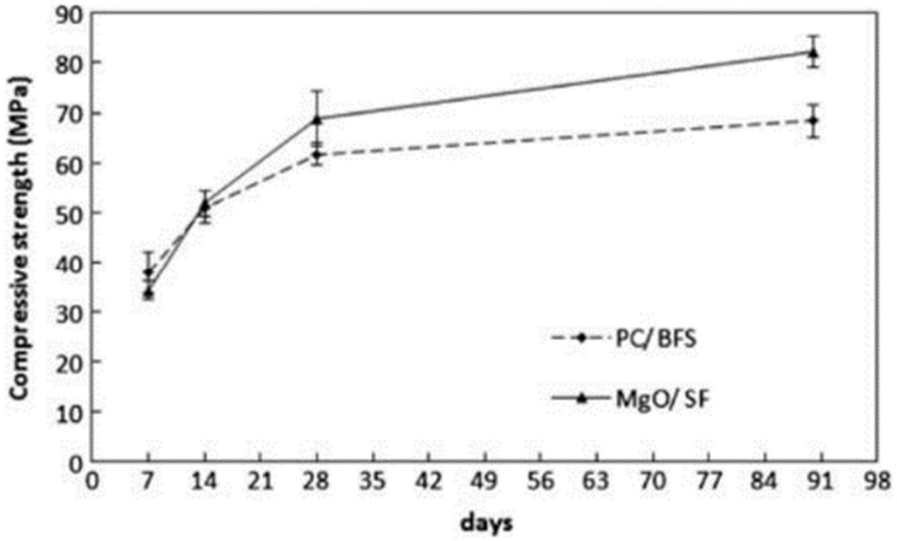

Figure 2-9. Compassion of the strength development of M-S-H and Portland Cement [169]

2.5.2 Magnesium oxychloride cement system

Magnesium oxychloride cement (MOC), also as known as Sorel cement [181], is produced by mixing magnesia with magnesium chloride solution. The aqueous reaction between MgO and $MgCl_2$ produces a variety of phases (shown in *Equation 2-11* and

Equation 2-12) that are highly dependent on the precursor molar ratios, temperature and magnesium reactivity[182, 183].

$$3MgO + MgCl_2 + 11H_2O \rightarrow 3Mg(OH)_2 \cdot MgCl_2 \cdot 8H_2O \qquad \textit{Equation 2-11}$$

$$5MgO + MgCl_2 + 13H_2O \rightarrow 5Mg(OH)_2 \cdot MgCl_2 \cdot 8H_2O \qquad \textit{Equation 2-12}$$

MOC cement does not need water curing and has good resistance to abrasion as well as some chemicals. It has high early strength and good bonding properties to different types of fillers[151, 184, 185]. It is relatively light and has a low coefficient of thermal expansion[186]. The ability of MOC cements to bind and consolidate large quantities of diverse filler materials ranging from granite to sawdust, with good compressive and tensile strengths, has furthered their adoption[186].

It is used in industrial floorings, ship decks, railway passenger coach floorings, hospital floors, ammunition factory floors and underground armament factories and bunkers. However, its poor resistance to excessive exposure to water has restricted its outdoor applications. In order to improve the water -resistance of the MOC, phosphates were added and can significantly improve the compressive strength retention[153].

2.5.3 Magnesium oxy-sulphate cement system

Magnesium oxy-sulphate (MOS) cements are similar in concept to MOC cements, except that $MgSO_4$ is used instead of $MgCl_2$ [187, 188]. A similar nomenclature scheme is applied to the $x\text{Mg(OH)}_2 \cdot y\text{MgSO}_4 \cdot z\text{H}_2\text{O}$ phases, which are thus described analogously as the 3 phase and 5 phases; however, these phases are not isostructural to those formed in oxychloride cements that share the same names. Typically, the formation will follow the equations (the latter if heated), although several other phases can also be formed.

$$3MgO + MgSO_4 + 11H_2O \rightarrow 3Mg(OH)_2 \cdot MgSO_4 \cdot 8H_2O \quad \text{Equation 2-13}$$

$$5MgO + MgSO_4 + 7H_2O \rightarrow 5Mg(OH)_2 \cdot MgSO_4 \cdot 2H_2O \quad \text{Equation 2-14}$$

MOS cements gained interest because of the less hygroscopic nature of magnesium sulphate compared to magnesium chloride and were claimed to have superior resistance to weathering. MOS cements are more difficult to form because of the solubility of $MgSO_4 \cdot 7H_2O$ at room temperature, but the development of these materials based on sulphates does avoid the use of chlorides, making them significantly less damaging to steel reinforcing, although they still suffer from poor water resistance. Weak acid, such as tartaric acid, was added to modify the magnesia-based cement by improving the stability of the hydration film of active MgO in magnesium sulphate[189].

2.5.4 Magnesium phosphate cement system

Magnesium phosphate cements (MPC) are formed through an acid−-base reaction between MgO and a soluble acid phosphate (typically an ammonium or potassium phosphate), forming a magnesium phosphate salt with cementitious properties[190]. The reaction between magnesia and ammonia phosphate was shown in Equation 2-15.

$$MgO + NH_4H_2PO_4 + 5H_2O \rightarrow NH_4MgPO_4 \cdot 6H_2O \quad \text{Equation 2-15}$$

Formation of magnesium phosphates through this acid−base process can also be simply achieved through the reaction of MgO with H_3PO_4 [191, 192]. MPCs possess some advantages over other cementitious materials[193-195]: (1) quick setting and hardening (can be demoulded within 30 minutes after casting) ; (3) high early strength (compressive strength can reach 28 MPa in one hour and above 40 MPa in three hours); (4) quick setting in a low -temperature environment even at -20 ℃; (5) high bonding strength with old concrete; (6) excellent resistance to abrasion and frost; (7) low drying shrinkage; (8) fire-

proof behaviour; and (9) low thermal expansion coefficient. These properties make its potential application as a rapid repairing material.

2.5.5 Reactive magnesia cement

Reactive magnesia cements were developed and patented by Harrison in 2008 [196]. The invention provided cement compositions containing substantial proportions of reactive magnesia that hydrate to form brucite, which is a useful cementitious component. A research group in the University of Cambridge performed an extensive study on this system[197-204].

The MgO used for this system is manufactured at a much lower temperature (650~800 ˚C) compared to Portland cement clinker and dead burnt MgO used in MPC system. Therefore, this type of MgO is highly reactive. In the presence of water and sufficient CO_2 in the curing atmosphere (5~20%), the produced brucite was found carbonated, forming one or more hydrated magnesium carbonates. (reaction equation shown below). These hydrated carbonates produce networks with effective binding abilities, and this leads to significant strength increase.

$$MgO + H_2O \rightarrow Mg(OH)_2 \quad \textit{(Brucite)} \quad \textit{Equation 2-16}$$

$$Mg(OH)_2 + CO_2 + 2H_2O \rightarrow MgCO_3 \cdot 3H_2O \quad \textit{(Nesquehonite)} \quad \textit{Equation 2-17}$$

$$5Mg(OH)_2 + 4CO_2 \rightarrow Mg_5(CO_3)_4(OH)_2 \cdot 4H_2O \quad \textit{(Hydromagnesite)} \quad \textit{Equation 2-18}$$

$$5Mg(OH)_2 + 4CO_2 + H_2O \rightarrow Mg_5(CO_3)_4(OH)_2 \cdot 5H_2O \quad \textit{(Dypingite)} \quad \textit{Equation 2-19}$$

The main applications for the reactive magnesia cement system including porous blocks, concrete, ground improvement, waste immobilisation, contaminated land remediation and wastewater decontamination.

2.6 Magnesium silicate mineral-based cement

Since the cementitious magnesium silicate hydrate gel can be formed through the reaction between magnesium oxide and silica in water, it would be of great significance to investigate the minerals which are abundant in both magnesium oxide and silica, such as olivine and serpentine.

It is reported that olivine, one of the common magnesium -rich minerals, can react with water to form serpentine in addition to $Mg(OH)_2$ and molecular hydrogen[32]. Serpentine can be further processed at high temperature to obtain both MgO and SiO_2 as components for the binder.[205, 206].

If the Mg^{2+} ion was in the presence of $MgCl_2$ or $MgSO_4$, it could react with the MgO to form cementitious materials as well. It may be also possible to use the magnesium -rich mineral to form the magnesia-based cement through some treatment and/or the addition of reactive MgO and/or SiO_2. However, there have only been very limited references on the topic of developing the cementitious material from olivine and/or serpentine.

2.6.1 Formation of magnesium silicates

In the system consisting of MgO + SiO_2 + H_2O, the formation of the magnesium silicate hydrates gel can be summarized in Figure 2-10. When the magnesium oxide

contacts with water, it hydrates to form brucite, which leads to an increase of the pH value and a release of heat in the first few hours. The brucite reacts with the dissolved silica to produce the M-S-H gel. According to the pH and heat evolution, this reaction usually takes place over 3 days. The formation of the M-S-H gel continued until either the reagent was completely consumed entirely. Depending on the variation of the Mg/Si of the raw material, the hydration products are different.

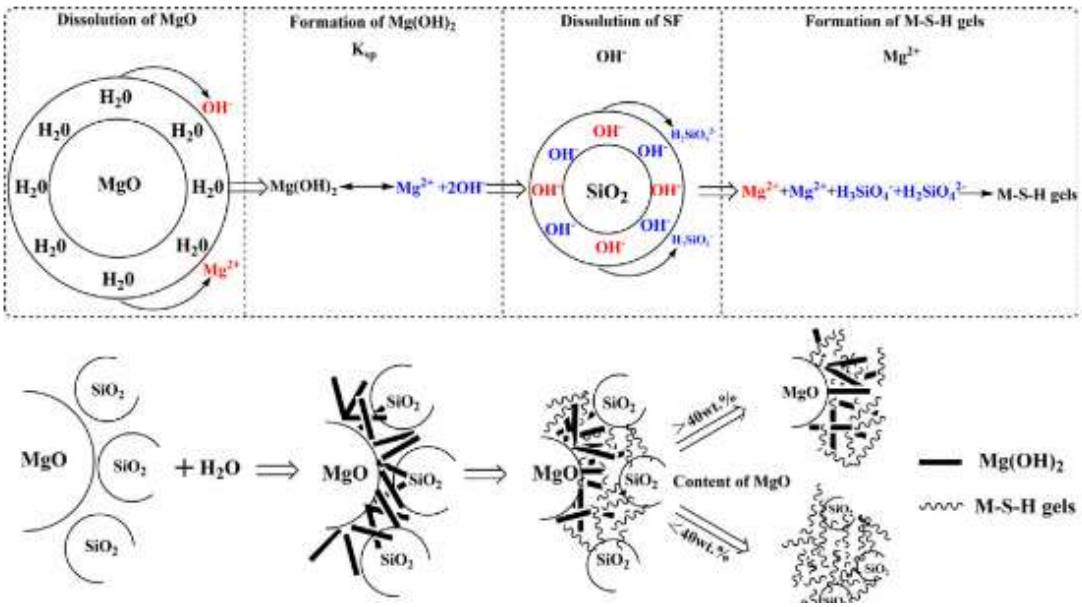

Figure 2-10. Schematic illustration of the formation of M-S-H gel.[207]

2.6.2 Use of magnesium silicates as M-S-H cement

In 1951, Mchedlov-Petrosyan[208, 209] showed that it was possible to make a hydraulic M-S-H cement by calcining serpentine rock. However, the mineralogical change or the hydration reaction were not clearly explained. Midgley[18, 210] investigated the reaction process using DTA and XRD techniques. The serpentine rock was calcined in an electric muffle furnace at 640 °C for 5 hours after it was crushed to around 5 mm size.

Then, it was ball milled to 5600 cm^2/g after calcination. The M-S-H cement to standard sand ratio was 1:3, and the hydrated samples' compressive strength was only 3.3 MPa after 12 months curing in water. According to this study, the strength development of the magnesium silicate system was extremely slow, and only low strengths were obtained. However, the high content of the MgO and SiO_2 in the serpentine still make it promising as they are hydraulic and thus can form cementitious materials through some special treatment.

Yang[177] studied the MgO-SiO_2-H_2O system under the temperature between 100-300 ˚C, and found that the silicic acid and diatomaceous earth (consisting of amorphous biogenic silica) were more active than crystalline silica. The study conducted by Jin [211] drew the same conclusion by selecting both micro-silica (amorphous silica) and silica flour (mainly consisting of crystalline silica) as the precursors. The results showed that the crystalline silica is not able to react with MgO, but synthesised or recovered amorphous silica shows reactivity.

2.6.3 Use of magnesium silicates as a silica source

Justnes [212] used hydrochloric acid (HCl, 37%) to digest the finely divided olivine. The reaction was done under 20 ˚C for 24 hours and 70 ˚C for 4 hours. The reaction was proposed below.

$$Mg_2SiO_4\ (s) + 4\ HCl\ (aq) \rightarrow MgCl_2\ (aq) + SiO_2\ (s) + 2H_2O \qquad \textit{Equation 2-20}$$

After the digestion, the slurry was purified by washing, filtering and decanting. The final product was characterised as a pozzolanic, amorphous silica. The consumption of calcium hydroxide by recovered silica was quantified through thermogravimetric analysis

(shown in Figure 2-11). Silica fume demonstrated higher reactivity in early ages (before 28 days) while after 28 days, the recovered silica showed comparable performance. Similarly, by measuring the strength (both flexural and compressive) in Figure 2-12, it suggested that the long term pozzolanic activity of the recovered silica is comparable to conventional silica fume obtained from ferrosilicon plants.

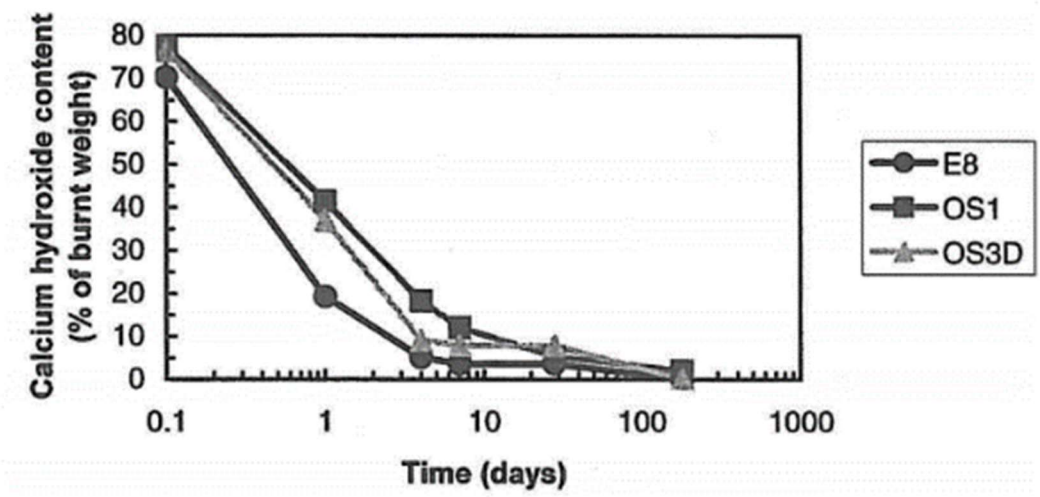

(Legend: E8: silica fume; OS1: silica recovered from olivine acid digestion at 20 ˚C; OS3D: silica recovered from olivine acid digestion at 70 ˚C)

Figure 2-11. Pozzolanic consumption of CH in lime - silica mixtures determined by DTA/TG [212]

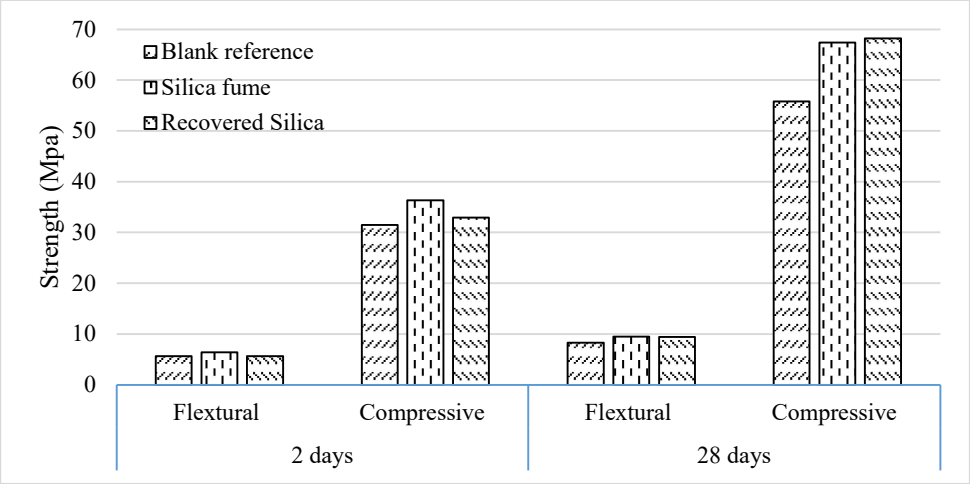

Figure 2-12. Strength comparison of the recovered silica from olivine with silica fume [212]

In 2009, a comprehensive study on using magnesium silicate minerals as pozzolana was carried out within the Concrete Innovation Centre in Norway[213]. The study focused on making pozzolana from naturally occurring minerals by chemical treatment and reviewed the possibility of making pozzolana for M-S-H cement and concrete by treatment with weak and strong acids. Olivine and serpentine were selected as the most feasible minerals, not only due to its potential in pozzolan activity, but also its availability in the Earth's crust.

2.7 Summary and research gap

This chapter first summarised the properties of olivine and serpentine and outlined the efforts to extract the magnesium from these magnesium silicate minerals. The mineral dissolution rate was reviewed under various environmental conditions, such as pH, temperature and pressure. However, the mechanical activation on the surface area, the

effect of different acid type and concentrations have been not systematically studied, especially from a practical perspective. The reviewed research on silica recovery was very minimal.

The properties of the commercially available magnesia and silica were reviewed, and this laid the foundation for characterising the recovered magnesium and silica products from minerals. The different measurements on MgO and SiO_2 reactivity were summarised, and activation methods of pozzolanic activity were also compared. Note that the MgO and SiO_2 are generally produced by conventional methods, thus the activities of the recovered MgO or SiO_2 from other materials are still unknow.

Five different types of different MgO-based cement were summarised from literature, and the reaction mechanisms were highlighted. This information has provided the cornerstone for the development of the magnesium-based binder system from the magnesium silicate minerals.

This chapter also presented the efforts on the development of the mineral -based cement: both using magnesium silicate as a M-S-H cement and as a silica source. It pointed out that the critical challenges for this initiative were the high energy consumption during processing, poor silica reactivity and low final strength of the M-S-H cement products.

3 Raw materials and experimental methodology

3.1 Introduction

This chapter introduces the details of the experimental methods, such as sampling, grinding and the parameters of the characterisation techniques. The properties of the raw materials used in this project are also described.

Based on the overall structure of the thesis and the different experiment parts illustrated in Figure 1-5, the raw material and methods used can be categorised into the following three sections as shown in Table 3-1. This chapter aims to present the general information of the material and methodology while more details of each material and methods can be found in the related section in each chapter.

Table 3-1. Material and methods used in different chapters

Dissolution (Chapter 4)	**Objective** To study the mineral dissolution properties.
	Main Materials Olivine, Serpentine, Acid and base, CO_2
	Key Methods Mechanical activation. Particle size analysis. Ion concentration measurement. Chemical phase (XRD) and composition (XRF) Microstructure observation (SEM and EDS) Thermal gravimetric analysis (TGA)
Extraction (Chapter 5 and 6)	**Objective** To extract and characterize the product from the mineral.
	Main Materials Olivine, Serpentine, Acetic acid, Hydrochloride acid. Other silica sources: silica fume, micro silica, rice husk ash, quartz sand.
	Key Methods Acid reaction, filtration, evaporation and calcination MgO activity test. Pozzolanic activity test: particle size analysis, chemical & phase composition, surface area measurement, conductivity test, ion concentration, microstructure, thermal gravimetric analysis and strength test.

(to be continued)

(continued)

Investigation (Chapter 7 and 8)	**Objective** To study the binder property derived from the recovered products.
	Main Materials Commercial MgO and SiO_2 Recovered MgO and SiO_2 Hydrochloride acid, Magnesium chloride, Sea water
	Key Methods Cement sample preparation: casting and curing Solution analysis: ion concentration, pH Hydration heat measurement Mechanical properties: strength test Chemical phase (XRD) and composition (XRF) Microstructure: SEM & EDS

3.2 Raw Materials

3.2.1 Magnesium silicates minerals

The olivine sand was provided by MetCast Service Limited and is mined in the Dunedin area in New Zealand. It is a natural stone product that was crushed and processed. The median particle size of the raw olivine sand was 386.89 μm while the mean size was 408.24 μm.

The serpentine was provided by South Serpentine, screened to 3mm. It has not been calcined or blended with any other product. The deposit is near Lumsden, New Zealand. The median size and the mean size of the raw serpentine was 153.99 μm and 352.57 μm, respectively.

The particle size distributions of olivine and serpentine are shown in Figure3-1 and Figure3-2, respectively.

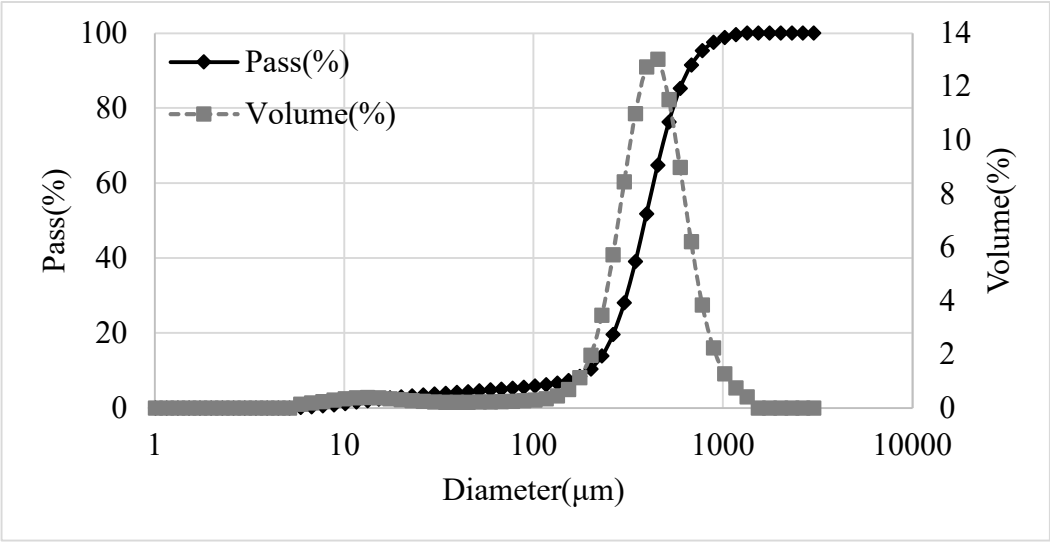

Figure3-1. The particle size distribution of raw olivine sand

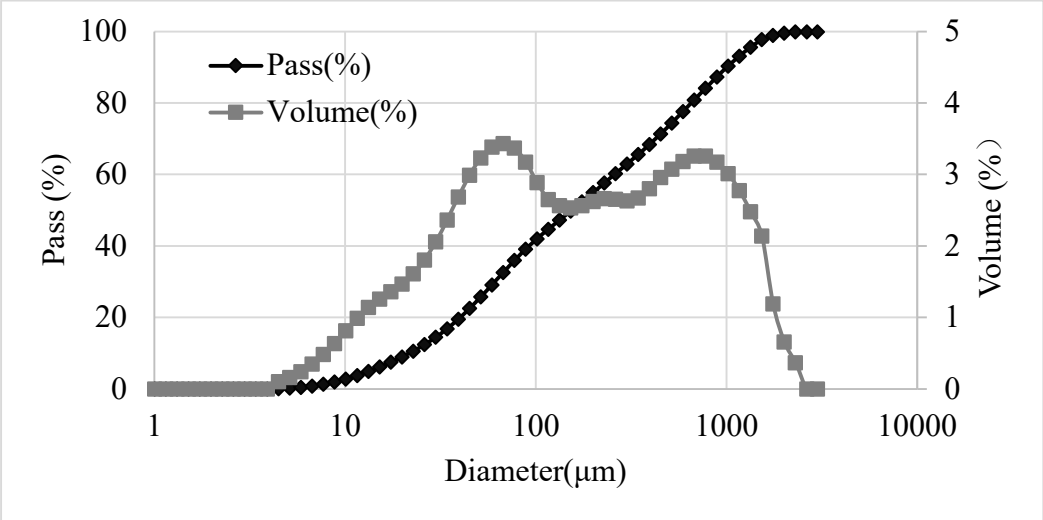

Figure3-2. The particle size distribution of raw serpentine sand

The chemical composition of olivine and serpentine, as characterised by X-ray Fluorescence (XRF), is provided in Table 3-2. According to the X-ray Diffraction (XRD) results (shown in Figure3-3), the main mineral present in the olivine is forsterite (Mg_2SiO_4).

Table 3-2. Chemical composition of olivine sand and serpentine

	MgO	SiO_2	$Fe_2O_3^T$	TiO_2	Al_2O_3	MnO	CaO	Na_2O	K_2O	L.O.I.	Total
Olivine	45.03	39.59	10.65	0.03	0.38	0.15	0.73	0.14	0	3.21	100
Serpentine	37.27	40.7	7.84	0.05	1.04	0.11	0.32	0.01	0.03	12.01	99.37

$Fe_2O_3^T$: XRF only provide total iron oxide, including FeO and Fe_2O_3.

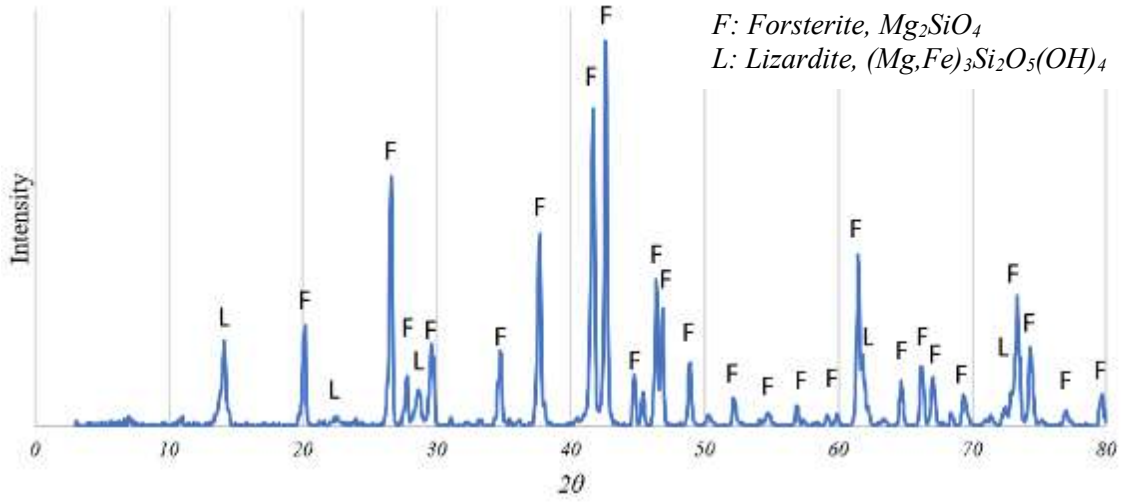

(a). Olivine

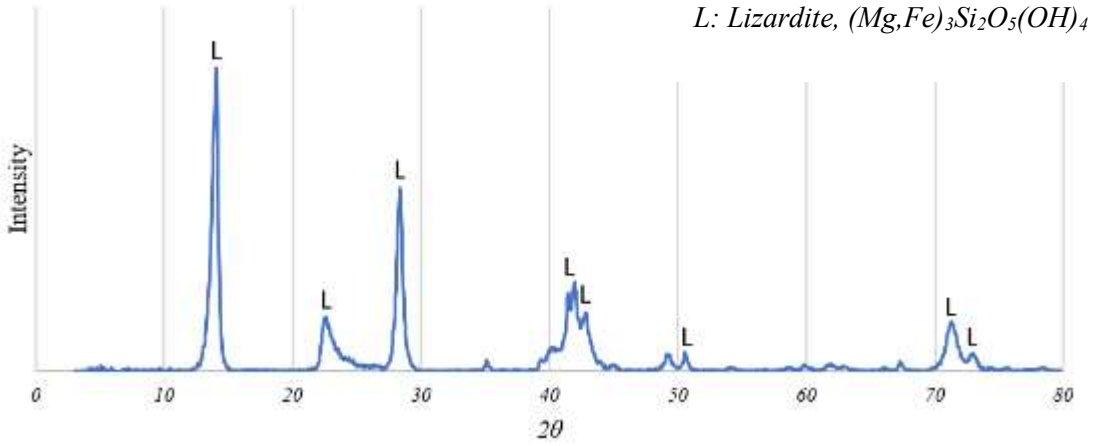

(b) . Serpentine

Figure3-3. XRD analysis of the olivine and serpentine sand

The TG comparison analysis of olivine and serpentine is presented in Figure3-4. The olivine sample is relatively stable under different temperature while serpentine sample

experienced a mass loss around 650 ºC. The mass loss can be attributed to the decomposition of serpentine to forsterite as described in Equation 2-5.

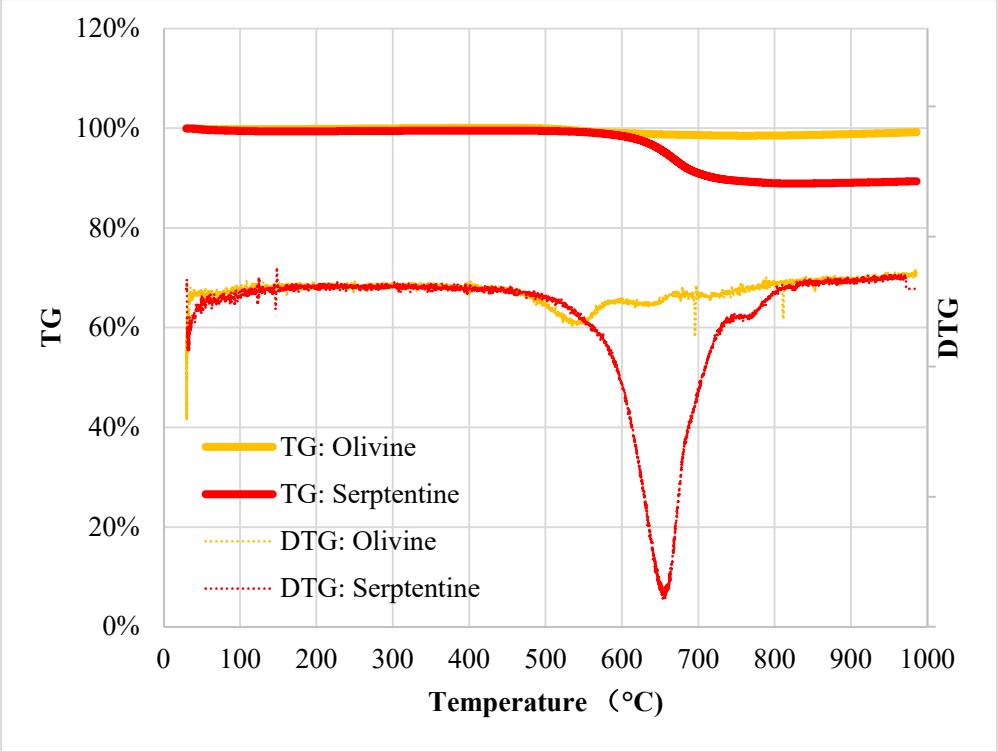

Figure3-4. The TG and DTG curve of olivine and serpentine sand

The microscopy of the particle was observed by Scanning Electron Microscopy (SEM) and shown in Figure3-5 and **Error! Reference source not found.**. The shapes of these as-received mineral particles are both irregular while the observed particle size aligns with the particle size laser analysis. From the EDS results, the elemental compositions of olivine and serpentine are very similar, both primarily consist of Mg, Si, O and Fe. The olivine contains slightly higher amount of Mg and Fe compared to serpentine.

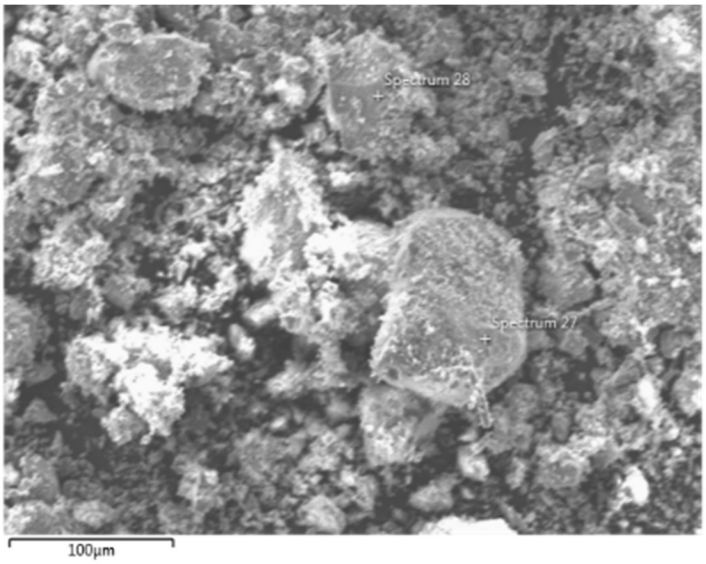

	wt%
O	*42.8*
Si	*20.0*
Mg	*30.4*
Fe	*6.8*

(a) SEM (b) EDS

Figure3-5. Microscopy of the olivine particle

	wt%
O	*44.5*
Si	*24.9*
Mg	*26.3*
Fe	*3.6*

(a) SEM (b) EDS

Figure3-6. Microscopy of the serpentine particle

3.2.2 Magnesia

The magnesia (MgO) used was produced through the calcination of magnesium carbonates, and it was imported from Calix Ltd, Australia. The particle size distribution is

shown in Figure3-7. The median size of the magnesia is 10.03 μm, while the mean size is 17.18 μm.

The specific surface area of the commercial MgO determined by the BET method is 3.7655m^2/g. The chemical composition analysed by XRF is shown in Table 3-3. Details on the reactivity of the commercial material compared to the recovered material is provided in Chapter 4.

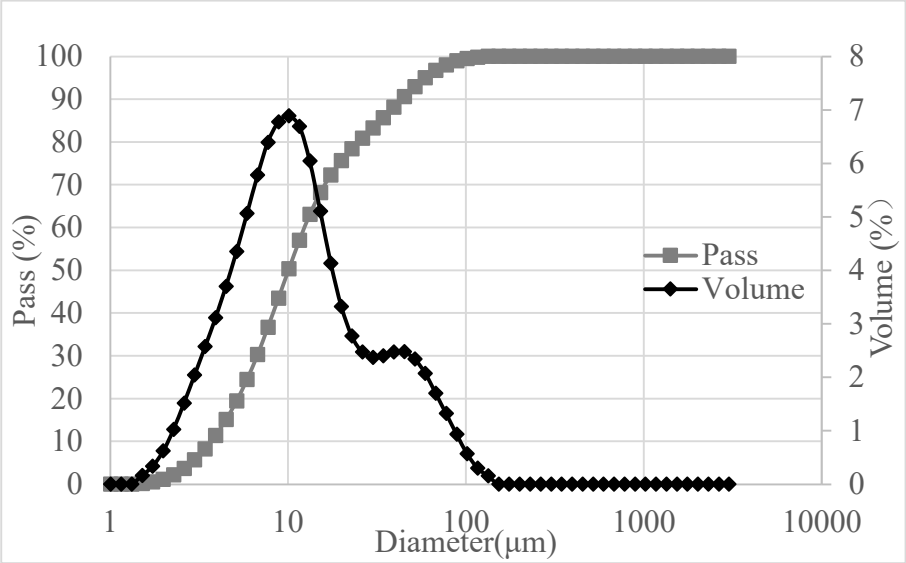

Figure3-7. The particle size distribution of raw magnesia

Table 3-3. Chemical composition of magnesia

%	SiO_2	Al_2O_3	Fe_2O_3	CaO	MgO	Na_2O	K_2O	LOI	Total
MgO	9	0.52	0.25	3.47	65.8	0.19	0.11	19.65	99.07

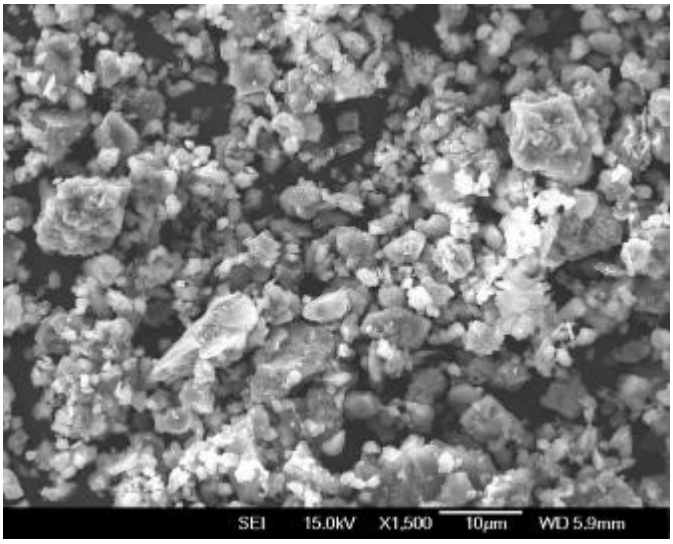

Figure3-8. Microscopy of the magnesia particle

3.2.3 Silica fume

The condensed silica fume (SF) was supplied by SIKA NZ. The particle size distribution of the condensed silica fume is shown in Figure3-9. The mean and the median size of the silica fume is 124.21 and 92.17 μm, respectively. It should be noted that this type of silica fume includes agglomerates of particles although the individual silica fume particles had a median particle size around 0.1 μm.

The specific surface area of the SiO_2, determined by BET method is 19.0687 m^2/g. As can be seen from the comparison of the microscopy of the particle at the different magnitude, shown in Figure3-10(a) and (b), the finer silica particles were condensed together thus presenting a coarser grain.

The XRD spectra of the silica fume is shown in Figure3-11, where a broad peak around 20~30 ° was observed with no additional crystalline impurities.

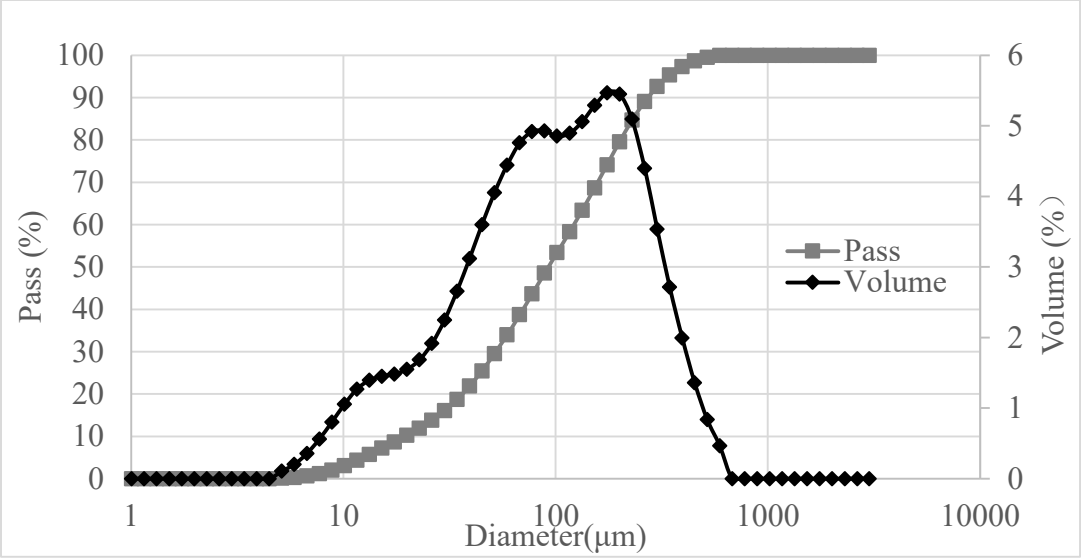

Figure3-9. The particle size distribution of the silica fume

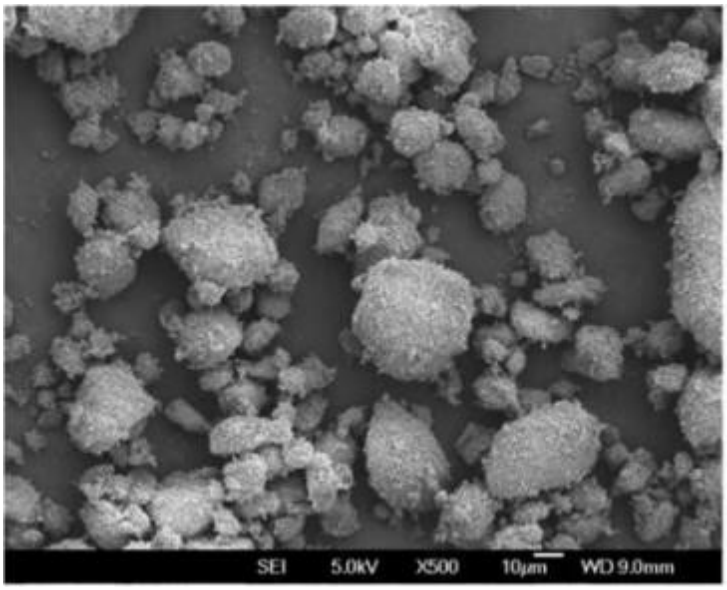

(a). magnification at 500

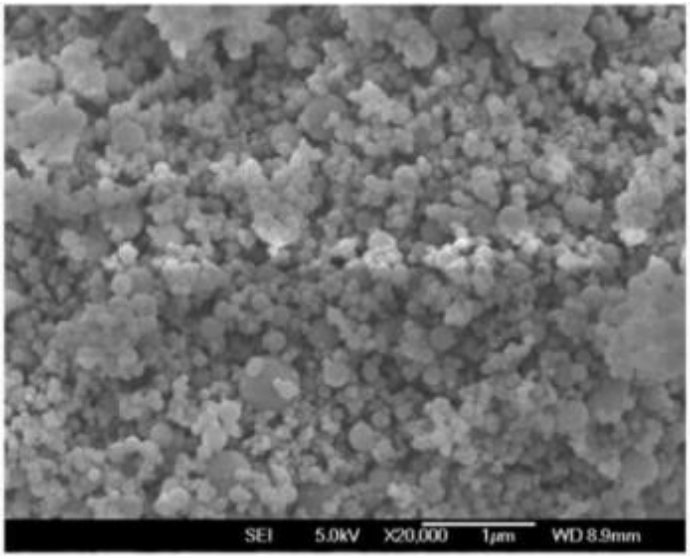

(b). magnification at 20,000

Figure3-10. Microscopy of the silica fume particle

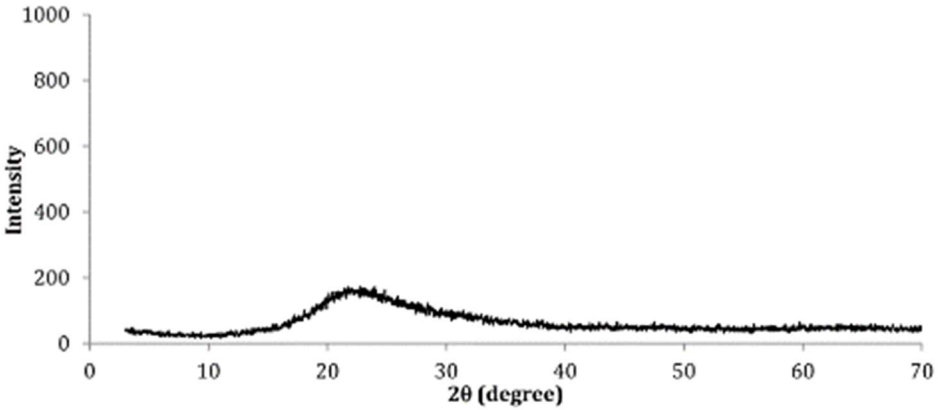

Figure3-11. XRD pattern of the silica fume [214]

3.2.4 Quartz

The quartz sand was used as an inert filler, as well as a reference due to its limited silica reactivity. The particle size of the quartz is shown in Figure3-12. The mean and the median size of the quartz sand are 237.78 μm and 240.68 μm, respectively.

The SEM images and the XRD pattern of the quartz source are shown in Figure3-13 and Figure 3-14, respectively.

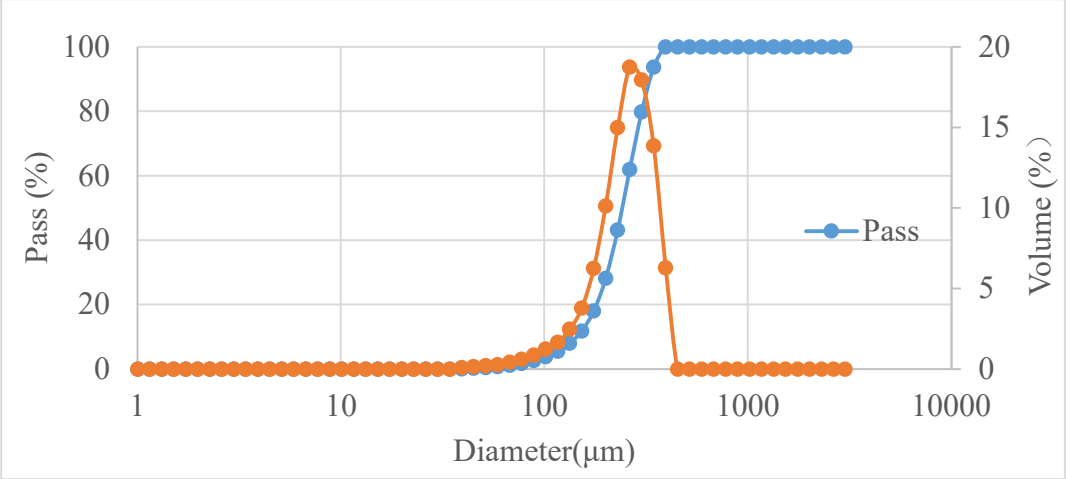

Figure3-12. The particle size distribution of the quartz sand

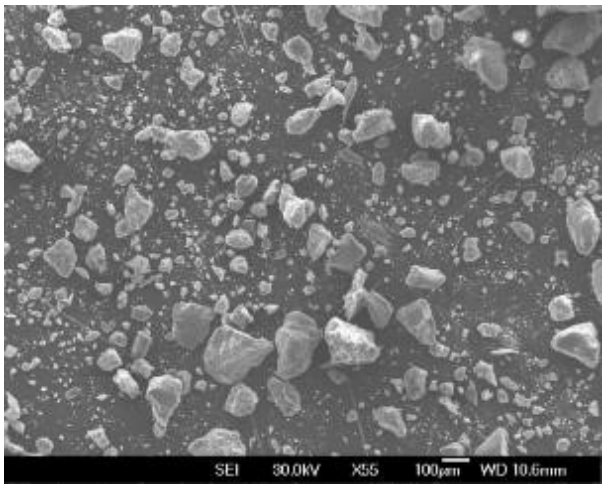

Figure3-13. Microscopy of the quartz sand particle

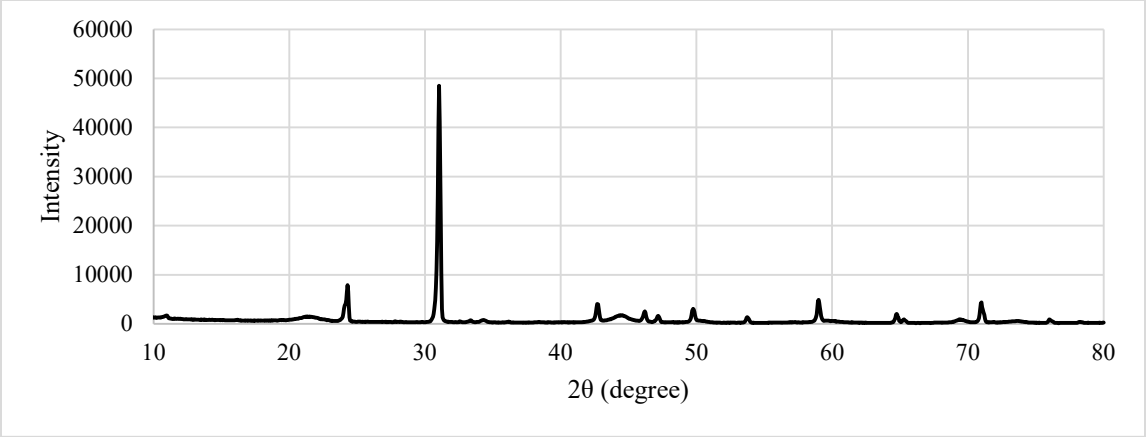

Figure 3-14. XRD of the quartz

3.2.5 Acids and bases

Chemical grade hydrochloric acid (HCl) (37%, supplied by Ajax) and sodium hydroxide (NaOH) (>98%, supplied by Sigma-Aldrich) were used in the digestion and recovery process. Glacial acetic acid (CH_3COOH, 99%) was supplied by Sigma-Aldrich while nitric acid (HNO_3 ,70%) was supplied by Thermo Fisher Scientific. The concentration and the amount of the chemicals will be detailed in each chapter where relevant.

The carbonated water contains dissolved carbon dioxide gas, and commercially available Schweppes Soda Water is used in this study.

3.3 Experiment methods and techniques

3.3.1 Sampling method

As the granular materials, such as olivine and serpentine sand, ground magnesia cement powder, and silica fume, tend to segregate with fine particles in the centre while coarse particles stay at the bottom, the *golden rules of sampling*[215] were applied. Tthe cone and quartering method was used as per British standard EN 932-1 and EN 932-2. The powder sample was first sieved and collected on a flat plastic sheet. The top conical shape was flatted, as shown in Figure3-15. The cone was then divided into quarters and the two opposite quarters combined. The process was repeated until a suitable sample size was obtained.

Figure3-15. Illustration of the cone and quartering method[216]

3.3.2 Sample preparation

Grinding the minerals will decrease the particle size significantly and thus increase the contact surface area with the leaching agent. This is a common method to improve the reactivity of the mineral. In this experiment, the Rocklabs ring and puck mills (shown in Figure3-16) were used. Different durations of grinding were applied: 20, 60, 90 and 120 seconds.

Figure3-16. The Ring and puck mill

For calcination, the samples were calcined under different temperatures using a box furnace as shown in Figure3-17. The furnace was set to increase the temperature at approximately 10°C/min until the desired temperature was reached. The box furnace was ventilated in a fume hood and porcelain crucibles were used to accommodate the materials for heating.

Figure3-17 The box furnace

Vacuum filtration was used to separate the solids from a reacted solution. The solution was filtered using a Buckner funnel with a cellulose MF-Millipore™ membrane filter. This membrane filter has a pore size of 0.45μm and the setup was shown in Figure3-18(a). Additionally, syringe filters were used to separate samples for analysis. The PTFE syringe filter was provided by Thermo Scientific and Target2 ^{TM} was used. The diameter of the filer is 30 mm while the pore size is the same as the membrane filter (0.45 μm).

(a). vacuum filtration *(b). filter filtration*

Figure3-18. The filtration setup

3.3.3 pH and conductivity monitoring

A Thermo Scientific Orion Star A210 pH metre was used to measure the pH level of the solutions in this study. The pH metre was calibrated using buffers with a pH of 4, 7 and 10 before each set of measurements measuring. For continuous measurement, the time interval between each recording was three seconds.

The conductivity test was carried out by a Metrohm 856 Conductivity module together with *tiamo*^{TM}, unit shown in . The measuring range was 0.005~100 ms/cm while the temperature range is 0~70 °C.

For the measurement, 4 grams of the sample was dissolved in 80 mL solution. The solution was agitated during the measurement. Conductivity data were recorded every 3 seconds.

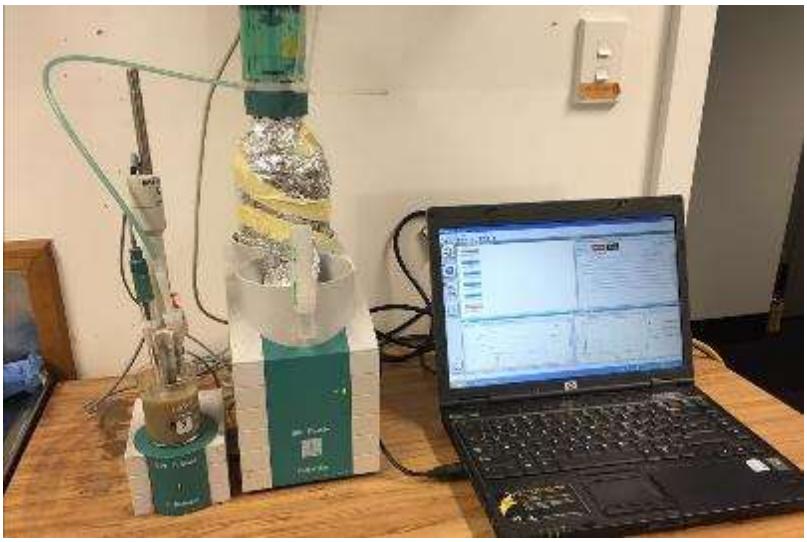

Figure 3-19 The conductivity test setup

3.3.4 Ion concentration measurement

Ion concentration was measured by three different types of methods in this study according to the ion strength of the samples. Inductively coupled plasma mass spectrometry (ICP-MS) was used for trace elements while microwave plasma atomic emission spectrometer (MP-AES) was used for determination of major and minor elements. A titration test was also employed to calculate the total ion concentration of magnesium and calcium.

3.3.4.1 Inductively coupled plasma mass spectrometry

Inductively coupled plasma mass spectrometry (ICP-MS) is a combination of a high temperature inductively coupled plasma (ICP) source with mass spectrometry (MS). The ICP source first converts the atoms of the elements to ions before they were separated and

detected by the mass spectrometer. In this study, an Agilent 7500cx model was used for the analysis with a standard set-up (Sample depth:8.3mm, Argon carrier gas:0.92L/min). The sample preparation of the ICP-MS involves digestion using nitric acid (0.5 mol/L, 12 hours) and filtration through the 0.45μm syringe filter. The detection limit of this ICP-MS instrument is 3 part per trillion (ng/L).

3.3.4.2 Microwave Plasma Atomic Emission Spectrometer

Microwave Plasma Atomic Emission Spectroscopy (MP-AES) consists of a microwave-induced plasma interfaced to an atomic emission spectrometer. The microwave energy was employed to produce the plasma discharge using the nitrogen. The emissions from the excitation process were measured with a monochromator and detector. An Agilent 4200 MP-AES was used in this study, and the sample preparation was the same as with the ICP-MS process. The detection limit for of this instrument for magnesium ion is 0.09 part per billion (μg/L).

3.3.4.3 Complexometric titration

Complexometric titration is a volumetric analysis where the formation of a coloured complex is the indicator of the endpoint of a titration.

In this study, EDTA was used to form a complex with calcium and magnesium ions, while Eriochrome Black T was used as an indicator. During the titration, the calcium and magnesium ions in the sample first reacted with an excess of EDTA, and the colour was blue when the indicator was added. Prepared magnesium chloride solution (0.025mol/L) was then added as a back titration. The added magnesium ion formed a complex until the excess EDTA was entirely consumed. The remaining magnesium ions then began to complex with ErioT indicator, which changes its colour from blue to pink.

The detection limit of titration method depends on the smallest amount of reagent that can be added during a titration to cause a chemical change. In this case, the detection limit is 1.0 part per million (mg/L).

3.3.5 Cement sample preparation and curing

3.3.5.1 Mortar specimens for mechanical property test

Ordinary Portland cement (supplied by Golden Bay Cement, New Zealand) was mixed with sand and water to produce the mortar samples. For the mechanical property investigation, mortar cubes were prepared. The size of the cubes were 20×20×20 mm. The binder to water ratio will be detailed in the following relevant chapters, while the sand to binder ratio was fixed at 1:1. Deionised water was used to avoid the contamination of chlorine from tap water. Superplasticiser (Sika, Visocrete-555) was used at a weight percentage of 3%. After 24 hours of curing, the samples was removed from the mould and placed in the specified curing regimes.

3.3.5.2 Paste samples for microstructure analysis

To avoid the complications associated with aggregates for microstructure analysis, paste samples were cast at the water to binder ratio of 0.6 in cylindrical plastic moulds with a diameter of 30 mm and height of 120 mm. No sand or superplasticisers were added. After 24 hours of casting, the samples were demoulded and cured in same designed curing conditions for the required length of time.

3.3.5.3 Curing

After casting, the demoulded samples (both mortar and paste) were then cured in a controlled environmental chamber: the temperature at 20 °C, relative humidity at 50 %

with the ambient CO_2 concentration (0.04%). The samples were cured for 3, 7, 28, 56 and 90 days.

3.3.6 Sample hydration arrestment and storage

Prior to analysis, the hydration in the paste samples needed to be arrested. To preserve the microstructure, especially for those samples at early ages, a solvent exchange technique was used. According to the literature[217], isopropanol is the most effective organic solvent. The samples were first ground by hand in an agate mortar before soaking in the isopropanol for 3 days. After the water was exchanged and diluted in the solvent, the sample was dried at a temperature of 40 °C for 1 hour. The dry samples were then stored in a vacuum chamber to avoid any further reaction with the moisture or carbon dioxide until testing.

3.3.7Compressive strength

The compressive strength of the sample was measured after curing for the designed time intervals. The axial compressive load is applied to the cubic specimens until rupture occurs. The loading rate set for this project was approximately 1 kN/s with the testing capacity of 3,000 kN. The compression machine is motorised with a Servo-Plus control unit (fully automatic model) as shown in Figure3-20.

Three samples were tested for each mix, and the result is reported as an average value. The compressive strength is then calculated by dividing the average load by the cross-section area (Equation 3-1):

$$S=P/A \qquad \textit{Equation 3-1}$$

Where, S is the compressive strength, MPa, P is the average load, N, and A is the cross-section area, mm^2.

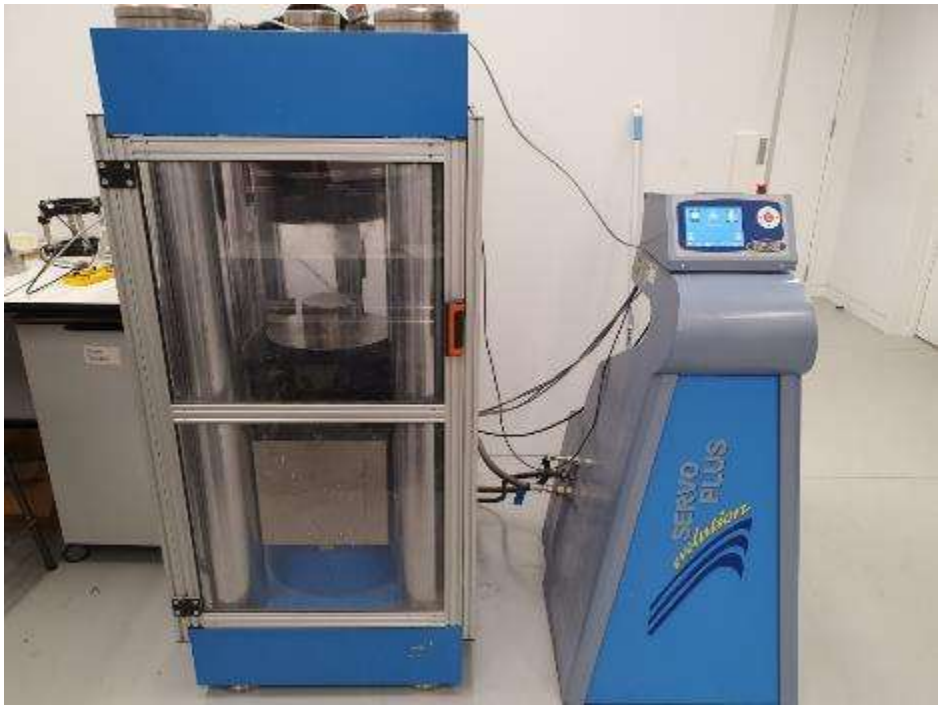

Figure3-20. The compressive strength setup

3.3.8Mortar workability test

The workability of the mortar was determined by the flow table test. In this test, a brass flow mould (100mm base, 70mm top and 60mm height) was filled with mortar and placed at the centre of the table. The flow mould was then removed before manually dropping the flow table 25 times. The spread diameter of the sample was measured and recorded at two vertical directions.

3.3.9X-ray powder diffraction and X-ray fluorescence

X-ray diffraction (XRD) was used in the characterisation of the crystal structural properties of the materials used and produced in this study. In this technique, a continuous X-ray beam is incident on the sample, and the crystalline structure causes the X-rays to diffract into many specific directions. The diffraction pattern (angels and intensities are detected by photographic film, while many publications are available to describe the physical principals in details[218, 219].

In this study, the sample were collected and ground into fine particles. A Rigaku SmartLab 3kw Powder XRD was used for the test. The X-ray radiation was CuKα with generator operation at 45kV, 40mA. The angle (2θ) ranged from 4 to 80° with step size at 0.025°, and the time for each step is 1 second.

X-ray fluorescence (XRF) was used to analyse the elemental composition of materials by detecting the fluorescent X-ray emitted from the sample when excited by a primary X-ray source.

3.3.10 Thermogravimetric analysis

Thermogravimetric analysis (TGA) is a technique that monitors the sample's mass change as a function of temperature in a controlled atmosphere. TGA is a widely applied method in cement and mineral studies. The hydrates and minerals can undergo a wide range of thermal reactions, such as dehydration, decomposition, decarbonisation and oxidation etc., and these reactions can generally lead to mass changes.

In this study, the TGA was mainly used for the quantification of bound water in hydrates, the decomposition of hydroxide and the decomposition of the carbonates. The

thermal gravimetric analyser (TGA, Netzsch Jupiter F3 STA, with a rhodium furnace) was used to identify the reactions. The temperature ramp for the TGA is 20 °C/min up to 800 °C, and the N_2 flow rate is 100 mL/min. Platinum crucibles were used to accommodate the sample, and the sample size was around 20 mg for each test.

3.3.11 Scanning Electron microscopy (SEM)

The electron microscope obtains images by using a controlled beam of electrons[220]. As shown in Figure 3-21, an electron beam was generated from a thermionic source and focused onto the sample. As a result of the electron-matter interaction volume, different types of signals are generated. The secondary electrons were due to inelastic collisions, while backscattered electrons were caused by the elastic collision. The characteristic X-rays are emitted when an electron knocks out an electron from the inner atom-shell. The images are formed by scanning the electron beam in a raster scan pattern and detecting signals of the position of the beam.

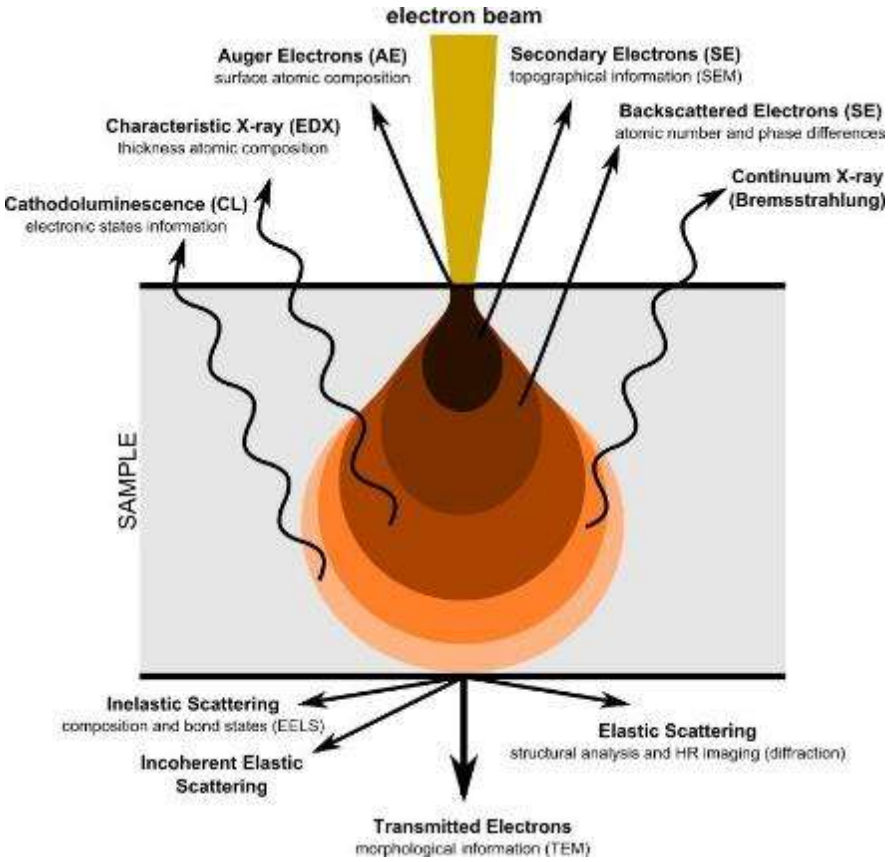

Figure 3-21. Electron-matter interaction volume[221].

3.3.11.1 Secondary electrons imaging

The secondary electrons contain the topographic information of the sample at the location of the electron beam probe. In this study, JEOL JSM 7000F Scanning Electron Microscopy (SEM) was used. All the samples were carbon coated with a thickness of around 15nm.

3.3.11.2 Backscattered electrons (BSE)

The backscattered electron images provide the information on the different phases due to the contrast of atomic number: larger atoms are more energetic scatters of electrons compared to light atoms, which create a higher signal (brighter area). Prior to the

examination, samples were well polished after the impregnation and setting of a low-viscosity epoxy resin.

3.3.11.3 Energy-dispersive X-ray spectroscopy (EDS)

The Energy-dispersive X-ray spectroscopy (EDS) was made on polished samples under high vacuum conditions. Key elements in this study are oxygen (O), magnesium (Mg) and silicon (Si). Oxygen detection is not very reliable due to its low energy peak, but the quantification of it by stoichiometry can be used to differentiate the hydrates and anhydrous material[222]. The atomic ratios from the EDS results were reported.

A polished section is necessary to avoid shadowing and to keep the equal escape path for BSE and EDS analysis. Samples were first impregnated with epoxy before polished on a polishing disc. After the polishing, the samples were stored in a vacuum desiccator. JEOL IT-300 was selected for the test, and an Oxford Aztec system with a 50 mm^2 SDD detector was used for the EDS.

3.3.12 Particle analysis

The particle size distribution and the specific surface area provides the data about the agglomeration and morphology of the powder material. These properties have a significant influence on its dispersibility, chemical reactivity, and the rheology of a suspension.

3.3.12.1 Laser diffraction particle size analysis

Particle size distribution was analysed using the HORIBA's LA-350 laser diffraction particle size distribution analyser. The laser diffraction is about the relationship between particle size and the angle and intensity of the scattered light, and it measures the

light scattered, diffracted and adsorbed by a powder dispersed in a liquid. This data is then calculated based on the Mie Scattering Theory to give the information on particle size.

The sample was dispersed in deionised water, and ultrasonic treatment was used to ensure the dispersion. The suspension was kept circulated and stirred at the stirring speed at 1500 rpm just prior to analysis.

3.3.12.2 Specific surface area test

The laser diffraction can be used to determine the specific surface area (SSA) based on the assumption of the spherical shape of the sample particles. However, the SSA calculated by laser diffraction is considerably lower than the actual value due to the sample's surface roughness and porous nature.

In this case, nitrogen adsorption technique was used as it considers the irregularities and porosity of the particles, which produces a more reliable result. Nitrogen was used as an adsorbate gas with a purity of 99.9%. Before the test, the sample was degassed under vacuum for 12 hours to remove the physically adsorbed gas molecules from the surface. The surface area was calculated based on the Brunauer-Emmett-Teller (BET) equation. A Gemini VI surface area and pore size analyser was used for carrying out the specific surface area test.

3.3.13 Hydration Heat Measurement

The hydration of the cementitious material is generally related to enthalpy changes, and the hydration heat and heat production rate were measured by calorimeters. Two types of calorimeters were used in this study. One technique is isothermal calorimetry that monitors the heat generation rate from the paste samples while the other is semi-adiabatic

thermocouples. For the semi-adiabatic method, the paste sample was insulated, and the temperature change was directed measured.

3.3.13.1 Isothermal calorimeter

In this technique, both the sample and the surrounding environment are maintained at isothermal conditions and the hydration heat flow is directly measured. In this study, a TAM model was used.

Figure 3-22. The calorimeter used for this study.

3.3.13.2 Semi-adiabatic thermocouple

To attain the adiabatic conditions, the sample was put into a special insulated chamber. The temperature rise of the sample was measured using thermocouples, and it indicated the heat being produced during the reaction. More details about the preparation and procedures can be found in EN 196-9 (2010)[223].

4 Study on olivine solubility for magnesium extraction

4.1 Introduction

Olivine is present in basalts and ultramafic rocks which are widely distributed on the Earth's surface. Compared to other silicate minerals, olivine dissolves in water relatively quickly due to its mineral structure that contains isolated silica tetrahedra (T.Herzberg 1979) and its comparative instability at lower temperatures [224-226]. In natural conditions, olivine in aqueous environments undergoes hydrolysis to produce serpentine and other products in a process commonly referred to as olivine weathering (B.Moody 1976, Moody 1976), olivine hydrolysis or serpentinization [227-229]. With CO_2 reactions, olivine may contribute Mg^{2+} or Fe^{2+} that can secure the greenhouse gas by forming environmentally stable carbonates. Thus, it is considered a promising mineral for achieving CO_2 capture and storage [13, 14, 230-232]. Several olivine carbonation approaches have been previously proposed including:

a) solid carbonation: using CO_2 gas directly [27];
b) aqueous direct carbonation: dissolve CO_2 in water to react with olivine [233-235];
c) aqueous indirect carbonation: dissolve the olivine in solutions before introducing CO_2 to the solution [22, 236, 237].

The overall reactions between olivine with dry CO_2 were found to be extremely slow. Therefore, most studies on olivine-CO_2 sequestration have focused on improving the dissolution rate using an aqueous environment. High-temperature and high-pressure conditions are effective for rapidly establishing the reaction equilibrium [238], however, achieving these conditions is generally energy intensive.

Oelkers et al. [53] undertook a critical review of olivine dissolution and summarised the four major factors influencing forsteritic olivine dissolution rates as: a) pH, b) water activity, c) temperature, and d) mineral-fluid interfacial surface area. An increase in salinity (water activity) for instance has been shown to reduce the reaction rate for olivine [239]. Prigiobbe et al. [54] showed that of the variables including: temperature, pH, CO_2 pressure and salinity (water activity). Among them, pH was the most is significant. Wogelius and Walter [55] measured the dissolution rates, Equation 4-1, of olivine in aqueous solutions with pH in the range of 2 ~ 12.4 at 25 °C, and with a low partial pressure of CO_2.

$$R=9.07 \times 10^{-12} (a_{H^+})^{0.54} +5.25 \times 10^{-15} +2.33 \times 10^{-17}(a_{H^+})^{-0.31} \qquad \textit{Equation 4-1}$$

Where, R is the rate of olivine dissolution (mol/cm^2/s) and a_{H^+} is the activity of H^+ in solution. It should be noted that in basic solutions, olivine dissolution rates are nearly pH independent throughout the pH range 6 ~ 12. Chen [56] confirmed the rate of olivine dissolution at a temperature of 65 °C between pH 2 and 5 and derived the simplified dissolution rate (R) law as shown in Equation 4-2.

$$R=10^{-8.54} \times (a_{H^+})^{0.70} \qquad \textit{Equation 4-2}$$

Crundwell[240] summarised the data from Pokrovsky and Schott [241], Rosso and Rimstidt [242] and Wogelius and Walter [55], and instead of fitting the dissolution rate data into a single reaction order, two regions were proposed. At values of pH below 6, it

has an order of reaction with respect to H^+ of 0.5, and the value reduced to 0.25 with pH values above 6.

Acid leaching generates a soluble magnesium salt which builds up in solution and is then separated from the insoluble residue, and later refined. Commonly used lixiviants are hydrochloric acid and other inorganic and organic acids.

In addition to adding acids to lower the pH, mechanical activation of materials is also very important for mineral dissolution rates. Kleiv and Thornhill [243] found that 60 minutes of dry milling increased the reaction rate of olivine in acid by a factor of 9 while the specific surface area increased from 1.18 to 2.12 m^2/g. Baláž [244] observed physico-chemical and structural changes of olivine after using different milling techniques. Haug et.al [21] used a planetary mill for 60 minutes to mechanically activate the olivine sample. The initial specific reaction rates were improved approximately three orders of magnitude compared to an untreated sample.

Unlike previous studies involving the dissolution of olivine in acid, Turianicová et. al [245] compared the reactivity of olivine with CO_2 at ambient temperature. High-pressure mineral carbonation was performed with the formation of hydro-magnesite ($(MgCO_3)_4 \cdot Mg(OH)_2 \cdot 4H_2O$) as the magnesium carbonate product. The effect of mechanical activation on carbonation conversion in a direct aqueous carbonation process were measured by Li and Hitch [246]. As a result of the grinding, the surface area of the material was increased and also accompanied by micro-strains which enhanced the carbonation process. Rigopoulos [247] also confirmed that ball milling activation could improve the CO_2 uptake of ultramafic rocks and concluded that the milling process resulted in particle size reduction and structural disordering.

In this chapter, we offer a comprehensive study from an engineering perspective that identifies the factors which may influence forsterite-rich olivine dissolution, such as particle size, acid/base condition, reaction duration, and other environmental effects (CO_2 content and pressure). The objective of this work is to provide supporting information to continue efforts for a low energy process for dissolving/releasing $Mg^{2+}_{(aq)}$ from natural olivine, which can be used for CO_2 storage, producing MgO based cementitious materials or other purposes.

4.2 Characterisation of the factors that affect olivine dissolution

4.2.1 Effect of mechanical activation

The mechanical activation process changes the reactive properties of the olivine particles not only by decreasing the particle size and increasing the surface area (Tromans and Meech 2001, Haug, Kleiv et al. 2010) ,but also by lowering the activation energy caused by dislocations and microcracks in the crystal lattice [21, 248-251]. Therefore, mechanical activation is considered an efficient method to improve the reactivity of the mineral. The olivine was ground up using a ring mill for different durations prior to testing in order to decrease the average particle size. Table 4-1 shows the median and the mean particle size (calculated based on the volume basis) corresponding to the grinding time. The mean size of the raw olivine sand was 408.24 μm, while after grinding for 20 s in the

ring mill, the mean size was decreased to 122.84 µm, and the particle size distribution also changed significantly as shown in Figure 4-1. Increasing the grinding time further decreased the mean size of olivine. However, it should be noted that prolonging the grinding time from 90 s to 120 s had little impact on its particle size.

A Scanning Electron Microscope (SEM) image of the olivine sand ground for 120 seconds is shown in Figure 4-2 with its EDS results. The olivine particle size was approximately 20 µm which agrees with the particle size distribution measurement and the elemental composition results are similar to the previous X-ray Fluorescence (XRF) analysis of the *as-received* material.

Table 4-1. The particle size distribution of the olivine after different grinding time

Duration (s)	*as-received*	20 s	60 s	90 s	120 s
Median size (µm)	386.89	75.26	50.64	22.32	17.26
Mean size (µm)	408.24	122.84	88.72	45.71	28.32

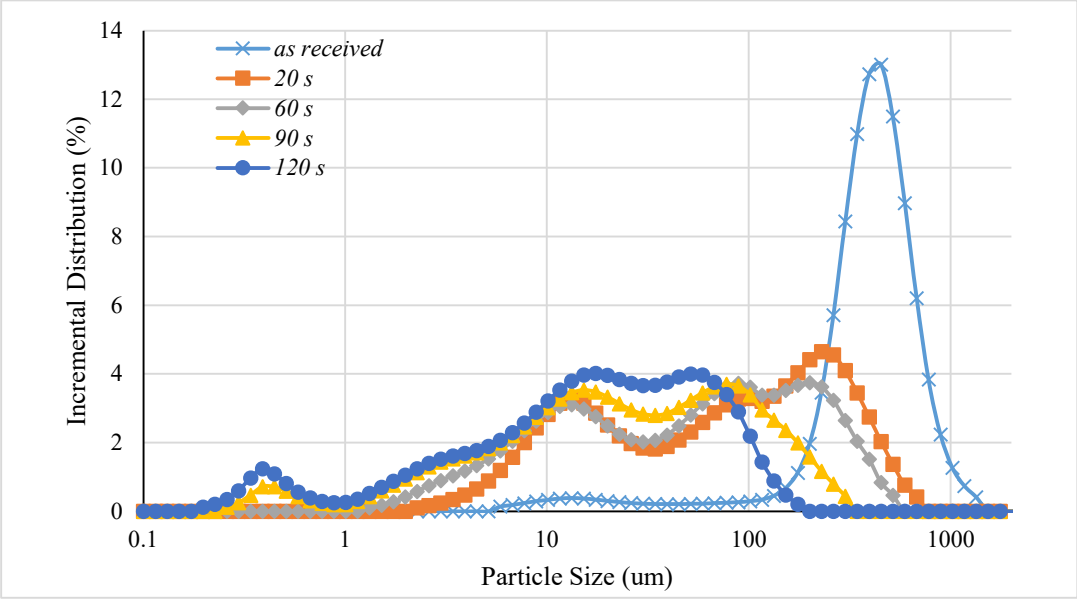

(a). Incremental Distribution

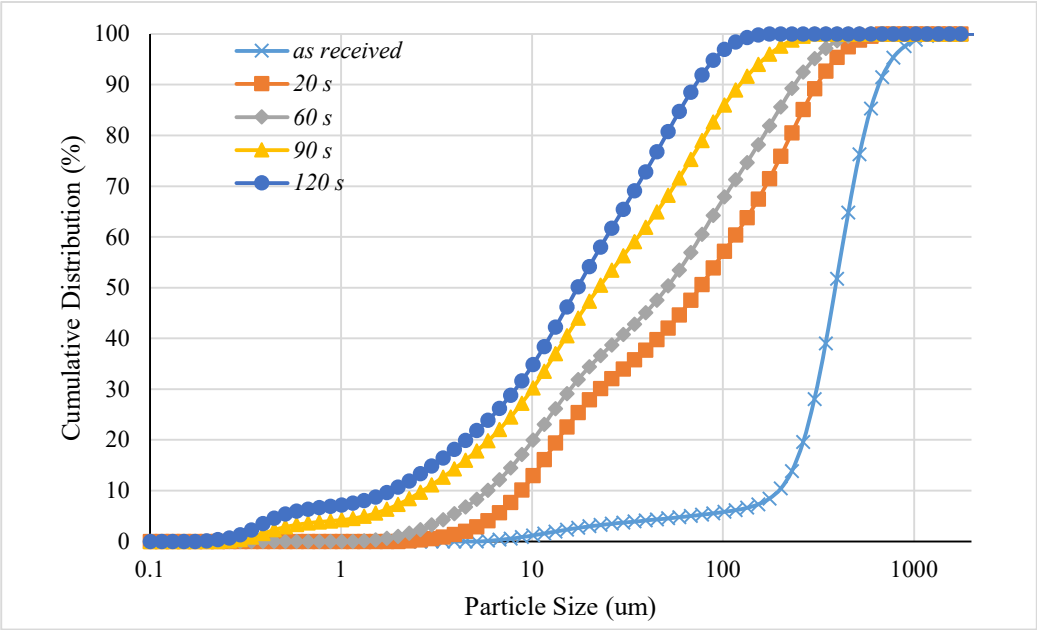

(b). Cumulative Distribution

Figure 4-1. The particle size distribution of olivine samples with different grinding times.

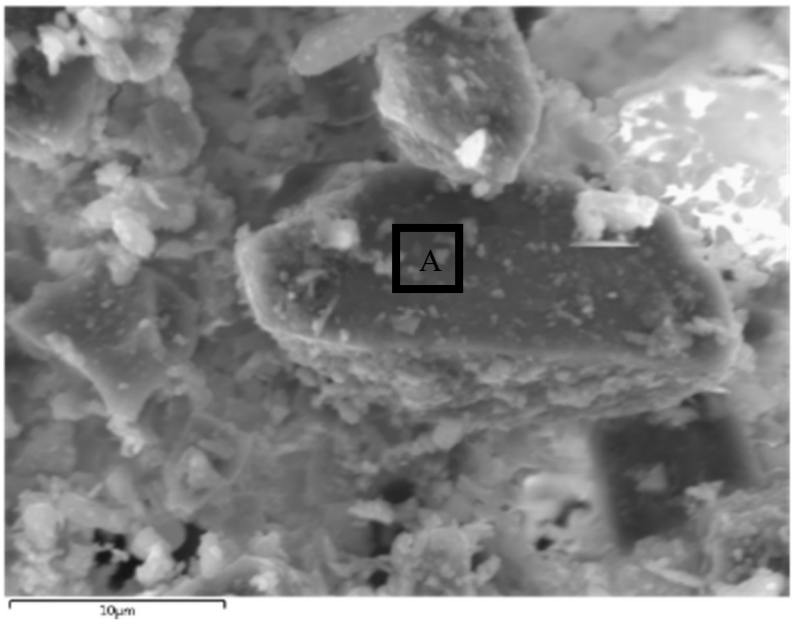

EDS results (wt %)	
	Area A
O	*43.4*
Si	*19.6*
Mg	*30.3*
Fe	*6.6*

Figure 4-2. Electron microscopy analysis of the sample after grinding.

Olivine (4 g) was added to water (80 mL) to assess changes in pH. Figure 4-3(a) illustrates the pH profile of the olivine in water. The pH of the as-received olivine increased rapidly and reached a pH of 10 in 3 minutes. In comparison, the pH of the ground olivine sample increased faster. The olivine sample ground for 120 seconds reached a pH of 10 after 60 seconds. However, a similar trend was occurred with the particle size distribution, further prolonged grinding time did not have an obvious positive effect on the rate of pH change. Conductivity results (Figure 4-3(b)) demonstrated a difference with regards to sample grinding and this type of analysis provides a reliable indicator of the total dissolved solids. The longer the grinding duration of the olivine samples, the higher the conductivity due to the increased solids dissolved. The dissolved Mg ion (Mg^{2+}(aq)) concentrations of the ground olivine samples are shown in Figure 4-4 after mixing in D.I. water for 120

minutes. Increasing the olivine grinding time, improved the dissolved magnesium ion concentration until it reached a plateau after 60 seconds of grinding.

A previous study[252] has established that olivine dissolution is surface-reaction-limited under conditions found in the natural environment. Prolonged grinding can increase the surface area which leads to a higher dissolution rate. However, in the dry milling process, agglomeration is usually observed. In Kleiv and Thornhill[243]'s study, the olivine sample reached its highest proportion of fines after 5 mins grinding in a planetary mono mill. Beyond this duration, instead of showing a further net increase in surface area, an obvious decrease was observed. Similarly, in this study, the particle size distribution and the proportion of the fine particles did not change significantly after grinding for 60 seconds in the ring mill. Compared to another study on mechanical activation[245], the olivine dissolution reaction reached its equilibrium at a relatively large particle size, because water is used as the solvent instead of an acidic solution. The effect of hydrogen activity will be discussed in the following sections.

From this point on, olivine samples used for the remaining experiments were ground in the ring mill for 120 seconds unless otherwise specified.

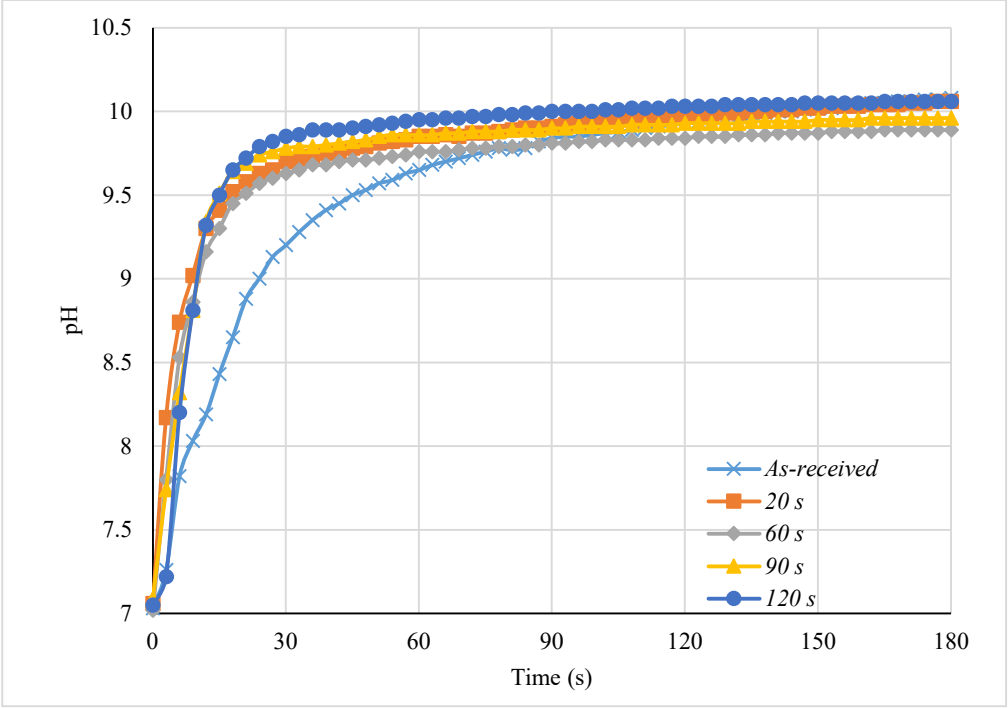

(a) pH

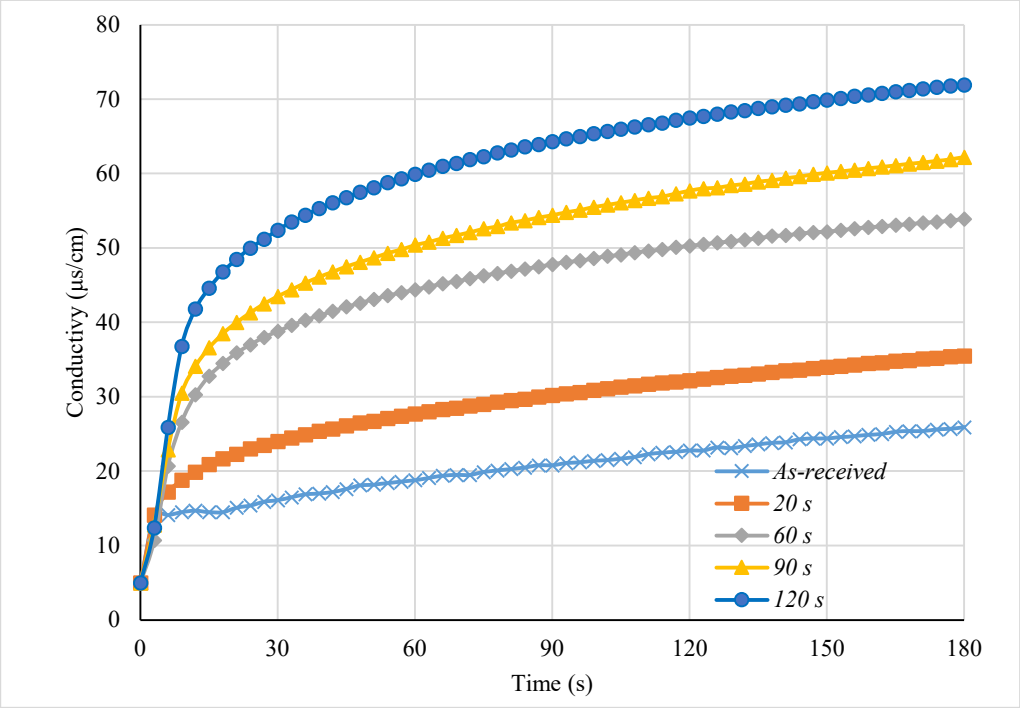

(b) Conductivity

Figure 4-3. The pH and conductivity profile of the olivine with different grinding times.

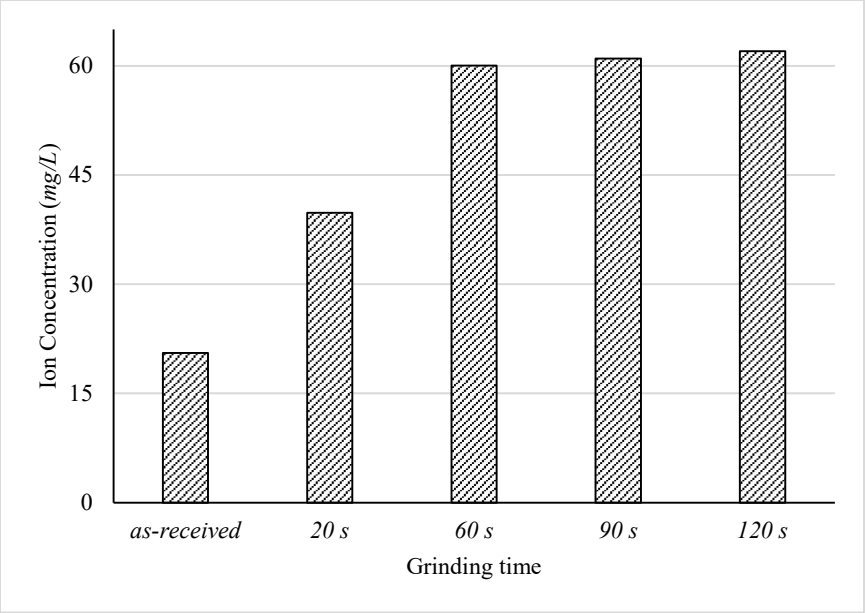

Figure 4-4. The Mg^{2+}(aq) concentration of olivine in water with different grinding times.

4.2.2 Effect of pH

Hydrochloric acid (0.01 mol/L, 80 mL, pH = 2), sodium hydroxide (0.1 mol/L, 80 mL, pH = 13), and D.I. water (80 mL, pH=7) were mixed with the olivine (4 g) to assess the effect of pH on olivine dissolution. The pH changes with respect to time after the olivine was mixed with different pH solutions are shown in Figure 4-5. When olivine was added to the acidic solution, it dissolved quickly in the first twelve minutes (0.2 h) and the pH continued to increase afterwards. The pH value of the alkaline solution did not change noticeably which indicated that the dissolution of olivine is inhibited by a high pH environment. The pH of the D.I. water reaction increased from 7 to a maximum of 10 before it decreased slightly due to the carbonation. This value is close to the pH of a MgO solution or a $Mg(OH)_2$ solution.

Table 4-2 shows the comparison of $Mg^{2+}_{(aq)}$ concentration in different pH solutions. The dissolution of olivine in acidic solution, expressed in terms of the $Mg^{2+}_{(aq)}$ concentration (235 mg/L), was more than 10 times greater than that with D.I. water (20 mg/L). Only a small amount of dissolved Mg ions (0.2 mg/L) was detected in the alkaline solution, which was in accordance with the unnoticeable pH change.

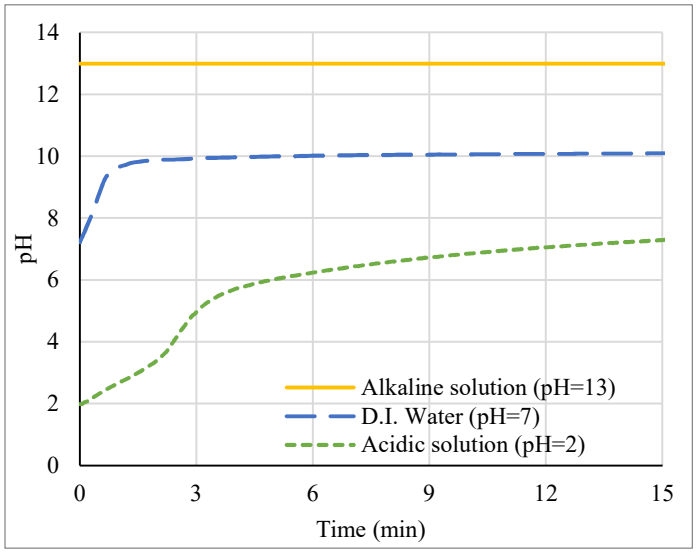

(a). In first 15 minutes.

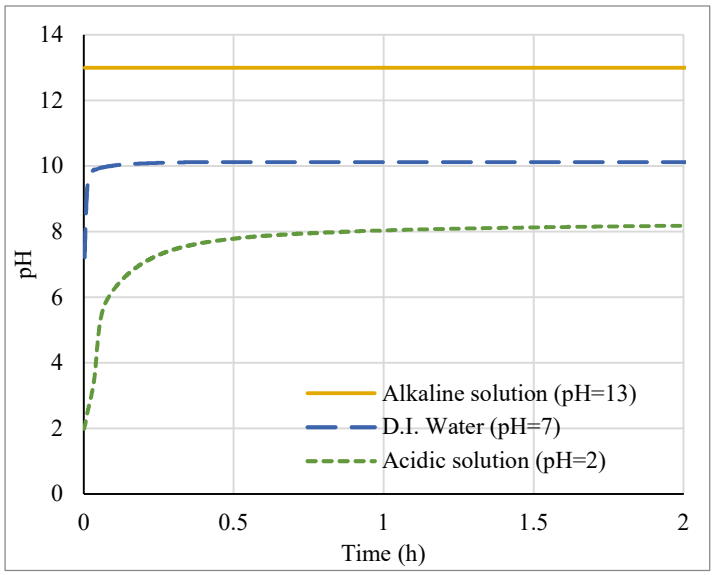

(b). In first 2 hours

Figure 4-5. The pH changes of olivine mixed with different solutions.

Table 4-2. The magnesium ion concentration in different pH solutions

Solution	Initial pH	Final pH (after 2 hours)	Temperature	Duration	$Mg^{2+}_{(aq)}$ Concentration (mg/L)
Acidic	2.0	7.9	20 ± 2 °C	2 hours	235
D.I. water	7.0	9.9			20
Alkaline	13.0	13.0			0.2

4.2.3 Effect of acid type

Since lowering the pH was beneficial to the release of $Mg^{2+}_{(aq)}$ from olivine, the effect of different acids, including strong and weak acids, at the same pH were studied. Hydrochloric acid (HCl, 0.01 mol/L) and nitric acid (HNO_3, 0.01 mol/L) were used as strong acids (pH = 2), while the selected weak acid was acetic acid (CH_3COOH, 1 mol/L, pH = 2.38).

The pH profiles for olivine reacting with these acids are shown in Figure 4-6. For the olivine sample mixed with HCl, the pH increased quickly, and the solution was neutralised in 40 minutes. It also demonstrated that the reaction between olivine and nitric acid is faster compared with hydrochloric acid, as it took only 15 mins to reach a pH of 7. The final pH values for both HCl and HNO_3 with olivine were around 8. Combined with the magnesium concentrations of these solutions at different time intervals (Figure 4-7), it can be seen that after one hour, the $Mg^{2+}_{(aq)}$ concentration in HCl and HNO_3 remained stable with reaction time. This suggested the equilibrium of the reaction had been reached. In this case, it was due to the complete consumption of hydrogen ions.

$$Mg_2SiO_4+4H^+ \rightarrow 2Mg^{2+}+SiO_2+2H_2O \qquad \textit{Equation 4-3}$$

In contrast, the olivine mixed with acetic acid showed a different pattern. The pH increased from 2.38 to 3 in the first 15 mins while after that, the pH gradually increased to 3.33 and kept stable after 2 hours indicating that the acetic acid was present in excess compared to olivine. The $Mg^{2+}_{(aq)}$ concentration continually increased with reaction time. Note that the acetic acid concentration (1 mol/L) is always higher than nitric and hydrochloric acid (0.01 mol/L); however, the $Mg^{2+}_{(aq)}$ concentration did not correspond to the acid concentration. This may be due to a solubility limit, a slow reaction rate, or a reaction equilibrium limitation of olivine in acetic acid.

This leads to a conclusion that pH is normally considered as the most significant factor for olivine dissolution, however, these results demonstrated it was the amount of the active hydrogen in the solution in real time that matters rather than the initial solution pH.

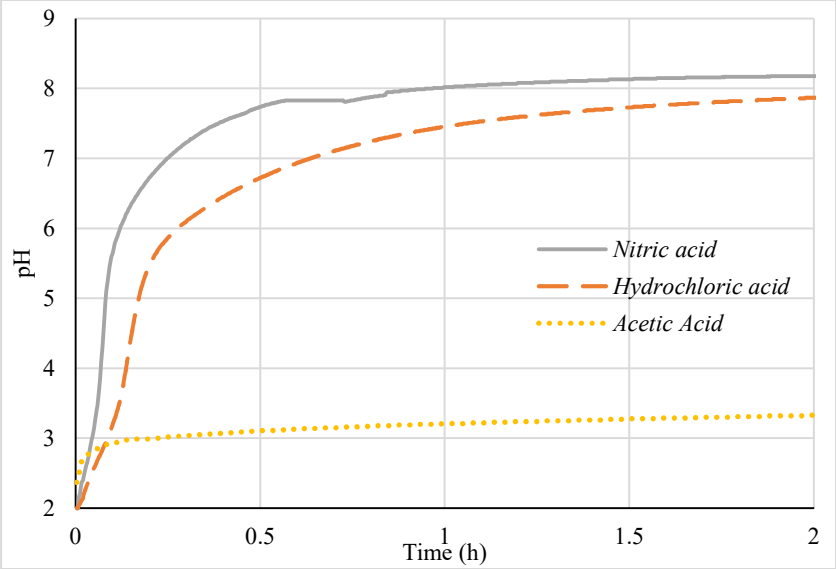

Figure 4-6. The pH profile of olivine in different acids.

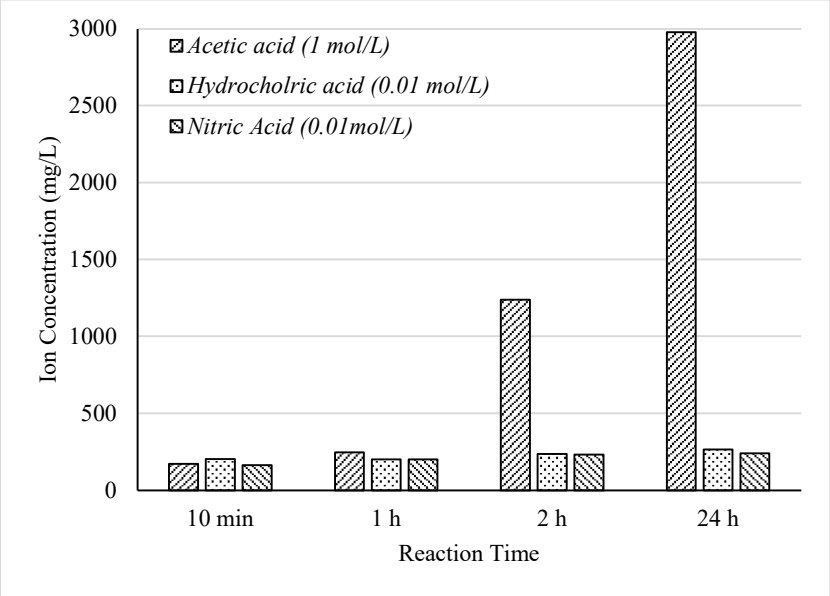

Figure 4-7. The $Mg^{2+}_{(aq)}$ concentration of olivine with different acids at different time intervals.

4.2.4 Effect of acid concentration

The reaction rate between olivine and nitric acid was the highest among the strong acids, thus the effect of different concentrations of nitric acid was studied (0.01 mol/L, 0.1 mol/L, 1 mol/L and 10 mol/L). In order to quantify the amount of dissolved Mg^{2+} as a fraction of the total Mg in the olivine sample, the dissolving degree, *D*, was proposed and calculated as follows:

$$D = \frac{C \times V}{1000 \times m \times MgO\% \times {}^{M1}/_{M2}} \times 100\% \qquad \textit{Equation 4-4}$$

where *C* is the Mg concentration (mg/L), *V* is the volume of the olivine solution (0.08 mL), *m* is the mass of the olivine sample (4 g), *MgO%* is the weight fraction of MgO in olivine sample (as per XRF results, 45.03%), M_1 is the molar mass of the magnesium (24 g/mol), and M_2 is the molar mass of the magnesium oxide (40 g/mol).

As can be seen from Figure 4-8, increasing the molar concentration of nitric acid can improve the release of $Mg^{2+}_{(aq)}$ from olivine. The $Mg^{2+}_{(aq)}$ concentration in 10 mol/L HNO_3 was 8,902 mg/L compared to 240 mg/L in 0.01 mol/L acid. Even with 10 mol/L HNO_3, less than 70% of the total Mg was dissolved. However, using such a high concentration acid may not be practical due to issues with safe handling and materials compatibility of processing equipment.

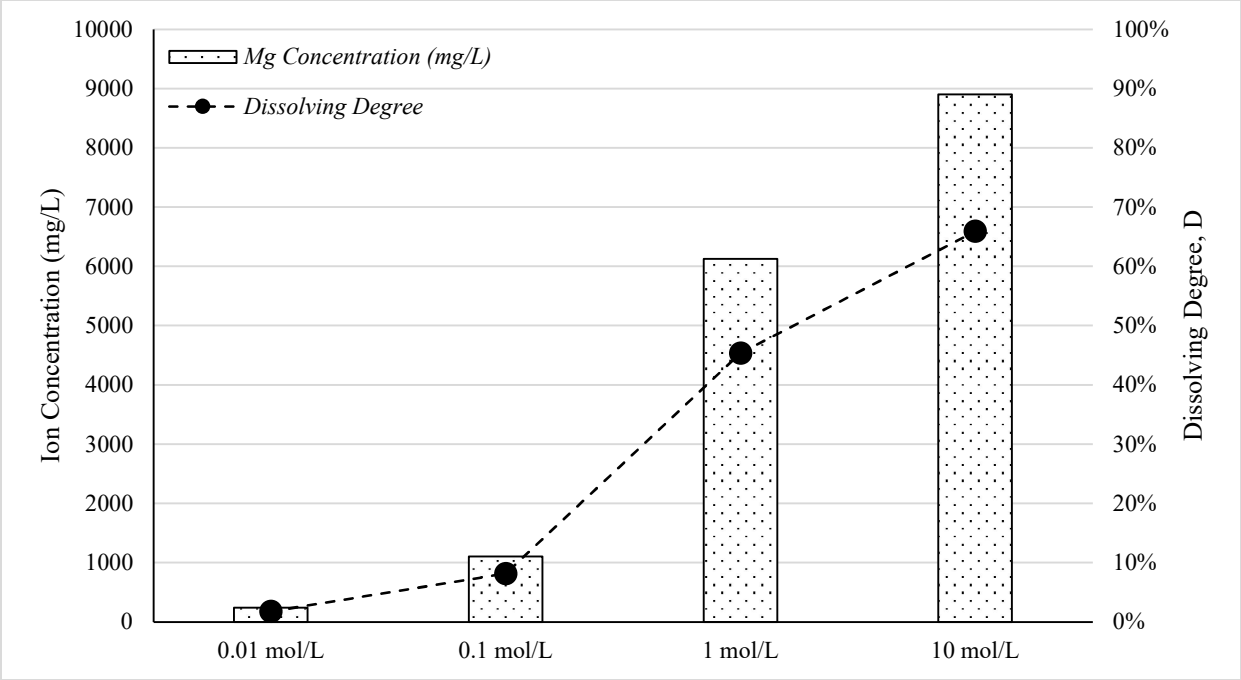

Figure 4-8. Mg^{2+}(aq) released from olivine under different nitric acid concentrations.

4.2.5 Effect of CO_2 content

Serpentinization can take place under ambient temperatures and pressures, but the reaction rate is limited [253-255]. To accelerate the reaction rate, CO_2 was introduced to the system with the presence of water. In this experiment, an air pump was used to keep blowing the fresh air or CO_2 into the slurry. Carbonated water was also used to compare the extraction efficiency against deionised water.

The pH results are shown below in Figure 4-9 while the ICP-MS results are summarised in Figure 4-10. When air bubbles were blown into the slurry, the pH of the system was constantly lower than that of the D.I. water. This suggests that the dissolved magnesium hydroxide is partially consumed by the carbonic acid, thereby, shifting the

dissolution equilibrium to the reaction products and increasing the dissolution of olivine. This was confirmed by the higher $Mg^{2+}_{(aq)}$ concentration. The pH value of the CO_2 bubbled water and carbonated water were much lower and steadily increased with time. The concentration of $Mg^{2+}_{(aq)}$ from olivine increased to 162 mg/L and 172 mg/L in carbonated water and CO_2 bubbling water, respectively. The higher $Mg^{2+}_{(aq)}$ concentration in CO_2 conditions may be attributed to the production of a Mg-carbonate. As noted by Saldi et al[256] the formation of magnesite however is very slow at ambient temperatures around 25ºC. Further details on the formation of Mg-carbonates are provided in section 3.9. When the CO_2 was introduced, the dissolved $Mg(OH)_2$ may have reacted to form $MgCO_3$, which is more soluble than $Mg(OH)_2$. The solubility of $MgCO_3$ is 180 mg/L while only 6.9 mg/L for $Mg(OH)_2$ at 25℃ [257]. Considering the $Mg^{2+}_{(aq)}$ concentration under CO_2 conditions were 162 mg/L (in carbonated water) and 172 mg/L (in CO_2 bubbled water), this indicated it may have reached the $MgCO_3$ solubility limit (180 ml/L). The slightly higher concentration in CO_2 bubbling water might be caused by the agitation effect when CO_2 bubbles were purged compared to the carbonated water.

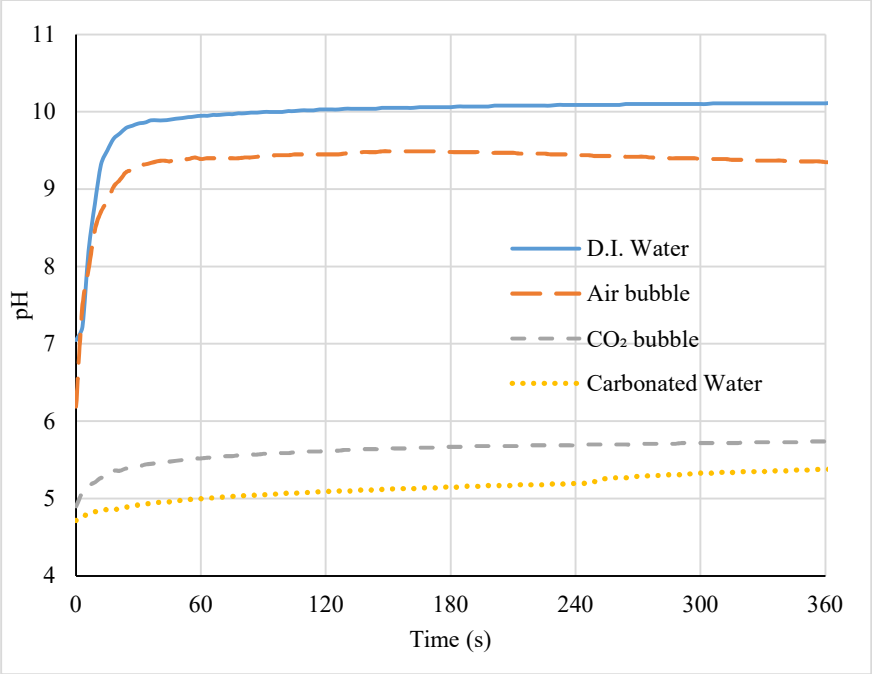

Figure 4-9. pH profile of olivine mixed with various CO_2 content solution.

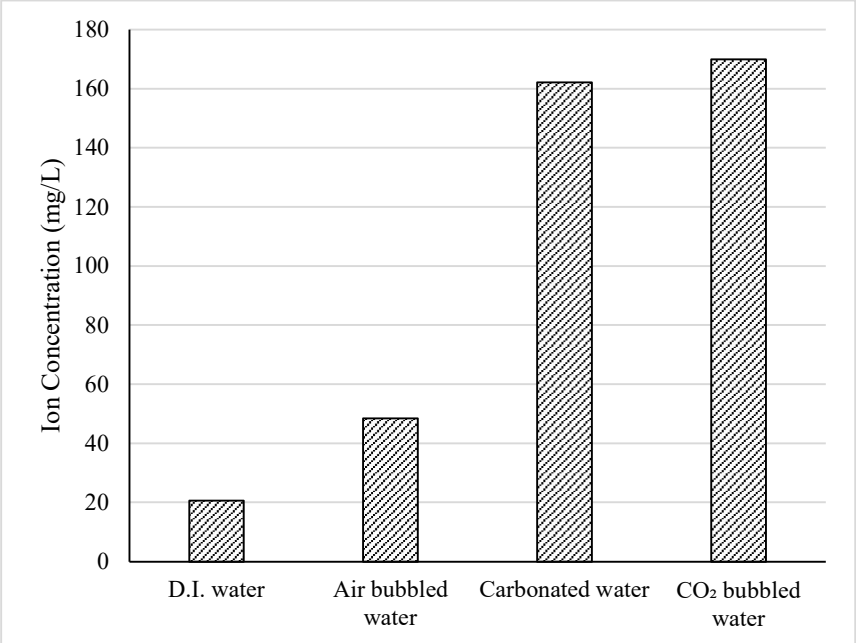

Figure 4-10. Magnesium concentration of olivine with different CO_2 content solution.

4.2.6 Effect of CO_2 pressure

Apart from the CO_2 content, the influence of CO_2 pressure was also studied. The olivine in solution was placed in a pressurised reaction vessel to assess various CO_2 pressures via a regulator. The reaction was under ambient temperature (20 ± 2 ˚C) and lasted for 24 hours. As shown in Figure 4-11, increasing the CO_2 pressure resulted in increasing $Mg^{2+}_{(aq)}$ concentrations. This was potentially caused by the greater amount of CO_2 that dissolved into water producing more carbonic acid. The pH of each solution was measured, and the calculated CO_2 solubilities are shown in Table 4-3. The higher CO_2 partial pressures increased the CO_2 solubility, thus, lowering the pH. However, compared to mixing olivine with carbonated water, the solubility of $Mg^{2+}_{(aq)}$ was not significantly improved.

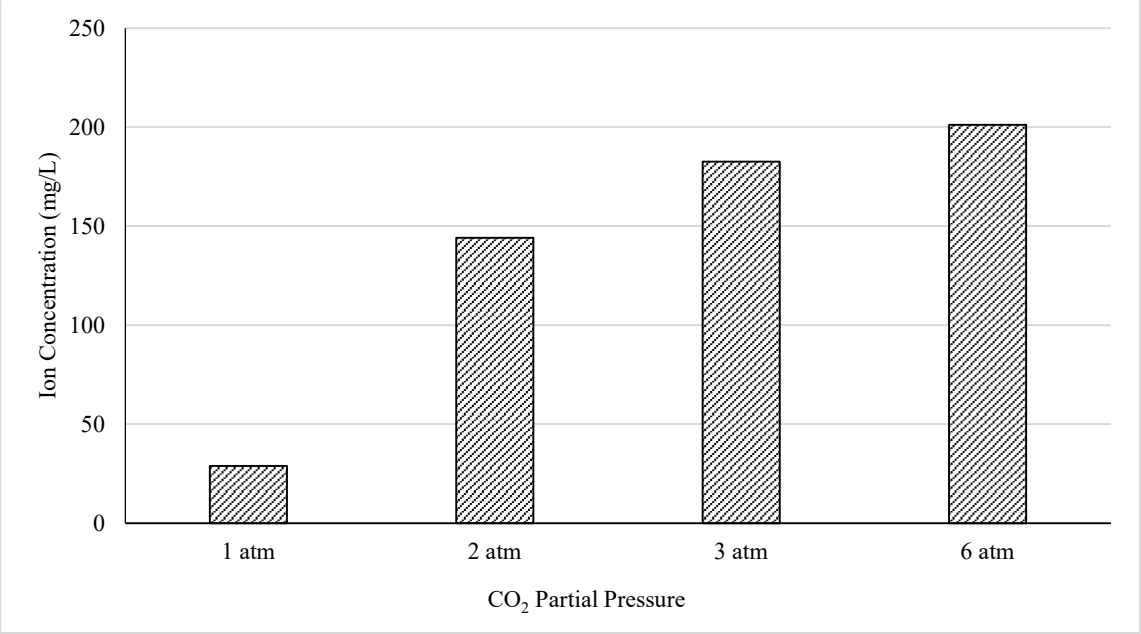

Figure 4-11. Effect of CO_2 pressure on olivine solubility after 2 hours.

Table 4-3. The pH and CO_2 solubility under various CO_2 partial pressure

	CO_2 partial pressure			
	1 atm	**2 atm**	**3 atm**	**6 atm**
pH	6.32	6.18	6.01	5.93
CO_2 solubility [257] (1000× mole fraction of CO_2 in water)	0.704	1.408	2.112	4.224

4.2.7 Effect of reaction duration

Longer reaction duration increases the contact time between olivine and water, potentially leading to higher dissolved ion concentrations. Figure 4-12 shows the effect of reaction time on $Mg^{2+}_{(aq)}$ concentration, while other parameters are constant at ambient temperature (20 °C) and pressure (1 atm). Increasing the reaction duration from 10 min to 2 hours had an obvious effect on the $Mg^{2+}_{(aq)}$ concentration with the introduction of CO_2. However, further increasing the reaction time did not demonstrate much improvement.

The reaction rate is the measure of the change in $Mg^{2+}_{(aq)}$ concentration per unit time (second). As shown in the Figure 4-12, the reaction rate decreased with reaction duration, indicating that the equilibrium between the undissolved mineral and dissolved aqueous phase was being approached.

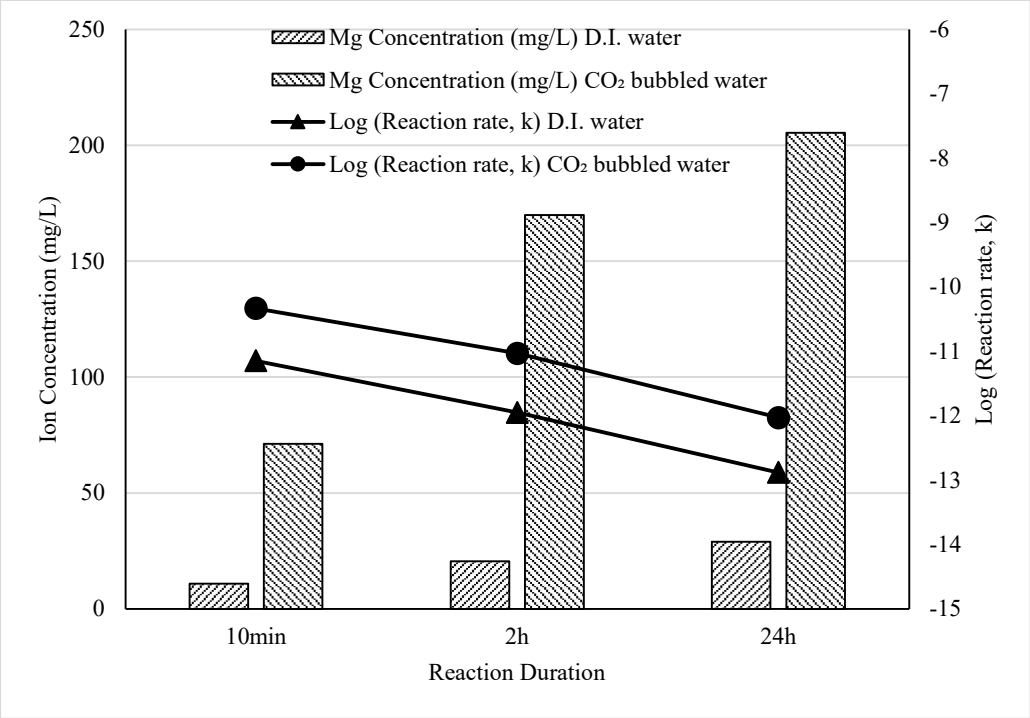

Figure 4-12. $Mg^{2+}_{(aq)}$ concentration and reaction rate with different reaction times.

4.3 Characterisation of the recovered magnesium composite

The presence of CO_2 in the solution can increase the olivine dissolution rate and Mg^{2+}(aq) release. One reason is that when CO_2 is dissolved in water, it lowers the pH, while another reason is that a reaction reaction between olivine and CO_2 to form an hydrated Mg-carbonate product. At ambient temperatures Mg-bearing materials typically form hydrated magnesium carbonates such as nesquehonite ($MgCO_3 \cdot 3H_2O$) or hydromagnesite ($Mg_5(CO_3)_4(OH)_2 \cdot 4H_2O$) [258]. The solubility of nesquehonite for instance (Ksp = $10^{-5.3}$) is much higher than $Mg(OH)_2$ (Ksp = 1.2×10^{-11}).

Figure 4-13 shows the thermal gravimetric (TG) analysis of the chemical-grade references: $Mg(OH)_2$, $MgCO_3$, and the composite recovered from the olivine sample. For the TG curves of the recovered products, two major stages of weight loss were observed.

The first stage (I) occurs at approximately 100°C. This mass loss is caused by the evaporation of absorbed water in the composite. In the range of 300°C to 500°C (II), these two curves experienced obvious weight loss which was similar to the references; and associated with the decomposition of $Mg(OH)_2$ and $MgCO_3$.

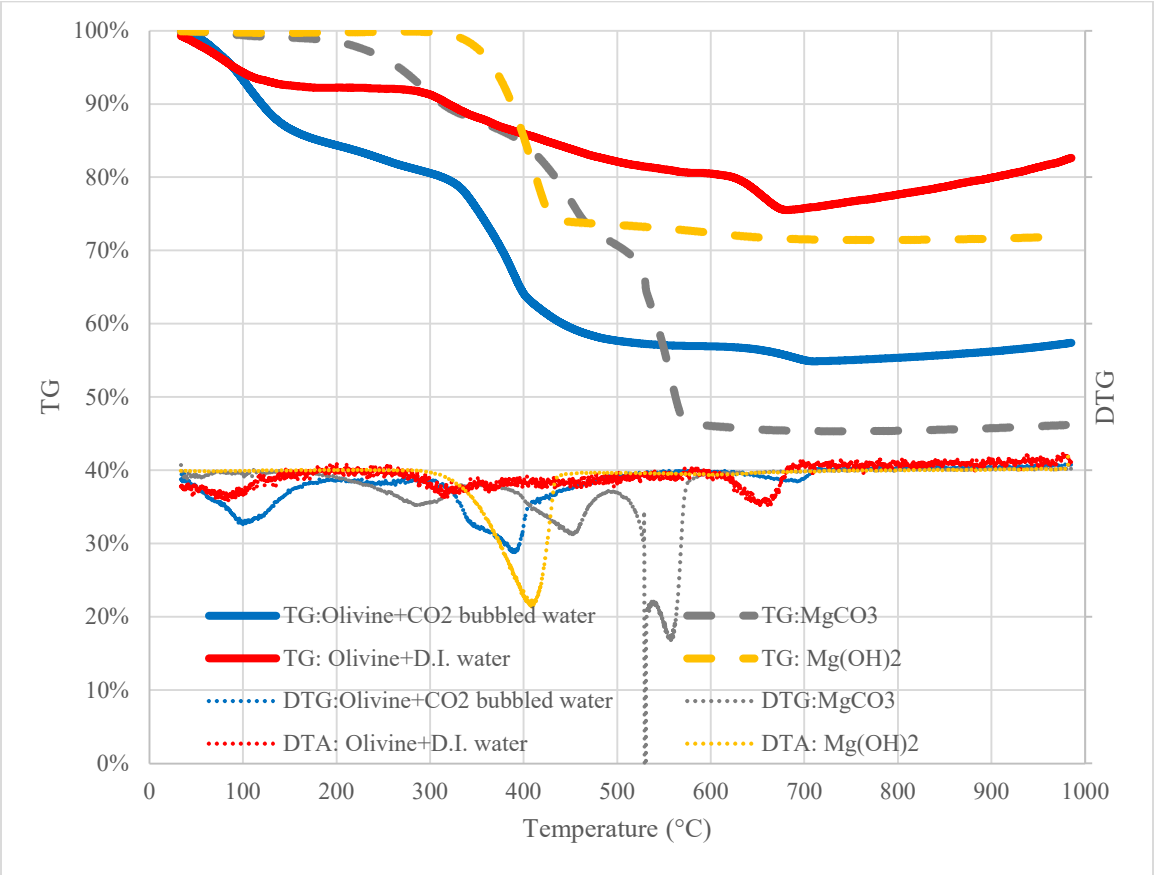

Figure 4-13. TG/DTG curves of references and composites recovered from olivine.

The TG results for the recovered olivine-CO_2 material suggest a significant hydrated component and coupled with the XRD analysis provided in Figure 4-14, the recovered Mg-carbonate is likely to be giorgiosite, which is a metastable phase between nesquehonite and hydromagnesite. A small amount of silicon dioxide was also detected.

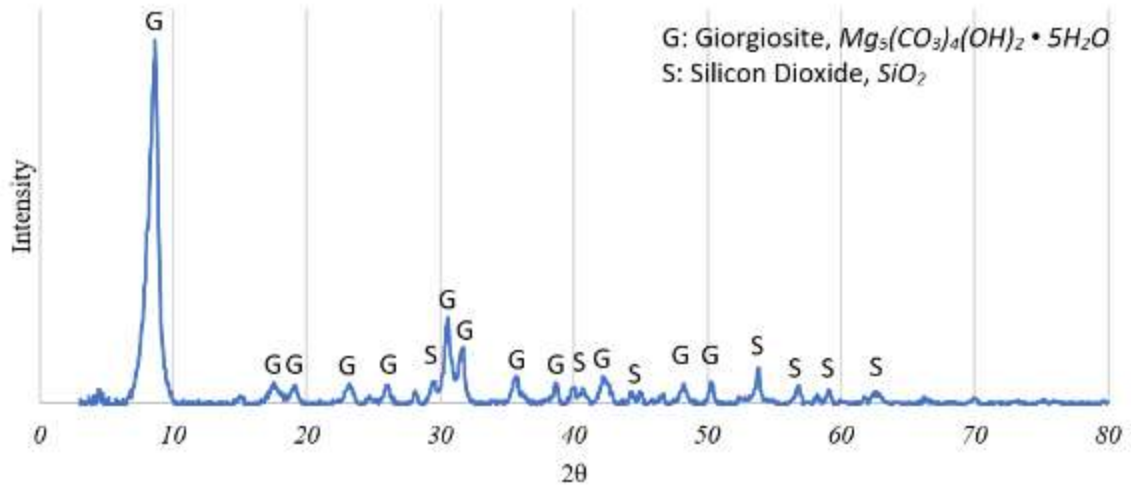

Figure 4-14. XRD analysis of the recovered products from olivine solution.

Additionally, Figure 4-15 shows the microscopy of the sample recovered from the olivine mixed with CO_2 bubbled water. As the product was recovered by a slow evaporation process in a 50 °C oven, it precipitated with a smooth surface and close packing between particles. According to the elemental analysis of area A, Mg was the main metal found in the composite which supports the TG and XRD analysis. It can also be seen that there were some small particles that accumulated around the magnesium products, these particles are very fine with a size of around 0.1 μm. From the EDS analysis of area B, silicon was detected. This is caused by the dissolution and precipitation of the silica in olivine. The particle size and morphology agree well with previous studies [233, 259].

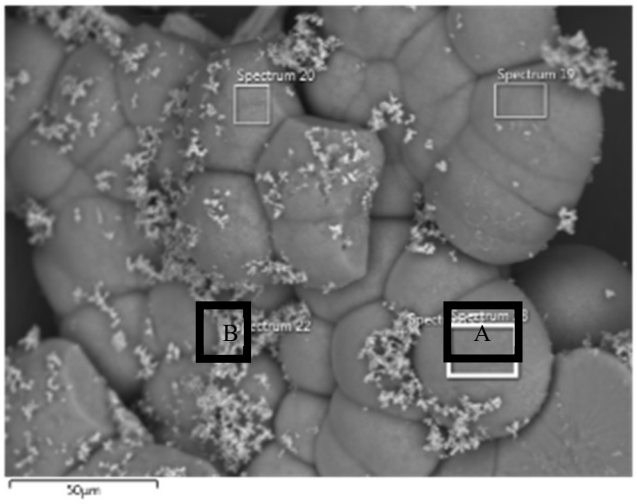

EDS results (wt %)		
	Area A	*Area B*
O	*59.7*	*52.8*
Si	*-*	*23.7*
Mg	*39.8*	*23.2*
Ca	*0.5*	*-*

Figure 4-15. Microscopy of Mg-composite recovered from olivine with CO_2 bubbled water.

In fact, this also could be a potential alternative for nano-silica production if olivine was dissolved in acid [260]. The silica appeared as individual particles and no silica rich layers were observed under SEM. The reaction products reported in this investigation were recovered as seperate precipitates from the solution and not directly on the olivine surface as reported by Bearat et al.[261]. The silica concentration from the olivine dissolved in CO_2 water was considerably higher than it from water, as shown in Table 4-4.

Table 4-4. The Mg and Si concentration from olivine mixed with D.I. water and CO_2 water

	Olivine with D.I. water	**Olivine with CO_2 water**
Mg concentration (mg/L)	20.57	169.90
Si concentration (mg/L)	5.01	112.42

4.4 Olivine dissolution: Thermodynamics, kinetics and mechanisms

Olivine used in these experiments was mainly forsterite (Mg-rich) in character according to XRD and XRF analyses. Despite some iron (10.65%) being present in the olivine, the composition for forsterite (Mg_2SiO_4) will be used to simplify the reactions. The overall reaction equation of olivine hydrolysis is:

$$2Mg_2SiO_{4s}\ (Forsterite) + 3H_2O \rightarrow Mg_3Si_2O_5(OH)_4\ (Serpentine) + Mg(OH)_2 \qquad \textit{Equation 4-5}$$

The thermodynamic data of the reactants and products are listed in Table 4-5. The standard Gibbs free-energy change for the olivine dissolution (ΔG) is a negative value (-53.60 kJ/mol), at this pressure and temperature, thus the reaction can happen spontaneously. In fact, the change in free energy for constant temperature is defined as:

$$\Delta G = \Delta H - T\Delta S \qquad \textit{Equation 4-6}$$

This suggests that the reaction proceeds spontaneously at low temperatures. Note that the conversion of the reaction product serpentine to the reactant forsterite takes place during serpentine calcination at approximately 800°C [262]. This agrees with previous results demonstrating that increasing the reaction temperature did not favour product formation; however, increasing the temperature did increase the dissolution rate.

In the presence of CO_2, the overall reaction becomes complex and can be divided into the following elementary steps. First, the olivine begins to dissolve and produce the hydroxide making the solution alkaline (Equation 4-5). Concurrently, the CO_2 partially dissolves into the water and produces active hydrogen ions and bicarbonate:

$$CO_2+H_2O \rightleftharpoons HCO_3^- + H^+ \qquad \textit{Equation 4-7}$$

Therefore, the hydroxide produced by olivine was continuously consumed and converted to a carbonate. The olivine dissolution proceeded until the new equilibrium was achieved. The overall reaction can be written excluding hydrogen and water:

$$Mg_2SiO_4+2CO_2 \rightarrow 2MgCO_3+SiO_2 \qquad \textit{Equation 4-8}$$

In acidic conditions with a higher concentration of the active hydrogen ion and greater solubility of the reaction products (magnesium chloride, nitrate or acetate), more olivine was dissolved. The reaction between olivine with acid is:

$$Mg_2SiO_4+4H^+ \rightarrow 2Mg^{2+}+SiO_2+2H_2O \qquad \textit{Equation 4-9}$$

According to the thermodynamic analysis, the change in free energy for the above overall reactions are all negative values and support the observation that these reactions can happen spontaneously at conditions under 1atm and 25 °C (or 298.15 K).

Table 4-5. Thermodynamic analysis during olivine dissolution (at 1 atm, 298.5K) [263]

		Reactants		**Products**		**Overall**
Olivine dissolution in water (Equation 4-5)		$2Mg_2SiO_4$	$+3H_2O \rightarrow$	$Mg_3Si_2O_5(OH)_4$	$+Mg(OH)_2$	
	ΔG^0_f (kJ/mol)	-2051.3	-237.2	-4034.0	-833.8	ΔG= -53.6
	ΔH^0_f (kJ/mol)	-2170.4	-285.8	-q	-924.7	ΔH= -88.2
	S^0 (J/(k·mol))	95.2	69.9	221.3	63.1	ΔS= -115.7
		Reactants		**Products**		**Overall**
Olivine dissolution in water with the presence of CO_2		Mg_2SiO_4	$+2CO_2 \rightarrow$	$2MgCO_3$	$+SiO_2$	
	ΔG^0_f (kJ/mol)	-2051.3	-394.4	-1029.3	-805.0	ΔG= -23.5
	ΔH^0_f (kJ/mol)	-2170.4	-393.5	-1112.9	-859.3	ΔH= -127.7
	S^0 (J/(k·mol))	95.2	213.6	65.7	41.8	ΔS= -349.2

(Equation 4-8**)**

		Reactants		**Products**			**Overall**
		Mg_2SiO_4	$+4H^+ \rightarrow$	$2Mg^{2+}$	$+SiO_2$	$+2H_2O$	
Olivine dissolution in acid (Equation 4-9)	**ΔG^0_f (kJ/mol)**	-2051.3	0.0	-456.0	-805.0	-237.2	ΔG= -140.1
	ΔH^0_f (kJ/mol)	-2170.4	0.0	-462.0	-859.3	-285.8	ΔH= -184.4
	S^0 (J/(k·mol))	95.2	0.0	-118.0	41.8	69.9	ΔS= -149.5

In terms of the reaction rates, the following Arrhenius equation shows the empirical relation between the reaction rate and other factors:

$$r=Ae^{-Ea/(RT)} \qquad \textit{Equation 4-10}$$

where E_a is the activation energy of the reaction (kJ/mol), R the gas constant, T the absolute temperature, e the base of natural logarithm scale, and A the frequency factor which represents the collision frequency between hydrogen and olivine surface:

$$A=k_0 \cdot [H^+]^n \cdot [Mg_2SiO_4]^m \qquad \textit{Equation 4-11}$$

By taking the logarithm of both sides of Equation 4-10 and substituting Equation 4-11, the following equation results:

$$\log (r)=\log (k_0) +n \cdot \log ([H^+])+m \cdot \log ([Mg_2SiO_4]) -(E_a \cdot \log e)/RT \qquad \textit{Equation 4-12}$$

Since the amount of undissolved olivine was constant for each experiment, the value for $[Mg_2SiO_4]^m$ will be constant and can be combined with $\log(k_0)$ and incorporated into a new parameter, $\log(k'_0)$, as described below.

$$\log(k'_0)= \log (k_0) +m \cdot \log ([Mg_2SiO_4]) \qquad \textit{Equation 4-13}$$

The overall equation can be rearranged to the following linear equation:

$$log\ (r)=n\cdot(-pH)+log(k'_0)-(E_a\cdot log\ e)/RT \qquad \text{Equation 4-14}$$

By summarising and plotting all the dissolution rate data under different pH conditions, the linear relation between pH and *log r* is shown in Figure 4-16. In this study, log *e*=0.434, R=8.314 J/(K·mol) and T=298.15 K. The value for the activation energy has previously been reported [264-266] and ranged from 38.1 to 126 kJ/mol. We have used the value found in Hanchen's results of 52.9 kJ/mol [267]. Therefore, by regressing the data using Equation 4-14, it can be concluded that n=0.31 ± 0.03, $\log(k'_0)$ = -1.45 ± 0.17. Thus, the reaction rate can be written as:

$$log\ (r)= -0.31\ pH - 2763.31/T - 1.45 \qquad \text{Equation 4-15}$$

Equation 4-15 demonstrates that by decreasing the pH and increasing temperature, the dissolution rate could be improved, as shown in Figure 4-16. This is in accordance with the results of other researchers [241, 267, 268] who studied the olivine dissolution rate at temperatures of 25°C, 90°C, 120°C and 150°C. The reported olivine dissolution rate value varies slightly, and this might be a consequence of different types of olivine and various experiment methods. Please note that the reaction order ($n=0.31\pm 0.03$) is very close to the value of 1/3, which often indicates a chain reaction or other complex reaction mechanism. However, for now, it is an empirical rate equation, and determining the fundamental reaction mechanism using elementary reactions is beyond the scope of the current work.

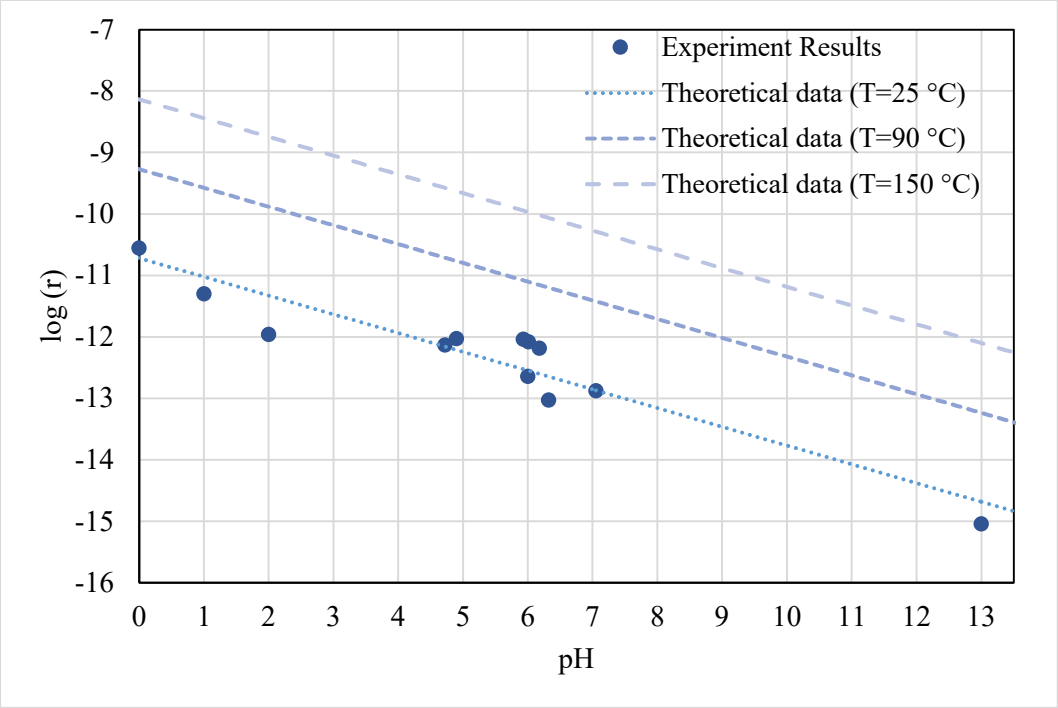

Figure 4-16 The linear relation between pH and log *(r)*.

From the previous discussion, it is known that olivine dissolves faster in acidic versus alkaline solutions. Since olivine has limited solubility in water, the reaction between the olivine with active hydrogen ions mainly happens at the surface of the mineral. The crystal structure of olivine contains isolated silica tetrahedrons which are bound together only by ionic bonds from interstitial cations [269]. Therefore, once olivine interacts with an active hydrogen ion (H^+), the dissolution begins as each of the magnesium atoms are exchanged for two hydrogen protons. It was proposed by Pokrovsky [241] that this reaction leads to the silica tetrahedrons' polymerization and that the formation of the surface mixture is the rate-controlling step of the dissolution. This was later confirmed by Olsson [233] using atomic force microscopy and X-ray photoelectron spectroscopy. These images showed the surface of the olivine exposed to water was covered with loosely bound

material which is the remaining silica after Mg^{2+} was leached. In alkaline conditions and due to the common ion effect with the addition of OH^-, the olivine dissolution equilibrium was shifted towards the reactants, thus, it showed a lower dissolution rate. A passivating layer of $MgOH_2^+$ complex could be formed, thus, controlled the dissolution rate. However, this thin film has not been directly observed and characterised. In order to better understand the olivine dissolution mechanism, a determination of the surface chemistry involving various macroscopic and spectroscopic techniques, such as AFM, XPS and SEM, is needed.

4.5 Summary and conclusion

To investigate the properties of olivine dissolution, different factors such as particle size, pH, acid type and concentration, CO_2 content and pressure, reaction duration and temperature were analysed.

- It was found that the log of the dissolution rate (*log r*) had a linear relation with the pH. The olivine solubility in acidic solutions is much higher than in alkaline solutions and the formation of the surface complex is the rate-controlling step of the dissolution.
- For the solution with the same pH, olivine dissolved more readily in weak acid (CH_3COOH, in this study) than strong acid (HCl and HNO_3).
- Olivine samples that were ground to finer particle size had a higher dissolution rate due to their higher surface area and were able to approach equilibrium faster.

- By introducing CO_2 bubbles or using carbonated water, the $Mg^{2+}_{(aq)}$ concentration was increased. Elevated CO_2 partial pressure also had a positive effect on the olivine solubility since more CO_2 was dissolved into water thus lowering the pH.
- Prolonging the reaction time will increase the $Mg^{2+}_{(aq)}$ concentration but the reaction rate decreased with time, which suggests that hydrolysis mainly happens in the early stages.

Future work is necessary to understand the reaction mechanism and the potential application of the reaction by-products.

5 Investigation on the magnesium composites extracted from olivine

5.1 Introduction

Olivine is considered as one of the most promising minerals to achieve carbon mineralisation by forming stable magnesium carbonates and hydrated carbonates [21, 270-272]. In the previous chapter, the dissolution property of olivine under different environmental conditions such as: pH, acid type, temperature, pressure and presence of CO_2 presence were investigated and discussed.

Until now, there are no identified publications on MgO recovery from olivine for the use in cement production. This is mainly because of the slow rate of hydration, also known as serpentinization. Under standard conditions, olivine is sparingly soluble, with less than 6 mg/L of magnesium ion concentration. This makes it impossible for magnesia recovery as it leads to excessive energy demands. However, with finely ground olivine particle size in acidic solution, olivine solubility increases significantly. This makes it feasible to extract MgO from the olivine.

Since MgO does not exist in nature, the current main sources, as outlined in Section 2.4.1.1 in 2, are from the calcination of magnesite (magnesium carbonates) or brucite

(magnesium hydroxides). One of the most important properties of the MgO is its reactivity, especially in cement application. Reactive MgO is commonly used in MgO-SiO_2-H_2O, MgO-$MgCl_2$-H_2O, MgO-$MgSO_4$-H_2O and reactive magnesia cement systems, whereas low reactivity MgO can be used in magnesium phosphate cement. In terms of the Portland cement system, depending on its reactivity, MgO can be considered as a potential risk to the volume stability due to its low hydration reaction rate [273] or used as an expansive additive (high reactivity) to compensate the concrete shrinkage [274]. When MgO is used as an expansive agent in cement materials, Figure 5-1 illustrates the influencing variables.

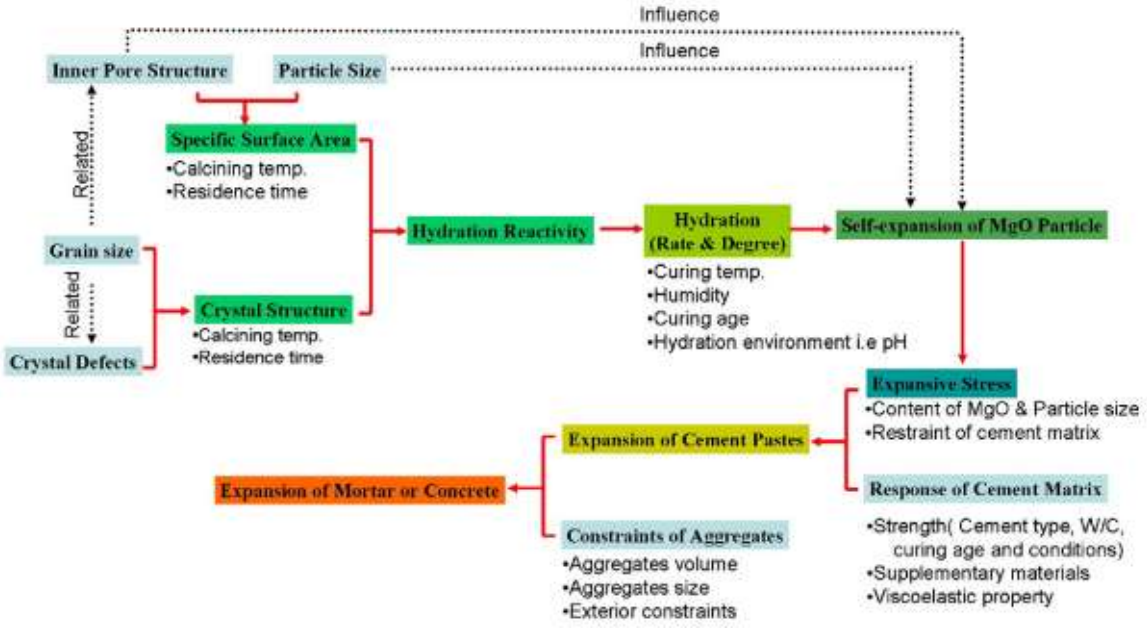

Figure 5-1. Different factors that influencing the MgO hydration in cement materials[275].

The key factors for MgO reactivity are particle size, surface area and the concentration of surface defects of the MgO crystals [276], and these properties could be regulated by controlling the calcining temperature and residence time during the MgO

production. Higher calcination temperature and longer residence time lead to the agglomeration of MgO grains, less surface defects and a decrease in specific surface area, thus decreasing the hydration activity of MgO[73].

In this chapter, we discuss the synthesis of magnesium oxide from olivine; and compare its property and reactivity with commercial magnesia, for the potential application in a cementitious binder system.

5.2 Processing method

The olivine used for this chapter was identical with previous experiments and described in chapter 3 to be composed mainly of the mineral Forsterite Mg_2SiO_4. The material was ground for 120 seconds in the ring mill (see Figure 4-1 for the particle size distribution). According to the previous study, the pH is the most important factor that influence the olivine dissolution. Acetic acid demonstrated a higher magnesium extraction rate compared to the hydrochloric and nitric acid at the same pH level. Therefore, acetic acid (CH_3COOH) (glacial, supplied by Sigma-Aldrich) was selected as the solvent.

The olivine processing consists of four steps: acid reaction, filtration, evaporation and thermal decomposition. The simplified processing diagram was shown in Figure 5-2.

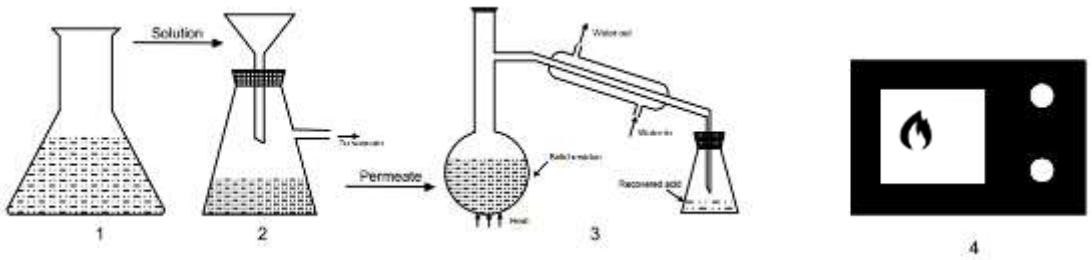

1. Olivine reaction with acid; 2. Filtration;
3. Evaporation and acid recovery; 4. Thermal decomposition

Figure 5-2 The simplified processing diagram of olivine

5.2.1 Acid reaction

Forty grams of olivine was mixed with 2 mol/L acetic acid at the solid/liquid ratio of 1:20 under ambient temperature (20±2 °C) and pressure. The mixture was constantly stirred by the magnetic stirrer at the speed of 300rpm for the duration of 24 hours.

After 24 hours of stirring the mixture was left for settlement for another 24 hours. The upper solution was decanted for filtration while the slurry residue was washed using de-ionised water till the pH was neutral. After washing, the slurry was placed into an oven at a temperature of 50 ˚C to dry until no weight change was observed. The composition and properties of the olivine solid residue were determined by SEM and XRD methods with details provided in Section 3.3 of Chapter 3.

5.2.2 Filtration

After digesting olivine in acetic acid, the Mg dissolves to the solution. As the solubility of magnesium acetate is approximately 1200 g/L in water at 15 ˚C, the Mg ion concentration of the olivine in acetic acid sample (approximately 3 g/L in 1 mol/L acetic acid for 24 hours) was far below the solubility limit. The produced magnesium acetate, noted as MgAc, is in the solution and can be separated from unreacted olivine or silica.

A membrane filter with a pore size of 0.45μm was used to separate the unreacted solids and liquid. A Buchner funnel was used for the vacuum filtration. After filtration, the permeate which passed through the filtering membrane, contained the dissolved MgAc as well as any unreacted acetic acid.

5.2.3 Evaporation

The permeate was poured into a condenser, and the temperature set for the sand bath was 99 °C. The boiling point of the acetic acid is 118.1 °C , thus it evaporated slowly, leaving the precipitated solids in the bottom.

In order to recycle the excessive acid, water was used for coolant circulation in the condenser. The recovered acid was collected in the conical flask, shown in Figure 5-3.

Figure 5-3. The evaporation and condensation process

5.2.4 Thermal decomposition

The solids left after evaporation were collected from the condenser for calcination. The decomposition took place in a furnace at the temperature of 500°C for two hours. The MgO was obtained through the following reaction in Equation 5-1:

$$Mg(CH_3COO)_2 \rightarrow MgO + (CH_3)_2CO \uparrow + CO_2 \uparrow \qquad \textit{Equation 5-1}$$

To identify the gas emitted during the decomposition, a thermal degradation test was done on the recovered sample. The sample (0.5010 g) was gradually heated (temperature ramp rate was 2 °C/min) and then held constant for 90 minutes at 200, 300 and 400 °C in a temperature-programmable furnace (GSL-1100X, MTI Corporation). Argon was used as the sweeping gas to flow through the sample bed while the flow was regulated by a mass flow controller (ALICAT Scientific) at 10 sccm. The emitted CO_2 was analysed via Gas Chromatography (SRI 8610C, SRI Instruments, USA). The actual sample temperature measured by thermocouple (Intech Instruments) was recorded by TracerDAQ software, whereas the analysis was done by PeakSimple software (Peak444-32bit, SRI Instruments).

5.2.5 Characterisation methods

After the magnesium products were recovered from the olivine, their properties were studied using various techniques. XRD and XRF were used to identify their phase and mineral composition while SEM was adopted to observe their microstructure. Their thermal degradation was analysed by DTA. The details of these techniques were described in Chapter 3.

To characterise and compare the reactivity of the recovered MgO with commercially available MgO, an accelerated reactivity assessment was performed based on the method proposed by Chau and Li [87] shown in Figure 5-4. The assessment was conducted by reacting 5g of a magnesia sample with 100ml of acetic acid (HAc, CH_3COOH, 0.5mol/L). The reaction between MgO and HAc is shown in the Equation 5-2:

$$MgO + 2CH_3COOH = Mg(CH_3COO)_2 + H_2O \qquad \text{Equation 5-2}$$

Since the MgO is supplied in excess compared to the acetic acid, the acidic solution was quickly neutralised after the addition of MgO, thus lead to a pH change. The change of pH during the reaction was recorded and the reactivity value, *R*, is defined as the time (in seconds) needed for an increase in pH to 7.

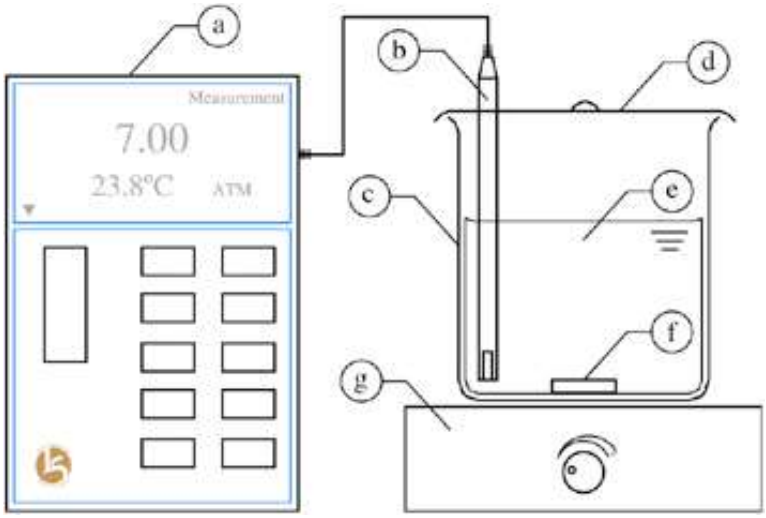

Figure 5-4. Experimental setup of the accelerated reactivity test:

(a) pH meter; (b) probe; (c) plastic beaker; (d) plastic lid; (e) aqueous solution of magnesium oxide and acid; (f) magnet; (g) stirrer. [87]

For the hydration test of the recovered and commercial MgO, 10 grams of magnesia was manually mixed with 10 grams of deionised water in a small mixing bowl. The slurry samples were then cured in 20 °C, RH 50%. The curing period was 28 days before testing.

5.3 Olivine residue after acid digestion

A summary of the mineral extraction process and recovered materials is presented in Figure 5-5. The recovered acetic acid and magnesium oxide are the final products while

olivine residue and precipitated magnesium acetate were also investigated as intermediate products. The recovered acetic acid was recycled for reuse in the acid reaction.

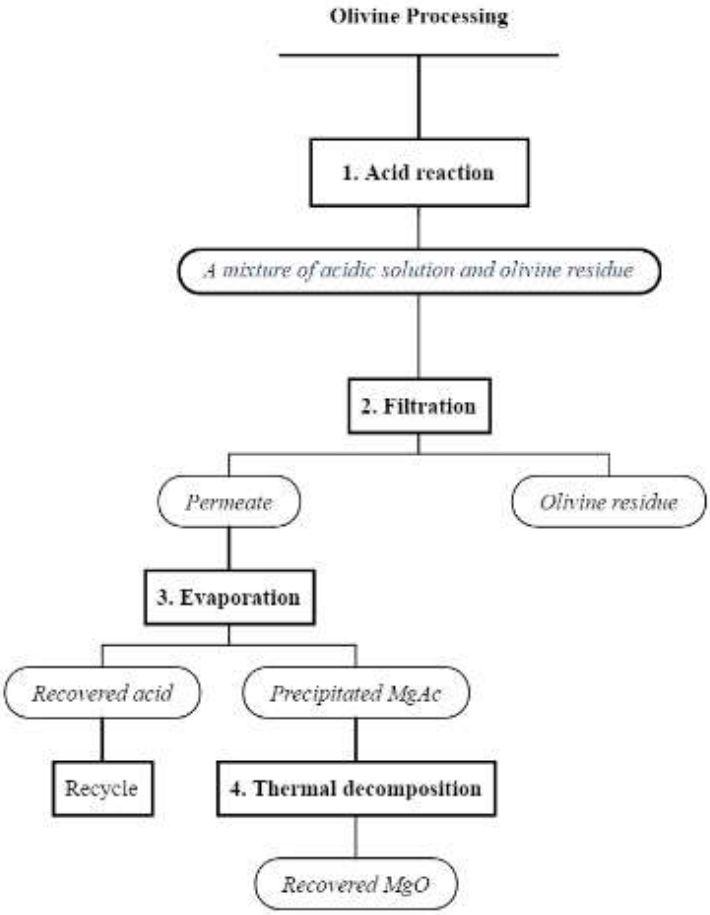

Figure 5-5. The olivine processing and its products

According to the study in Chapter 4, olivine particles remain partially unreacted even at the end of the reaction period. In order to quantify the amount of the dissolved magnesium and the degree of recovery, it's critical to investigate the characteristics of the olivine residue.

5.3.1 Composition of the olivine residue

The solids separated by the filtration step were collected and dried an oven at 50°C. An X-ray Fluorescence (XRF) spectrometer was used to compare the chemical composition of the olivine before and after the digestion (Table 5-1). It's clear that the amount of MgO and SiO_2 in the sample both decreased after the reaction by 24% and 21%, respectively. This indicates the dissolution of Mg and Si of olivine is in accordance with the solution analysis. It can be noted that the LOI (loss on ignition) of olivine residue (21.9%) was considerably higher than that of raw olivine (3.21%), and this could be attributed to the decomposition of some volatile substances in the residue, such as some residual acetic acid.

Table 5-1. The chemical composition of the olivine residue after acid leaching

%	**SiO_2**	Al_2O_3	Fe_2O_3	CaO	**MgO**	Na_2O	K_2O	LOI	Total
Raw Olivine	**39.59**	0.38	10.65	0.73	**45.03**	0.14	0	3.21	100
Olivine residue	**31.30**	0.26	7.54	0.39	**34.20**	0.03	0.09	21.9	96.16

Figure 5-6 provides the XRD data of the raw olivine and the olivine residue after HAc digestion. It's clear from the figure that the peaks of the two patterns were very similar, and there are signs of the presence of large amount of unreacted olivine. Nevertheless, the intensity of the peaks decreased after reaction.

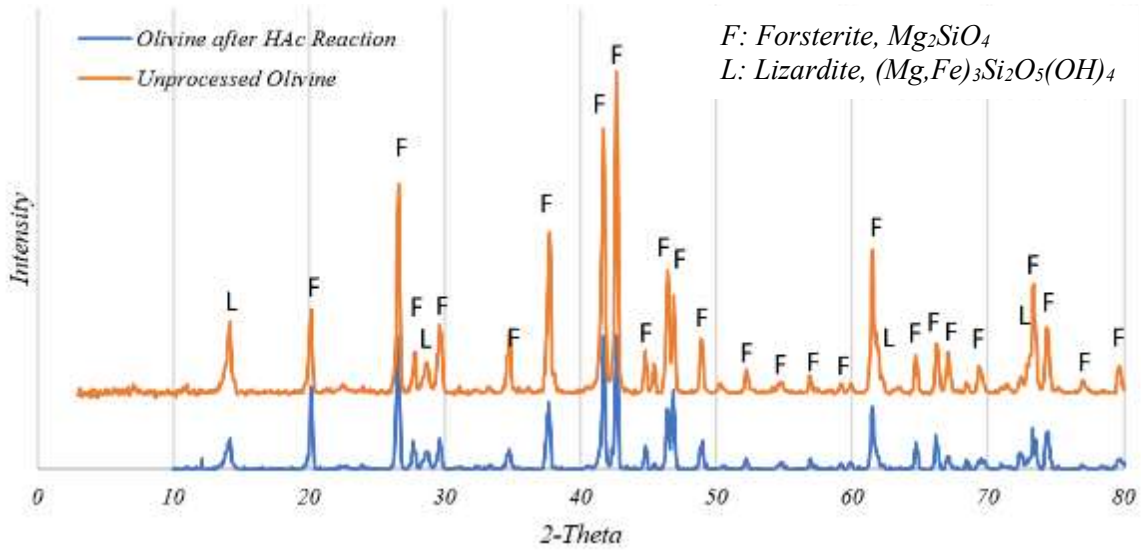

Figure 5-6 The XRD comparison of olivine before and after reaction

5.3.2 Microstructure of the olivine residue

Figure 5-7 showed the typical particles presented in the olivine samples before and after acid digestion. The median particle size of the unreacted olivine is 17.2 μm according to the particle laser analysis, and the size did not change after the reaction when comparing Figure 5-7 a) and b). However, from the comparison of Figure 5-7 c) and d), the surface of the olivine after digestion showed a more porous surface texture. This can be attributed to the dissolution of the magnesium and silicates after the digestion with the main reaction:

$$Mg_2SiO_4 + 4CH_3COOH \rightarrow 2Mg(CH_3COO)_2 + 2SiO_2 + 2H_2O \qquad \text{Equation 5-3}$$

As it was shown in Equation 5-3, the olivine digested in the acetic acid and produced magnesium acetate ($Mg(CH_3COO)_2$) which was soluble, and the silica partially dissolved in the solution while mainly precipitated at the particle surface. The dissolution-

precipitation process contributed to the unique microstructure of the olivine residue after acid digestion.

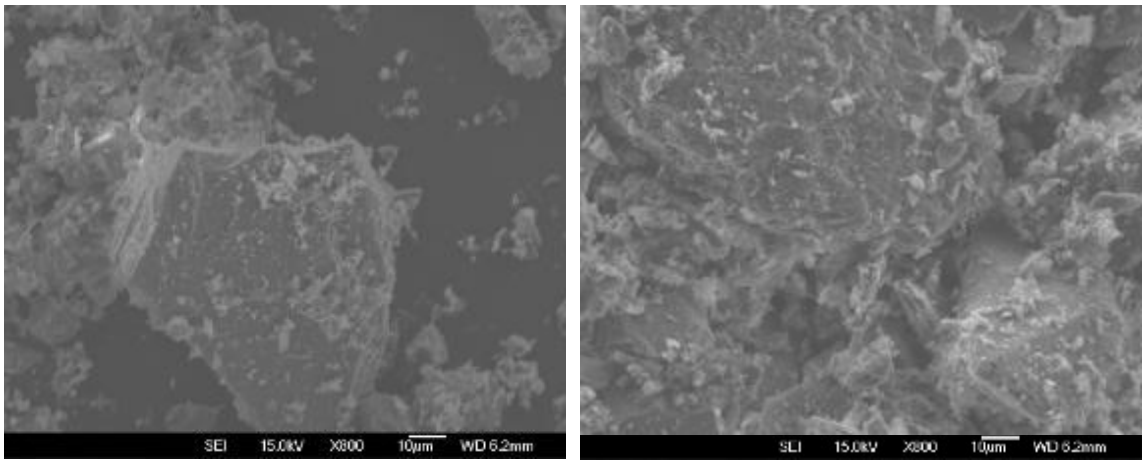

a) Olivine before reaction (×800) *b) olivine after reaction (×800)*

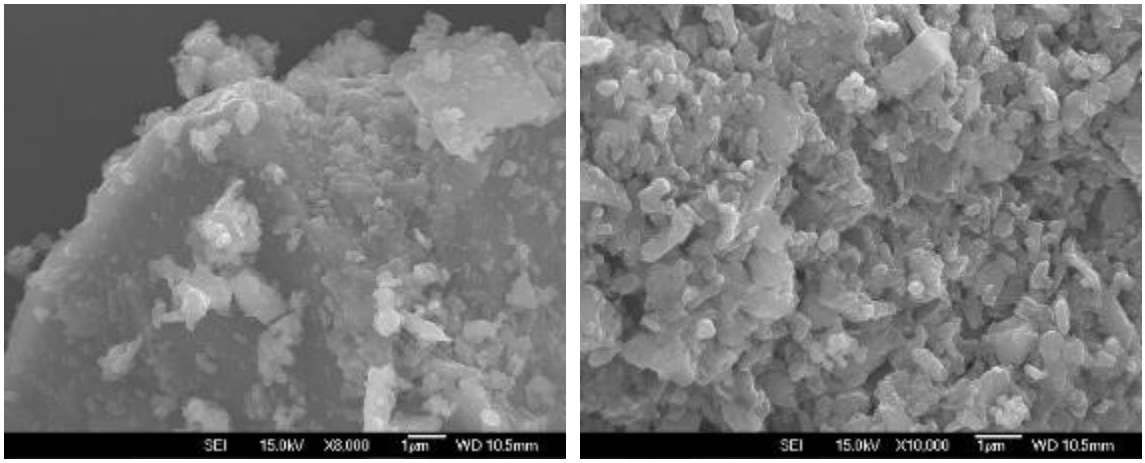

c) Olivine before reaction (×8,000) *d) olivine after reaction (×10,000)*

Figure 5-7. Microscopy of the olivine before and after digestion

5.4 Magnesium acetate recovered (R-MgAc) from the reaction solution

Magnesium acetate was obtained by evaporating the permeate from the reaction solution, see previous sections for details of the process. This product was characterised by thermogravimetric analysis, X-ray diffraction and microstructure examination.

5.4.1 Thermogravimetric analysis of the R-MgAc

The precipitated solids after the evaporation process were collected for thermogravimetric analysis. Figure 5-8 provides the mass loss and differential mass loss of the samples during the heat treatment from ambient temperature to 800 °C .

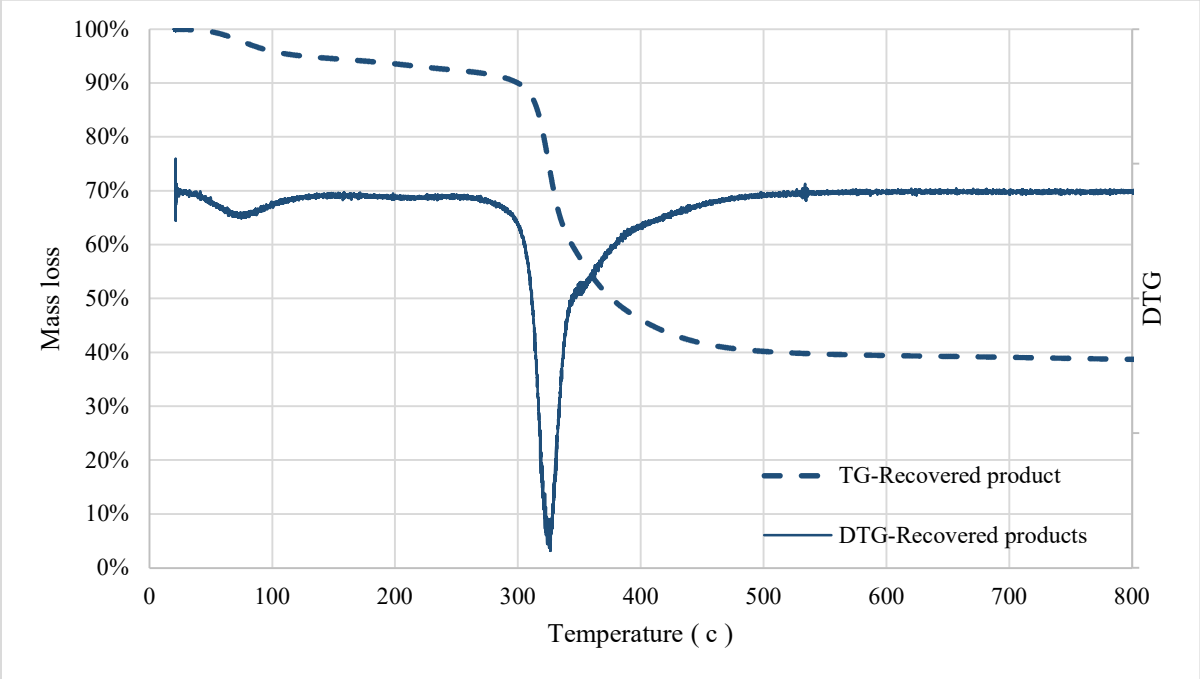

Figure 5-8 Thermogravimetric analysis of the recovered product

For the product recovered from the solution, a significant weight loss in the TG curve between 300~400 °C was observed. The Derivative Thermogravimetry (DTG) curve first demonstrated a minor peak around 80 °C before peaking at 326 °C. Form the reference

[277], the dehydration of magnesium acetate begins at 80 °C and next anhydrous salt decomposes at 323 °C. Other magnesium composite that decomposes in similar temperature range could be magnesium carbonates [278] or hydroxide[279]. However, due to the acidic environment (pH around 3), the magnesium acetate is the most likely product present.

For the magnesium acetate, the thermal decomposition is shown in the following equation:

$$Mg(CH_3COO)_2 \rightarrow MgO + (CH_3)_2CO \uparrow + CO_2 \uparrow \qquad \textit{Equation 5-4}$$

Since it is the emission of the acetone ($(CH_3)_2CO$) and carbon dioxide (CO_2) that lead to the mass loss, the quantity of the decomposed magnesium acetate can be calculated by Table 5-2.

Table 5-2. Quantification of the magnesium acetate produced from olivine acid dissolution

	$Mg(CH_3COO)_2$	Decomposed products		
		MgO	$(CH_3)_2CO$	CO_2
Molar mass (g/mol)	142.39	40.30	58.08	44.01
Mass change from 250~500°C	M_1	M_2	52%	
Calculation	$M_1 = \frac{142.39 \times 52}{(58.08+44.01)} = 72.52\%$			

The thermal degradation of the recovered products was also investigated, and results are illustrated in Figure 5-9. The carbon release peak was observed after 360 minutes while the temperature was approximately 325 ˚C, which was in accordance again with the magnesium acetate decomposition temperature from reference [280].

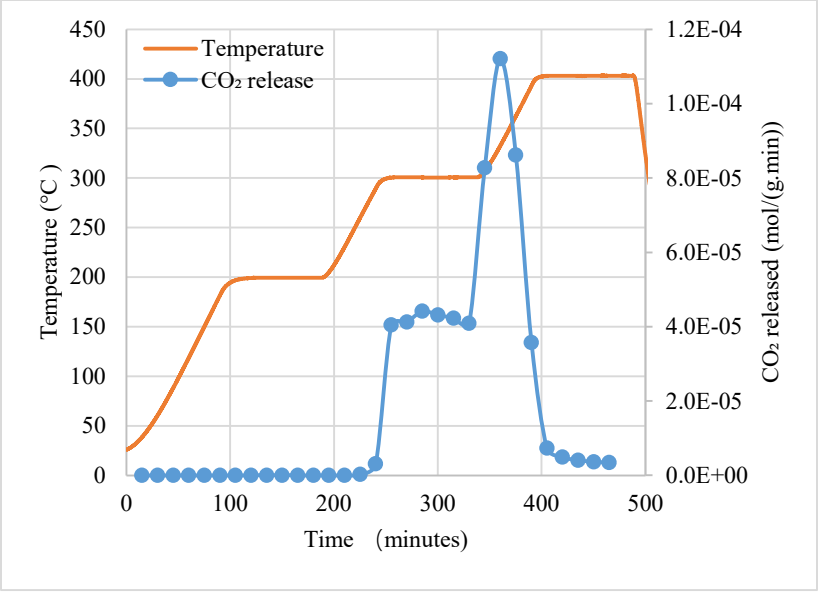

Figure 5-9 The thermal degradation analysis of the recovered products

5.4.2 XRD and microstructure analysis of the R-MgAc

Figure 5-10 shows the XRD traces of the product that precipitated after the evaporation process. By comparing this XRD pattern with the raw olivine XRD in Figure3-3, it's obvious that any peaks identified as forsterite in unreacted olivine have disappeared in the recovered sample. The new peaks in the range from 10˚ to 20 ˚ were confirmed to be magnesium acetate. This suggests that after the acid digestion and filtration process, the olivine was completely removed with the formation of the new product: magnesium acetate ($Mg(CH_3COO)_2$).

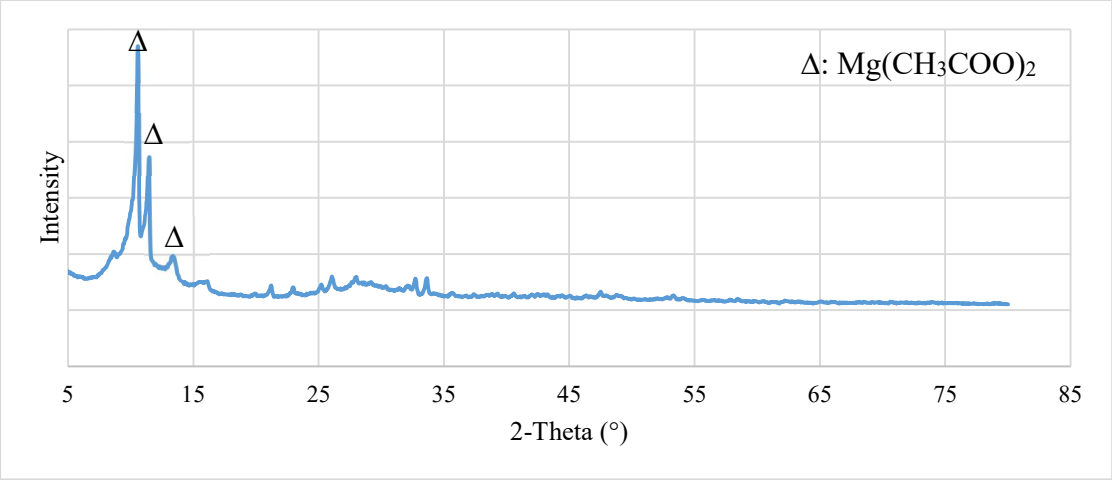

Figure 5-10 X-ray diffraction results of the recovered product

The microscopy of the recovered product, magnesium acetate (MgAc), is shown in Figure 5-11. Due to the crystal growth and agglomeration during the evaporation and precipitation process, the surface morphology of the recovered MgAc was significantly different from that of the unreacted olivine.

Figure 5-12 shows the element mapping of the recovered MgAc, with the major elements: Mg, Si and Fe in three different colours. According to the element mapping, the magnesium and silicon was widely distributed in the product, with minor amounts of iron present. Silica was present in almost all of the recovered MgAc. Distinct particles of MgAc and silica were not observed.

Table 5-3 provides quantitative elemental elements analysis of the whole area by Energy Dispersive Spectroscopy (EDS). The most abundant element detected was oxygen which accounts for 57.6% by weight of the recovered product, followed by Mg (25.4%) and Si (11.5%). The molar content based on the weight results and their molar mass were

also calculated. The molar ratio of magnesium to oxygen is 1:3.6 which is close to the ratio in magnesium acetate, $Mg(CH_3COO)_2$, which is 1:4.

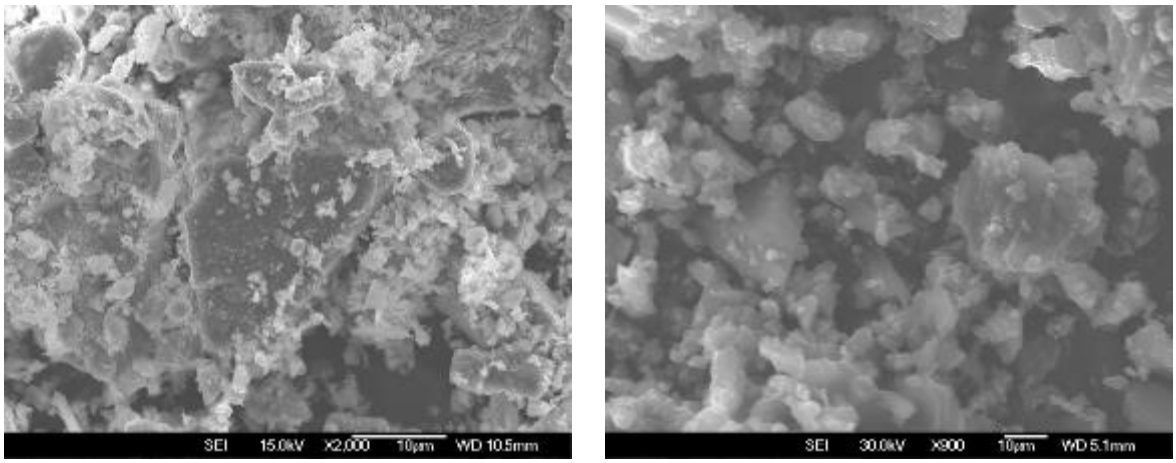

(a). Unreacted olivine *(b). Recovered Magnesium acetate*

Figure 5-11. The microscopy of the olivine and the MgAc recovered from olivine

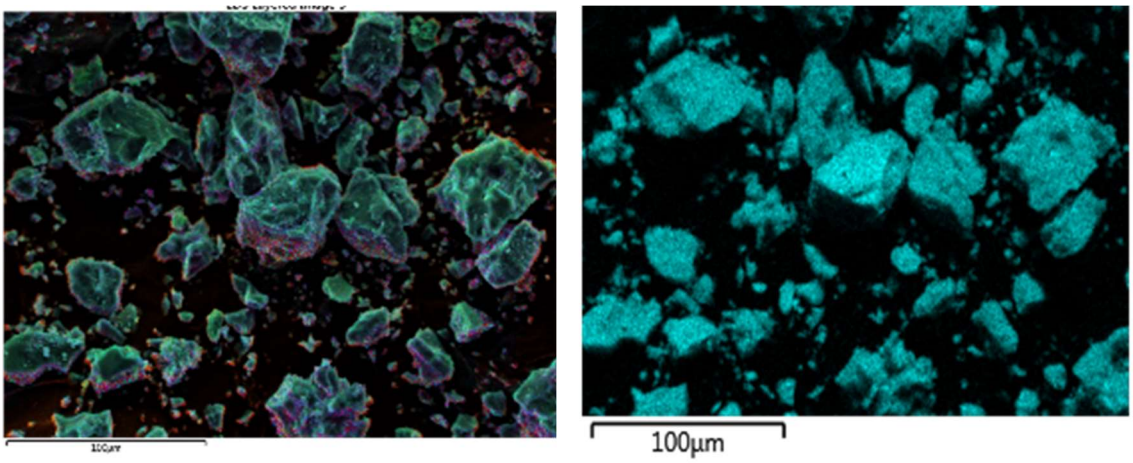

(a). EDS layered image *(b). Magnesium distrubiton*

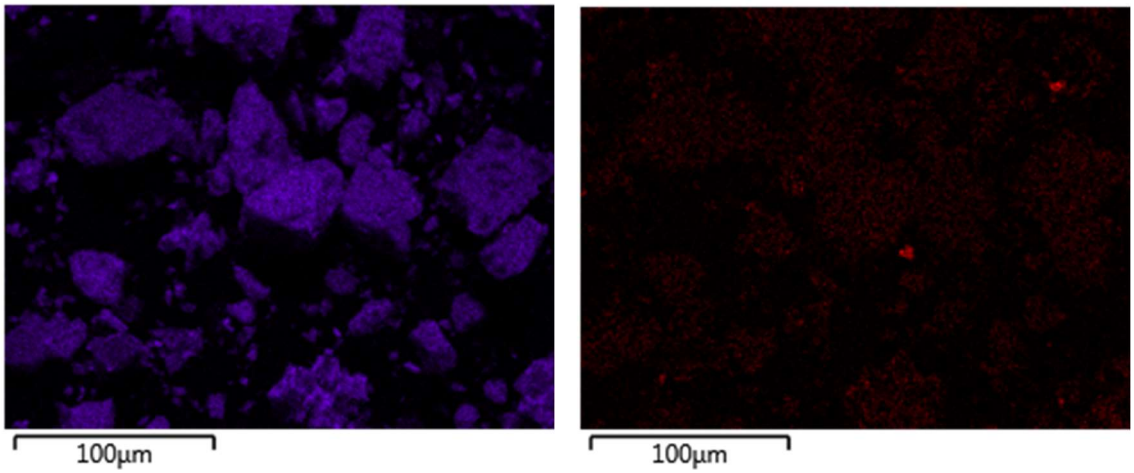

(c). Silicon distrubiton *(d). Iron distrubiton*

Figure 5-12. The element mapping of the recovered MgAc

Table 5-3. The element analysis of the recovered MgAc from olivine dissolution

Element	Oxygen (O)	Magnesium (Mg)	Silicon (Si)	Iron (Fe)	Calcium (Ca)
wt %	57.6	25.4	11.5	4.5	0.8
Molar ratio	3.6	1.0	0.4	0.1	0.0

Through the TG, XRD, SEM and EDS analysis, the recovered product from olivine acid digestion was confirmed to be magnesium acetate.

5.5 Magnesia obtained from the calcination of the recovered MgAc

According to the thermogravimetric analysis, the recovered MgAc decomposition occurs within the temperature range of 250~500 ˚C. To examine the products obtained after the decomposition, the recovered MgAc was put into the furnace at 500 °C for calcination (2 hours). This section reports on the properties of the magnesium products obtained after the calcination process (stated as R-MgO in the following section).

5.5.1 Chemical composition and X-ray diffraction of the R-MgO

During the calcination, according to the calculations, 20.52% of the R-MgAc converted magnesium oxide, while 52% of the mass emitted to the environment in the form of carbon dioxide and acetone, with the rest (27.28%) being thermally stable impurities.

Table 5-4 shows the chemical composition of the product obtained from MgAc calcination, using the X-ray fluoresce technique. The MgO content in R-MgO is 52.1%, which is in the same range as the TG results. The amount of silica (SiO_2) is 27.9%, followed by Fe_2O_3 at a value of 8.33%. It was confirmed by previous results that silicon was dissolved in the acid and precipitated during the evaporation. Therefore, after calcination, SiO_2 was detected. Note the loss of ignition (LOI) was considerably high, this may be caused by the decarbonation of the magnesium carbonate (produced by MgO reacted with moisture in air).

The XRD results shown in Figure 5-13 identified the crystalline in the calcined product. The most common mineral in the product was found to be periclase, which is the mineral form of magnesium oxide (MgO). The peak around 40 degree for forsterite (Mg_2SiO_4) was also found but the intensity was weak. The forsterite was either present as an impurity from the reaction process or formed during the calcination process. Given that there were no forsterite peaks present in the XRD results from the recovered MgAc, it appears that foresterite may have formed from the MgO and silica amorphous during the calcination process.

Table 5-4. Chemical composition of the recovered and commercial MgO

wt%	MgO	SiO_2	Al_2O_3	Fe_2O_3	CaO	Na_2O	K_2O	LOI	Total
Recovered	52.1	27.9	0.03	8.33	1.18	0.05	0.03	8.23	98.08
Commercial	65.8	9.0	0.52	0.25	3.47	0.19	0.11	19.6	99.07

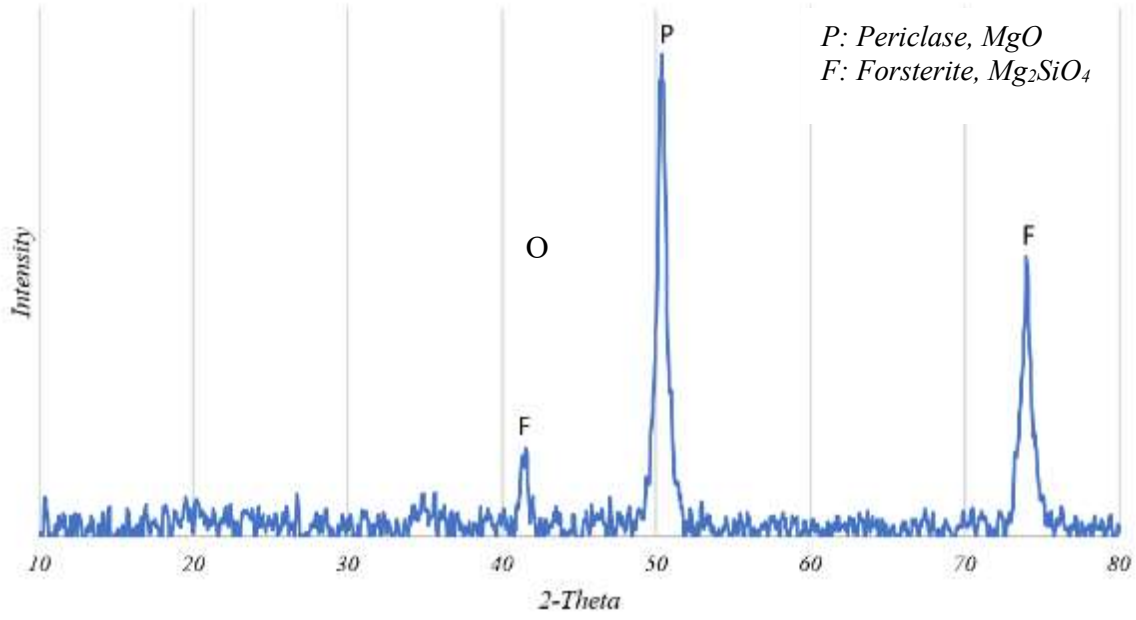

Figure 5-13 The XRD pattern of the recovered MgO from Olivine

5.5.2 Microstructure and element analysis of the R-MgO

The typical electron microscopy of the recovered product particles and its EDS result are shown in Figure 5-14.

Magnesium accounts for 45.01% of the total mass while the silicon occupied 13.75%, with the remaining oxygen (38.76%) and limited amount of iron and calcium (1.34% and 1.14%, respectively). This demonstrates a similar elemental composition with the XRF results.

From the higher magnification images Figure 5-14(c) a large quantity of small particles were found at the surface of the R-MgO. This could lead to a greater specific surface area, thus a higher reactivity. However, the limitation of the EDS technique makes

it not suitable for surface analysis, especially under high magnification. Therefore, the EDS results in Figure 5-14 (d) at higher magnification could not identify whether these small particles are precipitated silica, magnesia, or a combination. It shows similar results with Figure 5-14 (b).

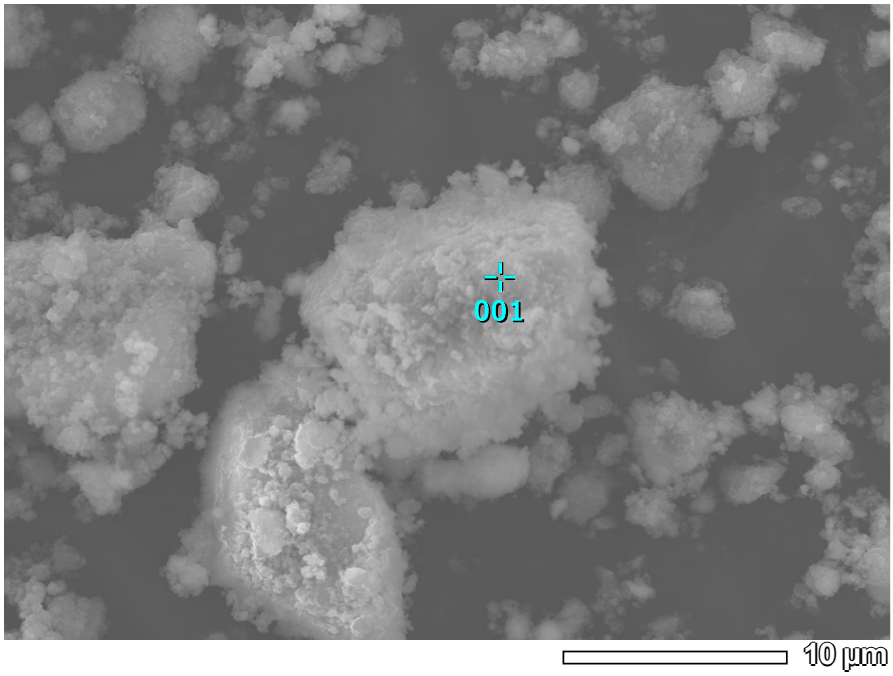

(a) Recovered Magnesium oxide

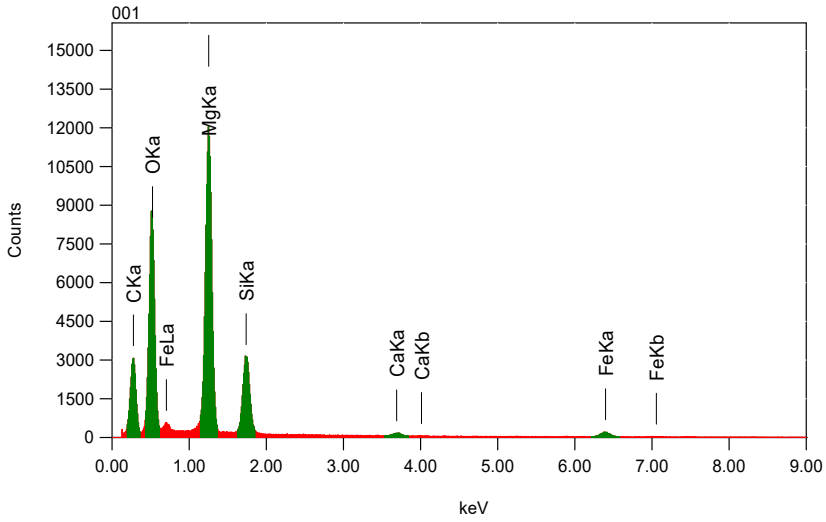

Element	Mass%
O	*38.76*
Mg	*45.01*
Si	*13.75*
Ca	*1.14*
Fe	*1.34*
Total	*100*

(b) *EDS of the* point 001

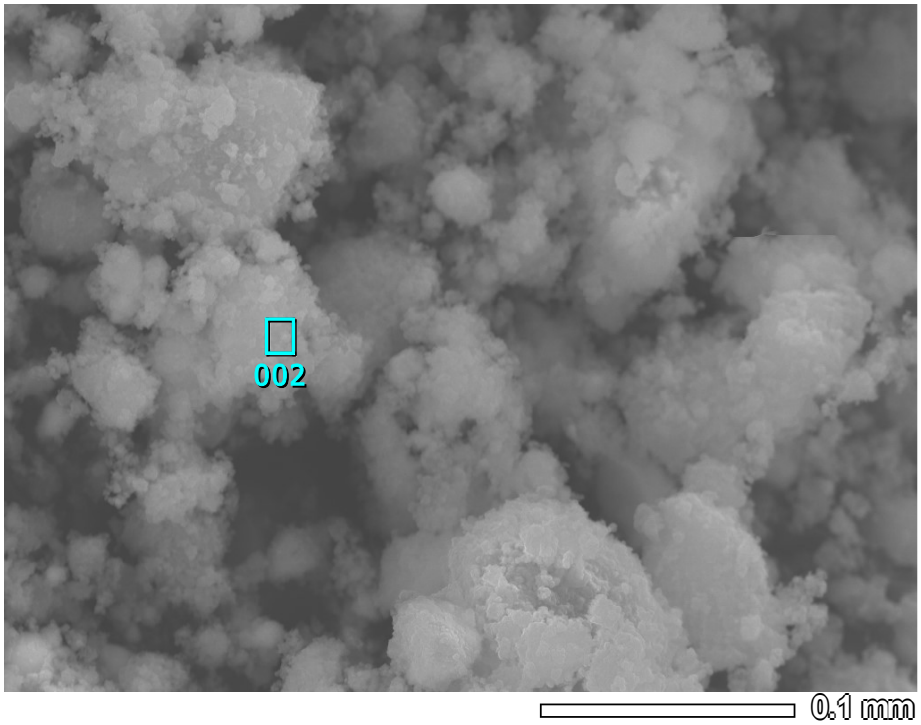

(c) Recovered Magnesium oxide at higher magnification

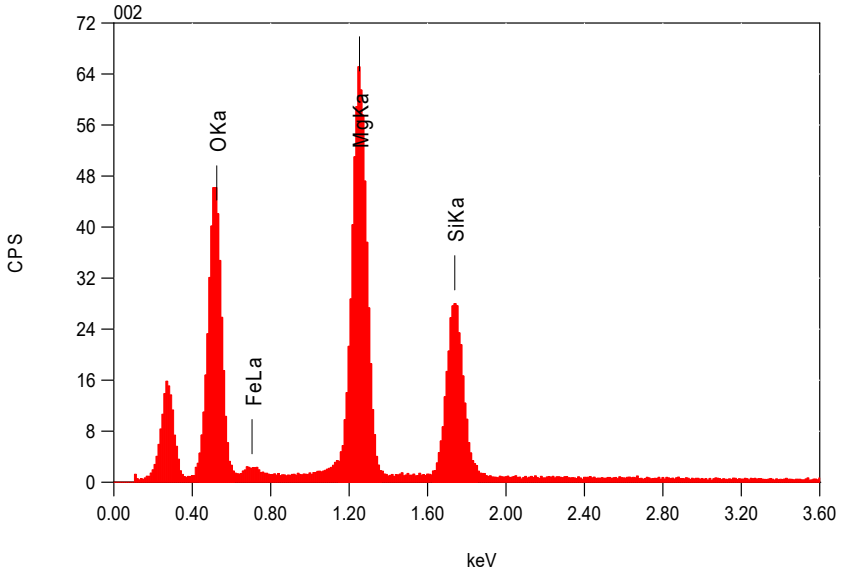

Element	Mass%
O	*25.37*
Mg	*48.80*
Si	*21.40*
Fe	*4.43*
Total	*100*

(d) *EDS of the point 002*

Figure 5-14. The microscopy and the EDS of the recovered magnesia from olivine

5.5.3 Activity test of the R-MgO

Figure 5-15(a) shows the change in pH of the acidic solution with time after the addition of commercial MgO, recovered MgO and unreacted olivine samples. Once the commercial MgO was added to the solution, the pH increased to 7 in the first 27 seconds (R=27), which indicates a high reactivity of the light burnt commercial MgO. The recovered MgO, on the other hand, demonstrated a slower increase. The solution became neutral after 249 seconds (R=249). However, for the acidic solution mixed with raw olivine, only a slight increase was noticed within 30 seconds and the pH remained at its peak around 3.2.

In Figure 5-15(b), a longer duration (30 minutes) of the pH change of the solution is provided. The final pH of the solution mixed with commercial MgO stabilised at approximately at 9.6 while the value of the recovered MgO was just over 9. The solution mixed with raw olivine showed no significant change and remained acidic.

The increase in pH of the recovered MgO obtained from the olivine indicates it is in a chemically active form, yet its reactivity is somewhat lower than commercial MgO due to the presence of the other elements. Apart from the impurities, the particle size and surface area could also act as influencing factors. Further grinding the recovered MgO or lowering the calcination temperature may lead to higher reactivity.

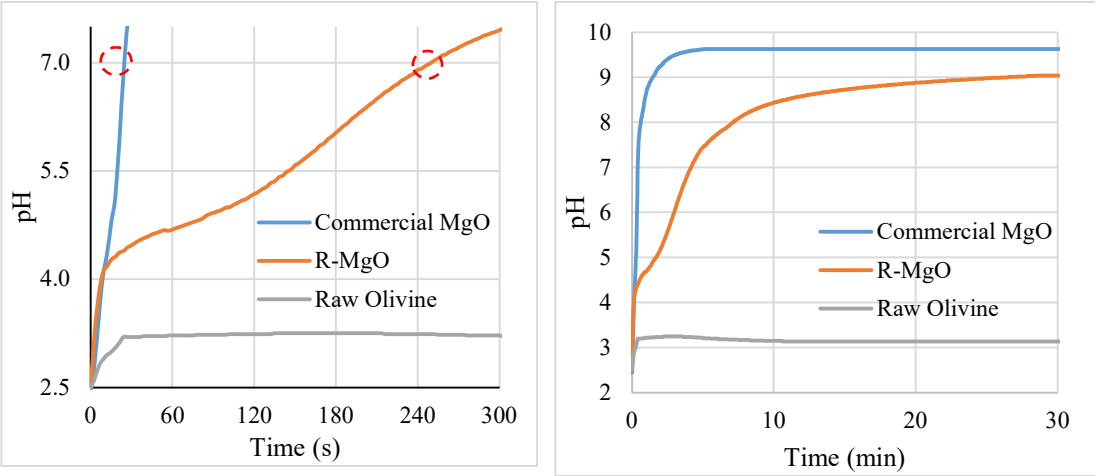

(a)in first 300 seconds *(b)in first 30 minutes*

Figure 5-15. The pH profile of the MgO activity test

5.5.4 Hydration products of the R-MgO

The hydration products formed from the commercial magnesia and recovered magnesia were characterised by SEM and shown in Figure 5-16. The hydration products of commercial magnesia(C-MgO), shown in Figure 5-16(a), is the crystal form of magnesium hydroxide. Whereas in Figure 5-16(b), the morphology of the hydration products from recovered magnesia(R-MgO) is significantly different. The size of the crystals was smaller than C-MgO sample and the structure was denser and more compact. This may be attributed to the presence of amorphous silica in R-MgO which can react with magnesia, forming a homogeneous magnesium silicate hydrate (M-S-H) gel. The morphology of the hydration products (M-S-H) from the recovered MgO was in accordance with the literature[281, 282].

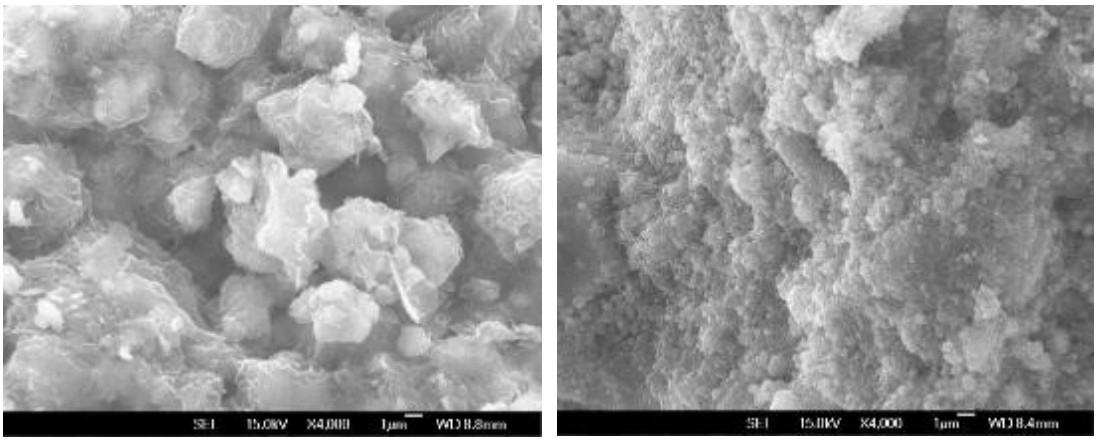

(a). Commercial MgO *(b). Recovered MgO.*

Figure 5-16. Microscopy of the hydration products from different sources of magnesia

Figure 5-17 shows the mass loss curves of three different materials after they had been mixed with water, namely: the raw olivine, the commercial magnesia (C-MgO) and the recovered magnesia (R-MgO). The olivine sample demonstrated little mass loss while the C-MgO curve experienced a significant weight loss around 400° C. This mass change is related to the dihydroxylation of $Mg(OH)_2$ to MgO and H_2O and indicates the amount of brucite (magnesium hydroxide, $Mg(OH)_2$) that is present.

$$Mg(OH)_2 \rightarrow MgO + H_2O \qquad \textit{Equation 5-5}$$

However, the R-MgO hydration product profile demonstrated a different pattern. The mass loss in the range from 300 to 400 °C was considerably less than C-MgO counterpart, which suggests less brucite. Note that there was a constant mass loss after 50 °C, this was due to the loss of the free water around 100 °C and bound water in later stage. The R-MgO hydration product thermogravimetric curve is similar to the synthesised

magnesium silicate hydrates (M-S-H) using commercial MgO and silica fume[167, 283], which suggests the formation of M-S-H in R-MgO sample.

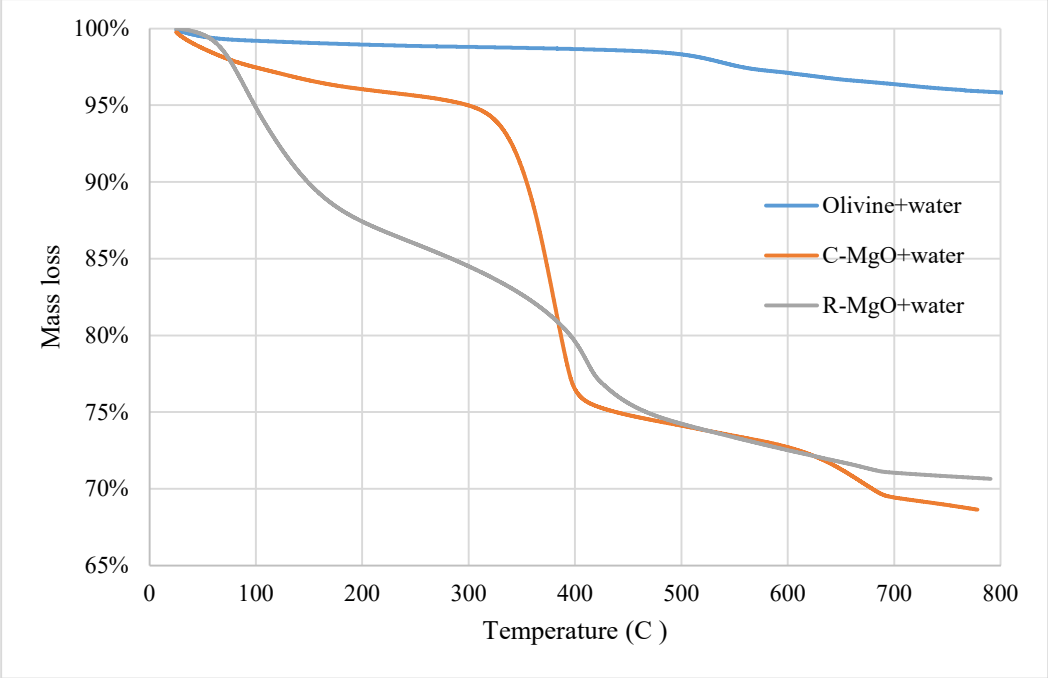

Figure 5-17. The TG curves of different hydration products from olivine and magnesia

5.6 Summary and conclusion

This chapter contains the results of the investigation into the magnesia extraction process from olivine. The extraction process consists of four stages: (a) olivine digestion in acetic acid, (b) the separation and (c) evaporation of the liquid phase, and finally (d) the thermal decomposition. Each stage of the process has been studied and the intermediate products from each step had been examined as well.

The olivine after acid digestion had a lower MgO content compared to the raw material, due to its dissolution yet there was no significant change in terms of the crystal structures.

After evaporation of the permeate from the olivine and acid solution, the recovered products were found to be mostly magnesium acetate, characterised by TG and XRD techniques. The recovered products also contained other impurities, primarily amorphous silica and ferric acetate .

Magnesia was obtained by the calcination of the recovered magnesium acetate. The XRD pattern revealed mainly MgO peaks, but some forsterite was also present. The composition analysis of the product showed 52.1% MgO and 27.9% SiO_2 with some impurities of iron. The activity tested produced an R value of 249s which was greater than the commercial MgO. The impurities, especially the reactive SiO_2 from the products, affected the hydration reaction. Apart from the formation of brucite, magnesium silicate hydrates was also produced when the recovered MgO reacted with water. The gel was identified by SEM images and TG analysis.

6 Pozzolan reactivity assessment of the silica recovered from magnesium silicates

6.1 Introduction

In addition to the recent interest in alternative binder systems to reduce the carbon dioxide emissions associated with the construction industry, the use of pozzolans has had a long and successful history as partial replacements for cement. Nevertheless, costs and availability of a reactive silica source have limited its more widespread use in some regions, particularly where industry by-product such as silica fume, slag or fly ash are not readily available.

Compared to preparing magnesium compounds from magnesium silicates, which was discussed in the previous chapters, little attention has been devoted to processing of the insoluble residual (SiO_2) into products tailored for applications in industry or in environmental protection. However, it may be a good alternative of the silica source for the application in cement industry.

In 1951, Mchedlov-Petrosyan[284] studied the thermal behaviour of serpentine and kaolin and proposed that it was possible to make hydraulic cement by calcining serpentine rock. However, the cement preparation, mineralogical change, hydration reaction have not been explained. In 1978, Midgley [18] investigated the reaction process by DTA and XRD techniques. The serpentine rock was calcined in an electric muffle furnace at 640 ˚C for 5 hours after it was roughly crushed to around 5 mm size. After calcination, it was ball milled to 5600 cm^2/g. The product was mixed with standard sand at the ratio of 1:3 but the compressive strength was only 3.3MPa after 12 months curing in water. According to Midgeley's study, the strength development was extremely slow and reshowed low strength data. However, the high content of the MgO and SiO_2 in the serpentine still draw researchers' attention as they are hydraulic and thus may form cementitious materials through some special treatment.

In 2001, Justnes[212] successfully produced amorphous silica with high whiteness and surface from olivine by acid digestion. The olivine (200 g) was first dispersed in 300 ml water before 500 ml 37% hydrochloric acid (HCl) was added. The reaction lasted for 4 hours under 70 ˚C. After decanting, a second stage of acid digestion took place: 200 ml of 6 mol/L HCL was added for 2 hours reaction at 50 ˚C. Once the reaction was finished, water was used to wash the residual 3 times before filtering. The solid residual was then dried at 105 ˚C to remove adsorbed water. The amount of recovered silica was about 18% of the original olivine weight. The BET surface area of the recovered silica was 101 m^2/g. Mortars samples were made with Portland cement, 7% replacement of cement with each of silica fume and recovered silica. The results demonstrated that the recovered silica was comparable with silica fume in improving the compressive strength. Justnes[285] later

reviewed the possibilities of producing pozzolans from natural minerals by chemical treatment. The research selected several minerals suitable for chemical pozzolana production, such as olivine, serpentine and anorthite. Among them, it was concluded that olivine and serpentine were the most feasible minerals. The minerals can react with weak carbonic acid forming a mixture of magnesium carbonates and silica, which can be used as excellent fillers and pozzolans in concrete.

Lázaro [286-288] also reported that it is feasible to obtain nano-silica from olivine and explored its application in building materials. They recovered nano-silica using sulfuric acid leaching which had a specific surface area between 100 ~ 300 m^2/g and a primary particle size between 10 ~ 25 nm. They concluded that increasing the reaction temperature, surface area of olivine, activity of the hydrogen ions and number of washing steps results in an increase in the nano-silica surface area.

A research group from US Department of Energy[14, 289] dissolved serpentine with hydrochloric acid as a preliminary for carbon sequestration, and silica particles were also observed. They concluded that the carbonation reaction products of serpentine consisted of magnesite (60%), free silica (25%) and residual silicates (15%). However, it was outside their scope to recover the produced free silica.

Pietriková[290, 291] investigated the acid leaching of serpentine to produce silica powder. Different factors such as acid concentration, leaching temperature and time were studied and they stated that the highest reaction efficiency was achieved with 25% hydrochloric acid with a solid to liquid phase ratio of 1:4, with an optimum 1 hour of reaction time 105 ˚C. After the reaction, the solid product was separated by filtering and washed with hot water for several times until the wastewater was neutral. After it had been

dried at 105 ˚C for 2 hours, it was then heated at 1000 ˚C for 2 hours. From this process, the unreacted SiO_2 had a purity range from 97 to 99%. The chemical reaction of the serpentine acid leaching can be simplified in Equation 6-1.

$$xMgO{\cdot}ySiO_2{\cdot}zH_2O + 2xHCl = xMgCl_2 + ySiO_2 + (z+x)H_2O \qquad \textit{Equation 6-1}$$

Fedoročková et al.[70, 292] also produced high purity (99.4%) amorphous silica powders by leaching the serpentine in 10 mol/L hydrochloric acid at the temperature of 60 °C. The specific surface area of the silica products was 541 m^2/g. They stated the silica sample obtained from the highly acidic solution was mesoporous. However, the study on the silica reactivity was beyond the scope of that investigation on the use of processed serpentine, or the waste solution, with cement binder system.

Overall, it was confirmed by previous studies that the silica can be extracted from silicate minerals through acid leaching. The recovered silica may have pozzolanic reactivity that is comparable to other traditional silica source. However, there has been no systematic investigation on extracting the silica which then compares it with other silica sources as a supplementary cementitious material. In this chapter, we focus on extracting and characterising the silica from serpentine. The pozzolanic reactivity of the recovered silica will be further assessed and compared to other commonly available silica sources.

6.2 Silica extraction process

The silica extraction process from serpentine is conceptually similar to the magnesia recovery process from olivine, as shown in Figure 6-1. However, a strong acid (HCl) was used rather than the weak acid (CH_3COOH) based on the findings from previous studies.

The serpentine was first ground using the ring mill (see Chapter 3 for detailed grinding methods) to reduce its particle size and to improve its reactivity with acid. Afterwards, the ground serpentine was mixed with 2 mol/L HCl at a solid to liquid ratio of 1:20. The reaction was performed at ambient laboratory pressure and temperatures (approximately 20 ˚C) for 24 hours. These reaction parameters were modified from Justnes's research[212] on olivine leaching. Considering the experiment was carried out under ambient temperature, a longer reaction duration of 24 hours was used compared to previous studies[290, 291].

After the leaching, the solution was filtered on a 45 μm size membrane. A filtration process was applied to the slurry to separate the liquid and solid. The solids residual was collected for analysis. The solid was first washed several times with deionized water until it reached a pH of 7. After that, it was put into the oven at 105 °C until it reached a constant weight. This sample is labelled as recovered silica (RS).

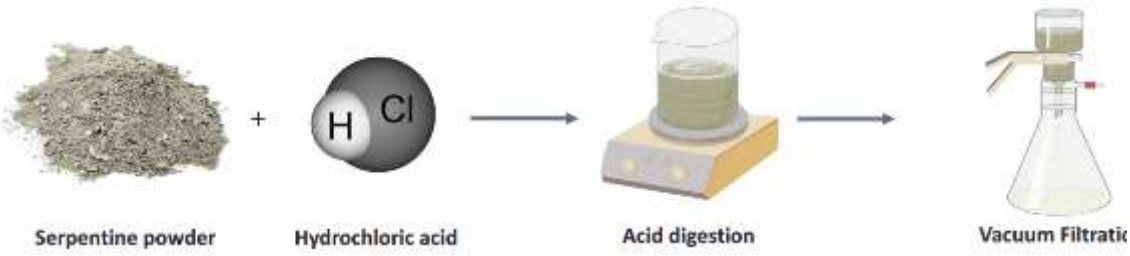

Figure 6-1. The illustration of the serpentine process.

6.3 Pozzolan reactivity test

The silica extracted from the serpentine was assessed for its pozzolan reactivity. The overall assessment used in this study involved a number of components as follows:

6.3.1 Conductivity test

The pozzolan particle will react with the dissolved $Ca(OH)_2$ in the solution which decreases electrical conductivity. By calculating and comparing the conductivity loss of the solution, the reactivity of the pozzolan particle can be determined. The greater conductivity loss the greater the fixation of the dissolved $Ca(OH)_2$, thus the higher reactivity of the pozzolan particles. The conductivity test was based on the methods proposed by Luxán [108]and modified by Paya[109, 293].

Saturated lime solution was commonly used in previous studies, however, due to the slow dissolution rate of lime, it can take several days to reach a saturation equilibrium. In the current investigation, an unsaturated lime solution (0.8 g/L) was prepared: 0.2 g $Ca(OH)_2$ was add into a volumetric flask and filled with de-ionised water to 250 mL. The temperature of the sealed flask was raised to 80 °C to accelerate the dissolution rate. Afterwards, the unsaturated solution was cooled down to the temperature of the experiment. 80ml of the solution was used for each experiment. The silica particles were mixed with the lime solution at the ratio of 1: 20 (4 g: 80 mL) and the conductivity recorded over a test duration of 10000 seconds ($\approx$2.7 hours) with a time interval of every 3 seconds. The pozzolan reactivity of the material is then determined by the conductivity change of the solution.

6.3.2 Ion concentration

Fratini (1950) and Chapelle (1958) proposed to evaluate the activity of a pozzolanic material, based on the consumption of $Ca(OH)_2$ in a saturated water medium. The consumption was measured by titration. In this study, MP-AES was used as a more

accurate method to measure the consumption of the lime ($Ca(OH)_2$) instead of acid titration. The lime solution and the mixing ratio was identical with the conductivity test. The reaction duration was 3 hours and was under ambient temperature.

The calcium concentration was measured before and after pozzolan reaction and the concentration change was calculated using the following equation:

$$\Delta C = C_{CH} + C_{in\ water} - C_{in\ CH}$$

Where, ΔC is the concentration change of calcium;

C_{CH} is the calcium concentration of the original CH solution;

$C_{in\ water}$ is the calcium concentration of the silica material in D.I. water (before reaction);

$C_{in\ CH}$ is the calcium concentration of the silica material in CH solution (after reaction);

6.3.3 Sample mixed with silica with lime for micro analysis test methods

The silica source powder (15 g) was mixed with calcium hydroxide (15 g) powder at a ratio of 50:50. After mixing, 21 grams of water was added. The mixture was sealed in a plastic tube to avoid carbonation and placed at 50 ˚C in the oven to accelerate its hydration. At the age of 3 days and 28 days, the sample was obtained for microscopy observation and thermogravimetric analysis.

The details of scanning electron microscopy (SEM) and thermogravimetric analysis (TGA) was described in Chapter 3.

6.3.4 Strength activity index test.

The strength activity index test, modified from BS 3892, is a method used to compare the strength development of cement which contains different pozzolans. In this study, General Purpose (GP) Portland cement was used as a control reference and the replacement ratio of the silica source to GP cement was 20%. The water to cement ratio was fixed at 0.6 while the cement to sand ratio was 1:3. See Table 6-1 for the mixing proportion in details.

Table 6-1.The mixing design of the strength activity index test

Code	Materials	GP Cement (g)	Pozzolan (g)	Sand (g)	Water (g)
CO	Control sample	100	0	300	60
QS	Quartz sand	80	20	300	
AS	As-received Serpentine				
GS	Ground Serpentine				
MS	Micro silica				
SF	Silica fume				
RA	Rice husk ash				
RS	Recovered silica				

The strength samples were cast in the cube of $20 \times 20 \times 20$ mm at ambient temperature (20 °C). After casting, the samples were covered by plastic sheet and then demoulded after 24 hours. The samples were water cured at a temperature of 20 °C until tested for compressive strength at 3, 7, 28 and 90 days. The strength activity index (SAI) was calculated by Equation 6-2.

$$\mathrm{SAI} = \frac{\mathrm{CS_t}}{\mathrm{CS_0}} \times 100\% \qquad \text{Equation 6-2}$$

Where, CS_t is the compressive strength of the test sample at a certain age, and CS_0 is the compressive strength of the control sample.

6.4 Silica reactivity test results

6.4.1 The extracted silica from serpentine

To improve the reactivity of the serpentine, the *as-received* material was first ground into fine particles. The median and mean particle size of serpentine under different grinding duration (increased from 20, 60 and to 120 seconds) is shown in Table 6-2. It was obvious that the particle size decreased with grinding duration.

After grinding for 120 seconds, the median size of the particle decreased from 154.0 μm to 12.6 μm. The serpentine with finest particle size was selected for silica extraction trials.

Table 6-2. The particle size of the serpentine under different grinding durations.

	As-received	**20 s**	**60 s**	**120 s**
Median Size(μm)	154.0	28.0	21.7	12.6
Mean Size(μm)	352.6	103.9	86.5	32.7

As shown in the simplified reaction of the serpentine with hydrochloric acid in Equation 6-3, if the reaction is completed, the serpentine dissolves in the acid and forms silica in addition to Mg-chloride.

$$Mg_3Si_2O_5(OH)_4 + 6HCl = 3MgCl_2 + 2SiO_2 + 5H_2O \qquad \textit{Equation 6-3}$$

Table 6-3 compares the chemical composition of the *as-received* serpentine and the leached serpentine (noted as recovered silica). The silica content after the leaching process increased from 39.7% to 50.8% while the percentage of MgO and Fe_2O_3 both decreased. The MgO and Fe_2O_3 dissolved into the hydrochloric acid solution and stayed as Mg^{2+} and Fe^{3+}. The presence of ferric chloride changed the colour of the solution to light brown/yellow.

Table 6-3. The chemical composition of the serpentine before and after HCl leaching

(wt%)	SiO_2	MgO	Fe_2O_3	Al_2O_3	CaO	Na_2O	K_2O	LOI	Total
***as-received* serpentinite**	39.7	37.9	7.68	0.8	0.24	0.01	<0.01	13	99.3
Recovered silica	50.8	29.5	4.69	0.91	0.11	0.04	0.01	13.45	99.5

The XRD results shown in Figure 6-2 demonstrated that no new mineral was produced after the acid leaching, though there may have been a relative increase in amorphous silica around 20 – 30˚. Nevertheless, the intensity of the peak for serpentine significantly decreased suggesting some dissolution of the serpentine mineral.

In Figure 6-3, the microscopy of the serpentine before and after grinding, and before and after acid leaching were compared. The geometry shape of the *as-received* serpentine particles, shown in Figure 6-3a, was irregular polygon with the size around 150 μm. This was in accordance with the laser particle size analysis. After grinding for 120 seconds (Figure 6-3b), it changed to a more spherical-like shape with the decrease in particle size. In Figure 6-3c, the particle became smoother after the reaction, due to the dissolution which occurred at the surface.

The EDS (Energy Dispersive X-Ray Spectroscopy) results showed the elemental analysis of an individual particle and is summarised in Table 6-4. The amount of the main elements, i.e.: Mg, Si, O, Fe, were very similar in the serpentine before and after grinding as expected. The difference was caused by the variation of the individual grains between the *as-received* and ground samples. However, in the recovered silica sample, the Mg percentage decreased from 26.3% to 4.9% while the Si percentage increased. This showed the Mg was dissolved in acid, but the leaching was not complete with 4.9% Mg remaining.

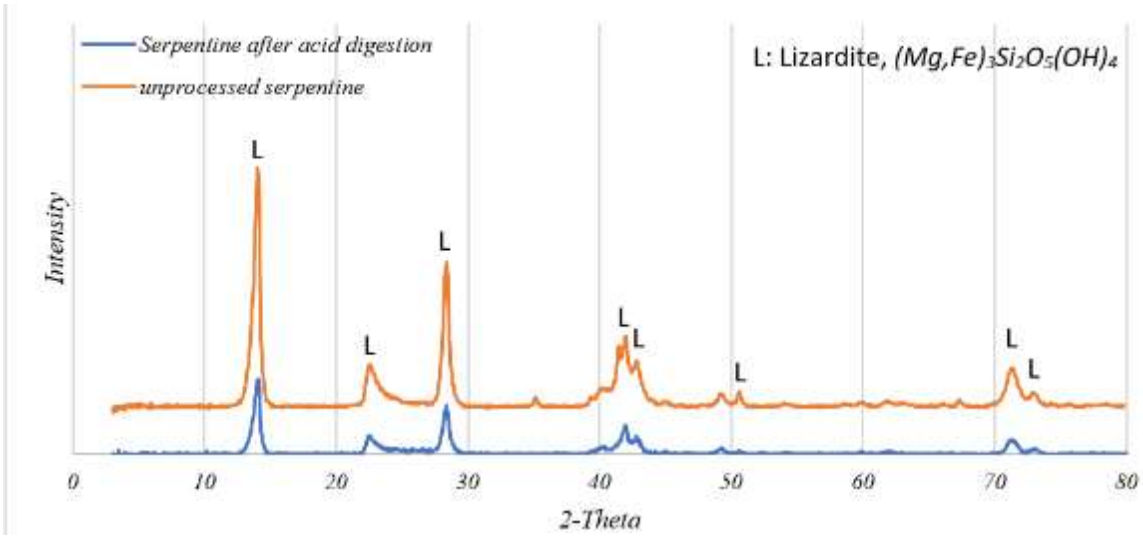

Figure 6-2. The XRD pattern of the serpentine before and after leaching

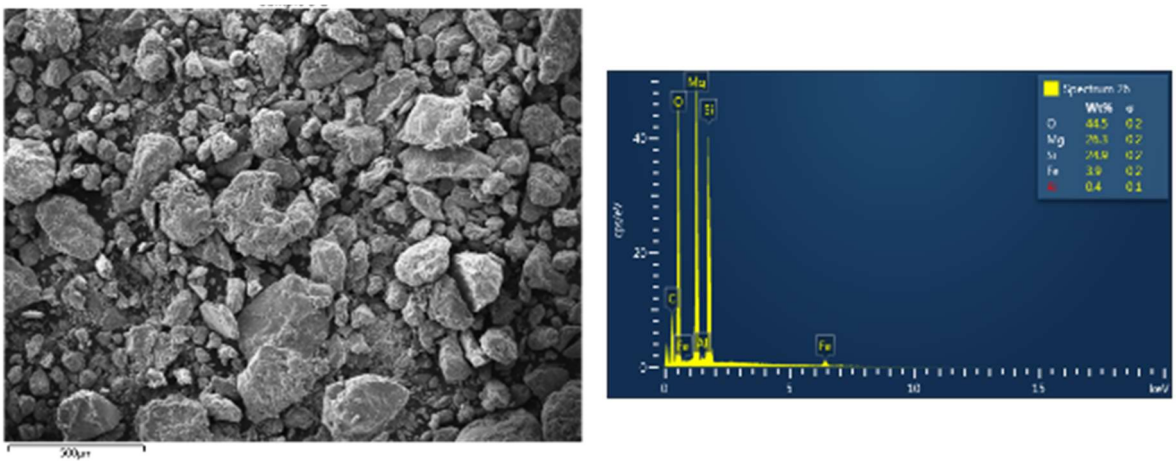

(a). Microscopy and EDS of the as received serpentine.

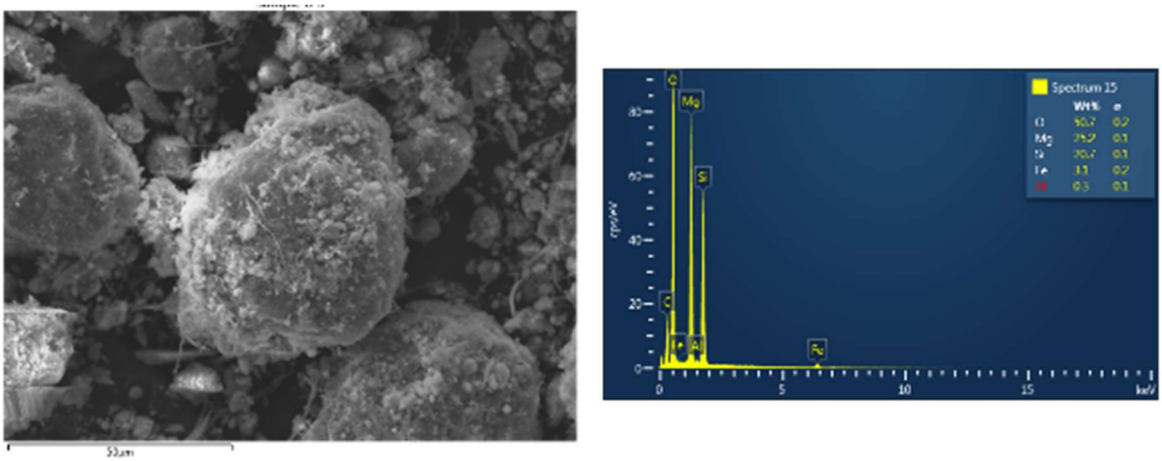

(b). Microscopy and EDS of the ground serpentine.

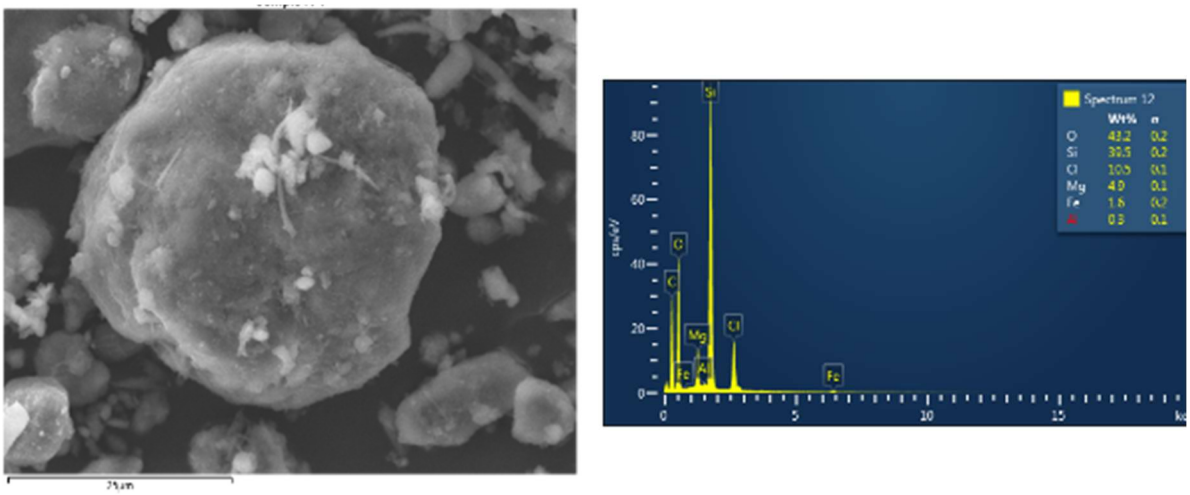

(c). Microscopy and EDS of the leached serpentine (recovered silica).

Figure 6-3. Microscopy and the EDS results of the serpentines

Table 6-4. The comparison of the EDS results of different serpentines.

(wt%)	**Mg**	**Si**	**O**	**Fe**	**Cl**
As-received serpentine	26.3	24.9	44.5	3.6	-
Ground serpentine	25.2	20.7	50.7	3.1	-
Leached Serpentine	4.9	39.5	43.2	1.6	10.5

The results from the elemental EDS analysis are consistent with the values obtained by XRF. Noting the presence of Cl, it was originated from the hydrochloric acid. The microstructure observation of the particles compared the particle size change after the grinding process and the EDS analysis confirmed the Mg dissolution in acid leaching.

Compared to other studies, the silica content in the leached serpentine reside was relatively low. This was due to the difference of the reaction conditions. In other studies, extended reaction duration (72 hours), higher acid concentration (37.5% HCl), elevated reaction temperature (90 ˚C) and multiple stages of acid reaction were adopted. However, these also inevitably led to an increase of the energy consumption during the reaction which was not a cost-effective way to produce the silica alternative. Therefore, in this study, a

practical approach of using 2 mol/L HCl for 24 hours of reaction under ambient temperature was used to process the serpentine. The recovered silica was then accessed in the following sections.

6.4.2 Chemical composition and phase identification

The chemical composition of the solution studied was characterized by the XRF technique and presented in Table 6-5. The silica content in silica fume was the highest (92.6%) while only 50.8% of silica was found in recovered silica. However, the high silica content cannot justify high silica reactivity as silica, if in crystal form, such as quartz sand, shows limited reactivity. Only amorphous silica is active enough to react with $Ca(OH)_2$ to form C-S-H gel.

The XRD results in Figure 6-4 showed the crystalline phase identification of these three silica sources. Note the pattern of the recovered silica was identical with it in Figure 6-2, but with a different intensity scale. The micro silica, which is a natural amorphous silica source, was quarried from a local site in New Zealand. In this sample, silica in the crystalline quartz form were detected around the peak 26° and 30°. The XRD of silica fume shows no indication of crystalline phase and with a broadboard hump located at the peak of cristobalite, which are polymorphs of SiO_2. It proves the amorphous silica phase of the silica fume. The XRD spectra of recovered silica, on the other hand, showed obvious peaks around 14°, 28° and 42° for the unreacted serpentine ($Mg_3Si_2O_5(OH)_4$). Nevertheless, a board peak around 20°~30° was also observed which indicating the amorphous silica may be present in the recovered silica.

Combining the results of chemical and phase information of these silicas, the silica fume has the greatest silica reactivity due to its highest silica content and amorphous form. The micro silica has the second highest silica content, but some silica was in the crystal form. For the recovered silica, it has the smallest silica content and some silica was in the unreacted serpentine. This made the recovered silica the lowest reactive material among those three.

Table 6-5. Chemical composition of the silica sources

	SiO_2	Al_2O_3	Fe_2O_3	CaO	MgO	Na_2O	K_2O	TiO_2	MnO	LOI	Total
Silica Fume	92.6	0.6	1.0	0.7	1.1	0.6	1.4	0.0	0.1	1.8	99.9
Micro silica	85.1	6.3	0.4	0.1	<0.05	0.3	0.8	1.0	0.0	4.0	98.0
Recovered silica	50.8	0.9	4.7	0.1	29.5	0.0	0.0	0.1	0.1	13.5	99.6

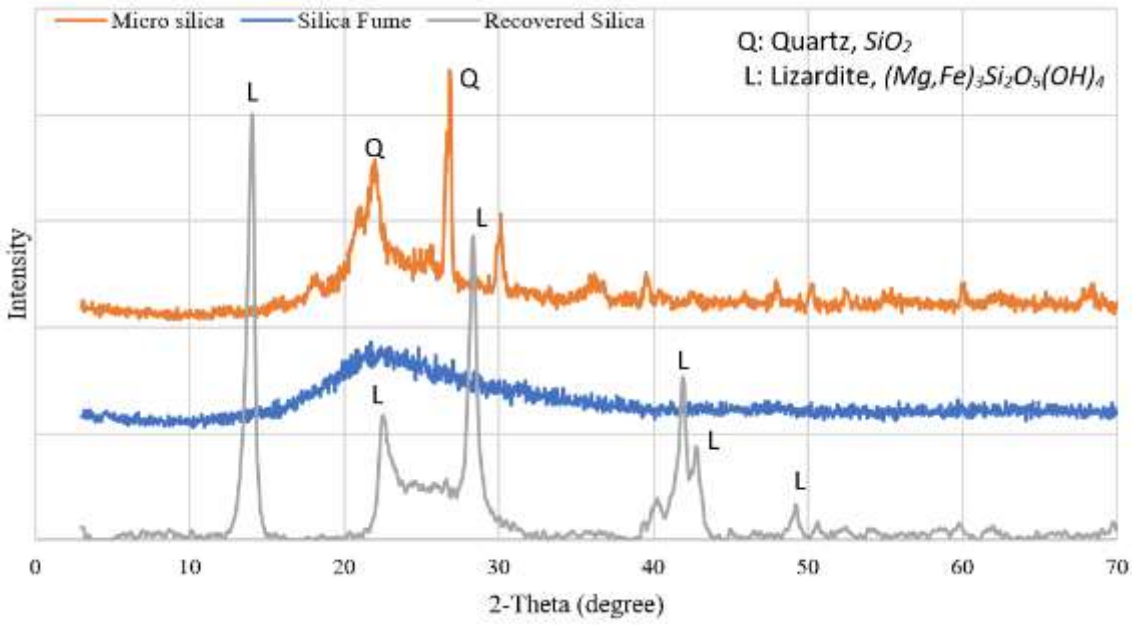

Figure 6-4. XRD pattern of different silica sources

6.4.3 Particle size and surface area analysis

The pozzolan activity is generally related to both the percentage of amorphous material and the particle size and surface area. Smaller particle sizes result in a higher surface area and normally improved reactivity.

The particle size distribution and diameter of these silica materials are presented in Figure 6-5. The coarse quartz sand and as-received serpentine showed the largest particle size with lowest conductivity change. Note the median particle size of the silica fume was 135 µm. This is significantly larger than other studies (less than 1 µm). This was caused by the agglomerated silica particles. The individual spherical particle sizes of the silica fume seen in SEM analysis are approximately 0.15 µm.

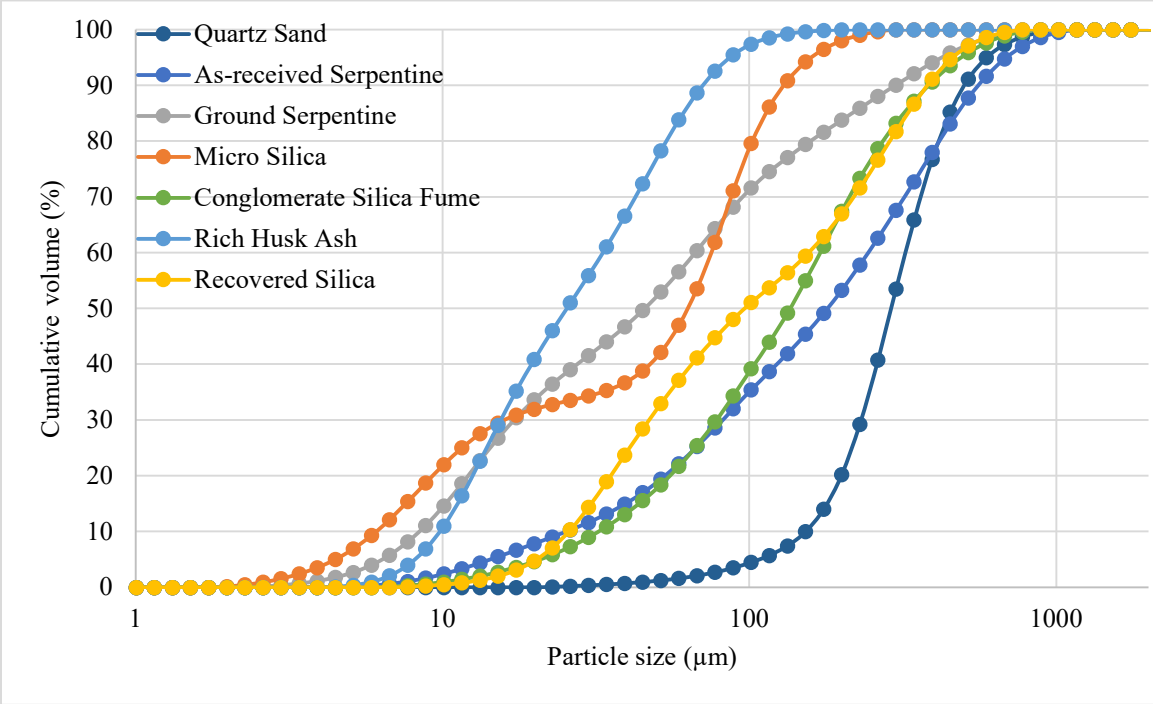

(a). Particle size distribution

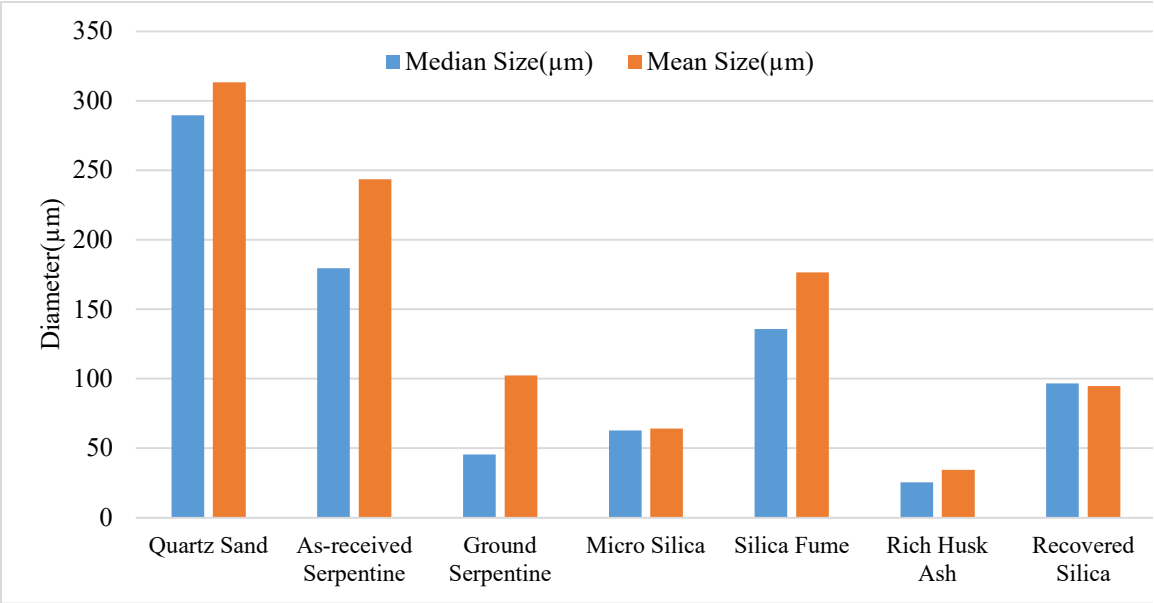

(b) Particle diameter

Figure 6-5. Particle size analysis of the silica materials.

Table 6-6 shows the results of the surface area of the recovered silica, ground serpentine and the silica fume measured by BET. The BET surface area of the recovered silica was 81.56 m^2/g, which was lower than previous studies where around 100~300 m^2/g. This is due to the presence of unreacted serpentine. However, it was higher than the ground serpentine (before acid leaching) and silica fume. The recorded BET surface area for silica fume was 19.07 m^2/g which is in the typical range of other research (15~30 m^2/g).

Figure 6-6 shows: (a) the isotherm adsorption and (b) the pore area distribution of these three materials. The recovered silica showed largest amount of absorbed nitrogen under the same partial pressure compared to ground serpentine and silica fume, and the isotherm also indicated the porous structure of the recovered silica. From the pore area distribution curves (Figure 6-6b), it was clear that there were a number of mesopore (diameter between 0.002 µm and 0.05 µm) in the recovered silica.

The dissolution of metal ions ($Mg^{2+}$and Fe^{3+}) from the serpentine in acid, lead to the mesoporous nature of the recovered silica, which make it higher surface area than ground serpentine and silica fume.

The high surface area of the recovered silica may attribute to its pozzolan reactivity.

Table 6-6. The comparison of the surface area between serpentine and silica fume.

Surface area (m^2/g)	Recovered Silica	Ground Serpentine	Silica Fume
BET Surface Area:	81.56	26.08	19.07
Langmuir Surface Area:	119.70	38.28	28.02
t-Plot Micropore Area:	1.68	0.06	0.53
t-Plot External Surface Area:	79.88	26.02	18.54

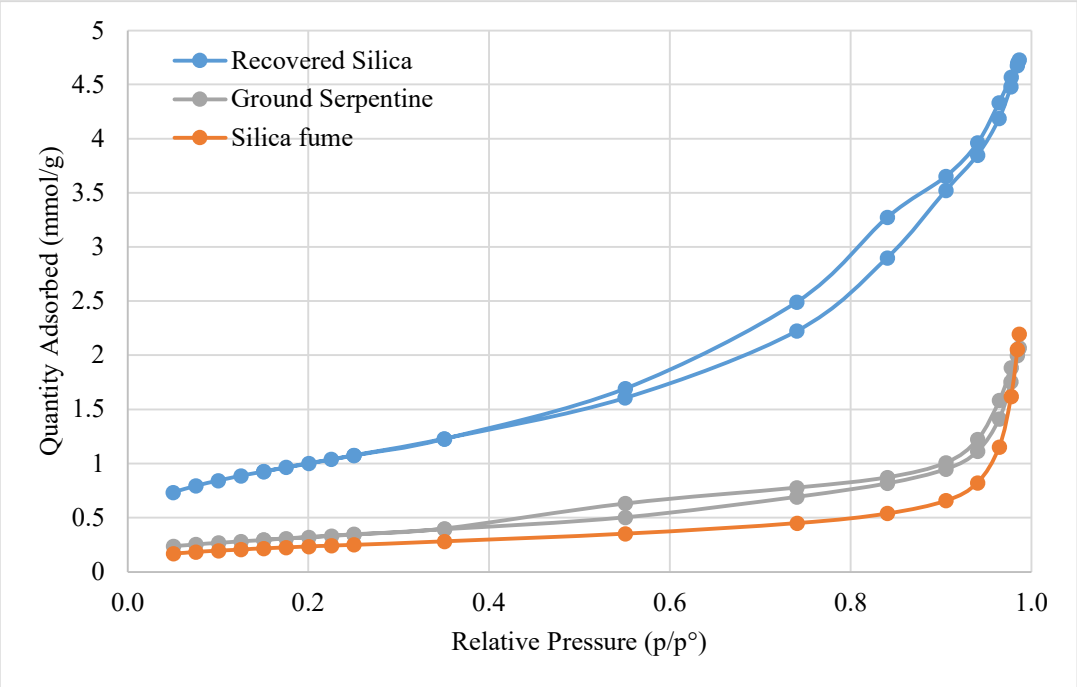

(a). Isotherm Report

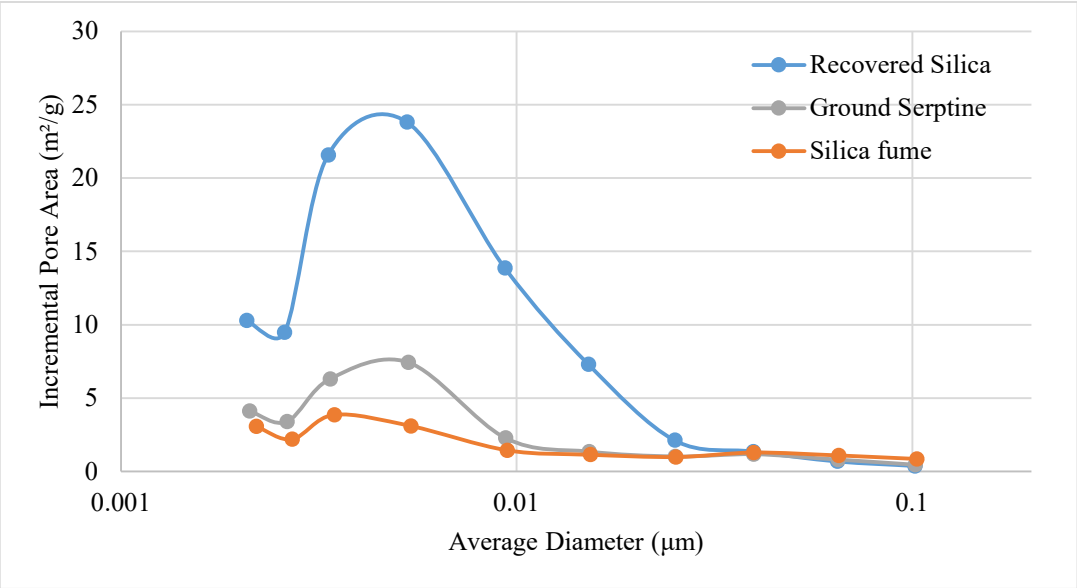

(b) Pore area distribution

Figure 6-6. The surface area and pore volume analysis of the silica materials

6.4.4 Conductivity Test

The conductivity test method was used to understand the reactivity of the difference silica materials. The change of the conductivity is used to indicate their silica reactivity. The results of the conductivity test are shown in Figure 6-7.

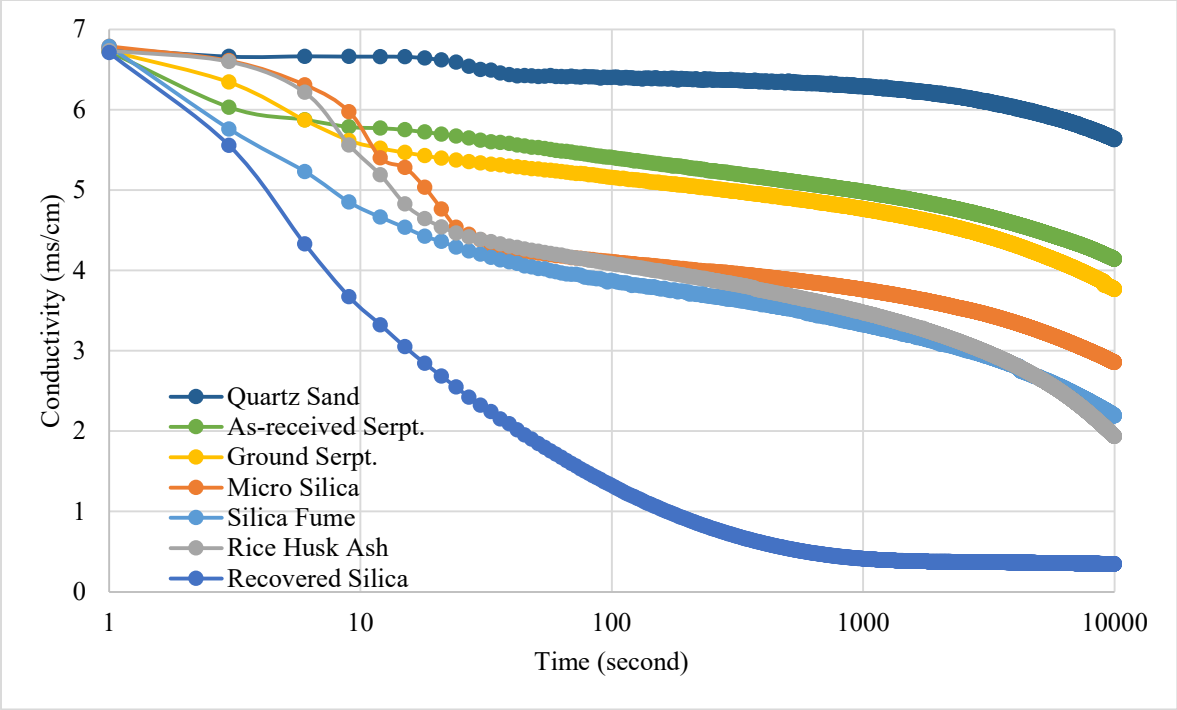

Figure 6-7. The conductivity test of the different silica materials mixed with lime water

From Figure 6-7, it was clear that the different materials can be classified into four different grades according to their reactivity.

Grade I: This is the curve demonstrated by the non-reactive silica material, quartz sand. This mix showed little conductivity change with time, especially over the first 1000 seconds. The conductivity drop in later age was caused by the carbonation of the CH solution: the dissolved CH reacted with the atmospheric CO_2 forming calcium carbonates.

Grade II: The as-received and ground serpentine had a higher consumption of the Ca^{2+} compared to quartz sand, indicating the raw serpentine possessed some limited reactivity.

Grade III: These curves represent widely used conventional silica sources, i.e.: micro silica, silica fume and rice husk ash. Among them, the silica fume and rice husk ash showed comparably high reactivity while micro silica the least.

Grade IV: The recovered silica from extracted serpentine demonstrated the highest CH consumption and the fastest reaction rate. This would indicate the high pozzolanic activity of the leached serpentine. However, the rapid change in conductivity associated with the recovered silica may also be a result of some residual contamination by HCl, as indicated by the higher chloride measurements.

6.4.5 Ion concentration test

Table 6-7 presents the concentration of the calcium ion in the solution mixed with several silica sources with unsaturated CH solution. Figure 6-8 reveals the change in Ca^{2+} concentration. The Ca^{2+} concentration change in ground serpentine mix was the lowest which suggested the least silica reactivity. The change then further increased from micro silica, silica fume, rice husk ash and then recovered silica from serpentine. The ion concentration results agree well with the results of the conductivity test, suggesting the recovered silica reacts with calcium hydroxide quickly and consumes a significant amount of dissolved calcium compared to conventional silica source in the test.

Table 6-7. The calcium ion concentration of the CH solution mixed with different silica sources

No.	Solute	Solvent	Ca^{2+} Concentration (mg/L)

1	Calcium hydroxide	D.I. water	320.67
2	Ground serpentine	CH solution	300.23
3	Ground serpentine	D.I. water	9.75
4	Micro silica	CH solution	175.77
5	Micro silica	D.I. water	2.10
6	Silica fume	CH solution	194.67
7	Silica fume	D.I. water	32.97
8	Rice husk ash	CH solution	112.35
9	Rice husk ash	D.I. water	4.41
10	Recovered silica	CH solution	62.16
11	Recovered silica	D.I. water	1.26

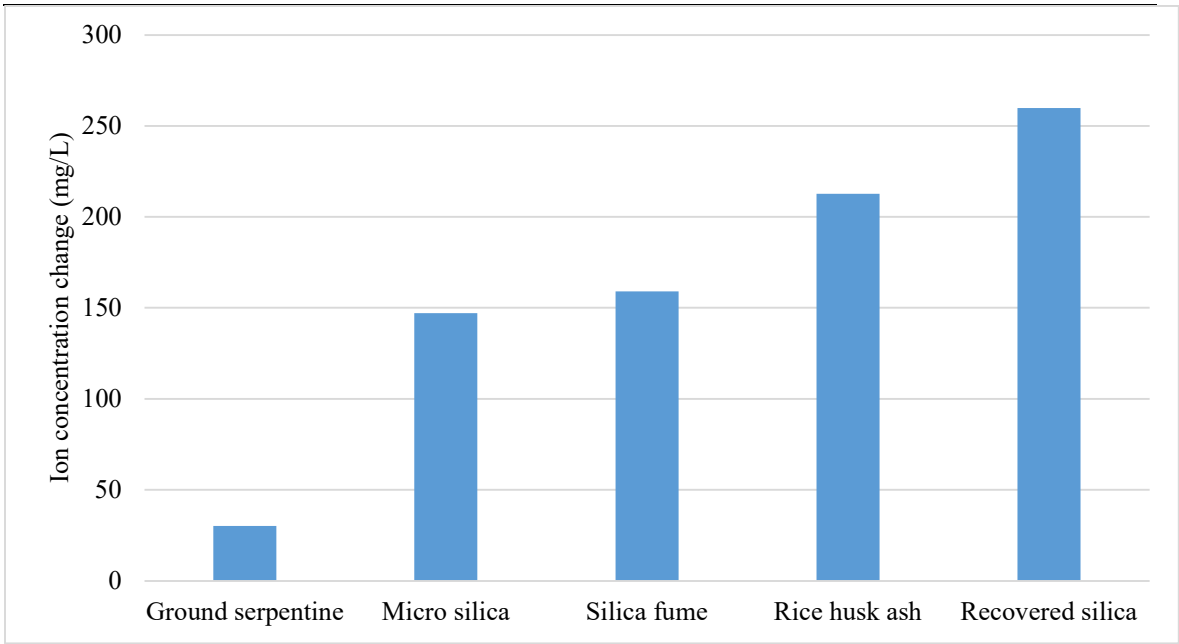

Figure 6-8. The ion concentration change of calcium in different silica solutions.

6.4.6 Microstructure observation

As shown in Figure 6-9, the SEM provided a direct observation of the silica samples mixed with CH powder, at a 1:1 ratio, for an age of 28 days.

Figure 6-9(a) shows a particle of quartz sand in the centre with CH powder scattered around, combined with the EDS results in Figure 6-9(a-1) and Figure 6-9(a-2). The

interface of the two materials does not show any hydration reaction. In the ground serpentine sample, as shown in Figure 6-9(b), a larger amount of CH particles were observed on the surface of the serpentine compared to the quartz sand. Figure 6-9(b-1) showed the main elements in serpentine were Mg, Si and O while Figure 6-9(b-2) revealed the combination of Ca. This may indicate the formation of small quantity of Calcium Silicate Hydrates (C-S-H).

For the samples with CH mixed with micro silica and silica fume, their microstructure (Figure 6-9(c) and Figure 6-9(d)) both showed interfacial reaction. The EDS results revealed the element composition of the products and the Ca to Si ratio was similar to the ratio formed in C-S-H. This suggests that the surface of the silica particle was completely covered by the hydration products.

There were more CH particles on the surface of the recovered produced (Figure 6-10) compared to quartz sand and ground serpentine,. This suggests it has higher reactivity. However, the Ca: Si ratio was lower than in C-S-H indicating some silica in the sample remained unreacted or existed in a crystalline form which has limited activity. Besides, the hydration products from the recovered silica and the CH were not interlocked together and so formed a loose structure. This may lead to poor strength when compared to using silica fume or micro silica.

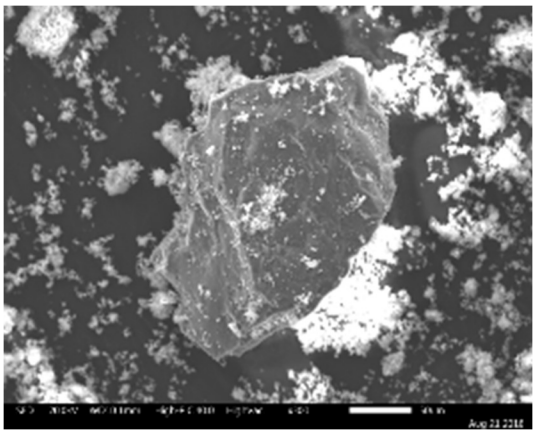

(a). Quartz sand

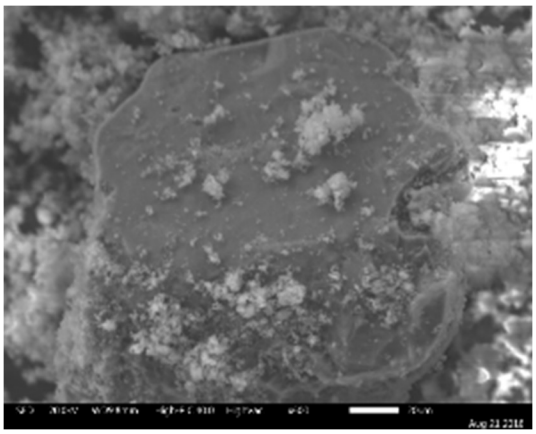

(b). Ground serpentine

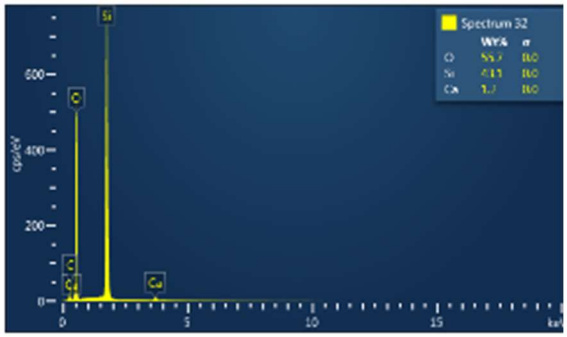

(a-1). EDS of point a1

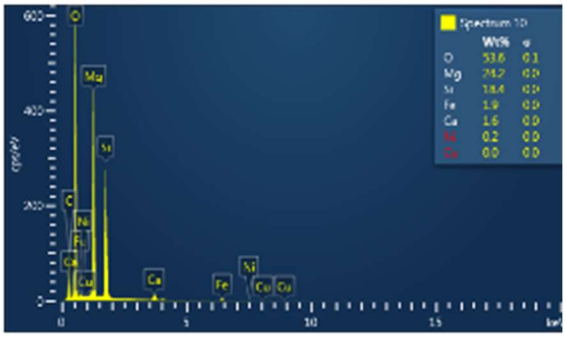

(b-1). EDS of point b1

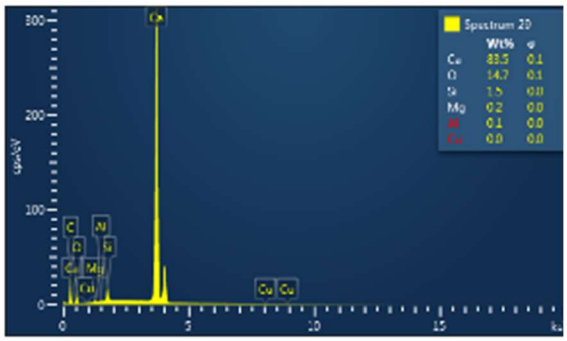

(a-2). EDS of point a2

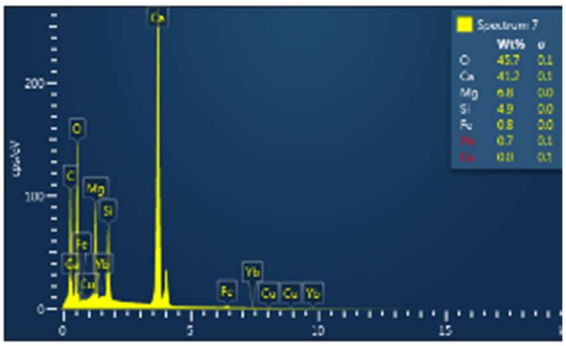

(b-2). EDS of point b2

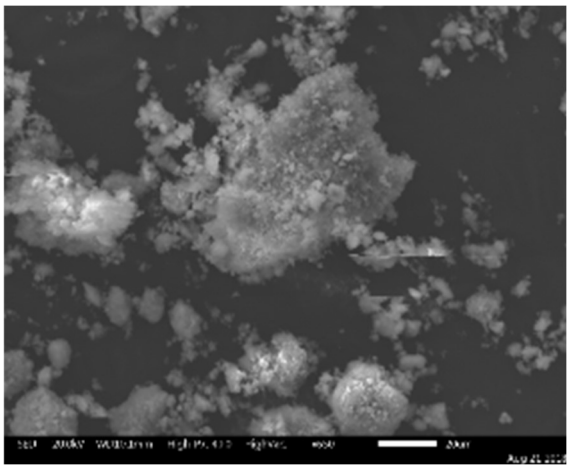

(c). Micro silica

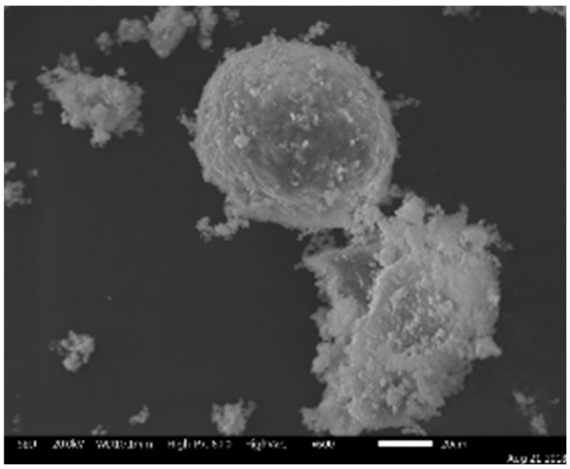

(d). Silica fume

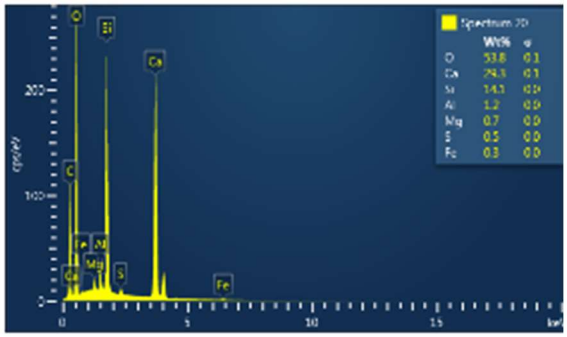

(c-1). EDS of point c1

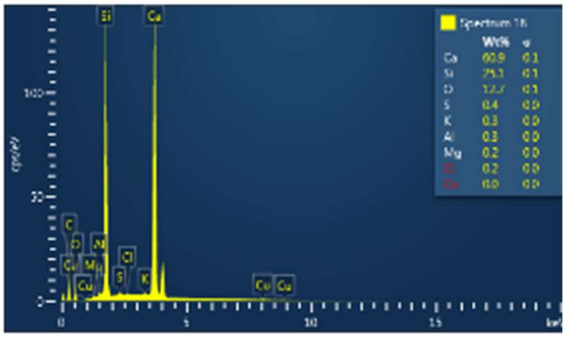

(d-1). EDS of point d1

Figure 6-9. The microscopy of different silica materials mixed with CH at 28 days

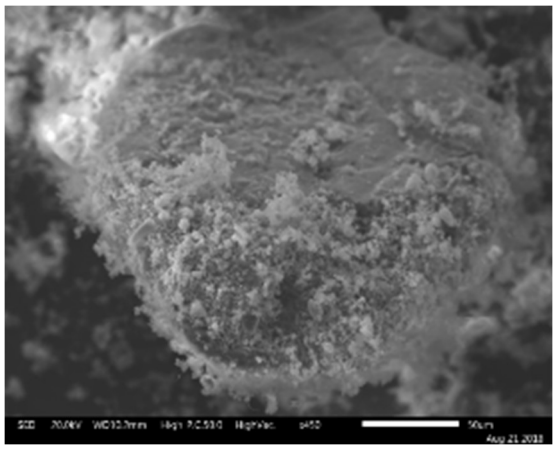

(a). Recovered silica

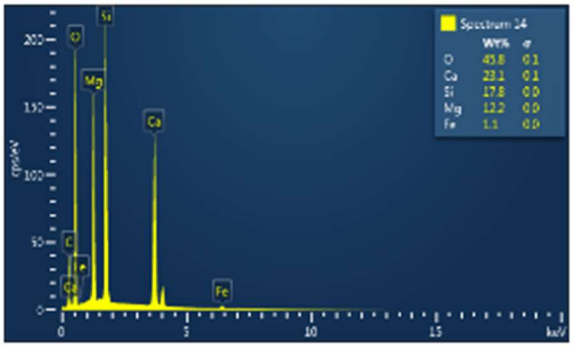

(b). EDS of point f1

Figure 6-10. The microscopy of recovered silica mixed with CH at 28 days

6.4.7 Thermogravimetric analysis

The thermogravimetric analysis of the silica and CH hydrated sample quantifies the amount of residual CH present after reaction. The higher the amount of the residual (unreacted) CH, the less the silica reactivity of the sample material.

In the TG curve weight loss from 380 ˚C ~480 ˚C which is caused by the thermal decomposition of the calcium hydroxide and the reaction is shown in the Equation 6-4. By measuring the mass loss of the evaporated water, the amount of $Ca(OH)_2$ can be calculated.

$$Ca(OH)_2 = CaO + H_2O\uparrow \qquad \textit{Equation 6-4}$$

Figure 6-11 compares the TG curves of the mixtures at different ages: 7 days and 28 days. From the Table 6-8. , it can be seen that the residual CH content for the quartz sand reference was 38.6% while 30% of CH remained for other silicas after 7 days reaction. After 28 days of curing, the residual CH decreased. For the micro silica, which showed the least residual CH of 8.8%, this indicates the highest capability to consume the CH, therefore the greatest silica reactivity. The recovered silica and the silica fume had 15% and 17.9% residual CH respectively, suggesting the recovered silica had comparable silica reactivity to silica fume.

From the perspective of the formation of the hydration products, the amount of the produced calcium silicate hydrates gel (C-S-H) can only be estimated based on the water loss between 105 and 380° C as its decomposition overlaps with other phases and the stoichiometry of C-S-H is not constant. There was clearly no C-S-H formation in the quartz sand sample regardless of the age, whereas the C-S-H production increased with age for other amorphous silicas. The silica fume sample had a higher C-S-H amount compared to

the recovered silica at both 7 and 28 days. Among them, the micro silica demonstrated highest CH consumption and largest amount of C-S-H at the age of 28 days.

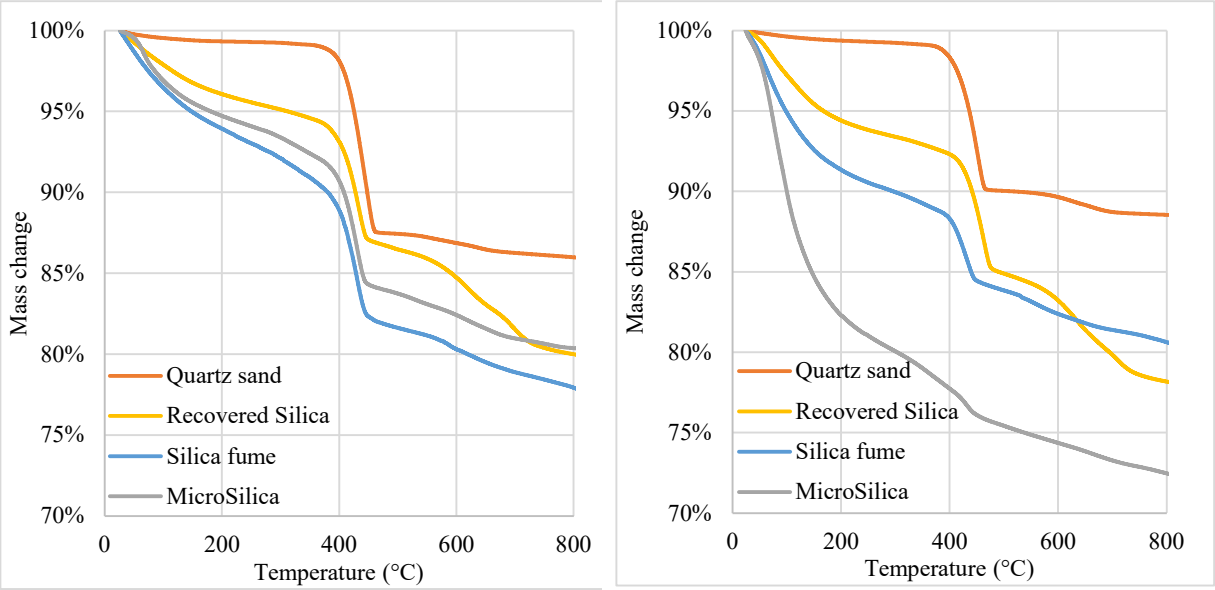

(a). 7 days *(b). 28 days*

Figure 6-11. TG curves of the silica sources mixed with CH powder at different ages.

Table 6-8. The residual CH content of the CH + SiO_2 mixture at different ages

Age	Mass	Quartz sand	Recovered silica	Silica fume	Micro silica
7 d	at 380 ˚C	98.8%	94.1%	90.0%	91.7%
	at 480 ˚C	89.5%	87.1%	82.3%	84.3%
	change (380~480 ˚C)	9.4%	7.0%	7.7%	7.4%
	Residual CH content	**38.6%**	**28.8%**	**31.6%**	**30.5%**
28 d	at 380 ˚C	98.9%	92.6%	88.8%	78.2%
	at 480 ˚C	92.6%	88.9%	84.5%	76.1%
	change (380~480 ˚C)	6.3%	3.7%	4.3%	2.1%
	Residual CH content	**26.1%**	**15.0%**	**17.9%**	**8.8%**

6.4.8 Strength activity test

The compressive strength development of the mixtures is listed Table 6-9 while Figure 6-12 shows the average strength activity index (SAI) at 28 days.

Considering the pozzolan replacement ratio was 20% of cement, the strength activity index should be 80% of the control if the pozzolan addition was completely inert. However, other factors also contribute to the strength development except for the dilution effect. Therefore, the quartz sand, which acted as a non-reactive silica reference, set the zero SAI baseline at 60%. The SAI of the *as-received* and ground serpentine samples were both 62% indicating little silica reactivity. The limited reactivity of the *as-received* serpentine is consistent with the reactivity test results. The conventional reactive silica source: micro silica and silica fume, demonstrated highest SAI, at 102% and 105% respectively. The rich husk ash was somewhat lower (81%), while the recovered silica sample was 71%.

The recovered silica sample did not show significant strength improvements compared to the non-reactive silica source, and the SAI value was lower than other commonly known silica referencesreference.

Table 6-9. The compressive strength of the sample mixed with different silica materials.

	PC	Quartz Sand	As-received Serpentine	Ground Serpentine	Micro Silica	Silica Fume	Rice Husk Ash	Recovered Silica
3 d	7.9	5.0	5.4	5.3	8.6	10.0	7.6	6.3
7 d	15.3	9.5	10.1	8.9	13.6	15.2	11.9	10.4
28 d	25.9	14.3	16.1	15.9	29.0	26.1	19.6	18.1
90 d	32.5	19.8	16.8	19.4	31.3	30.3	24.8	21.9

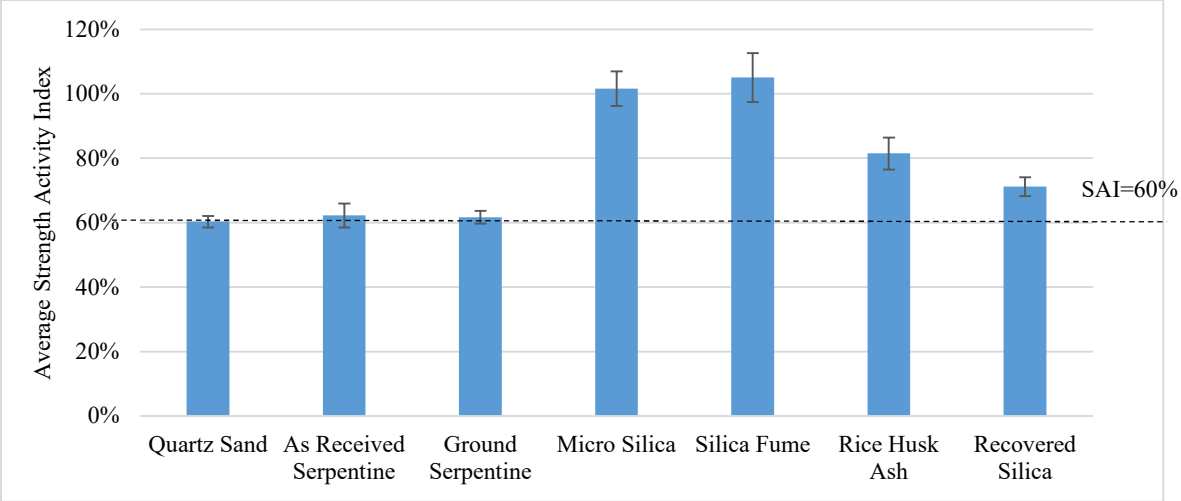

Figure 6-12. Strength activity index of the silica materials

6.5 Comparison of the different assessing methods

Eight different techniques were used in this study to compare the pozzolanic reactivity of the residual silica along with different silica sources. Figure 6-13 summarised the silica reactivity results of these materials in quantified ranking: from 1 the least reactive (inside ring) to 7 the most reactive (outside ring).

Among these methods, chemical and phase indication (XRD &XRF), particle size and surface area characterisation are methods that directly measure the effects of the silica source. Other methods: conductivity, ion concentration, microstructure observation (SEM), thermogravimetric analysis and strength, are indirect measures that focus more on its hydration reaction process/products with calcium hydroxide/Portland cement.

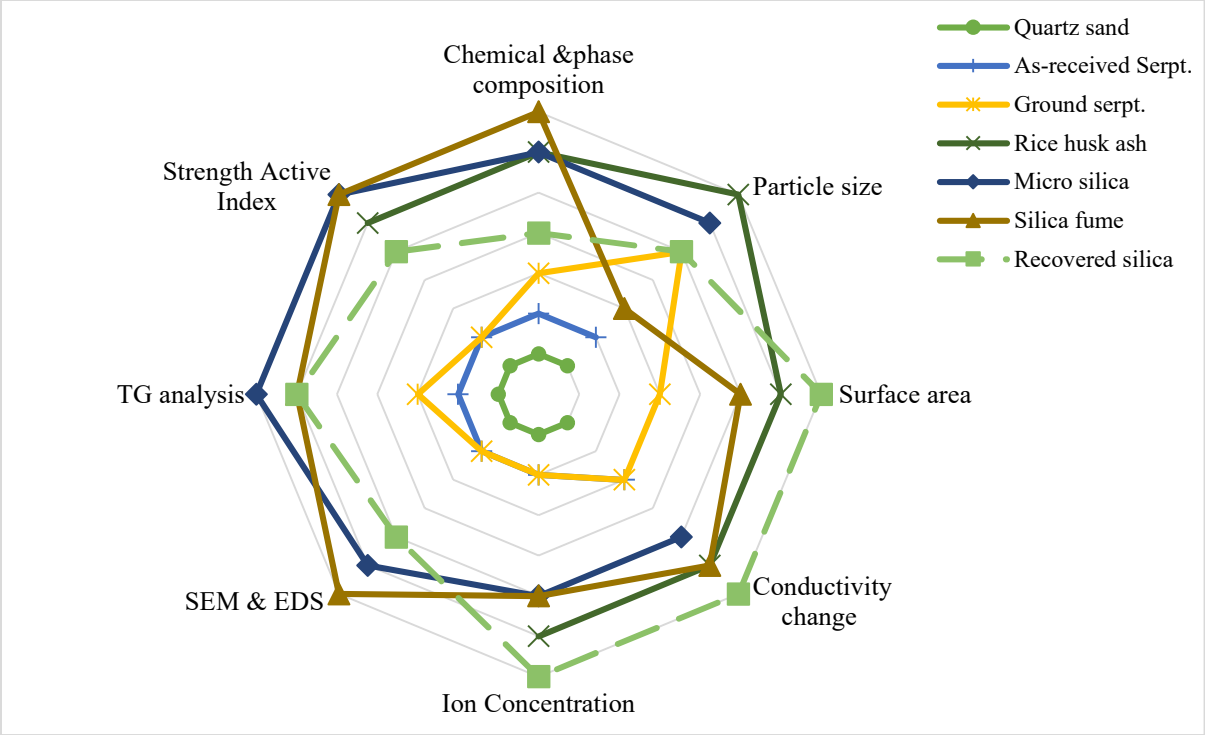

Figure 6-13. The comparison of silica reactivity of different materials using various techniques.

(inside ring: the least reactive, outside ring: most reactive)

Donatello et al.[94] compared three different methods to assess pozzolanic activity: Frattini test, saturated lime (SL) test and strength activity index (SAI) test. The Frattini test and saturated lime test are both methods that are based on measuring the ion concentration change (consumption) of the dissolved Ca^{2+} and OH^-. In the Frattini test, a solution containing cement was used while saturated $Ca(OH)_2$ solution was prepared for SL test. This study concluded that the Frattini test and SAI test results correlated with each other while there was no correlation between SL test with the other two. It was suggested that these methods should be combined with an independent determination of $Ca(OH)_2$ content, such as thermal or diffraction methods.

The crystalline silica source, quartz sand, acted as the non-reactive reference and demonstrated the least reactivity in all test methods that were carried out, so sit in the inside ring in the radar chart. For the reactive silica sources, like silica fume, micro silica and rice husk ash, they both lie on the outside position which indicates high pozzolan activity as measured by most methods.

However, the data from particle size shows contradicting results. The ground serpentine has a smaller particle size compared to silica fume but in fact it is much less reactive. There are two reasons attributed to this. The first is the silica fume is dry densified form which was not disperse into individual silica fume spheres in diameter. The size of the undispersed agglomerates can be up to several millimetres[294]. Secondly, the fine particle size does not ensure its silica reactivity. Even though it was reported[123] when quartz and basic or devitrified volcanic rocks, which are non-reactive silica sources, were ground to ultra-fine powders, they became beneficial to the hydration process. This was caused by the nucleation effect based on its particle size instead of the formation of the C-S-H gel. Therefore, the particle size alone cannot be used as an indicator for the silica reactivity. Nevertheless, it is required by ASTM standard C 618 that the amount retained on 45 micrometres sieve should be less than 34%.

Similarly, high specific surface area may contribute to a higher reaction rate and improve cement's early age properties. However, the high surface area itself cannot lead to a high silica reactivity.

The conductivity and ion concentration tests are rapid measures that can compare the calcium consumption in the first few hours. These methods are useful for characterising a silica source whether it is active or not. The shortcoming of this methods is that it requires

that any impurities of the test material does not react with calcium hydroxide. For example, if the raw material contains SO_4^{2-}, it will quickly react with Ca^{2+} to precipitate $CaSO_4$ which can also lead to a dramatic change of Ca^{2+} ion concentration and conductivity change. Therefore, it is essential to find out the chemical composition and mineral identification of the material by XRF and XRD before these tests.

The TG analysis and SEM&EDS observation are methods that focus on characterising the unreacted calcium hydroxide and the hydration products: calcium silicate hydrate gel. TG analysis is a good way to quantify the amount of residual calcium hydroxide and then back calculate how much calcium was consumed. But again, like the conductivity and ion concentration tests, the composition of the raw material needs to be understood before the analysis to avoid other reactions that may also consume calcium. The SEM combined with EDS provide a powerful tool to directly observe the reaction products and the interfacial area between calcium hydroxide and raw materials. The drawbacks of this method are that it only provides local area observations, the amount of hydration products cannot be quantified and is subject to the observer.

In this study, it was found that the Strength Activity Index test results correlate well with other methods except for the particle size (reason explained above). Therefore, this can be a simple but reliable pozzolanic reactivity test. Since the strength is one of the most important mechanical properties, and the measuring methods are easy to do compared to other analytical methods, it was selected by both ASTM C1240, BS EN 450 and NZS 3123:2009 standards as an important indicator for pozzolan materials. However, a study[295] tested 72 mixes in compliance with the standard methods (both EN and ASTM) and pointed out the inconsistencies. To be able to make reproducible and comparable test

results, it was suggested that additional information, such as chemical admixtures /superplasticiser, sand and cement types, should be given.

6.6 Comparison of the pozzolanic reactivity

It is clear that quartz sand, as a non-reactive silica source reference, showed the least reactivity in the various tests. The *as-received* and ground serpentine also showed limited reactivity. For the other silica sources, micro silica and silica fume demonstrated higher pozzolanic reactivity than recovered silica in the strength test, chemical and phase indication, microstructure observation, and TG analysis.

The recovered silica demonstrated a certain degree of pozzolanic reactivity but was not comparable with the conventional silica sources. Even though the recovered silica showed the highest activity in the conductivity and ion concentration changes, these methods are indirect measures and are relatively short term. The conductivity and the ion concentration change, for example, only record the information over the first 3 hours. Nevertheless, it was very interesting to note that the recovered silica had the highest surface area. This may explain its superior reactivity in short term tests (conductivity and ion concentration tests) due to its high reaction rate with calcium hydroxide in early ages.

It was very clear from the XRF results that the silica content in recovered silica is the lowest compared to other reactive silica source, at only 50.8% with some unreacted serpentine residue. According to the TGA and SEM observation, the amount of hydration products it produced, was the lowest too. With less formation of the hydration products, it leads to lower strength development of the mortar samples.

The recovered silica demonstrated a great potential for the pozzolanic reactivity due to its high surface area. If the purity of the silica content could be increased by optimising the processing method, such as using a higher concentration acid, elevated reaction temperature, prolonged reaction duration, multiple stages of processing and purification, it may produce more C-S-H when in contact with calcium hydroxide.

6.7 Silica precipitation

During the serpentine leaching process, the silicates also dissolved into the solution. Based on previous studies, the silica dissolution is a very complex process and difficult to predict. It was found that both the temperature[296, 297], pH[297] and ionic strength[298] have a significant influence on the solubility of amorphous silica and the forms of silica present in a solution. Impurities such as iron, aluminium[299-301] and magnesium ion[302] can reduce the solubility of silica at equilibrium, while the calcium ion has no effect on the solubility of silica[303].

A study by Zuhl and Amjad[304] reported that silica supersaturation occurred and pointed out that a high degree of silica supersaturation increased the polymerisation reaction rate. In this study, it was observed that the silica was precipitated after settling for 7 days, as shown in Figure 6-14. The silicon ion concentration was recorded at 457.0 mg/L just after the reaction while it decreased to 57.5 mg/L after a week of settling. It has been suggested by Sheikholeslami's study[305] that any dissolved silica may come out of the supersaturated solution as suspension particles after polymerized silica grows to form a 3D polymer. These colloidal particles form large particles that may deposit on surfaces.

The precipitated material was carefully collected and then oven dried at a temperature of 105 °C. The XRD analysis iswas shown Figure 6-15. As can be seen, there is a broad peak around 20 to 30 ° and this indicates the material to be amorphous silica.

Further study on the silica precipitation is helpful to understand the whole process, and it also would be interesting to quantify the amount of produced silica, and to characterise the property of the precipitated silica. However, they are out of the scope of this study.

Figure 6-14. The settled silica precipitation from leached serpentine solution.

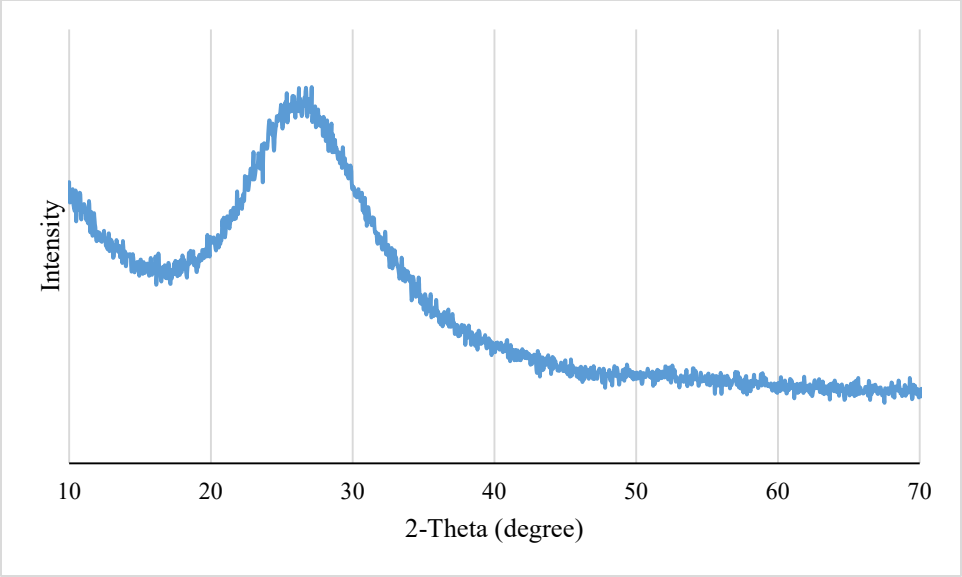

Figure 6-15. XRD pattern of the precipitated silica from leached serpentine solution.

6.8 Summary and conclusion

Silica was extracted from serpentine using the acid digestion method. In order to use the recovered silica as a supplementary cementitious material, the silica reactivity was systematically investigated. Seven different characterisation techniques were used to compare its reactivity with other silica sources: from non-reactive silica sand to unprocessed raw material, and widely used traditional silica sources. These techniques cover the mechanical properties, chemical and phase indication, the study of the hydration products (both in quantity and the microstructure observation), the reaction solution property and the information on material particles. By combining these test results, it provides a robust assessment of the pozzolanic reactivity of the silica materials.

To conclude, the recovered silica from the serpentine acid dissolution demonstrated some pozzolan reactivity due to the presence of the amorphous silica. The extracted silica showed a high reaction rate with calcium hydroxide due to its large specific surface area,

which led to the high silica reactivity in some short-term based indirect measurement. The strength test and the chemical and phase composition of the material confirmed the highly reactive of the silica fume and micro silica.

Considering the low silica content in the recovered silica, it still showed some good reactivity. If the acid leaching process could be modified to dissolve more serpentine, less unreacted serpentine may lead to the higher amorphous silica content and higher pozzolanic activity. Methods to improve its leaching efficiency could be using a higher concentration acid, elevation of the reaction temperature or prolonging the reaction time. A second stage of alkaline leaching followed by precipitation could be used to obtain silica in higher purity and increase the reactivity of the recovered silica.

7 The cementitious properties of the recovered products from olivine and serpentine

7.1 Introduction

The previous chapters revealed the process of recovering magnesia from olivine and silica from serpentine. In the following sections, the cementitious properties of these two materials will be discussed.

In recent years, the combination of reactive magnesia and silica have been shown to produce a magnesium silicate hydrate (M-S-H) [306, 307]. The effect of different silica sources in Portland cement and its application has been extensively investigated in the previous decades[308-310]. However, the development of the MgO-SiO_2 binder system is relatively new and has only been investigated recently. Zhang et al. [170] developed a low pH cement system for waste encapsulation using a light burned periclase (magnesium oxide, MgO) and silica fume. Wei et al.[165] investigated pastes mixed with magnesia and micro-silica at different ratios and temperatures, with the main hydration products being brucite (magnesium hydroxide, $Mg(OH)_2$) and a magnesium-silicate-hydrate (M-S-H) gel. Jin and Al-Tabbaa [211, 311] studied the formation of amorphous M-S-H at room temperature which was confirmed by various techniques including Fourier-Transform

Infrared Spectroscopy (FTIR), X-Ray Diffraction (XRD), Thermalgravimetric Analysis (TGA) and microstructure analysis.

This chapter focus on the binder system that is derived from the ultramafic minerals, namely the olivine and serpentine used in this project. Olivine was the primary source of the magnesia (MgO) while serpentine provided reactive silica (SiO_2). The property of the MgO-SiO_2 binder system prepared by mixing the recovered MgO and silica fume was investigated, as well as with recovered silica. The recovered MgO was also mixed with water to study its property.

7.2 Mixing design

The commercial MgO (noted as C-MgO) was provided by Calix Ltd, and the particle size distribution is shown in Chapter 3. The recovered MgO (noted as R-MgO in this case), was obtained from the calcination of the magnesium acetate at the temperature of 500 °C, as detailed in Chapter 5.

The recovered silica (noted as RS) was recovered after the acid leaching of serpentine, which was demonstrated in Chapter 5. As a silica source comparison to other Mg-silica research, silica fume (SF) was used.

The chemical composition of these materials is summarised in Table 7-1. In order to study their cementitious properties, the two MgO sources were mixed with the two silica sources, resulting in a total of 4 mixes, as shown in Table 7-2.

Table 7-1. Chemical composition of the raw materials

(wt %)	MgO	SiO_2	Fe_2O_3	CaO	Al_2O_3	Na_2O	K_2O	LOI	Total

Commercial MgO	71.67	11.36	0.33	4.06	0.57	0.13	0.13	11.67	99.92
Recovered MgO	52.1	27.9	8.33	1.18	0.03	0.05	0.03	8.23	97.85
Silica fume	3.28	88.18	1.39	0.93	0.62	0.85	2.67	1.66	99.58
Recovered silica	29.5	50.8	4.69	0.11	0.91	0.04	0.01	13.45	99.51

Table 7-2. The mixing ratio of the magnesia with silica for strength test

Binder Type		**Mixing ratio (wt %)**					
		C-MgO	R-MgO	Silica Fume	Recovered silica	Quartz	D.I. water
MgO +SiO_2 +H_2O	CMSF	60	-	40	-	100	45
	RMSF	-	60	40	-	100	45
	CMRS	60	-	-	40	100	45
	RMRS	-	60	-	40	100	45
MgO +H_2O	CMDW	100	-	-	-	100	45
	RMDW	-	100	-	-	100	45

For the hydration samples used for heat calorimeter, TG and SEM tests, the Mg: Si weight ratio was 60%: 40% while the water to binder ratio was held constant at 0.45. Sand was added to prepare the mortar samples for strength test at the ratio of 1:1 (sand: binder). The methods details and the strength test for 3, 7 and 28 days are stated Chapter 3.

The mortar samples were cured in ambient conditions (temperature=20 ± 2°C, relative humidity= 50 ± 10%). The details of the compression test, hydration heat evolution and the thermogravimetric analysis are stated in Chapter 3. The microstructure tests, such as X-ray diffraction and scanning electron microscopy, were carried out as per described in section 2.13 and 2.16 in Chapter 3, respectively.

7.3 MgO + SiO_2 + H_2O binder system

7.3.1 Compressive strength

The magnesia from the commercial and recovery process were mixed with the silica from different sources: an industrial by-product (silica fume) and the silica recovered from serpentine. Figure 7-1 shows the compressive strength data of the samples at different ages.

The sample mixed with silica fume (SF) and commercial magnesia (CM), noted as CMSF, had consistently lower strength over the time compared to the recovered magnesia (RM) from olivine, noted as RMSF. The strength of CMSF at three days was 12.6MPa, and it increased to 15.6MPa at 7 days, with only a minor additional increase from 7 days to 28 days, reaching 17.5MPa. But for the RMSF samples, the strength data at 7 days was doubled compared to its counterpart and reached close to 40MPa at 28 days.

The strength developments of the recovered silica (RS) mixed with commercial and recovered magnesia are also shown in Figure 7-1. The mixture noted as RMRS, which contained the recovered magnesia and recovered silica, had a consistently higher strength compared to the CMRS. The early strength at 3 days of both samples was below 10MPa, yet the strength for RMRS increased to 24MPa compared to 9MPa (CMRS) at 7 days. Nevertheless, both samples showed little strength development from 7 days to 28 days.

Overall, the sample with recovered magnesia (RMSF and RMRS) had a higher compressive strength compared to that of commercial magnesia regardless of their silica source. This indicates that the magnesia source was the dominant factor that influenced strength development. The samples mixed with silica fume demonstrated constant higher strengths compared to the mixes with recovered silica. This suggests higher silica reactivity of the silica fume than the recovered silica, which is in agreement with the results presented in Chapter 5 for the Portland cement system.

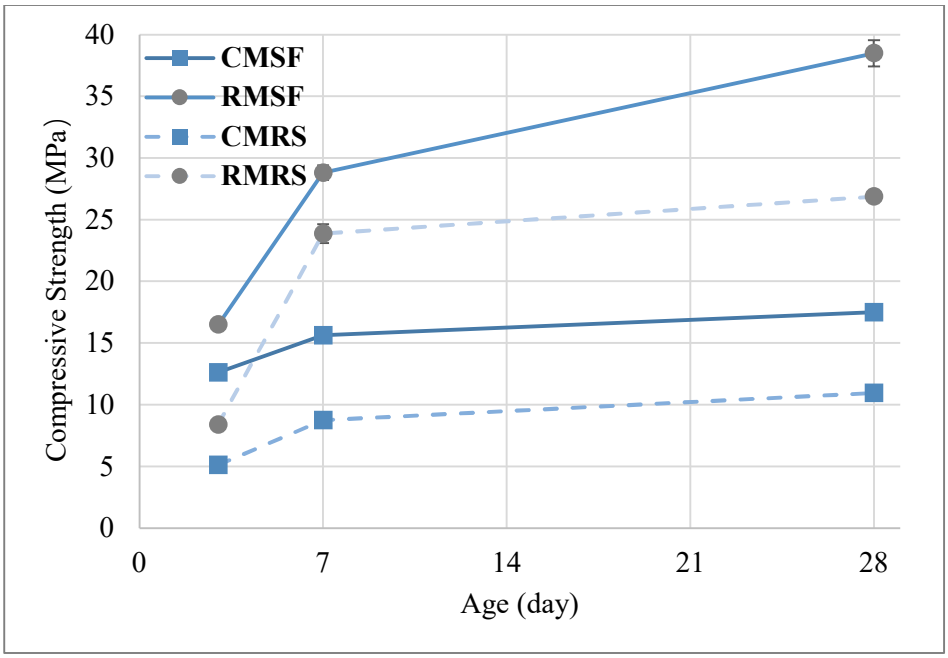

Figure 7-1. Strength development of the samples mixed from different magnesia and silica sources.

In terms of the strength development from 3 to 7 days, samples mixed with commercial MgO (CMSF and CMRS) both demonstrated a limited development rate. The high early strength can be attributed to the significant reactivity of the commercial MgO. Additional strength development from 7 to 28 days was also not significant. This agrees with Tran's [312] research on the effect of different curing conditions on MgO-SiO_2-H_2O binder systems. Samples cured in ambient conditions (50% RH, 20 °C) experienced insufficient water for continued hydration due to the water evaporation and drying. This led to limited strength development after 7 days. It was proposed that water curing is essential for M-S-H binder, like Portland cement. An explanation for the variations in strength between the commercial and recovered magnesia is presented in the following sections.

7.3.2 **Reaction products**

The TG curves shown in Figure 7-2 indicate the amount of hydration products in the samples at 28 days.

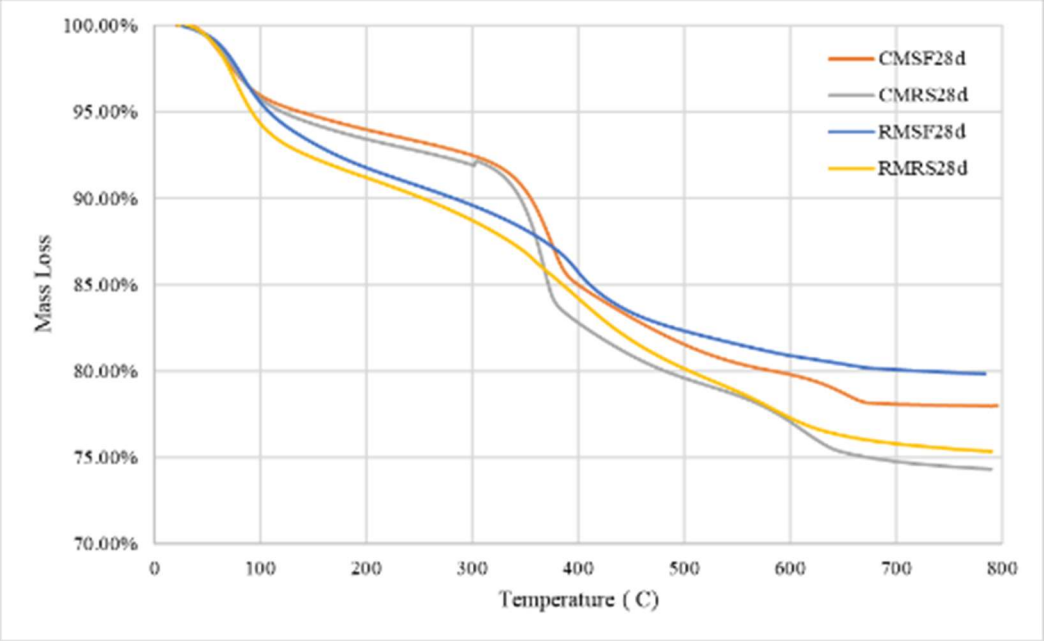

Figure 7-2. The TG curves of different MgO + SiO_2 samples at the age of 28 days

There are three significant mass changes in the profile and they align with previous studies on M-S-H products[167, 283]:

- From ambient to 105˚C: caused by the evaporation of the free water in the samples;
- 105 to 350˚C: mass change can be attributed to the decomposition of magnesium silicate hydrate (M-S-H).
- 350-550˚C: this change was due to the decomposition of the magnesium hydroxide.

The free water content of these samples was quite similar due to the same water to binder ratio and curing the ambient condition. However, the mass change at the temperature range from 105˚C to 350 ˚C began to show noticeable differences. The sample mixed with recovered magnesia (RMSF and RMRS) demonstrated more significant mass loss than their counterparts (CMSF and CMRS), which indicates a higher percentage of M-S-H was formed in the sample with recovered magnesia regardless of silica source. Combined with the strength results, it shows that the higher M-S-H content may lead to higher strength. This finding agrees well previous studies[170, 313] on the formation of M-S-H contributes higher than brucite to the strength development.

For the mass loss due to the decomposition of magnesium hydroxide around 400˚C, samples mixed with commercial MgO (CMSF and CMRS) showed higher mass loss due to more considerable amount of formed $Mg(OH)_2$. The $Mg(OH)_2$ in the commercial samples did not undergo a further reaction to M-S-H, and it was consistent with the reduced strength compared to the recovered magnesia samples.

For the samples mixed with different silica source, the difference of the mass loss is not apparent. However, the sample mixed with recovered silica (CMRS and RMRS) experienced a slightly higher mass loss around 400°C. This can be attributed to less silica reactivity of the recovered silica compared to the silica fume, so less consumption of the MgO and more $Mg(OH)_2$ residual was observed.

7.3.3 Microstructure

The microscopy of the mixtures at different ages is shown in Figure 7-3 (3 days) and Figure 7-4 (28 days) respectively.

Figure 7-3(a) and (b) compare the presence of silica fume particles in CMSF and RMSF. It can be seen that the silica particle is covered by some reaction products in the RMSF samples. When magnified the square areas (Figure 7-3(c) and (d)), the difference became more apparent. According to its appearance, the component in (c) is mainly magnesium hydroxide crystals (brucite, $Mg(OH)_2$), but the products in (d) show distinctive features more typical of M-S-H.

By comparing the mixtures after 28 days (shown in Figure 7-4), the amount of hydration products found on the surface of the spherical silica fume particles increased, particularly for the RMSF samples: the layer thickness (shown in Figure 7-4b) is almost doubled compared to 3 days (Figure 7-3b). However, the microscopy of the magnified area (Figure 7-4c and d) did not show any significant changes in structure with time except thickness.

The microstructure images of the sample mixed with commercial MgO source (Figure 7-4 (c) and (e)) showed more evidence of brucite hexagons while the sample with recovered MgO source (Figure 7-4 (d) and (f)) had more presence of M-S-H gel. This was in accordance with the TGA and strength results.

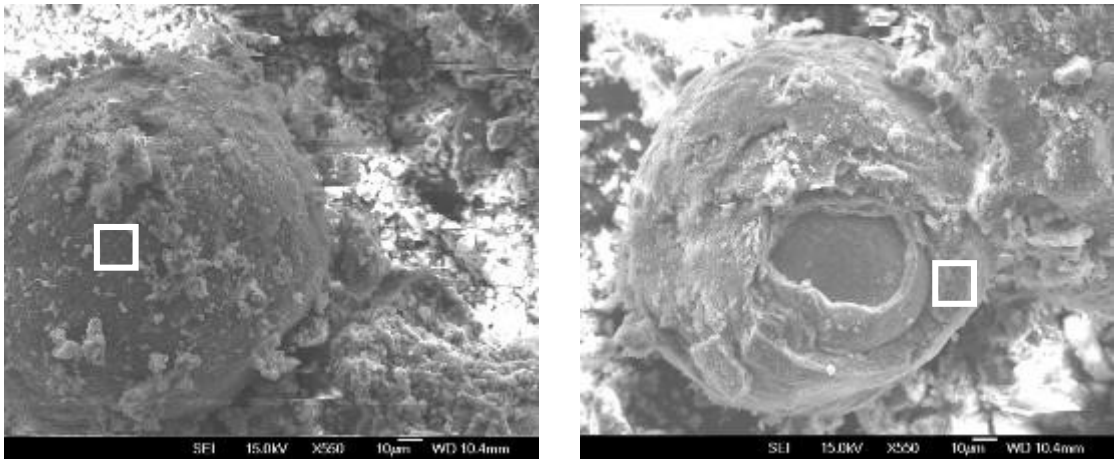

(a). CMSF-3d (500x)

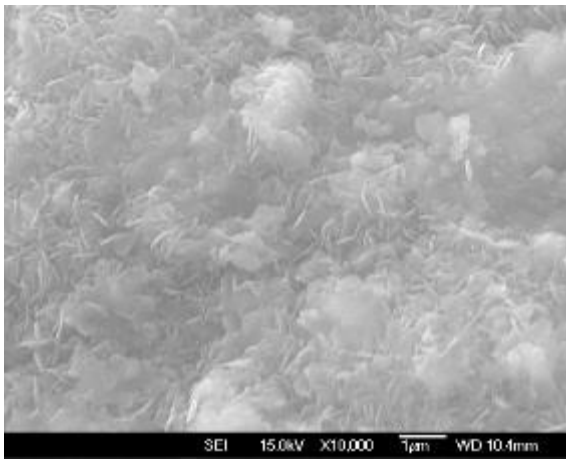

(b). RMSF-3d (500x)

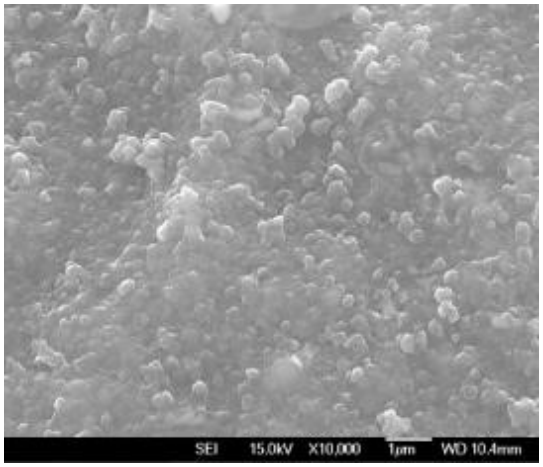

(c). CMSF-3d (10,000x)

(d). RMSF-3d (10,000x)

Figure 7-3. The microscopy of the mixture of MgO and SiO_2 at 3 days

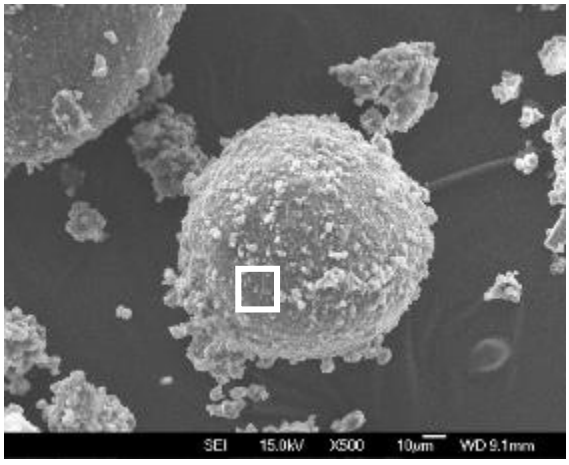

(a). CMSF-28d (500x)

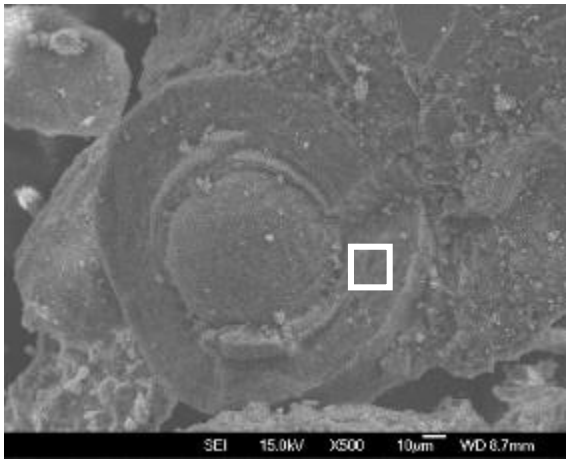

(b). RMSF-28d (500x)

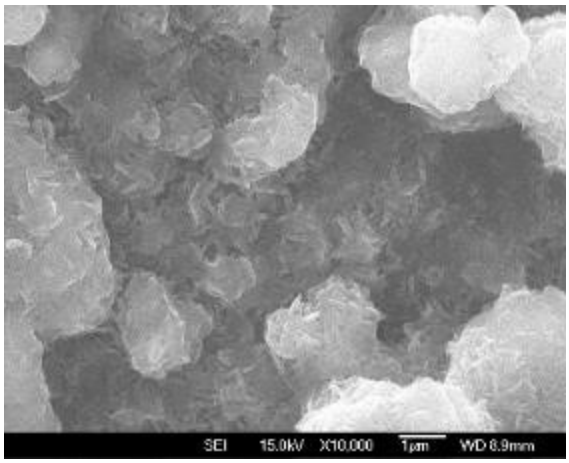

(c). CMSF-28d (10,000x)

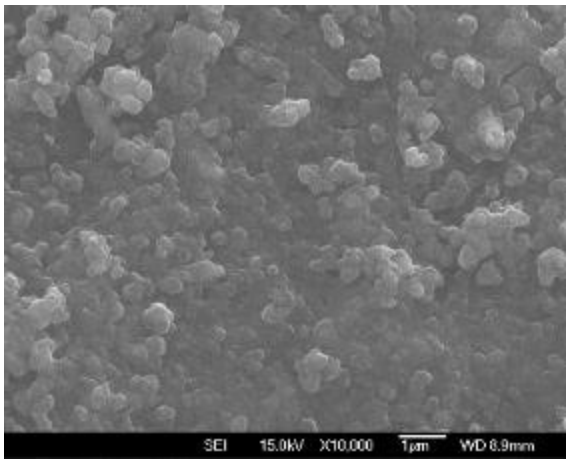

(d). RMSF-28d (10,000x)

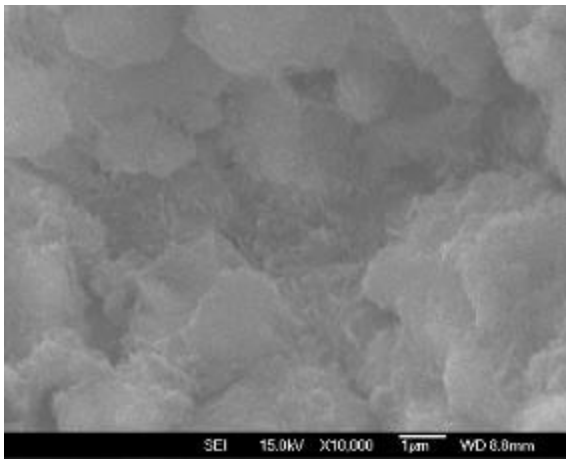

(e). CMRS-28d (10,000x)

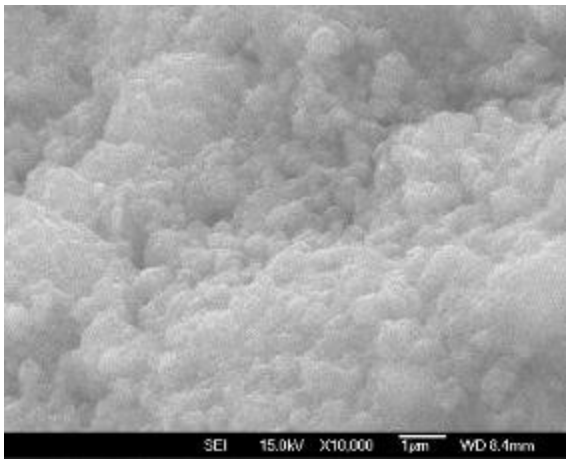

(f). RMRS-28d (10,000x)

Figure 7-4. The microscopy of the mixture of MgO and SiO_2 at 28 days

7.3.4 Comparison of the recovered silica with silica fume

The commercial MgO was mixed with recovered silica and silica fume. As compared in Figure 7-1, the strength mixed with silica fume (CMSF) was higher than it with recovered silica (CMRS). Combined with the TG results obtained from Figure 7-2, the production of M-S-H demonstrated the same trend.

This shows that in the MgO+SiO_2 system, the recovered silica is not as reactive as the silica fume. This is in accordance with the results presented in Chapter 5. It is interesting

to note that the even from the chemical composition analysis suggesting that there was 29.50% of MgO in the recovered silica, however, this MgO is not in an active form while in the presence of magnesium composites, i.e.: serpentine. ($(Mg, Fe)_3Si_2O_5(OH)_4$.)

7.3.5 Comparison of the recovered MgO with commercial MgO

Comparing the commercial MgO (CMSF) with the recovered MgO (RMSF) sample mixed with silica fume, it is clear from Figure 7-1 and Figure 7-2 that the sample mixed with recovered MgO demonstrated much higher compressive strength and substantially higher amount of magnesium silicate hydrates gel.

To characterise the hydration of these two samples, heat evolution during the reaction is presented in Figure 7-5. The heat of hydration released from RMSF reached its peak at 1.5 hours whereas it took CMSF around 7.5 hours to reach its maximum. The total heat generated from the reaction between silica fume and the recovered magnesia was also higher than the reaction with commercial magnesia.

The greater reactivity of RMSF compared to CMSF may be caused by two reasons:

a). since the recovered magnesia was obtained after the grinding process of the calcined recovered magnesium acetate, the R-MgO has a smaller particle size (9.7 μm) thus higher surface area compared to the commercial magnesia (17.2 μm);

b). The R-MgO also contained some reactive silica, composed of very fine amorphous particles. The fine silica remaining in the R-MgO may have accelerated the hydration process.

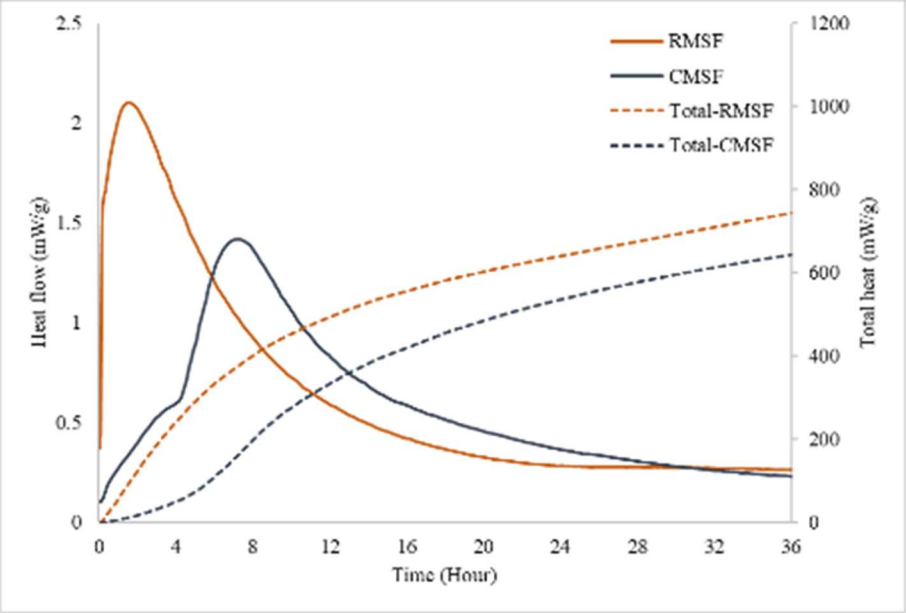

Figure 7-5. Heat flow of different magnesia mixed with silica fume

In the system consisting of $MgO+SiO_2+H_2O$, the formation of the M-S-H gel can be summarised from previous studies[165, 177-179] as below. When the magnesium oxide contacts water, it hydrates to form brucite, which leads to an increase of the pH value and release of heat in the first few hours. The brucite reacts with the dissolved silica to produce the M-S-H gel, and according to the pH and heat evolution, this reaction usually takes place in 3 days. The formation of the M-S-H gel continued until either reagent was consumed entirely. Depending on the variation of the Mg/Si of the raw material, the hydration products are different.

Figure 7-6 further shows the mass loss of the two different samples at different ages (3, 7, 28 and 90 days). As stated earlier, the mass loss between 105~350 °C was associated with the dehydration of M-S-H while 350 ~ 550 °C change was attributed to the decomposition of magnesium hydroxide or carbonates. From Figure 7-6(a), the mass loss

in this temperature range of RMSF was consistently higher than CMSF. This indicates a higher amount of M-S-H was produced in the recovered MgO samples regardless of age. It was worth noting that at the age of 3 days, the RMSF demonstrated a 14.89% mass loss compared to 0.5% of CMSF. This is a sign that shows the high reaction rate of the recovered MgO and silica fume. However, the mass loss kept stable after the age of 7 days suggested no further reaction. On the contrary, the CMSF showed a significant increase from 3 days to 7 days and a gradual increase until 90 days indicating further reaction.

Figure 7-6(b) presents the amount of residual magnesium hydroxide in the sample. Similar to the M-S-H formation, the RMSF sample demonstrated a high amount of magnesium hydroxide at very early ages and kept constant for the later ages. This suggests the recovered MgO is active in producing both M-S-H and $Mg(OH)_2$ at early ages. Unlike the RMSF, the CMSF showed a different pattern. The mass loss increased from 1.07% at 3 days till 12.32% at 28 days before it showed a downward trend to 90 days. This indicates the formation of $Mg(OH)_2$ increased with time but was consumed at a later age. Due to the increase of the M-S-H content shown in Figure 7-6 (a), the produced $Mg(OH)_2$ may have reacted with silica, forming M-S-H in the long term.

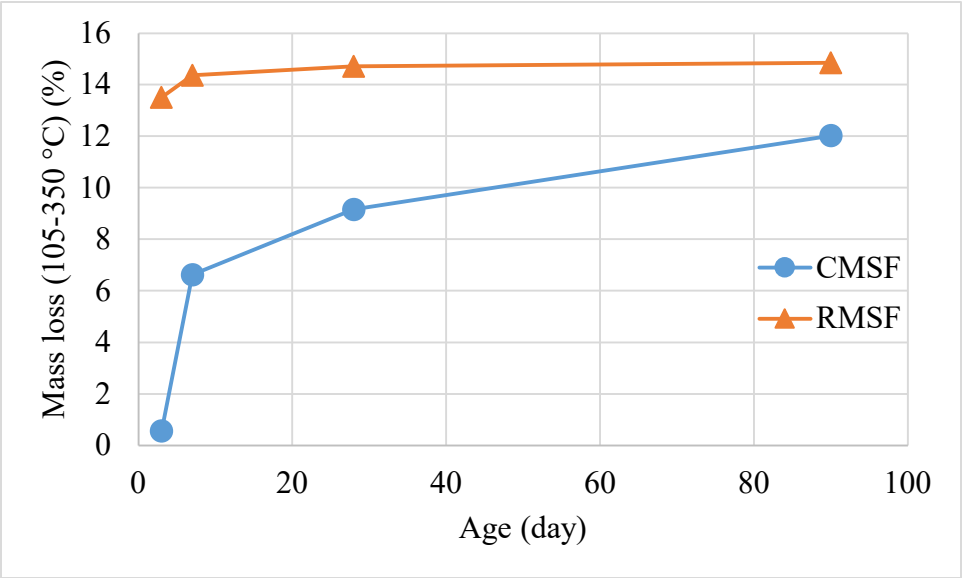

(a). mass loss between 105~300 °C

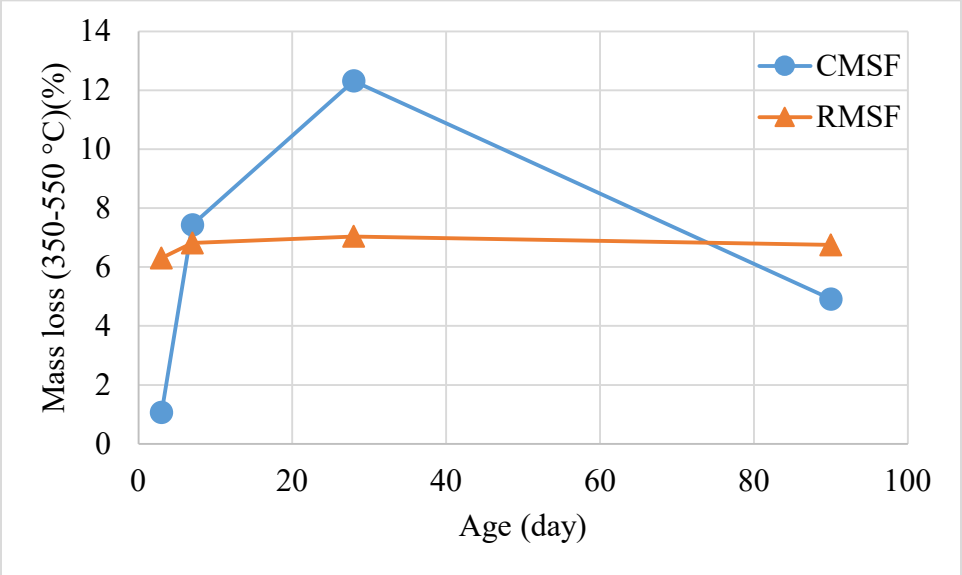

(b). mass loss between 300~500 °C

Figure 7-6. The quantified mass loss of CMSF and RMSF at different ages.

Figure 7-7 reveals the XRD pattern of the CMSF and the RMSF sample at the age of 28 days. The XRD result of the CMSF demonstrates a large amount of magnesium hydroxide (brucite) with the co-existence of M-S-H gel. For the RMSF, a very limited amount of brucite was observed while M-S-H was the dominating phase at this age.

It is not easy to confirm the presence of M-S-H in the sample as the X-ray diffraction was hampered by the large amorphous background and other crystalline phases in the mixture. According to the literature[167, 170], the broad peak at 10~13°, 20~30°, 35~39°, and 58~62° can be assigned to M-S-H gel.

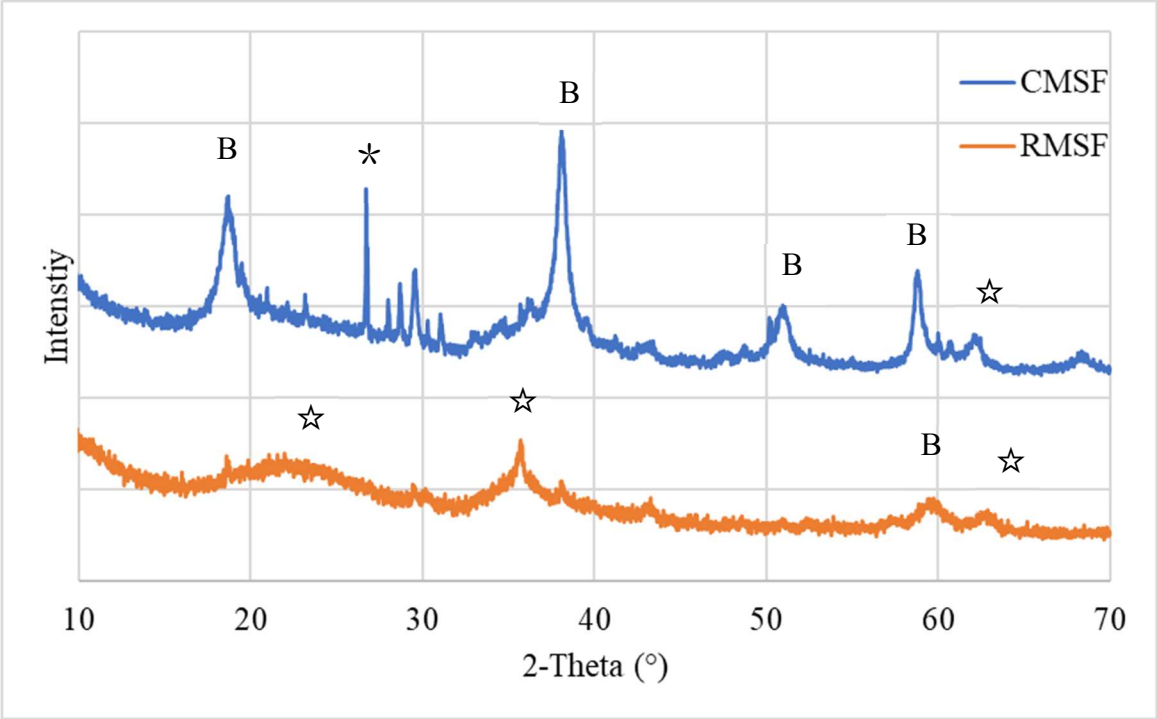

Figure 7-7. XRD results of the CMSF and RMSF at the age of 28 days.

（B：Brucite ⋆: Quartz ☆: M-S-H gel）

Figure 7-8 shows the XRD results of the RMSF sample at 3, 7 and 28 days. There were no noticeable phase nor intensity change with the development of curing, except for

the decreased peak intensity for the MgO (Periclase) with time. This was consistent with the TG analysis: the hydration products were produced in early ages and did not change significantly with age.

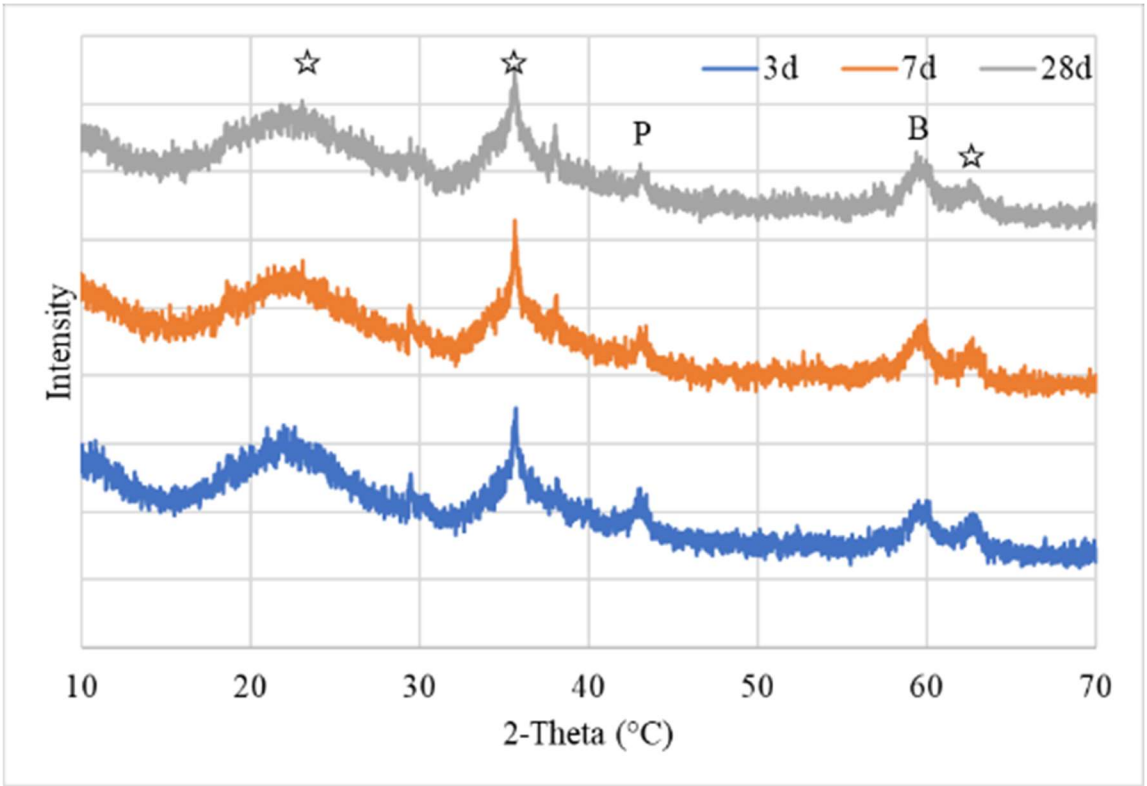

Figure 7-8. XRD results of the RMSF at different ages.

（☆: M-S-H gel; P: Periclase; B: Brucite）

Combining the hydration heat, TG, XRF and XRD results, it is evident that the recovered MgO did contain some silica and these silicas are reactive enough to participate/ accelerate the formation of the M-S-H, thus leading to the strength improvement.

7.4 Recovered MgO + H_2O binder system

It was evident in the previous section that the sample mixed with recovered magnesia consistently demonstrated higher strength and greater M-S-H content regardless of the source of silica (silica fume or recovered silica), compared to those samples mixed with commercial magnesia. This section investigated the properties of the recovered magnesia reaction products by examining the reaction of MgO source with deionised water, without any addition of the silica.

7.4.1 Compressive strength

The compressive strength of the sample mixed from different sources of magnesia and water at different ages is compared in Figure 7-9. The C-MgO samples (CMDW) had the lowest strength at all ages around 15 MPa, while the RMDW samples reached 55.3 MPa at 28 days. The primary hydration produce from CMDW is brucite (magnesium hydroxide), and its contribution to strength was in the same range as Liska' study[314]. Note that the carbonation process can transform the brucite into nesquehonite (hydrated magnesium carbonate) which has higher strength. However, it also pointed out that under ambient environment, the natural carbonation of the magnesia cement was minimal, so does do not have a significant influence on the mechanical properties. Therefore, this provided clear evidence that the brucite is providing the strength; the M-S-H was formed in samples with recovered MgO and significantly increased the strength.

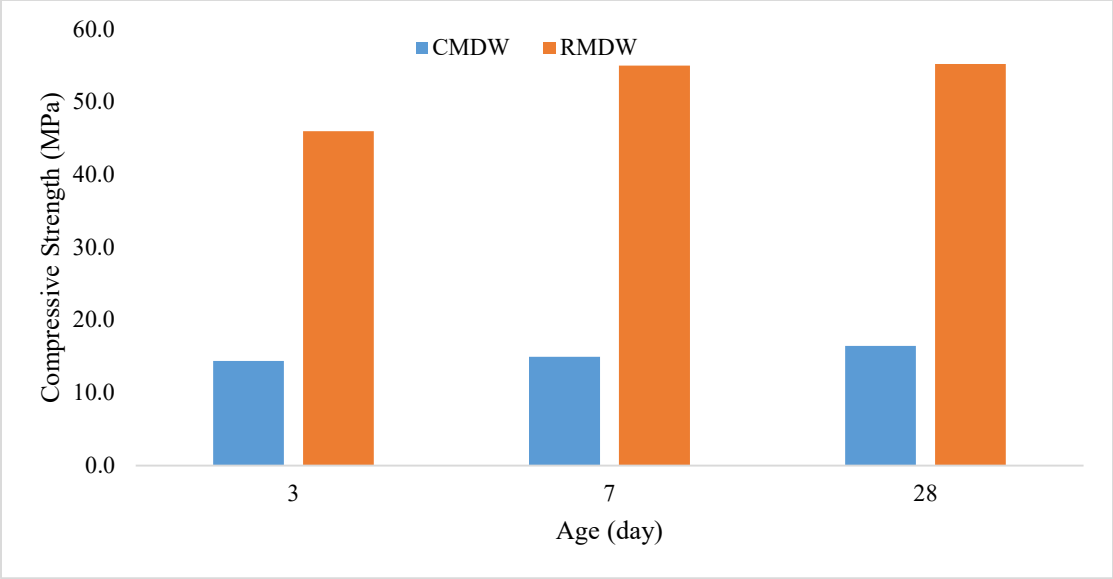

Figure 7-9. Strength comparison of the sample with different MgO sources

7.4.2 Reaction products

The microstructure of the hydration products, as shown in Figure 7-10, shows the difference between the two samples at the age of 28 days. The CMDW showed the existence of hexagon shape brucite, while in RMDW, M-S-H was observed.

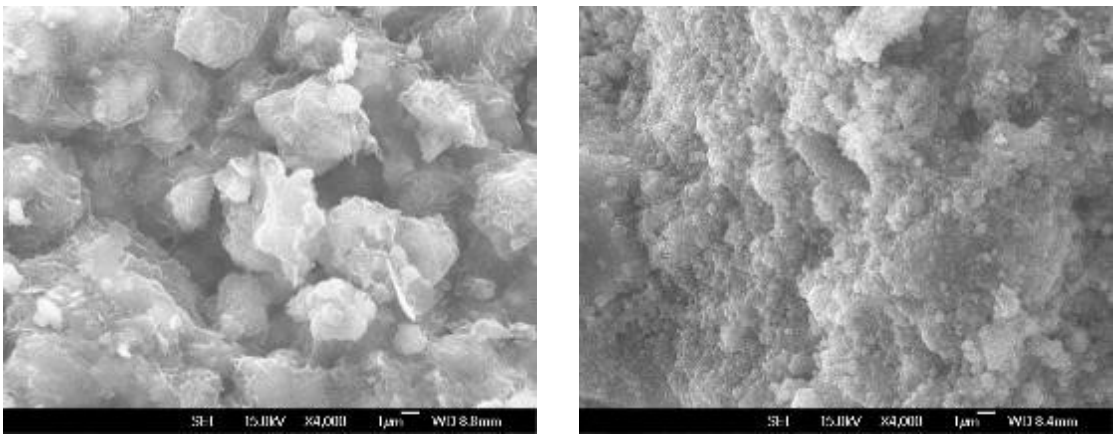

(a). CMDW *(b). RMDW*

Figure 7-10. The microscopy of the magnesia mixture at the age of 28 days.

As noted in Table 7-1, the recovered magnesia contained not only 52.1% magnesia (MgO) but also a considerable amount of silica (SiO_2, 27.9%). The silica was dissolved during the acid digestion process[315, 316]. There are different forms of the dissolved silica[296, 317, 318] and the least stable form of silica, which is the amorphous silica shows the highest solubility compared the most stable form, quartz with little reactivity[296]. In this study, at least part of this silica was in a reactive form and reacted with MgO to produce M-S-H, which has led to the strength increase.

Figure 7-11 compares the TGA differences between commercial MgO (CMDW) and recovered MgO (RMDW) reacted with di-ionised water. At the age of both 3 and 28 days, there was a significant mass loss around 400 °C in the CMDW samples. This mass loss is associated with the decomposition of $Mg(OH)_2$. It is also clear that there was very little change in mass for CMDW between 105 to 350 °C, which is associated with M-S-H. While the commercial magnesia contained approximately 11% silica, it did not appear to participate in any further hydration to form M-S-H. The RMDW samples at 3 and 28 days show a substantial mass loss between 105 to 350 °C, which indicates the presence of M-S-H, despite no additional silica being added. The silica present in the recovered MgO, which was approximately 28% as shown in Table 7-1, is capable of reacting with the brucite. This reaction has produced appreciable quantities of M-S-H. The formation of M-S-H shown in the previous section is, therefore, a product of both the mixed silica and also the silica contained in the recovered magnesia.

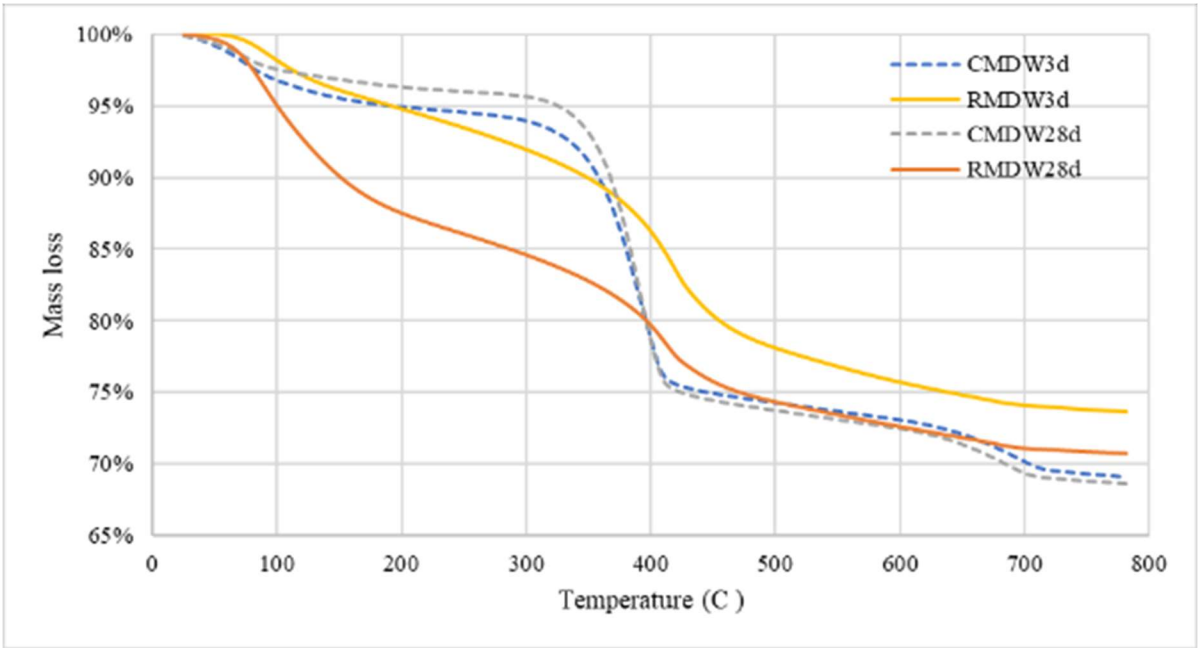

Figure 7-11. Comparison of the TG curves of different MgO sources with water

7.4.3 Comparison of the recovered MgO with water and with silica fume.

The previous results demonstrated that the recovered MgO had the ability to react with water without the addition of silica and to produce M-S-H gel. Here, the difference of the addition of silica was further discussed.

Figure 7-12 shows the heat generated from the reaction of recovered MgO with de-ionised water and compared it with silica fume addition (identical with previous data in Figure 7-5). It is evident that the recovered MgO mixed with water (RMDW) released considerably more heat compared to when it was mixed with silica fume (RMSF). From Chapter 5, it is known that the pozzolanic reactivity of silica fume mainly occurred at later ages. Therefore, any added silica fume to recovered MgO actually plays an inert role and

has diluted the reactant concentration. Consequently, it has generated a lower hydration heat.

It should be noted that there was only one peak during the early days. Considering the TG and XRD results of the sample at the age of 3 days, they already confirmed the formation of M-S-H. Therefore, the hydration peak in the first few hours suggested the reaction of both the brucite formation and M-S-H production.

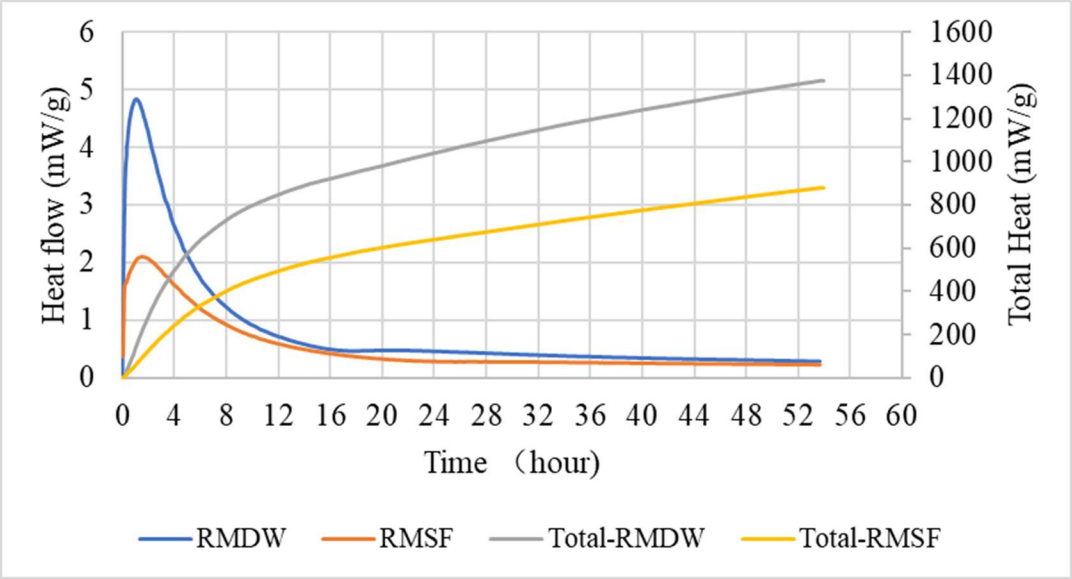

Figure 7-12. Heat evolution of the reactions with R-MgO with water and silica fume

Figure 7-13 compares the results from RMSF and RMDW at the age of 28 days. It was not surprising to see that without any addition of silica source, the RMDW showed very similar mineral phase with RMSM, especially the formation of M-S-H. This suggests it is feasible to use the recovered MgO along with water to produce cementitious materials without the need for the external silica source. This is a very interesting point as the sources of silica are, in fact, limited and typically expensive.

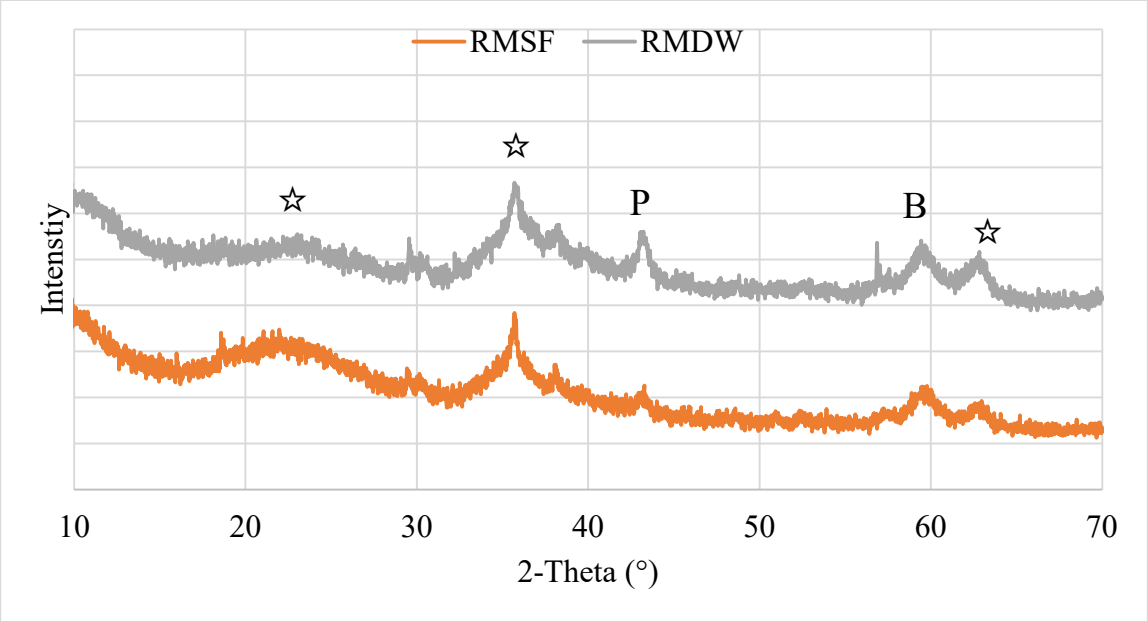

Figure 7-13. XRD results of the RMSF and RMDW at the age of 28 days.

（☆: M-S-H gel; P: Periclase; B: Brucite）

7.5 Summary and conclusion

This chapter has investigated the properties of the products recovered from the ultramafic minerals, including the recovered magnesia from olivine, and the recovered silica from serpentine.

The recovered magnesium oxide (R-MgO) demonstrated constant higher strength than commercial magnesium oxide in the MgO-SiO_2-H_2O binder system. This can be attributed to the higher amount of magnesium silicate hydrates gel formed in the sample, according to the evidence from various techniques. The formation of the M-S-H of recovered MgO with water can be attributed to the presence of SiO_2 in the recovered product (27.9%). This silica is in a partly active amorphous form. Future study can further

investigate the hydration reaction of the recovered magnesia since it contains both reactive magnesium oxide and fine particle silica source.

However, the recovered silica did not perform any favourable silica reactivity with either commercial or recovered MgO. The strength of the recovered silica mixtures was consistently lower than the specimens using silica fume. This agrees well with the previous chapter.

Overall, this study demonstrated the proof of concept of producing a cementitious binder material from the ultramafic minerals.

8 Investigation on the cementitious properties of a binder derived from the reaction of MgO with waste acid

8.1 Introduction

The investigation on the extraction of reactive silica from serpentine was discussed in Chapter 5. In addition to the solid phase (recovered silica), another product from the serpentine leaching was waste acid. In this chapter, the proof of concept of using waste acid to produce a cementitious material is proposed and investigated.

In chemical manufacture, hydrochloric acid and sulphuric acid represent the main acid by-products. In terms of waste acid management, neutralisation and conversion to inert solids as methods of disposal are of limited applicability[319]. By far, the most commonly used commercial process for waste acid management is to use lime(CaO) neutralisation[320, 321]. Using cement for heavy metal immobilisation has also been applied in recent decades[322-324]. Cement based stabilisation techniques improve the handling characteristics and lower the leaching rates of wastes by a combination of solidification and stabilisation.

However, for traditional Portland cement, the acid environment leads to the dissolution and leaching of calcium hydroxide and the calcium silicate hydrates, the major hydration products of the cement. As a consequence of this acid attack, capillary porosity would increase with an accompanying strength loss of the cement products[325, 326]. For instance, Chandra[327] investigated the hydrochloric acid attack on cement mortar and demonstrated that the clinker materials (mostly calcium) of Portland cement dissolved and formed soluble salts. Therefore, using conventional Portland cement is not a practical way to stabilise the acidic waste.

Nevertheless, it is worthwhile to note that by reacting an acid and a base, acid-base reaction cements can be formed. The salt-like products of the reaction, generally a hydrogel, have cementitious properties[328, 329]. In 1993, Wilson[330] described several types of acid-base cements, such as phosphate bonded cements and oxysalt bonded cements. Magnesium is an essential reactant for many kinds of binders, including magnesium phosphate cement (MPC), magnesium oxychloride (MOC) cement, and magnesium oxysulfide(MOS) cement.

The acid-base reaction cements provide the possibility of utilising waste acid to form stabilisation compounds. In this study, the waste acid is mainly consisting of hydrochloric acid and metal ions. Thus, the magnesium oxychloride cement system was selected for further investigation.

In this chapter, the reaction products of mixing waste hydrochloric acid with magnesium oxide are investigated. Reaction kinetics, hydration products and the mechanical properties of the binder system are reported.

8.2 Mixing design

The acid digestion of the serpentine process was described in Chapter 5. The permeate from the filtration process was collected for analysis and used in this investigation.

The ion concentration in the acid sample was quantified using the Agilent 7500 CX Inductively Coupled Plasma Mass Spectrometry (ICP-MS). The permeate was placed in an oven at 105 °C to evaporate the excess liquid. The residue was collected and analysed by XRD, as described in Chapter 3.

In order to compare the effect of waste acid, several solutions were used as a reference as they both contains chloride: a). the de-ionised water; b). seawater; c). pure magnesium chloride solution; and d). fresh hydrochloric acid.

The seawater was collected in Lyttleton Harbour in Christchurch, New Zealand. The addition of the same amount of seawater is to compare its influence with D.I water. The magnesium chloride was chemical grade while the fresh hydrochloric acid was unreacted acid at the concentration at 2 mol/L.

MgO from a commercial source was mixed with these solutions and the properties of the mixtures were compared. The pastes were prepared at a binder to water ratio 0.4. Waste acid was used as a replacement for water in the samples as shown in Table 8-1. In the $MgCl_2$ solution, $MgCl_2$ was added based on the calculation at the equivalent amount of $MgCl_2$ produced from the reaction of HCl and MgO. For example, when 500 g of MgO was added to 200 ml of 2 mol/L HCl, 19.02 g $MgCl_2$ was produced. The $MgCl_2$ was added to the water first to prepare the solution before mixing with MgO.

Table 8-1. Mixing proportion of the MgO-$MgCl_2$-H_2O system

Sample code	MgO	D.I. water	Seawater	HCl	Waste acid	$MgCl_2$
DW	500 g	200 ml	-	-	-	-
SW	500 g	-	200 ml	-	-	-
HA	500 g	-	-	200 ml	-	-
WA	500 g	-	-	-	200 ml	-
MC	500 g	200 ml	-	-	-	19.02 g

The MgO-$MgCl_2$-H_2O paste samples were cured in the environmental chamber under the relative humidity at 50% and 20±2 °C. They were cured to the designated age (3, 7, 28 and 60 days) before the strength and other tests.

Hydration temperature during the cement hydration was monitored using temperature sensors. The methods of measuring the hydration temperature were described in Chapter 3. Microstructure and additional elemental analysis were characterised by Scanning Electron Microscopy (SEM, JEOL IT-300 scanning electron microscope, 15kV) and Energy-dispersive X-ray spectroscopy (EDS, Oxford Aztec system with a 50mm^2 SDD detector).

8.3 Waste acid solution characterization

Among the different solutions, the magnesium chloride ($MgCl_2$) and hydrochloric acid (HCl) solution were prepared and thus have a known composition. The waste acid and seawater samples were collected and analysed by the ICP-MS. The metal ion concentration results are shown in Table 8-2.

Table 8-2. The ion concentrations of waste acid and seawater samples.

	Silicon [Si^{4+}]	Magnesium [Mg^{2+}]	Iron [Fe^{3+}]	Calcium [Ca^{2+}]
Waste acid	57.5 mg/L	996.5 mg/L	128.5 mg/L	62.0 mg/L
Sea water	6.3 mg/L	1274.9 mg/L	0.0 mg/L	511.7 mg/L

The magnesium content in waste acid after leaching is lower than in seawater. The silicon and calcium concentration in seawater were also significantly higher than it in waste acid. However, no iron was detected in seawater while 128.5 mg/L iron in was presented waste acid which resulted in the colour being light brown to yellow.

Table 8-3 compares the pH value of the various solutions. The pH of the unreacted HCl was -0.3 while the waste acid was slightly higher at 0.13. The low pH of waste acid indicates that the acid was in excess and did not completely react with serpentine. Combined with the low Mg^{2+} concentration in the waste acid solution, it is suggested the reaction degree/efficiency of the acid digestion process is relatively low after 24 hours of digestion. The pH of the $MgCl_2$ solution was slightly lower than 7, due to its hydrolysis. The de-ionised water was 7 while seawater was slightly more alkaline.

Table 8-3. The pH value of different solutions used for the MgO mixing

	HCl acid	**Waste acid**	**$MgCl_2$ solution**	**D.I. water**	**Seawater**
pH value	-0.3	0.13	6.7	7.0	8.0

To study the effect of the addition of MgO to the solution pH, 3.2 grams of MgO were added into the 80 ml D.I. water and waste acid respectively. Figure 8-1 shows the pH profile of the waste acid sample and the D.I. water when MgO was added into the solution.

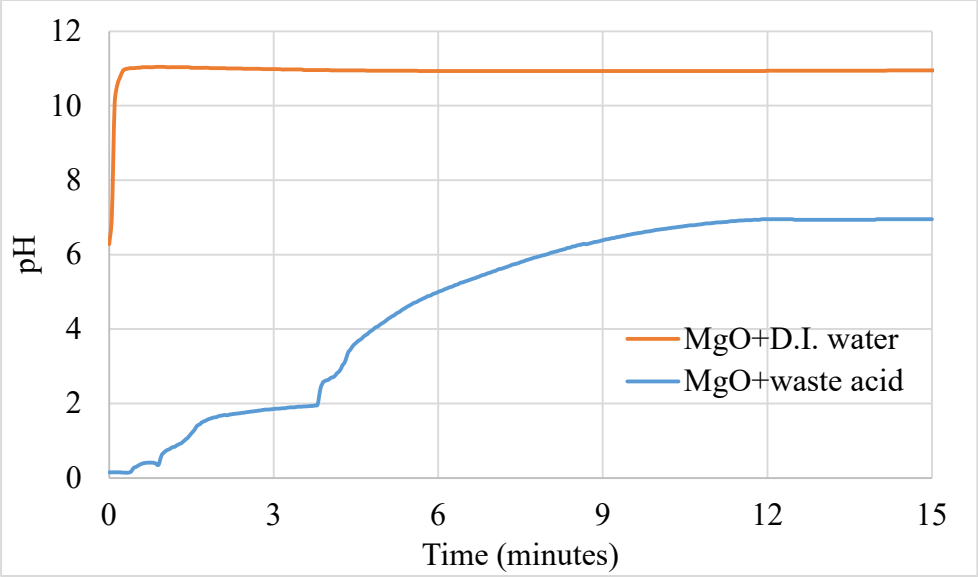

Figure 8-1. The pH profile with the addition of MgO to water and waste acid.

It can be seen from the curve that once mixed with MgO, the pH of the D.I. water increased rapidly in the first few seconds to 11 before stabilising. The waste acid sample, however, showed a relatively slow increase in pH gradually as a result of the reaction shown in Equation 8-1.

$$MgO+2HCl=MgCl_2+H_2O \qquad \textit{Equation 8-1}$$

It suggests that it would only take approximately 8 g of MgO to neutralise the 200 ml waste acid or HCl solution (2 mol/L). Therefore, according to the mixing plan shown in Table 8-1, only 8 g out of 500 g MgO reacted with the waste acid/ HCl and the rest (482 g) with the neutralised solution.

Note that due to the presence of Fe^{3+}, with the increment of pH, it started to precipitate and formed $Fe(OH)_3$ which turned the colour of the solution from yellowish-brown to reddish-brown (Figure 8-2).

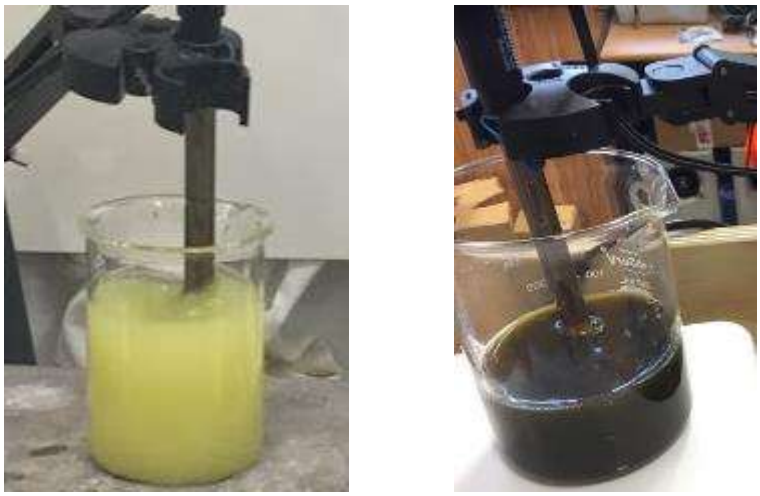

(a). Before the addition of MgO (b). After the addition of MgO

Figure 8-2. Colour change of the waste acid before and after the addition of MgO.

To further investigate the components in the waste acid, the solution was dried in the oven at 105 °C to evaporate the excess water and the residual precipitation was analysed. The XRD spectra of the oven-dried solids from the waste acid are shown in Figure 8-3. The peaks in the XRD pattern confirmed the majority of the solid was bischofite, $MgCl_2 \cdot 6H_2O$. This composition made it feasible for producing a magnesium oxychloride cement (MOC).

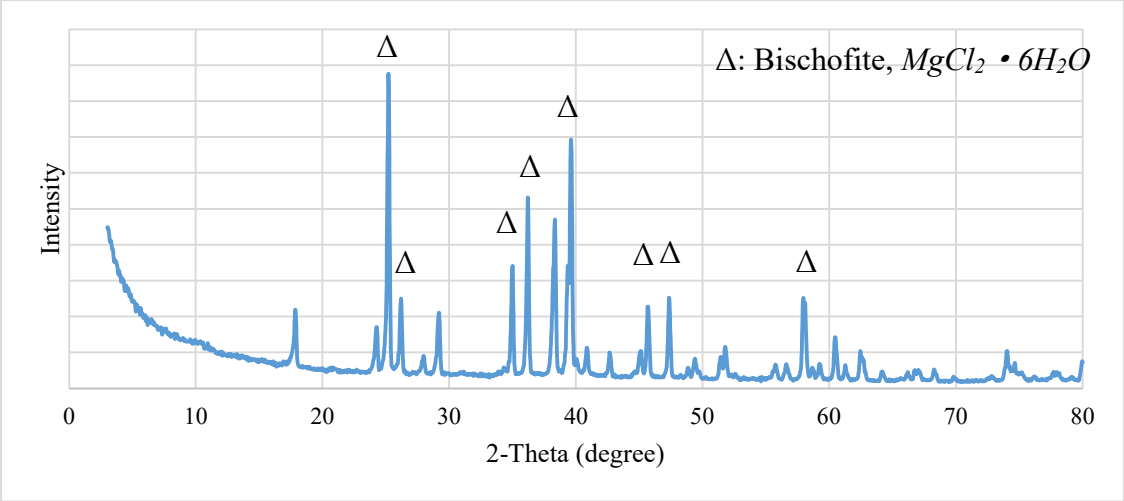

Figure 8-3. XRD results of the precipitates from the waste acid solution

8.4 Hydration temperature profile

When MgO was added to the waste acid solution, it started to hydrolyse or react with the acid. Both reactions were exothermic which led to the temperature increase. Figure 8-4 demonstrates the temperature change during the first 200 minutes when MgO was added to the waste acid or water. The temperature change of the ordinary Portland cement was also recorded as a comparasion.

Both of these curves with waste acid/water started to increase after the MgO addition. Among them, the MgO with the waste acid showed the highest temperature reaching 103 °C in 9 minutes. The mixture of MgO with water generated a similar amount of heat, with its temperature peak at 97 °C in 37 minutes. This suggests the H^+ in waste acid has accelerated the MgO dissolution and the acid-base reaction generates more heat compared to MgO hydration.

Both these mixtures with MgO showed a significantly higher temperature increase compared to the hydration of the ordinary Portland cement. The temperature of the OPC in

the first four hours are quite stable and in fact, depending on its water/cement ratio and cement types, it reaches its temperature peak around 35 ~50 °C around 10 to 16 hours according to previous research[331, 332]. This suggest a higher reaction rate of the MgO-$MgCl_2$-H_2O binder system and higher early strength.

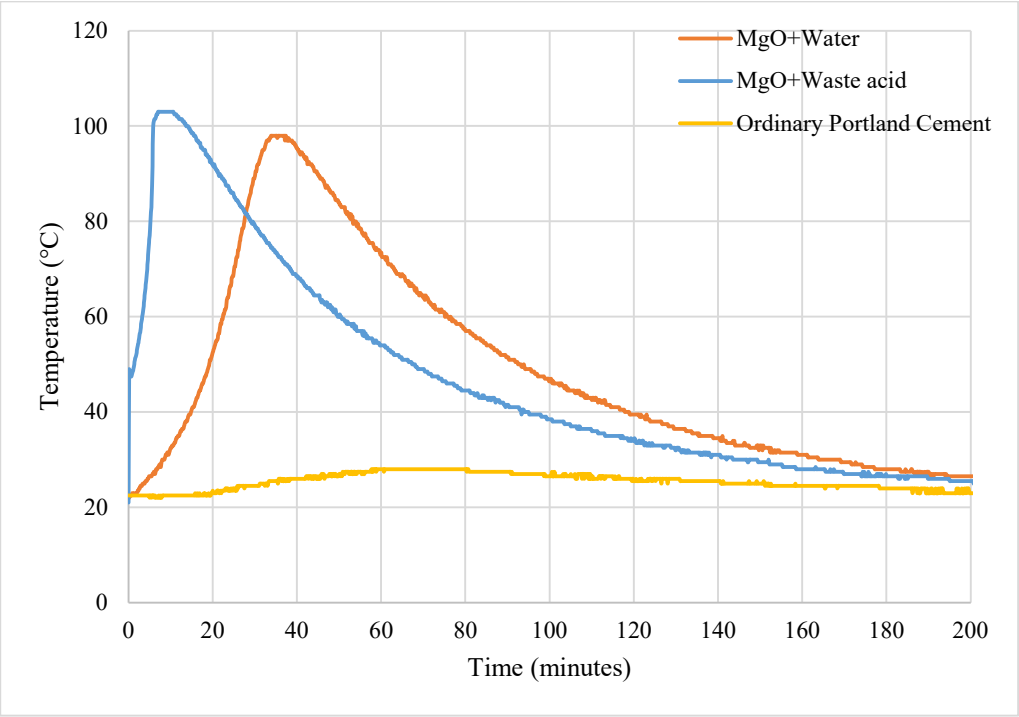

Figure 8-4. The hydration temperature profile of the MgO mixtures with water and waste acid and their comparison with OPC

8.5 Mechanical properties

The compressive strength development of the samples mixed with MgO is provided in Figure 8-5. Overall, the mixture strength increased from MgO mixed with D.I. water (DW), seawater (SW), $MgCl_2$ (MC) and HCl (HA), with the mixture with waste acid (WA) demonstrating the highest strength.

The early age strength at 3 days showed the most significant difference. The compressive strength of the sample mixed with D.I. water was 17 MPa when mixed with seawater and $MgCl_2$ solution showed 28.8 MPa and 31.7 MPa, respectively. For the MgO mixed with acid, the fresh HCl acid had a strength of 38.2 MPa which was more than double that of the mix with water. The waste acid sample had the highest strength of 43.7 MPa.

For the longer-term strength, i.e., at 28 days and 60 days, the sample with de-ionised and seawater had the lowest strength compared to their counterparts. The sample mixed with fresh HCl had the highest 28- and 60-day strengths and was similar to the waste acid samples.

In terms of strength development, DW sample has the greatest increase from 3 days to 60 days at 37%, followed by HA (26%) and MC (19%). The WA sample demonstrated the highest early compressive strength, however, only has a limited strength growth at 3%.

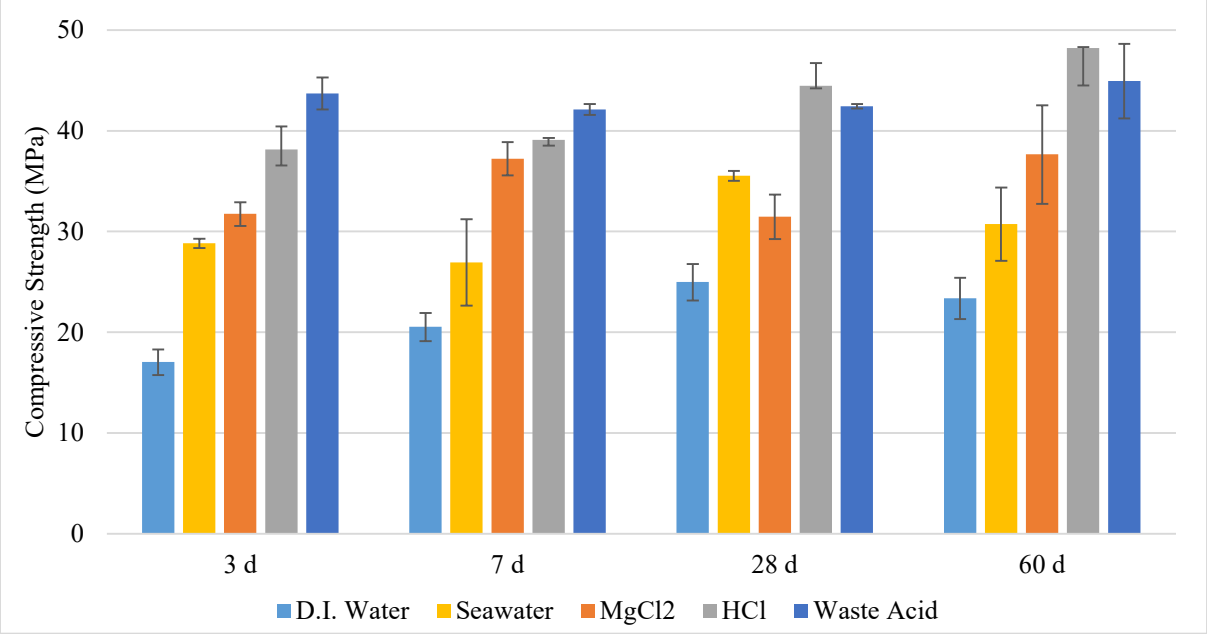

Figure 8-5. The strength development of different solutions mixed with MgO

The strength development may be a result of the hydration reaction and the strength difference between these samples may have a positive relationship with the chloride content of the solution.

For the MgO mixed with D.I water samples, the hydration products are mainly brucite, i.e.: magnesium hydroxide. The brucite hydration particle cannot interlock together to form dense structures which lead to the lowest strength compared to its counterparts. Since the samples were cured in ambient air, CO_2 from the air may react with magnesium hydroxide to produce magnesium carbonates. The carbonation process may provide some additional strength development. According to other studies on reactive magnesia cement, the hydration and carbonation reaction of the system can be simplified and described in the following equations.

$$MgO + H_2O \rightarrow Mg(OH)_2 \qquad \textit{Equation 8-2}$$

$$Mg(OH)_2 + CO_2 + 2H_2O \rightarrow MgCO_3 \bullet 3H_2O \qquad \textit{Equation 8-3}$$

Due to the capability of absorbing atmospheric CO_2 to from stable carbonates, this reactive magnesia cement was proposed as low carbon or carbon negative cement.

A positive relation was observed with the chloride content and the strength of the sample, as illustrated in Figure 8-6. There's obviously no Cl^- in de-ionised water and the Cl^- concentration in seawater was measured at 18.9 g/L. The chloride content in $MgCl_2$ solution, HCl and waste acid sample were in the same range around 71.0 g/L (this value was obtained by calculation). The strengths of the samples over different ages showed the corresponding trend with the increase of chloride content: D.I. water (no chlorine) < seawater (medium chlorine content) < $MgCl_2$, HCl and waste acid sample (high chloride content). The dash trend line of these strength results from different ages all demonstrated a very similar slope expect for the 28 days, while strength axis interception increased with

age. This suggests that the chloride content is the dominate factor for the strength, compared to other ions in the solution (Mg^{2+}, Si^{4+} or Ca^{2+}).

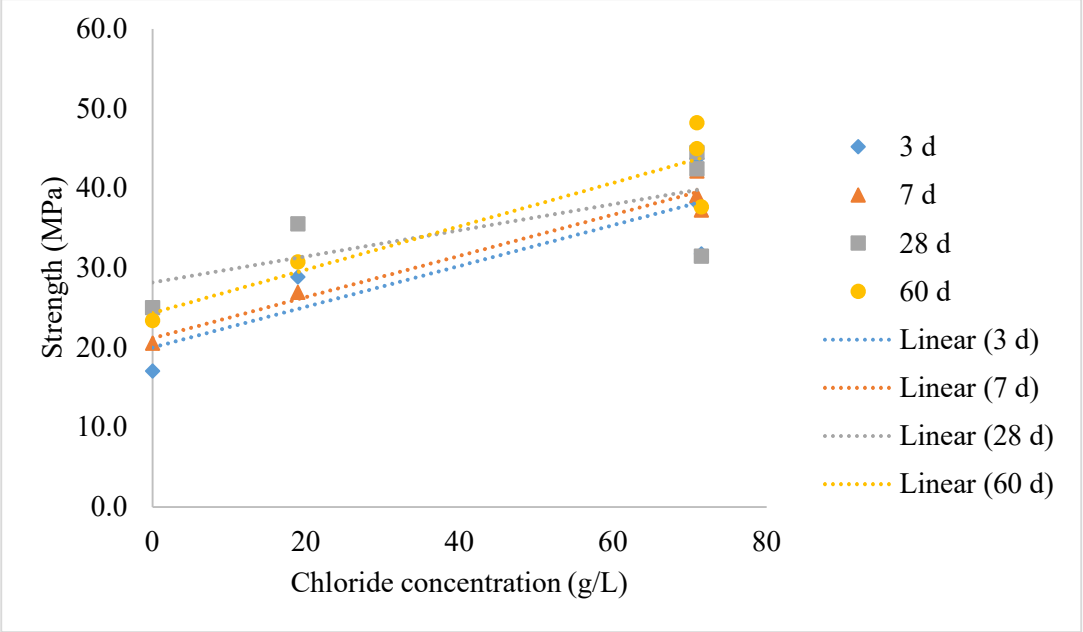

Figure 8-6. The correlation between sample strength and chloride concentration

In the hydration reaction of the Sorel cement ($MgO-MgCl_2-H_2O$) system, the $MgCl_2$ dissolves in water and reacts with MgO rapidly to form gel-like hydration products: $2Mg(OH)_2 \cdot MgCl_2 \cdot 4H_2O$ (phase 2), $3Mg(OH)_2 \cdot MgCl_2 \cdot 8H_2O$(phase 3), $5Mg(OH)_2 \cdot MgCl_2 \cdot 8H_2O$ (phase 5), and $9Mg(OH)_2 \cdot MgCl_2 \cdot 5H_2O$ (phase 9) . The rapid hydration provides the MOC sample with high early strength. For example, Li et al.[182] prepared the MOC sample and achieved 117 MPa at 3 days with the compressive strength further increasing to 150 MPa after 7 days air curing. This suggests that, with the presence of chloride ion in this study, the typical hydration products observed in Sorel cement may be formed. Therefore, it leads to an increase in strength. The hydration products from this system was discussed in the following section 3.4.

8.6 Reaction mechanism and hydration products

For the MgO sample mixed with water, the hydration process begins with the consumption of MgO and is followed by precipitation of the main hydration product, brucite, $Mg(OH)_2$. The water is first absorbed in the surface and then diffuses into the MgO particles. The hydration begins at the grain boundaries and forms a brucite ($Mg(OH)_2$) layer around the grain. The formation of brucite can be observed in the DW sample at the age of 3 days in Figure 8-7. (a) and (b). The particle size of the brucite was around 1 μm.

For those samples containing higher chloride content in acidic solution (MC, HA and WA), the hydration process was different. First, the free hydrogen (H^+) ion was neutralised by the added MgO with the dissolution of MgO and the increase of pH. Hydrated phases such as: $Mg_x(OH)_y \cdot Cl \cdot nH_2O$ were formed. Dehua and Chuanmei's research [183] suggested that the formation of these phases were not through simple ions $Mg^{2+,}$ Cl^- or OH^-, but through the complexes $[Mg_x(OH)_y(H_2O)_z]^{2x-y}$ and Cl^-, OH^- ions. These interlocked phases attributed to the higher early strength of the samples compared to DW.

The MgO + waste acid (WA) sample demonstrated a significantly different microstructure compared to other samples, as shown in Figure 8-7. (g) where crystalline phases are present. This may be caused by the presence of other metal ions in the waste acid solution. These ions helped the formation of the polynuclear complexes instead of mononuclear ones. These can be converted to a micro and continuous network consisting of the fibre-like hydrate crystals. These crystals were similar to those found in previous studies on magnesium chloride cement (MOC) [333, 334]. It was worth noting that in Dinnebier et al.'s study[335, 336], they exposed the magnesia cement to elevated

temperatures above 80 °C. Different magnesium chloride hydrates with the composition x $Mg(OH)_2$ • y $MgCl_2$ • z H_2O, (x:y:z =2:1:4 and 2:1:2) were characterised rather than the preferred formation (x:y:z =3:1:8, 5:1:8 and/or 9:1:4). Both phases (2-1-4 and 2-1-2) crystallise as fine needles and looked very similar to the hydrates in this study. As the hydration temperature of the WA sample went over 100 °C shown in Figure 8-4, it may create the same environment for the formation of 2-1-4 and 2-1-2 phase.

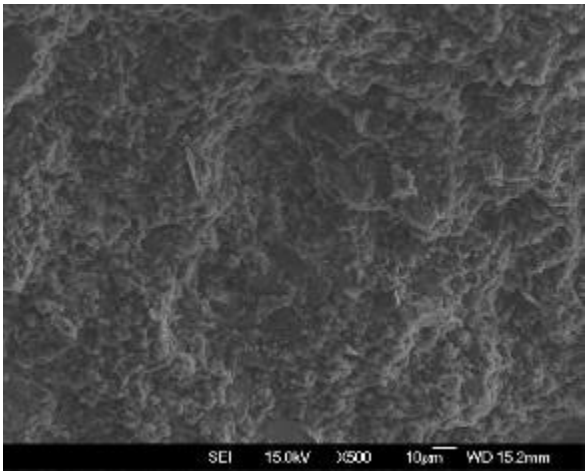

a) MgO +D.I. water (×500)

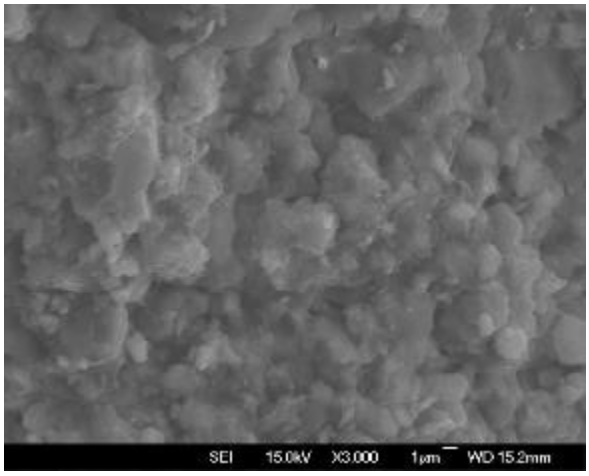

b) MgO +D.I. water (×3,000)

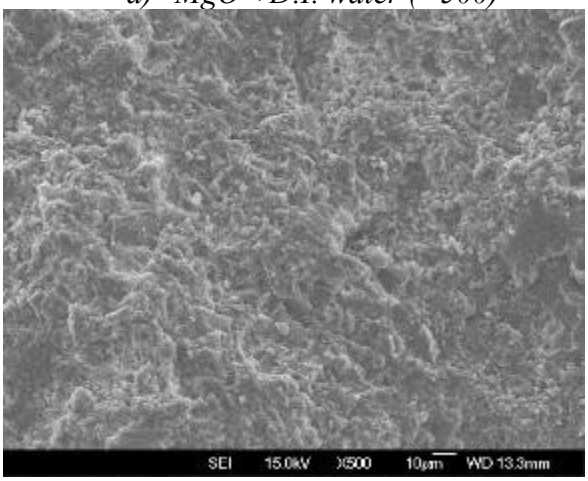

c) MgO +MgCl2 (×500)

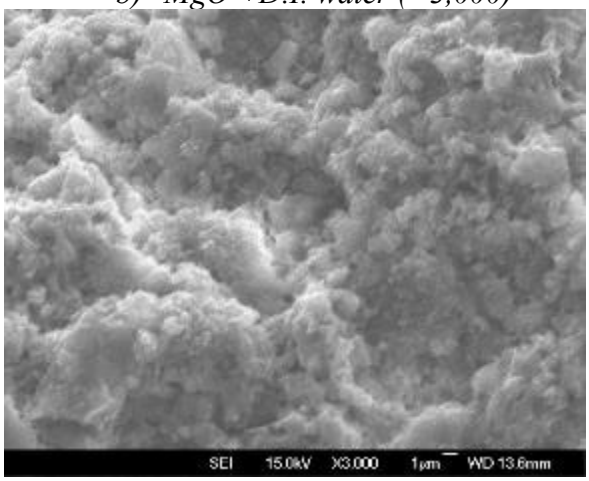

d) MgO + MgCl2 (×3,000)

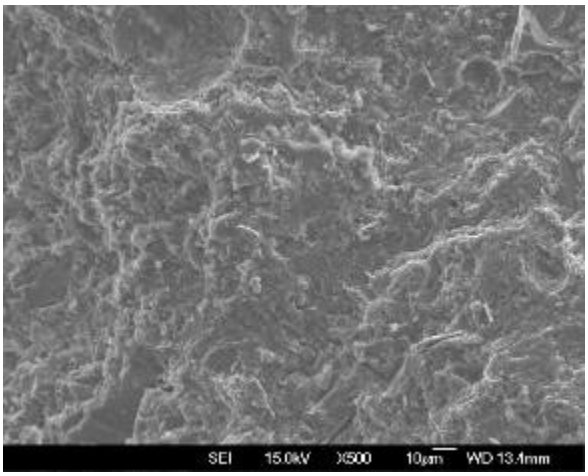

e) MgO +HCl (×500)

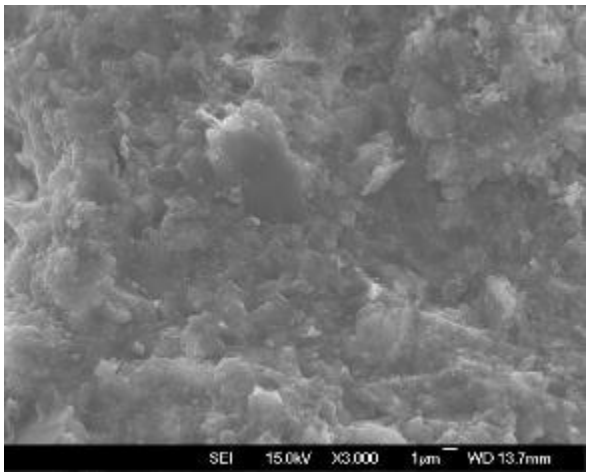

f) MgO +HCl (×3,000)

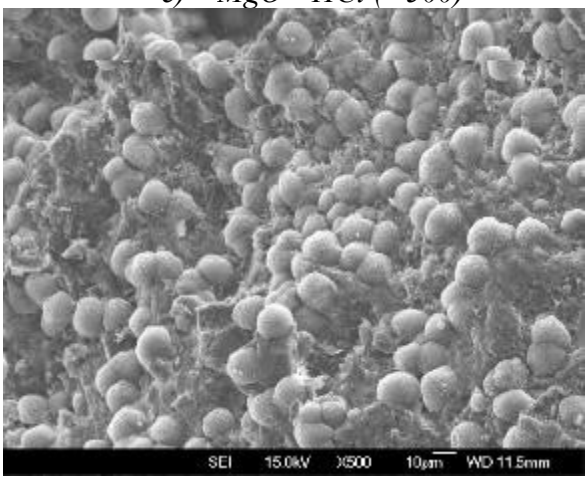

g) MgO +waste acid (×500)

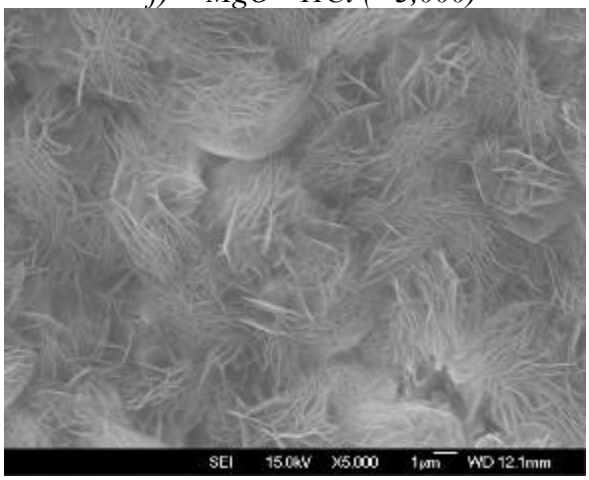

h) MgO +waste acid (×5,000)

Figure 8-7. The microscopy of the MgO samples with different solutions at the age of 3 days.

For the DW sample, compared to the samples in 3 days, their microstructure didn't change much as shown in Figure 8-8. The particle size of the crystal product increased and some magnesium carbonate products were produced. This aligns with the previous study [337].

The microscopy of the MC and HA samples at the age of 60 days are similar, while these hydration products were observed bridging and growing together, forming denser

structure. This leads to strength development over time. At this age, the MC sample (Figure 8-8 d) showed some of the similar products as WA sample (Figure 8-8 Figure 8-7. h) though not as pronounced. They are phase 5-1-8 ($5Mg(OH)_2$• $MgCl_2$ •$8H_2O$) as they present similar needle-like morphology in previous studies[338, 339].

For the MgO mixed with waste acid (WA) samples, there was no presence of the crystallised phase in 60 days and was similar to the HA sample. This was due to these crystallised phases (2-1-4 and 2-1-2) being stable only at high temperature (above 80 °C) and they had transformed to phase 3-1-8 ($3Mg(OH)_2$• $MgCl_2$ •$8H_2O$) after cooling down to room temperature[335]. It was interesting to note that the sample with waste acid promoted crystal development in early ages. This suggests that because the solution contains free H^+, Cl^- and other metal ions, it could be an alternative to mixing with addition MgO and generating a cementitious binder similar to MOC cement.

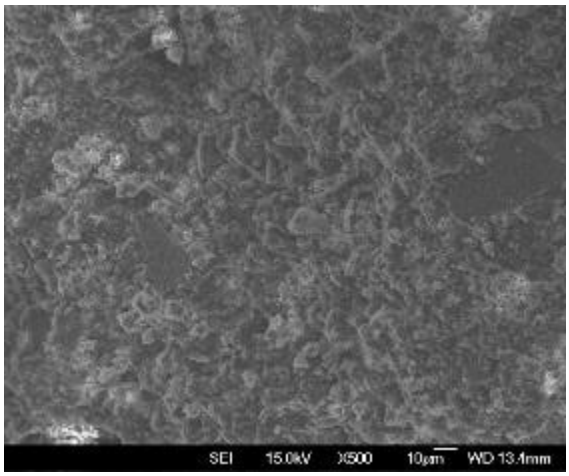

a) MgO +D.I. water (×500)

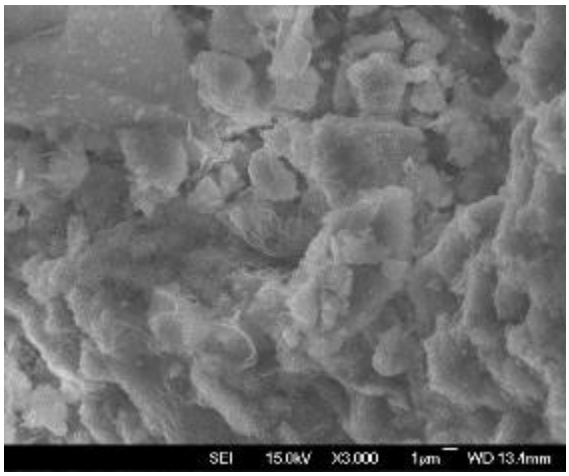

b) MgO +D.I. water (×3,000)

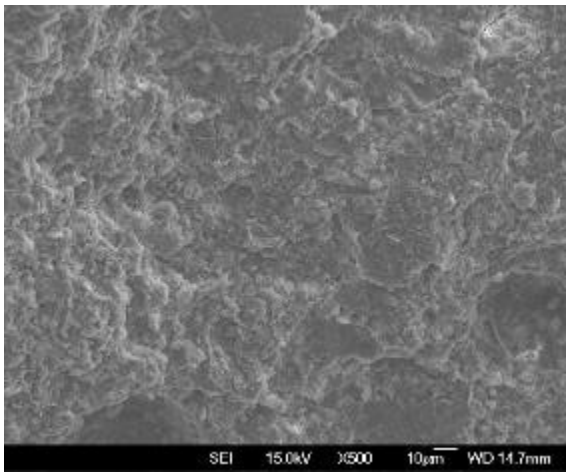

c) MgO +MgCl2 (×500)

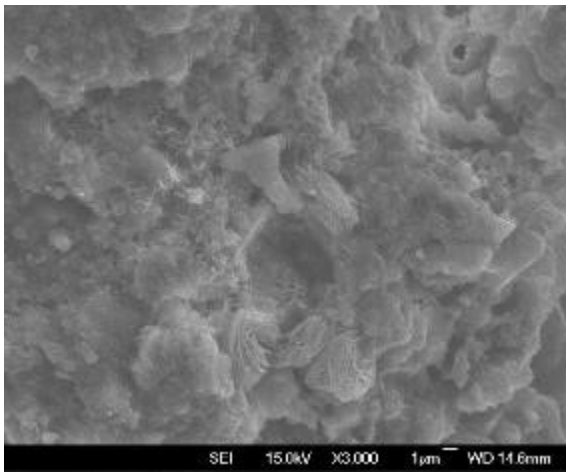

d) MgO + MgCl2 (×3,000)

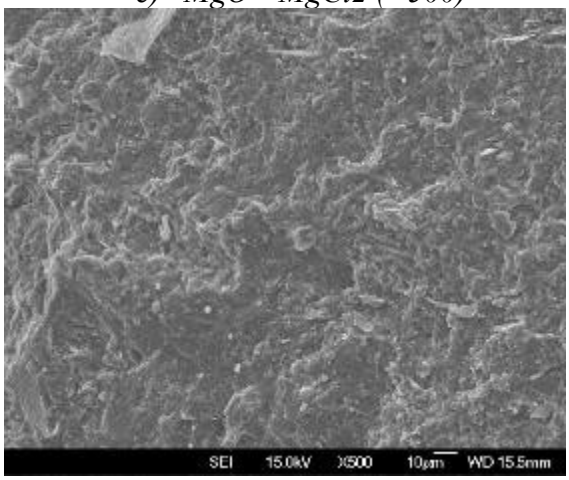

e) MgO +HCl (×500)

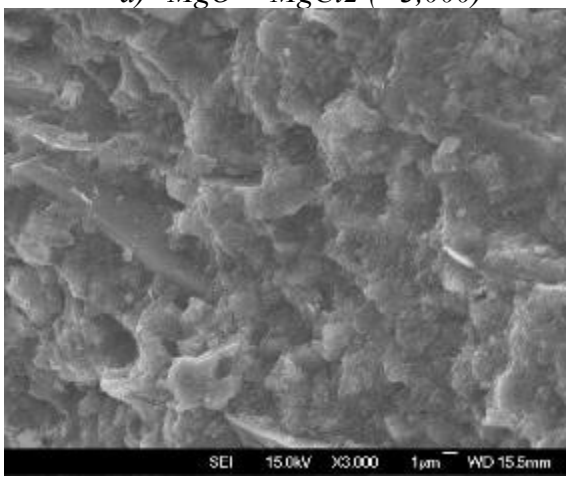

f) MgO +HCl (×3,000)

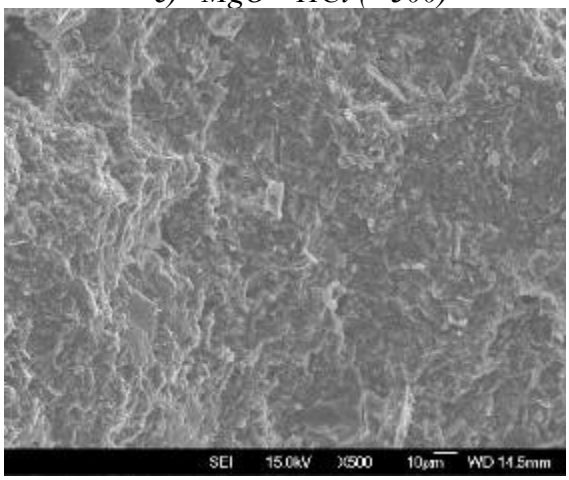

g) MgO +waste acid (×500)

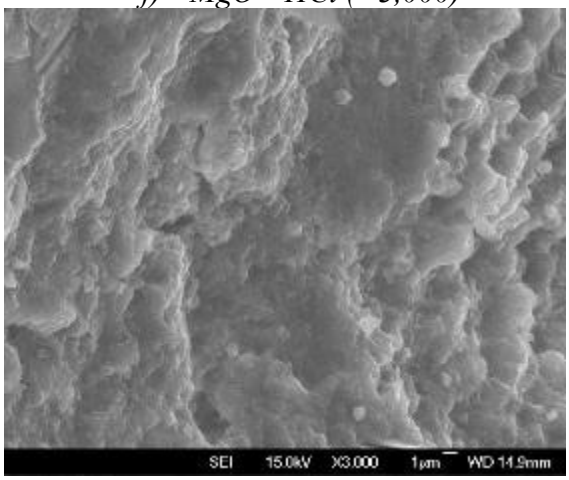

h) MgO +waste acid (×3,000)

Figure 8-8. The microscopy of the MgO samples with different solutions at the age of 60 days.

8.7 Material identification

The XRD patterns of the DW, WA and MC at the age of 28 days are provided in Figure 8-9. As can be seen from these peaks, the hydration products from different samples were similar: the major component was brucite $Mg(OH)_2$, with the presence of magnesium carbonates and unreacted MgO residue. The intensity of the peaks was in the same range as well.

This crystal hydration product of MgO-$MgCl_2$-H_2O gel (Phase 3, JCPDS 00-007-0412)[340] was identified around 2θ of 13 ° in WA and MC sample. The intensity of the peak, however, compared to the Sorel cement system was very low. This was due to the low $MgCl_2$/ MgO molar ratio of the sample mix (1.6:100) compared to 360~780:100 in Sorel cement[341, 342]. Therefore, the amount of $MgCl_2$ was limited to form MgO-$MgCl_2$-H_2O gel. In this spite of the limited amount of this product, it has contributed significantly to the strength development.

This indicates that with the presence of free chloride, polynuclear magnesium complexes were produced in water and hydration phases were formed similar to Sorel cement. It also confirmed the feasibility of using waste acid with MgO to produce a cementitious material, as it demonstrates similar properties and hydration products with using $MgCl_2$.

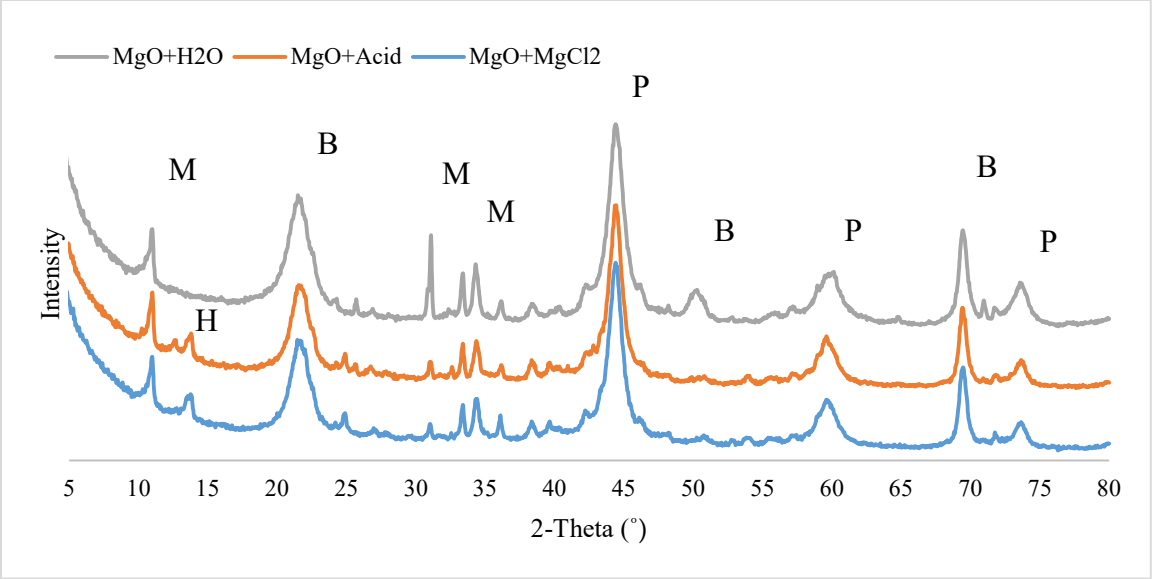

Figure 8-9. The XRD spectra of the MgO mixtures with different solutions

(B: Brucite; M: Magnesite; P: Periclase; H:3MgO-$MgCl_2$-8H_2O)

8.8 Summary and conclusion

The waste acid after the serpentine leaching process was collected and analysed. The main components in the waste acid solution were Mg^{2+} and Cl^-. The precipitated solid residue after evaporation was identified as $MgCl_2 \cdot 6H_2O$. When MgO was mixed with this waste acid, it released a significant amount of heat compared to contact with water or mixing with $MgCl_2$. This was due to the exothermic reaction of the acid-base reaction. This high temperature further increased the reaction rate of the hydration and increased its early mechanical strength at 3 days.

The strength developments of different samples were compared, including the MgO mixed with de-ionised water, seawater, $MgCl_2$ solution, fresh hydrochloride acid and waste acid. The compressive strength was found to be related to the chloride content: the higher the Cl^- content, the higher the strength. The strength of the sample mixed with waste acid

was similar to that with fresh acid, while slightly higher than the mix with the $MgCl_2$ solution. The strength of the waste acid sample was over 40 MPa at 3 days, which was more than double that of the MgO + D.I. water sample. However, the waste acid sample's strength development from 3 days to 60 days was not significant.

The hydration products were examined by SEM technique and it revealed the different microstructures of these samples. This supported the finding of the compressive strengths: MgO + D.I. water sample showed the loose structure of brucite while others showed the presence of an amorphous connected gel. It should be highlighted that the microstructures of the waste acid sample at the age of 3 days were found to be similar to the crystal hydration product phase in $MgO\text{-}MgCl_2\text{-}H_2O$ cement system. The major mineral identified by XRD was brucite as MgO addition was excessive compared to the $MgCl_2$ content.

This suggests that waste hydrochloride acid can be neutralised and used in the production of a MgO cement that is capable of achieving a compressive strength over 40 MPa. It would be a potential way to utilise large amounts of industrial waste hydrochloride acid, such as from the paper pulp industry.

Future research can further explore the reaction mechanism of the MgO + waste acid and it's potential to immobilise the heavy metal in the waste. The durability of this binder system has not been examined in this study and incorporating other industry by-products into the system to improve its long-term property can be of interests.

9 Conclusions and recommendations

9.1 Main findings

The aim of the present research was to examine the feasibility of using magnesium silicate minerals for developing cementitious materials. The findings of this study have supported this idea. The project's main contributions are summarised into four parts.

9.1.1 Extraction of the magnesia and silica from magnesium silicates

Different factors including pH, particle fineness, presence of CO_2, reaction duration and temperature were all investigated to understand their effect on olivine dissolution properties. A linear relationship was found between the log of the Mg dissolution rate (*log r*) and the pH value. Acetic acid, as a weak acid, was selected to lower the solution pH and digest the olivine. The introduction of CO_2 has a positive effect on its dissolution while grinding it to a particle size smaller than 88 μm also increases the dissolution rate. After acid digestion, filtration, evaporation and thermal decomposition, magnesia was

successfully recovered as the major mineral for the binder system. Similarly, silica was extracted through acid leaching of serpentine.

The studies on the mineral dissolution provided a systematic and practical guide for selecting suitable reaction conditions for magnesium and silica extraction. The acid leaching methods used for olivine and serpentine may also be applied to other minerals such as those commonly found in basalt.

9.1.2 Characterisation the activity of the recovered products

After the products were recovered from the minerals, the activities of these products were compared with commercial magnesia and other silica sources using various methods and techniques.

The activity of the recovered magnesia was lower than commercial MgO using the acetic acid activity measurement. The main challenge with the recovered magnesia was the high level of silica impurity at 27.9% of the total recovered magnesia. However, this could be turned into an advantage if the recovered magnesia was used to develop a magnesia silicate hydrate (M-S-H) binder system. Both the thermal-gravimetric analysis and the scanning electron microscopy demonstrated that the silica residue in MgO could react with the $Mg(OH)_2$, which was formed after contact between the MgO and water, forming the M-S-H gel.

The silica extracted from serpentine showed good pozzolanic reactivity. Seven different characterisation techniques were used to assess its mechanical properties, chemical and phase indication, and hydration products. The high specific surface area of the recovered silica resulted in the fastest reaction rate with calcium hydroxide solution

compared with other silica sources (such as silica fume and micro silica). Nevertheless, the long-term properties of mix with silica fume were superior that with recovered silica. This recovered product contains both amorphous and crystalline forms of silica.

Current results demonstrates that the main impurity of the recovered MgO is amorphous silica, while the recovered SiO_2 primarily contained unreacted crystalline forms of silica. However, at this *proof-of-concept* stage, it was out of the scope of this work to improve the purity of recovered products. In fact, the impurities in the products may not need to be removed if the application of the extracted products were in cementitious magnesium silicate hydrated materials. The reactive silica in MgO may accelerate the hydration with SiO_2 while the unreacted impurities may act as fine filler particles/aggregates.

9.1.3 Development of a cementitious material from the recovered products

In this study, magnesia recovered from olivine and commercial MgO were mixed with two types of silica (recovered from serpentine and silica fume), respectively. All of the mixes demonstrated some degree of cementitious properties.

For the system prepared by mixing with the recovered MgO and extracted SiO_2, magnesium-silicate-hydrates were observed to form. Even with the impurities in the recovered products and less reactivity, the compressive strength at 28 days of this mix sample (38.5 MPa) was two times higher than the mix of commercial MgO and silica fume (17.5 MPa). The strength test and the microstructure analysis of the sample mixed with

recovered MgO and water (no silica addition) demonstrated 55.3 MPa at 28 days and the presence of magnesium silicate hydrates was also noted.

It was confirmed that the fine amorphous silica present in the recovered MgO, as impurities, was beneficial to the hydration reaction and strength development. The recovered silica however demonstrated less reactivity in the M-S-H system which led to lower strength and lower M-S-H content. These findings provided important information on the potential and feasibility of deriving the cementitious materials from minerals. It was suggested to focus on the production of recovered MgO as it may be more cost-effective compared to refining the extracted SiO_2.

9.1.4 Utilisation of the material waste to produce cementitious systems

Based on the previous studies on the magnesia-based cement system, magnesia can react with water and magnesium chloride to produce a cementitious material. Therefore, this project investigated the feasibility of utilising the waste acid (the HCl after mineral treatment) to develop a Mg-based binder system.

The study compared samples mixed with MgO+ di-ionised water, MgO+ seawater, MgO+ waste acid and MgO+ fresh prepared acid. The compressive strength, hydration reaction and microstructure of the different MgO binders was investigated. All the mixes demonstrated binding characteristics. The results confirmed the presence of the free magnesium and chloride ion in the solution contribute to the hydration reaction and strength development.

Mixing the waste hydrochloric acid solution with magnesia produced a binder system that had a very high early strength: 43.7 MPa at the age of 3 days (w/b=0.4). The MgO + waste acid system produced similar hydration product of MgO-$MgCl_2$-H_2O gel (Phase 3) compared to the typical Sorel cement (MgO-$MgCl_2$-H_2O) system. However, the amount of this products was very low while this can be attributed to the low $MgCl_2$/ MgO molar ratio (1.6:100) compared to Sorel cement (360~780:100).

The formation of the cementitious product from the reaction between magnesia and waste hydrochloric acid provide the possibility of recycling the waste acidic solution: if both the extracted products and the waste material could be utilised, the carbon emissions during binder production will decease substantially.

Overall, returning to the question posed at the beginning of this study, it is now possible to state that it is feasible to develop a cementitious material from the magnesium silicates mineral using a low energy processing method.

9.2 Limitation and future study.

The major limitation of this study is the optimization of the process and deep understanding of the reaction mechanism.

- Different factors on olivine solubility were investigated while the reaction rate is still relatively low.
- The reaction mechanism of olivine dissolution was not clearly verified. The reaction on the particle surface is difficult to observe and the quantity of the products are limited. More surface observation techniques could be applied to study potential steps.

- The reactivity of the obtained silica from serpentine is limited and little effort was made to improve it in this study.
- This study only focused on the cement paste properties while concrete scale tests need to be conducted to provide practical knowledge.

However, due to the scope of the study, after achieving the proof of concept set forth in this research, future efforts can be made in order to further develop this idea into practical production.

9.2.1 Improve the mineral dissolution

By mechanical activation via grinding, the olivine serpentinization process was sped up significantly compared to natural weathering. However, more work can be done regarding the reaction rate. According to the Arrhenius equation, the rate constant of a reaction depends on the frequency factor, the activation energy and the temperature. This study has investigated the effect of the frequency factor (i.e. the concentration of active hydrogen ion (pH)) on the reaction rate. Future studies can aim to find a suitable catalyst that increases the rate by lowering the reaction activation energy. Another promising approach is to find an optimum temperature range that balances the reaction rate and energy consumption.

The reaction mechanism of mineral dissolution was not clearly verified. The reaction on the particle surface is difficult to observe and the quantity of the products are limited. More surface observation techniques could be applied to study potential steps. In order to discover the pathway as the reaction proceeds, isotope labelling could be beneficial to distinguish which bond was broken.

9.2.2 **Increase the purity of the recovered product**.

The recovered products, both MgO and SiO_2, were found to contain a large proportion of impurities.

For magnesium recovery, the purity requirements depend on the final application of the recovered products. For instance, if the recovered MgO is used for the development of M-S-H binder system, the amorphous silica, as the main impurity, may not need to be removed. For carbon storage application, other soluble ions such as chloride, may not be a concern, as long as these impurities do not affect the solubility of the produced carbonates. However, if the aim is to achieve high grade of magnesium oxide, using the following multiple stage processing to precipitate the magnesium composites and calcination may be feasible, as shown in Figure 9-1.

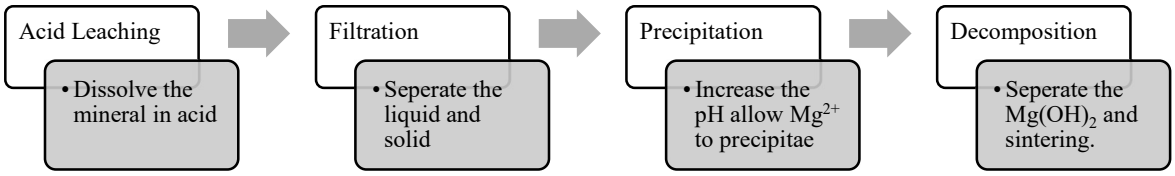

Figure 9-1. The proposed processing chart for olivine

For the extracted silica, only 50.8% of it identified by XRF was SiO_2 while 29.5% was MgO. This suggests an incomplete acid leaching process. The impurities act as fillers thus reducing the reactivity of the silica per unit mass. There are two approaches that may help to reduce the impurity. The first approach is to increase the reaction degree by mineral pre-treatment (finer particle size, calcination), using stronger acid for an extended reaction time, or elevated reaction temperature. Another way is also multiple stage processing: activation, acid leaching, decantation, silica filtration and precipitation.

9.2.3 Full utilization of the reaction products

This research has only focused on the main phase forsterite (Mg_2SiO_4) of Olivine. However, the oxidation of ferrous iron in olivine, even at lower content, during hydrolysis produces molecular hydrogen (H_2) as shown by the fayalite end member (Fe_2SiO_4;Equation 9-1) and the olivine from this study(Equation 9-2).

$$Fe_2SiO_4+2H_2O \rightarrow 2Fe_3O_4+3SiO_2+2H_2 \qquad \textit{Equation 9-1}$$

$$(Mg_{0.88},Fe_{0.12})_2SiO_4+1.34H_2O \rightarrow 0.5Mg_3Si_2O_4(OH)_4+0.26Mg(OH)_2+0.08Fe_3O_4+0.08H_2 \qquad \textit{Equation 9-2}$$

The by-product, H_2, if it can be collected, could be used as an energy source either in its own right or to supplement the energy requirements of the process.

The waste acid used in this reaction may be recycled. Acetic acid and hydrochloric acid are acids that have low boiling point (118 ˚C and 108.6 ˚C, respectively), and could be further recycled by simply evaporating the excessive acid solution after mineral reaction.

The characterisation of the products recovered from the olivine with CO_2 fed solution showed that it was composed of a magnesium composite and amorphous silica. It was confirmed that magnesium-silica-hydrate (M-S-H) can be formed from the reaction between MgO/$Mg(OH)_2$ and silica. Thus, it may be possible to use the processed olivine as a feedstock to form other cementitious products. In order to reach a suitable Mg/Si ratio, it can be blended with other reactive silica products such as silica fume or reactive magnesia. The olivine-magnesia-silica binder system may provide an excellent low carbon alternative to the conventional Portland cement.

9.2.4 Investigate the effect of seawater and waste acid on magnesia binder

The mixtures of seawater and waste hydrochloric acid with magnesia both showed superior strength compared with pure water. This was believed to be caused by the high content of the free magnesium and chloride ions in the solution. These ions affect the magnesia hydration and improved its reaction rates. However, the high concentration of chloride can also lead to corrosion of the steel reinforcement. If the free chloride can be contained in the hydration products, it may provide a wider application for utilising the MgO based cement with sea sand and sea water. MgO may also be used to immobilise the waste acid from industries and form stable concrete block. Alternatively, there are many application for unreinforced concrete where either chlorides or a lower pore solution pH are not detrimental.

9.2.5 Study on the durability of this binder

This research only studied the early hydration and mechanical properties up to three months. However, a more systematic understanding of this material is needed before any practical usage. The porosity of the binders has not been examined. As a typical weakness of the MgO based cement, most of them suffer from poor water resistance. It is not clear how this binder would behave under other detrimental conditions.

The carbonation of the MgO based material is also an interesting topic. For reactive MgO cement, accelerated CO_2 curing is used to improve its reaction degree and strength. Through carbonation, the CO_2 can be mineralised into the block and may achieve a carbon neutral binder cement. These behaviours of the binders need further investigation.

10 Reference

1. Andrew, R.M., *Global CO2 emissions from cement production.* Earth System Science Data, 2018. **10**(1): p. 195.
2. Statista. *Major countries in worldwide cement production from 2015 to 2019*. Worldwide cement production 2020 12 Feb 2020;.
3. Olivier, J.G., G. Janssens-Maenhout, and J.A. Peters, *Trends in global CO2 emissions: 2012 Report*. 2012, PBL Netherlands Environmental Assessment Agency The Hague.
4. Mohr, S.H., et al., *Projection of world fossil fuels by country.* Fuel, 2015. **141**: p. 120-135.
5. National Minerals Information Center , *Mineral commodity summaries 2016*. 2016: Government Printing Office.
6. Wyns, T., et al., *Industrial Transformation 2050–Towards an Industrial Strategy for a Climate Neutral Europe.* Brussels: Institute for European Studies, Vrije Universiteit Brussel..
7. Xu, J.-H., et al., *CO2 emissions reduction potential in China's cement industry compared to IEA's Cement Technology Roadmap up to 2050.* Applied Energy, 2014. **130**: p. 592-602.
8. Beyond Zero Emissions, *Zero Carbon Industry Plan-Rethinking Cement*. 2017.
9. International Energy Agency, *Technology Roadmap: Low-Carbon Transition in the Cement Industry*. 2018.
10. Favier, A., et al., *A sustainable future for the European Cement and Concrete Industry: Technology assessment for full decarbonisation of the industry by 2050*. 2018, ETH Zurich.
11. Scrivener, K.L., V.M. John, and E.M. Gartner, *Eco-efficient cements: Potential economically viable solutions for a low-CO2 cement-based materials industry.* Cement and Concrete Research, 2018. **114**: p. 2-26.
12. Pawson, J.F., *Abiotic Methane Formation at the Dun Mountain Ophiolite, New Zealand.* 2015.

13. Prigiobbe, V., et al., *Mineral carbonation process for CO2 sequestration.* Energy Procedia, 2009. **1**(1): p. 4885-4890.

14. O'Connor, W.K., et al., *Carbon Dioxide Sequestration by Direct Mineral Carbonation : Results from Recent Studies and Current Status.* Albany Re, 2005: p. 1874-1879.

15. Nduagu, E., et al., *Production of magnesium hydroxide from magnesium silicate for the purpose of CO 2 mineralisation - Part 1: Application to Finnish serpentinite.* Minerals Engineering, 2012. **30**: p. 75-86.

16. Gerdemann, S.J., et al., *Carbon dioxide sequestration by aqueous mineral carbonation of magnesium silicate minerals*. 2003, Albany Research Center (ARC), Albany, OR.

17. Justnes, H., *Pozzolana from minerals–State of the art. COIN P1 Advanced cementing materials and admixtures. SP 1.4 F Alternative pozzolans.* Concrete Innovation Centre Project report, 2009.

18. Midgley, H.G., *The use of calcined serpentine as a cement.* Cement and Concrete Research, 1979. **9**(2): p. 157-160.

19. del Real, P.G. and V. Vishal, *Mineral Carbonation in Ultramafic and Basaltic Rocks*, in *Geologic Carbon Sequestration*. 2016, Springer. p. 213-229.

20. Wogelius, R.A. and J.V. Walther, *Olivine dissolution kinetics at near-surface conditions.* Chemical Geology, 1992. **97**(1-2): p. 101-112.

21. Haug, T.A., R.A. Kleiv, and I.A. Munz, *Investigating dissolution of mechanically activated olivine for carbonation purposes.* Applied Geochemistry, 2010. **25**(10): p. 1547-1563.

22. Teir, S., et al., *Dissolution of natural serpentinite in mineral and organic acids.* International Journal of Mineral Processing, 2007. **83**(1-2): p. 36-46.

23. Dutrizac, J.E., T.T. Chen, and C.W. White, *Fundamentals of serpentine leaching in hydrochloric acid media*. 2000. 41-51.

24. Ha, M., et al., *Dissolution kinetics of fosteritic olivine at 90 – 150 ° C including effects of the presence of CO 2.* 2006. **70**: p. 4403-4416.

25. Dungan, M.A., *Metastability in serpentine-olivine equilibria.* American Mineralogist, 1977. **62**(9-10): p. 1018-1029.

26. O'Connor, W.K., et al., *Carbon dioxide sequestration: Aqueous mineral carbonation studies using olivine and serpentine*. 2001, Albany Research Center (ARC), Albany, OR.

27. Fagerlund, J., et al., *Carbonation of magnesium silicate mineral using a pressurised gas/solid process.* Energy Procedia, 2009. **1**(1): p. 4907-4914.

28. Lackner, K.S., *A guide to CO2 sequestration.* Science, 2003. **300**(5626): p. 1677-1678.

29. McCollom, T.M. and W. Bach, *Thermodynamic constraints on hydrogen generation during serpentinization of ultramafic rocks.* Geochimica et Cosmochimica Acta, 2009. **73**(3): p. 856-875.

30. Iyer, K., et al., *Serpentinization of the oceanic lithosphere and some geochemical consequences: Constraints from the Leka Ophiolite Complex, Norway.* Chemical Geology, 2008. **249**(1-2): p. 66-90.

31. Plumper, O., et al., *The interface-scale mechanism of reaction-induced fracturing during serpentinization.* Geology, 2012. **40**(12): p. 1103-1106.

32. Baumeister, J.L., *Chemical Weathering of the Mafic Minerals Serpentine and Olivine in Natural Environments.* Master Thesis, 2012: p. 156-156.

33. Yoo, K., et al., *Dissolution of Magnesium from Serpentine Mineral in Sulfuric Acid Solution.* Materials Transactions, 2009. **50**(5): p. 1225-1230.

34. Gualtieri, A.F., C. Giacobbe, and C. Viti, *The dehydroxylation of serpentine group minerals.* American Mineralogist, 2012. **97**(4): p. 666-680.

35. Hršak, D., J. Malina, and A. Hadzipasic, *The decomposition of serpentine by thermal treatment.* Materiali in Tehnologije, 2005. **39**(6): p. 225-227.

36. Dutrizac, J.E., T.T. Chen, and C.W. White, *Fundamentals of serpentine leaching in hydrochloric acid media*. Magnesium Technology 2000. 2000. 41-51.

37. Sanna, A., et al., *Enhancing Mg extraction from lizardite-rich serpentine for CO2 mineral sequestration.* Minerals Engineering, 2013. **49**: p. 135-144.

38. Wang, X.L. and M.M. Maroto-Valer, *Dissolution of serpentine using recyclable ammonium salts for CO2 mineral carbonation.* Fuel, 2011. **90**(3): p. 1229-1237.

39. A.Tyburzy, J. and T. J.Ahrens, *Dehydration Kinetics of Shocked Serpentine.* Statewide Agricultural Land Use Baseline 2015, 2015. **1**.

40. Rucklidge, J.C. and J. Zussman, *The crystal structure of the serpentine mineral, lizardite Mg3Si2O5(OH)4.* Acta Crystallographica, 1965. **19**(3): p. 381-389.

41. Whittaker, E. and J. Zussman, *The characterization of serpentine minerals by X-ray diffraction.* Mineralogical Magazine, 1956. **31**(233): p. 107-126.

42. Christodoulou, C., et al., *Comparing calcined and un-treated olivine as bed materials for tar reduction in fluidized bed gasification.* Fuel Processing Technology, 2014. **124**: p. 275-285.

43. Rauch, R., et al., *Comparison of different olivines for biomass steam gasification*. 2004: na.

44. Devi, L., et al., *Olivine as tar removal catalyst for biomass gasifiers: Catalyst characterization.* Applied Catalysis A: General, 2005. **294**(1): p. 68-79.

45. Qing, G., et al., *Study on Effect of Untreated and Calcined Olivine on Low Silicon Pellet Production Process and Quality*, in *Drying, Roasting, and Calcining of Minerals*, T.P. Battle, et al., Editors. 2016, Springer International Publishing: Cham. p. 135-141.

46. Mayhew, L.E., S.M. Webb, and A.S. Templeton, *Microscale imaging and identification of Fe speciation and distribution during fluid–mineral reactions under highly reducing conditions.* Environmental science & technology, 2011. **45**(10): p. 4468-4474.

47. Świerczyński, D., et al., *Characterization of Ni− Fe/MgO/olivine catalyst for fluidized bed steam gasification of biomass.* Chemistry of Materials, 2006. **18**(17): p. 4025-4032.

48. Michel, R., et al., *Phase transformation characterization of olivine subjected to high temperature in air.* Ceramics International, 2013. **39**(5): p. 5287-5294.

49. Hamilton, V.E., *Thermal infrared (vibrational) spectroscopy of Mg–Fe olivines: A review and applications to determining the composition of planetary surfaces.* Geochemistry, 2010. **70**(1): p. 7-33.

50. Hršak, D., G. Sučik, and L. Lazić, *The thermophysical properties of serpentinite.* Metalurgija, 2008. **47**(1): p. 29-31.

51. Midgley, H.G., *A serpentine mineral from Kennack Cove, Lizard, Cornwall 1.* Mineralogical Magazine and Journal of the Mineralogical Society, 1951. **29**(212): p. 526-530.

52. Nemie, E., D. Hršak, and A.B. Hadžipašić. *The influence of sulphuric acid concentration and molar ratio at the leaching of antigorite*. 2005.

53. Oelkers, E.H., et al., *Olivine dissolution rates: A critical review.* Chemical Geology, 2018. **500**: p. 1-19.

54. Prigiobbe, V., et al., *Analysis of the effect of temperature, pH, CO2 pressure and salinity on the olivine dissolution kinetics.* Energy Procedia, 2009. **1**(1): p. 4881-4884.

55. Wogelius, R.A. and J.V. Walther, *Olivine dissolution at 25°C: Effects of pH, CO2, and organic acids.* Geochimica et Cosmochimica Acta, 1991. **55**(4): p. 943-954.

56. Chen, Y. and S.L. Brantley, *Dissolution of forsteritic olivine at 65°C and 2<pH<5.* Chemical Geology, 2000. **165**(3): p. 267-281.

57. Teir, S., et al., *Dissolution of natural serpentinite in mineral and organic acids.* International Journal of Mineral Processing, 2007. **83**(1): p. 36-46.

58. Zhao, Q., et al., *Preparation of magnesium hydroxide from serpentinite by sulfuric acid leaching for CO2 mineral carbonation.* Minerals Engineering, 2015. **79**: p. 116-124.

59. Gabra, G., *A process for the production of magnesium oxide from serpentine by sulfur dioxide leaching and solvent extraction.* Hydrometallurgy, 1984. **13**(1): p. 1-13.

60. Lin, P.-C., et al., *Magnesium Hydroxide Extracted from a Magnesium-Rich Mineral for CO2 Sequestration in a Gas–Solid System.* Environmental Science & Technology, 2008. **42**(8): p. 2748-2752.

61. Nduagu, E., et al., *Production of magnesium hydroxide from magnesium silicate for the purpose of CO2 mineralisation – Part 1: Application to Finnish serpentinite.* Minerals Engineering, 2012. **30**: p. 75-86.

62. Nduagu, E.I., et al., *Mechanisms of serpentine-ammonium sulfate reactions: Towards higher efficiencies in flux recovery and Mg extraction for CO2 mineral sequestration.* RSC Advances, 2014. **4**(110): p. 64494-64505.

63. Zevenhoven, R., et al., *Carbon storage by mineralisation (CSM): Serpentinite rock carbonation via Mg(OH)2 reaction intermediate without CO2 pre-separation.* Energy Procedia, 2013. **37**: p. 5945-5954.

64. Stasiulaitiene, I., Fagerlund, J., Nduagu, E., Denafas, G., & Zevenhoven, R., *Carbonation of serpentinite rock from Lithuania and Finland.* Energy Procedia, 2011. **4**: p. 2963–2970.

65. Said, A., Eloneva, S., Fogelholm, C. J., Fagerlund, J., Nduagu, E., & Zevenhoven, R., *Integrated carbon capture and storage for an oxyfuel combustion process by using carbonation of Mg(OH)2 produced from serpentinite rock.* Energy Procedia, 2011(4): p. 2839–2846.

66. Fagerlund, J., Nduagu, E., & Zevenhoven, R., *Recent developments in the carbonation of serpentinite derived Mg(OH) 2 using a pressurized fluidized bed.* Energy Procedia, 2011. **4**: p. 4993–5000.

67. Teir, S., et al., *Production of magnesium carbonates from serpentinite for long-term storage of CO2.* International Journal of Mineral Processing, 2007. **85**(1): p. 1-15.

68. Horacio E. Bergna and W.O. Roberts, *Colloidal Silica: Fundamentals and Applications*. Vol. 131. 2005: CRC Press.

69. Pietriková, A., M. Búgel, and M. Golja, *Preparation of SiO2 Powder through Leaching of Serpentine.* Metalurgija, 2004. **43**(4): p. 299-304.

70. Fedoročková, A., et al., *Characteristics of amorphous silica prepared from serpentinite using various acidifying agents.* International Journal of Mineral Processing, 2014. **130**: p. 42-47.

71. Survey, U.S.G., *MINERAL COMMODITY SUMMARIES 2016*, U.S.D.o.t. Interior and U.S.G. Survey, Editors. 2016, U.S. Geological Survey: Reston, Virginia.

72. Colling, A. and J.B. Wright, *Seawater: its composition, properties and behaviour*. 1995: Pergamon.

73. Mo, L., M. Deng, and M. Tang, *Effects of calcination condition on expansion property of MgO-type expansive agent used in cement-based materials.* Cement and concrete research, 2010. **40**(3): p. 437-446.

74. Pradita, T., et al. *Controlled morphological structure of magnesium oxide particles*. in *AIP Conference Proceedings*. 2017. AIP Publishing LLC.

75. Kaneyasu, A., Y. Shin-Ichi, and A. Yoshida, *Magnesia raw materials with improved hydration resistance.* Taikabutsu Overseas, 1997. **17**(2): p. 21-26.

76. Birchal, V., et al., *A simplified mechanistic analysis of the hydration of magnesia.* The Canadian Journal of Chemical Engineering, 2001. **79**(4): p. 507-511.

77. Thomas, J.J., S. Musso, and I. Prestini, *Kinetics and activation energy of magnesium oxide hydration.* Journal of the American Ceramic Society, 2014. **97**(1): p. 275-282.

78. Kitamura, A., K. Onizuka, and K. Tanaka, *Hydration characteristics of magnesia.* Taikabutsu Overseas, 1996. **16**(3): p. 3-11.

79. Rocha, S.D., M.B. Mansur, and V.S. Ciminelli, *Kinetics and mechanistic analysis of caustic magnesia hydration.* Journal of Chemical Technology and Biotechnology, 2004. **79**(8): p. 816-821.

80. Ahari, K.G., J. Sharp, and W. Lee, *Hydration of refractory oxides in castable bond systems—I: alumina, magnesia, and alumina–magnesia mixtures.* Journal of the European Ceramic Society, 2002. **22**(4): p. 495-503.

81. Fisher, R.E., *Advances in Refractories Technology (Ceramic Transactions, Vol 4)*. Vol. 4. 1989, Westerville, Ohio, U.S.A: Amer Ceramic Society.

82. Jin, F., *Characterisation and performance of reactive MgO-based cements with supplementary cementitious materials*, in *Department of Engineering*. 2014, PHD Thesis, Cambridge University, UK: Cambridge.

83. Jost, H., M. Braun, and C. Carius, *The role of reactivity in syntheses and the properties of magnesium oxide.* Solid State Ionics, 1997. **101**: p. 221-228.

84. Aphane, M.E., *The hydration of magnesium oxide with different reactivities by water and magnesium acetate.* 2009.

85. van der Merwe, E., C. Strydom, and A. Botha, *Hydration of medium reactive industrial magnesium oxide with magnesium acetate.* Journal of thermal analysis and calorimetry, 2004. **77**(1): p. 49-56.

86. Strydom, C., E. Van der Merwe, and M. Aphane, *The effect of calcining conditions on the rehydration of dead burnt magnesium oxide using magnesium acetate as a hydrating agent.* Journal of thermal analysis and calorimetry, 2005. **80**(3): p. 659-662.

87. Chau, C.K. and Z. Li, *Accelerated reactivity assessment of light burnt magnesium oxide.* Journal of the American Ceramic Society, 2008. **91**(5): p. 1640-1645.

88. Jin, F. and A. Al-Tabbaa, *Characterisation of different commercial reactive magnesia.* Advances in Cement Research, 2014. **26**(2): p. 101-113.

89. Hassanali, A.A. and S.J. Singer, *Model for the water-amorphous silica interface: The undissociated surface.* The Journal of Physical Chemistry B, 2007. **111**(38): p. 11181-11193.

90. Frondel, C., *Dana's System of Mineralogy, Volume II. Silica Minerals*. 1962, Wiley, New York.

91. Sosman, R.B., *Properties of silica.* 1927.

92. Iler, R.K., *The chemistry of silica: solubility, polymerization, colloid and surface pro perties, and biochemistry*. 1979: Wiley.

93. Astm, *ASTM C125-Standard Terminology Relating to Concrete and Concrete Aggregates*. 2018, ASTM International West Conshohocken.

94. Donatello, S., M. Tyrer, and C.R. Cheeseman, *Comparison of test methods to assess pozzolanic activity.* Cement and Concrete Composites, 2010. **32**(2): p. 121-127.

95. Mostafa, N.Y., et al., *Characterization and evaluation of the pozzolanic activity of Egyptian industrial by-products: I: Silica fume and dealuminated kaolin.* Cement and Concrete Research, 2001. **31**(3): p. 467-474.

96. Cordeiro, G.C., et al., *Influence of particle size and specific surface area on the pozzolanic activity of residual rice husk ash.* Cement and Concrete Composites, 2011. **33**(5): p. 529-534.

97. Cordeiro, G.C., et al., *Ultrafine grinding of sugar cane bagasse ash for application as pozzolanic admixture in concrete.* Cement and concrete research, 2009. **39**(2): p. 110-115.

98. Agarwal, S.K., *Pozzolanic activity of various siliceous materials.* Cement and Concrete Research, 2006. **36**(9): p. 1735-1739.

99. Qing, Y.E., et al., *A comparative study on the pozzolanic activity between nano-SiO 2 and silica fume.* Journal of Wuhan University of Technology-Mater. Sci. Ed., 2006. **21**(3): p. 153-157.

100. Bich, C., J. Ambroise, and J. Péra, *Influence of degree of dehydroxylation on the pozzolanic activity of metakaolin.* Applied Clay Science, 2009. **44**(3-4): p. 194-200.

101. Moropoulou, A., A. Bakolas, and E. Aggelakopoulou, *Evaluation of pozzolanic activity of natural and artificial pozzolans by thermal analysis.* Thermochimica Acta, 2004. **420**(1-2): p. 135-140.

102. McCarter, W.J. and D. Tran, *Monitoring pozzolanic activity by direct activation with calcium hydroxide.* Construction and Building Materials, 1996. **10**(3): p. 179-184.

103. Payá, J., J. Monzó, and M.V. Borrachero, *Physical, chemical and mechanical properties of fluid catalytic cracking catalyst residue (FC3R) blended cements.* Cement and concrete research, 2001. **31**(1): p. 57-61.

104. García, R., et al., *The pozzolanic properties of paper sludge waste.* Construction and Building Materials, 2008. **22**(7): p. 1484-1490.

105. Frías, M., et al., *The effect that different pozzolanic activity methods has on the kinetic constants of the pozzolanic reaction in sugar cane straw-clay ash/lime systems: Application of a kinetic–diffusive model.* Cement and Concrete Research, 2005. **35**(11): p. 2137-2142.

106. Wild, S., J.M. Khatib, and A. Jones, *Relative strength, pozzolanic activity and cement hydration in superplasticised metakaolin concrete.* Cement and concrete research, 1996. **26**(10): p. 1537-1544.

107. Standard, B., *Pulverised-fuel ash. Part*, in *3892*. British.

108. Luxan, M.P.d., F. Madruga, and J. Saavedra, *Rapid evaluation of pozzolanic activity of natural products by conductivity measurement.* Cement and concrete research, 1989. **19**(1): p. 63-68.

109. Paya, J., et al., *Enhanced conductivity measurement techniques for evaluation of fly ash pozzolanic activity.* Cement and Concrete Research, 2001. **31**(1): p. 41-49.

110. De Rojas, M.I.S. and M. Frías, *The pozzolanic activity of different materials, its influence on the hydration heat in mortars.* Cement and Concrete Research, 1996. **26**(2): p. 203-213.

111. Lothenbach, B., K. Scrivener, and R.D. Hooton, *Supplementary cementitious materials.* Cement and concrete research, 2011. **41**(12): p. 1244-1256.

112. Juenger, M.C.G. and R. Siddique, *Recent advances in understanding the role of supplementary cementitious materials in concrete.* Cement and Concrete Research, 2015. **78**: p. 71-80.

113. Australia, C.C.A., *Amorphous Silica Properties, Characterisation and Uses*, in *Cement Concrete & Aggregates Australia - Technical Note*. 2018, Cement Concrete & Aggregates Australia: SYDNEY OFFICE:.

114. Duan, P., et al., *Enhancing microstructure and durability of concrete from ground granulated blast furnace slag and metakaolin as cement replacement materials.* Journal of Materials Research and Technology, 2013. **2**(1): p. 52-59.

115. San Nicolas, R., M. Cyr, and G. Escadeillas, *Performance-based approach to durability of concrete containing flash-calcined metakaolin as cement replacement.* Construction and Building Materials, 2014. **55**: p. 313-322.

116. Bu, Y., et al., *Properties of oil well cement with high dosage of metakaolin.* Construction and Building Materials, 2016. **112**: p. 39-48.

117. Ganesan, K., K. Rajagopal, and K. Thangavel, *Rice husk ash blended cement: Assessment of optimal level of replacement for strength and permeability properties of concrete.* Construction and Building Materials, 2008. **22**(8): p. 1675-1683.

118. Kennerley, R.A. and J. Clelland, *An Investigation of New Zealand Pozzloans*, D.o.S.a.I. Research, Editor. 1959, New Zeland Department of Scientific and Industrial Research: Wellington, New Zealand.

119. Ghafari, E., D. Feys, and K. Khayat, *Feasibility of using natural SCMs in concrete for infrastructure applications.* Construction and Building Materials, 2016. **127**: p. 724-732.

120. Ardoğa, M.K., S.T. Erdoğan, and M. Tokyay, *Effect of particle size on early heat evolution of interground natural pozzolan blended cements.* Construction and Building Materials, 2019. **206**: p. 210-218.

121. Massazza, F., *Pozzolana and pozzolanic cements.* Lea's chemistry of cement and concrete, 1998. **4**: p. 471-631.

122. Rahhal, V. and R. Talero, *Early hydration of Portland cement with crystalline mineral additions.* Cement and Concrete Research, 2005. **35**(7): p. 1285-1291.

123. Alexander, K.M. *Reactivity of ultrafine powders produced from siliceous rocks*. 1960.

124. Day, R.L. and C. Shi, *Influence of the fineness of pozzolan on the strength of lime natural-pozzolan cement pastes.* Cement and Concrete Research, 1994. **24**(8): p. 1485-1491.

125. Chatterjee, M.K. and D. Lahiri, *Pozzolanic activity in relation to specific surface of some artificial pozzolanas—Part II: Relationship between pozzolanic activity and specific surface.* Transactions of the Indian Ceramic Society, 1967. **26**(1): p. 71-74.

126. Dave, N.G. *Pozzolanic wastes and their activation to produce improved lime pozzolana mixtures*.

127. Shi, C., *An overview on the activation of reactivity of natural pozzolans.* Canadian Journal of Civil Engineering, 2001. **28**(5): p. 778-786.

128. Gregg, S.J., *The surface chemistry of solids*. 1961, Chapman & Hall.

129. Tironi, A., et al., *Assessment of pozzolanic activity of different calcined clays.* Cement and Concrete Composites, 2013. **37**: p. 319-327.

130. International, A., *ASTM C618 Standard Specification for Coal Fly Ash and Raw or Calcined Natural Pozzolan for Use in Concrete*. 2019. p. 5.

131. Aci, R., *Use of Fly Ash in Concrete.* Technical Report, 2003.

132. Bondar, D., et al., *Effect of heat treatment on reactivity-strength of alkali-activated natural pozzolans.* Construction and Building Materials, 2011. **25**(10): p. 4065-4071.

133. Shi, C. and R.L. Day, *Comparison of different methods for enhancing reactivity of pozzolans.* Cement and Concrete Research, 2001. **31**(5): p. 813-818.

134. Shi, C. and R.L. Day, *Acceleration of strength gain of lime-pozzolan cements by thermal activation.* Cement and Concrete Research, 1993. **23**(4): p. 824-832.

135. Maltais, Y. and J. Marchand, *Influence of curing temperature on cement hydration and mechanical strength development of fly ash mortars.* Cement and concrete research, 1997. **27**(7): p. 1009-1020.

136. Kjellsen, K.O., R.J. Detwiler, and O.E. Gjørv, *Development of microstructures in plain cement pastes hydrated at different temperatures.* Cement and concrete research, 1991. **21**(1): p. 179-189.

137. Kjellsen, K.O. and R.J. Detwiler, *Reaction kinetics of Portland cement mortars hydrated at different temperatures.* Cement and Concrete Research, 1992. **22**(1): p. 112-120.

138. Alexander, K.M., *Activation of pozzolanic materials by treatment with acid.* Australian Journal of Applied Science, 1955. **6**: p. 327-342.

139. Palomo, A., M.W. Grutzeck, and M.T. Blanco, *Alkali-activated fly ashes: A cement for the future.* Cement and Concrete Research, 1999. **29**(8): p. 1323-1329.

140. Roy, D.M., *Alkali-activated cements Opportunities and challenges.* Cement and Concrete Research, 1999. **29**(2): p. 249-254.

141. Garcia-Lodeiro, I., A. Palomo, and A. Fernández-Jiménez, *2 - An overview of the chemistry of alkali-activated cement-based binders*, in *Handbook of Alkali-Activated Cements, Mortars and Concretes*, F. Pacheco-Torgal, et al., Editors. 2015, Woodhead Publishing: Oxford. p. 19-47.

142. Shi, C., Della Roy, and Pavel Krivenko, *Alkali-activated cements and concretes*. 2003: CRC press.

143. Wang, S.-D., and Karen L. Scrivener, *Hydration products of alkali activated slag cement.* Cement and Concrete Research, 1995. **25**(3): p. 561-571.

144. Shi, C. and R.L. Day, *Acceleration of the reactivity of fly ash by chemical activation.* Cement and Concrete Research, 1995. **25**(1): p. 15-21.

145. Shi, C. and J. Qian, *Increasing Coal Fly Ash Use in Cement and Concrete Through Chemical Activation of Reactivity of Fly Ash.* Energy Sources, 2003. **25**(6): p. 617-628.

146. Shi, C. and R.L. Day, *Pozzolanic reaction in the presence of chemical activators: Part I. Reaction kinetics.* Cement and Concrete Research, 2000. **30**(1): p. 51-58.

147. Ali Allahverdi and J. Ghorbani, *CHEMICAL ACTIVATION AND SET ACCELERATION OF LIME-NATURAL POZZOLAN CEMENT.* Materials Science, 2006.

148. Boakye, K.A., *Improvement of setting times and early strength development of clay pozzolana cement through chemical activation.* Journal of Chemical Engineering and Chemistry Research, 2014. **1**(2): p. 77-83

149. Antiohos, S. and S. Tsimas, *Activation of fly ash cementitious systems in the presence of quicklime: Part I. Compressive strength and pozzolanic reaction rate.* Cement and Concrete Research, 2004. **34**(5): p. 769-779.

150. Li, Z.J., F. Qiao, and C.K. Chau, *Recent Development of Magnesium-Based Cements - Magnesium Phosphate Cement and Magnesium Oxychloride Cement.* Advances in Science and Technology, 2010. **69**: p. 21-30.

151. Li, Z. and C.K. Chau, *Reactivity and function of magnesium oxide in sorel cement.* Journal of materials in civil engineering, 2008. **20**(3): p. 239-244.

152. Wang, F., et al., *Microstructure and properties of cement foams prepared by magnesium oxychloride cement.* Journal Wuhan University of Technology, Materials Science Edition, 2015. **30**(2): p. 331-337.

153. Deng, D., *The mechanism for soluble phosphates to improve the water resistance of magnesium oxychloride cement.* Cement and Concrete Research, 2003. **33**(9): p. 1311-1317.

154. Walling, S.A. and J.L. Provis, *Magnesia-Based Cements: A Journey of 150 Years, and Cements for the Future?* Chemical Reviews, 2016. **116**(7): p. 4170-4204.

155. Qiao, H., et al., *The application review of magnesium oxychloride cement.* Journal of Chemical and Pharmaceutical Research, 2014. **6**(5): p. 180-185.

156. Chang, Y., et al., *Research Progresses on Durability of Magnesium Phosphate Cement Based Material.* Journal of The Chinese Ceramic Society, 2014. **42**(4): p. 486-493.

157. Yang, N., et al., *Research Progresses in Magnesium Phosphate Cement – Based Materials.* Journal of Materials in Civil Engineering, 2014. **26**(10): p. 040140711-8.

158. Yang, N., *Research on the Bonding Properties of Magnesium Phosphate Cement Based Materials*. 2014. p. 94-94.

159. Mestres, G. and M.P. Ginebra, *Novel magnesium phosphate cements with high early strength and antibacterial properties.* Acta Biomaterialia, 2011. **7**(4): p. 1853-1861.

160. Li, J., W. Zhang, and Y. Cao, *Laboratory evaluation of magnesium phosphate cement paste and mortar for rapid repair of cement concrete pavement.* Construction and Building Materials, 2014. **58**: p. 122-128.

161. Soudée, E. and J. Péra, *Influence of magnesia surface on the setting time of magnesia–phosphate cement.* Cement and concrete research, 2002. **32**(1): p. 153-157.

162. Park, J., K. Hwankim, and K.Y. Ann, *Fundamental properties of magnesium phosphate cement mortar for rapid repair of concrete.*

163. Li, Y. and B. Chen, *Factors that affect the properties of magnesium phosphate cement.* Construction and Building Materials, 2013. **47**: p. 977-983.

164. Harrison, A.J.W., *Reactive magnesium oxide cements*. 2008.

165. Wei, J., et al., *Reaction products of MgO and microsilica cementitious materials at different temperatures.* Journal of Wuhan University of Technology-Mater. Sci. Ed., 2011. **26**(4): p. 745-748.

166. Wei, J., Y.-M. Chen, and Y.-X. Li, *The reaction mechanism between MgO and microsilica at room temperature.* Journal of Wuhan University of Technology-Materials Science Edition, 2006. **21**(2): p. 88-91.

167. Nied, D., et al., *Properties of magnesium silicate hydrates (MSH).* Cement and concrete research, 2016. **79**: p. 323-332.

168. Chiang, W.-S., et al., *Multiscale structure of calcium-and magnesium-silicate-hydrate gels.* Journal of Materials Chemistry A, 2014. **2**(32): p. 12991-12998.

169. Zhang, T., L.J. Vandeperre, and C.R. Cheeseman, *Magnesium-silicate-hydrate cements for encapsulating problematic aluminium containing wastes.* Journal of Sustainable Cement-Based Materials, 2012. **1**(1-2): p. 34-45.

170. Zhang, T., C.R. Cheeseman, and L.J. Vandeperre, *Development of low pH cement systems forming magnesium silicate hydrate (MSH).* Cement and concrete research, 2011. **41**(4): p. 439-442.

171. Roosz, C.C.d., et al., *Crystal structure of magnesium silicate hydrates (M-S-H): The relation with 2:1 Mg-Si phyllosilicates.* Cement and Concrete Research, 2015. **73**(July): p. 228-237.

172. Santhanam, M., M.D. Cohen, and J. Olek, *Mechanism of sulfate attack: a fresh look: Part 2. Proposed mechanisms.* Cement and Concrete Research, 2003. **33**(3): p. 341-346.

173. Santhanam, M., M.D. Cohen, and J. Olek, *Mechanism of sulfate attack: a fresh look: part 1: summary of experimental results.* Cement and concrete research, 2002. **32**(6): p. 915-921.

174. Bonen, D., *Composition and Appearance of Magnesium Silicate Hydrate and Its Relation to Deterioration of Cement‐Based Materials.* Journal of the American Ceramic Society, 1992. **75**(10): p. 2904-2906.

175. Bakharev, T., J. Sanjayan, and Y.-B. Cheng, *Sulfate attack on alkali-activated slag concrete.* Cement and Concrete Research, 2002. **32**(2): p. 211-216.

176. Carlson, E.T., R.B. Peppler, and L.S. Wells, *Studies in the System Magnesia-Silica-Water at Elevated Temperatures and Pressures.* Journal of Research of the National Bureau of Standards, 1953. **51**(4): p. 179-184.

177. Yang, J.C.S., *The System Magnesia‐Silica‐Water Below 300° C.: I, Low‐Temperature Phases from 100° to 300° C. and Their Properties.* Journal of the American Ceramic Society, 1960. **43**(10): p. 542-549.

178. Mitsuda, T. and H. Taguchi, *Formation of magnesium silicate hydrate and its crystallization to talc.* Cement and concrete research, 1977. **7**(3): p. 223-230.

179. Brew, D. and F. Glasser, *Synthesis and characterisation of magnesium silicate hydrate gels.* Cement and concrete research, 2005. **35**(1): p. 85-98.

180. Vandeperre, L., M. Liska, and A. Al-Tabbaa, *Microstructures of reactive magnesia cement blends.* Cement and Concrete Composites, 2008. **30**(8): p. 706-714.

181. Sorel, S., *On a new magnesium cement.* CR Acad Sci, 1867. **65**(65): p. 102-4.

182. Li, Z. and C.K. Chau, *Influence of molar ratios on properties of magnesium oxychloride cement.* Cement and Concrete Research, 2007. **37**(6): p. 866-870.

183. Dehua, D. and Z. Chuanmei, *The formation mechanism of the hydrate phases in magnesium oxychloride cement.* Cement and concrete research, 1999. **29**(9): p. 1365-1371.

184. Macakova, S. *Immobilization of heavy metals from MSW incinerator ash via use of sorel cement*.

185. Chau, C.K., F. Qiao, and Z. Li, *Microstructure of magnesium potassium phosphate cement.* Construction and Building Materials, 2011. **25**(6): p. 2911-2917.

186. Misra, A.K. and R. Mathur, *Magnesium oxychloride cement concrete.* Bulletin of Materials Science, 2007. **30**(3): p. 239-246.

187. Beaudoin, J.J. and V.S. Ramachandran, *Strength development in magnesium oxysulfate cement.* Cement and Concrete Research, 1978. **8**(1): p. 103-112.

188. Chengyou, W., Z. Huifang, and Y. Hongfa, *Preparation and properties of modified magnesium oxysulfate cement derived from waste sulfuric acid.* Advances in cement research, 2016. **28**(3): p. 178-188.

189. Wu, C., et al., *The hydration mechanism and performance of modified magnesium oxysulfate cement by tartaric acid.* Construction and Building Materials, 2017. **144**: p. 516-524.

190. Yang, N., et al., *Research progresses in magnesium phosphate cement–based materials.* Journal of Materials in Civil Engineering, 2014. **26**(10): p. 04014071.

191. Soudée, E. and J. Péra, *Mechanism of setting reaction in magnesia-phosphate cements.* Cement and Concrete Research, 2000. **30**(2): p. 315-321.

192. Ding, Z. and Z. Li, *High-early-strength magnesium phosphate cement with fly ash.* ACI materials journal, 2005. **102**(6): p. 375.

193. Yang, Q., et al., *Properties and applications of magnesia–phosphate cement mortar for rapid repair of concrete.* Cement and concrete Research, 2000. **30**(11): p. 1807-1813.

194. Hall, D.A., R. Stevens, and B. El-Jazairi, *The effect of retarders on the microstructure and mechanical properties of magnesia–phosphate cement mortar.* Cement and Concrete Research, 2001. **31**(3): p. 455-465.

195. Pera, J. and J. Ambroise, *Fiber-reinforced magnesia-phosphate cement composites for rapid repair.* Cement and Concrete Composites, 1998. **20**(1): p. 31-39.

196. Harrison, A.J.W., *Reactive magnesium oxide cements*. 2008, Google Patents.

197. Vandeperre, L.J., M. Liska, and A. Al-Tabbaa, *Microstructures of reactive magnesia cement blends.* Cement and Concrete Composites, 2008. **30**(8): p. 706-714.

198. Al-Tabbaa, A., *Reactive magnesia cement*, in *Eco-efficient concrete*. 2013, Elsevier. p. 523-543.

199. Liska, M. and A. Al-Tabbaa. *Ultra-green construction: reactive magnesia masonry products*. Thomas Telford Ltd.

200. Ruan, S. and C. Unluer, *Influence of supplementary cementitious materials on the performance and environmental impacts of reactive magnesia cement concrete.* Journal of Cleaner Production, 2017. **159**: p. 62-73.

201. Unluer, C. and A. Al-Tabbaa, *Impact of hydrated magnesium carbonate additives on the carbonation of reactive MgO cements.* Cement and Concrete Research, 2013. **54**: p. 87-97.

202. Yi, Y., et al., *Carbonating magnesia for soil stabilization.* Canadian Geotechnical Journal, 2013. **50**(8): p. 899-905.

203. Liska, M., et al., *Scaled-up commercial production of reactive magnesia cement pressed masonry units. Part II: Performance.* Proceedings of the Institution of Civil Engineers-Construction Materials, 2012. **165**(4): p. 225-243.

204. Liska, M., et al., *Scaled-up commercial production of reactive magnesium cement pressed masonry units. Part I: Production.* Proceedings of the Institution of Civil Engineers-Construction Materials, 2012. **165**(4): p. 211-223.

205. Cheng, T.W. and C.W. Hsu, *A study of silicon carbide synthesis from waste serpentine.* Chemosphere, 2006. **64**(3): p. 510-514.

206. Fouda, M.F.R., R.E. Amin, and M. Mohamed, *Extraction of magnesia from Egyptian serpentine ore via reaction with different acids .1. Reaction with sulfuric acid.* Bulletin of the Chemical Society of Japan, 1996. **69**(7): p. 1907-1912.

207. Li, Z., et al., *Characterization of reaction products and reaction process of MgO–SiO 2–H 2 O system at room temperature.* Construction and Building Materials, 2014. **61**: p. 252-259.

208. Mchedlov-Petrossyan, O.P., *Changes in serpentine during heating and production of cementing material with serpentine as a base.* Proc. 1Y. Con. Exptl. Mineralogy and Petrography. 1951: M.L. edit. Akad. Nauk U.S.S.R.

209. Mchedlov-Petrossyan, O.P., *The cementing properties of magnesium silicates.* Dokl. Akad. Nauk U.S.S.R 78, 1951. **3**.

210. Midgley, H.G., *A serpentine mineral from Kennack Cove, Lizard, Cornwall.* Mineralogical Magazine, 1951. **29**(212): p. 526-530.

211. Jin, F. and A. Al-Tabbaa, *Strength and hydration products of reactive MgO–silica pastes.* Cement and Concrete Composites, 2014. **52**: p. 27-33.

212. Justnes, H. and T. Ostnor, *Pozzolanic, amorphous silica produced from the mineral olivine.* Special Publication ACI, 2001. **199**: p. 769-782.

213. Justnes, H., *Pozzolana from minerals – State of the art*, in *COIN Project report 16 – 2009*. 2009, Concrete Innovation Centre Norway: Norway.

214. Tran, H., A. Scott, and R. Dhakal, *Mechanical and durability properties of magnesium silicate hydrate binder concrete.* Magazine of Concrete Research, 2020. **72**(13): p. 693-702.

215. Allen, T., *Particle size measurement.* 1981: p. 678.

216. Standard, B., *BS EN 932-1:1997 Tests for general properties of aggregates. Methods for sampling*. 1997.

217. Zhang, J. and G.W. Scherer, *Comparison of methods for arresting hydration of cement.* Cement and Concrete Research, 2011. **41**: p. 1024-1036.

218. Dinnebier, R.E. and S.J.L. Billinge, *Principles of powder diffraction.* Powder Diffraction Theory and Practice, 2008. **19**.

219. Bish, D.L. and J.E. Post, *Modern powder diffraction*. Vol. 20. 2019: Walter de Gruyter GmbH & Co KG.

220. Goldstein, J.I., et al., *Scanning electron microscopy and X-ray microanalysis*. 2017: Springer.

221. Chauhan, A., *Deformation and damage mechanisms of ODS steels under high-temperature cyclic loading*. 2018.

222. Scrivener, K., R. Snellings, and B. Lothenbach, *A practical guide to microstructural analysis of cementitious materials*. 2018: Crc Press.

223. Standard, B., *BS EN 196-9:2010 Methods of testing cement, Heat of hydration, Semi-adiabatic method*, in *British Standard*. 2010.

224. Wogelius, R.A. and J.V. Walther, *Olivine dissolution at 25°C: Effects of pH, CO2, and organic acids.* Chemical Geology, 1991. **55**(4): p. 943-954.

225. Wogelius, R.A. and J.V. Walther., *Olivine dissolution kinetics at near-surface conditions.* Chemical Geology, 1992. **97**(1-2): p. 101-112.

226. T.Herzberg, C., *The solubility of olivine in basaltic liquids: an ionic model.* Geochimica et Cosmochimica Acta, 1979. **43**(8): p. 1241-1251.

227. B.Moody, J., *Serpentinization: a review.* Lithos, 1976. **9**(8): p. 125-138.

228. McCollom, T.M. and J.S. Seewald., *A reassessment of the potential for reduction of dissolved CO2 to hydrocarbons during serpentinization of olivine.* Geochimica et Cosmochimica Acta, 2001. **65.21**: p. 3769-3778.

229. Moody, J., *An experimental study on the serpentinization of iron-bearing olivines.* The Canadian Mineralogist, 1976. **14**(4): p. 462-478.

230. Keppler, H., M. Wiedenbeck, and S.S. Shcheka, *Carbon solubility in olivine and the mode of carbon storage in the Earth's mantle.* Nature, 2003. **424**(6947): p. 414.

231. Wang, F., et al., *Kinetics and mechanism of mineral carbonation of olivine for CO2 sequestration.* Minerals Engineering, 2019. **131**: p. 185-197.

232. Bobicki, E.R., Q. Liu, and Z. Xu, *Mineral carbon storage in pre-treated ultramafic ores.* Minerals Engineering, 2015. **70**: p. 43-54.

233. Olsson, J., et al., *Olivine reactivity with CO 2 and H 2O on a microscale: Implications for carbon sequestration.* Geochimica et Cosmochimica Acta, 2012. **77**: p. 86-97.

234. Munz, I.A., et al., *A continuous process for manufacture of magnesite and silica from olivine, CO2 and H2O.* Energy Procedia, 2009. **1**: p. 4891-4898.

235. O'Connor, W., et al., *Aqueous mineral carbonation.* Final Report, DOE/ARC-TR-04, 2005. **2**.

236. Park, A.-h.H.A.H.A. and L.-S.S. Fan, *CO2 mineral sequestration: Physically activated dissolution of serpentine and pH swing process.* Chemical Engineering Science, 2004. **59**(22-23): p. 5241-5247.

237. Köhler, P., Jens Hartmann, and D.A. Wolf-Gladrow., *Geoengineering potential of artificially enhanced silicate weathering of olivine.* Proceedings of the National Academy of Sciences, 2010. **107.47** p. 20228-20233.

238. Rimstidt, J.D., S.L. Brantley, and A.A. Olsen, *Systematic review of forsterite dissolution rate data.* Geochimica et Cosmochimica Acta, 2012. **99**: p. 159-178.

239. Lamadrid, H.M., et al., *Effect of water activity on rates of serpentinization of olivine.* Nature Communications, 2017. **8**(1): p. 16107.

240. Crundwell, F.K., *The mechanism of dissolution of minerals in acidic and alkaline solutions: Part II Application of a new theory to silicates, aluminosilicates and quartz.* Hydrometallurgy, 2014. **149**: p. 265-275.

241. Pokrovsky, O.S. and J. Schott, *Kinetics and mechanism of forsterite dissolution at 25°C and pH from 1 to 12.* Geochimica et Cosmochimica Acta, 2000. **64**(19): p. 3313-3325.

242. Rosso, J.J. and J.D. Rimstidt, *A high resolution study of forsterite dissolution rates.* Geochimica et Cosmochimica Acta, 2000. **64**(5): p. 797-811.

243. Kleiv, R.A. and M. Thornhill, *Mechanical activation of olivine.* Minerals Engineering, 2006. **19**(4): p. 340-347.

244. Baláž, P., et al., *Structural changes in olivine (Mg, Fe)2SiO4 mechanically activated in high-energy mills.* International Journal of Mineral Processing, 2008. **88**(1): p. 1-6.

245. Turianicová, E., et al., *A comparison of the reactivity of activated and non-activated olivine with CO2.* International Journal of Mineral Processing, 2013. **123**: p. 73-77.

246. Li, J. and M. Hitch, *Mechanical activation of ultramafic mine waste rock in dry condition for enhanced mineral carbonation.* Minerals Engineering, 2016. **95**: p. 1-4.

247. Rigopoulos, I., et al., *Ball milling effect on the CO2 uptake of mafic and ultramafic rocks: A review.* 2018. **8**(11): p. 406.

248. Tkáčová, K., *Mechanical Activation of Minerals* Vol. Developments in Mineral Processing. 1989: Elsevier Science Ltd.

249. Tromans, D. and J. Meech, *Enhanced dissolution of minerals: stored energy, amorphism and mechanical activation.* Minerals Engineering, 2001. **14**(11): p. 1359-1377.

250. Li, J. and M. Hitch, *Mechanical activation of magnesium silicates for mineral carbonation, a review.* Minerals Engineering, 2018. **128**: p. 69-83.

251. Kleiv, R.A. and M. Thornhill, *The effect of mechanical activation in the production of olivine surface area.* Minerals Engineering, 2016. **89**: p. 19-23.

252. Velbel, M.A., *Dissolution of olivine during natural weathering.* Geochimica et Cosmochimica Acta, 2009. **73**(20): p. 6098-6113.

253. Moody, J.B., *Serpentinization: a review.* Lithos, 1976. **9**(2): p. 125-138.

254. Coleman, R.G. and T.E. Keith, *A chemical study of serpentinization—Burro Mountain, California.* Journal of Petrology, 1971. **12**(2): p. 311-328.

255. Oze, C. and M. Sharma, *Have olivine, will gas: serpentinization and the abiogenic production of methane on Mars.* Geophysical research letters, 2005. **32**(10).

256. Saldi, G.D., et al., *Magnesite growth rates as a function of temperature and saturation state.* Geochimica et Cosmochimica Acta, 2009. **73**(19): p. 5646-5657.

257. Lide, D.R., *CRC handbook of chemistry and physics.* 12J204, 2012.

258. Swanson, E.J., et al., *Directed precipitation of hydrated and anhydrous magnesium carbonates for carbon storage.* Physical Chemistry Chemical Physics, 2014. **16**(42): p. 23440-23450.

259. Béarat, H., et al., *Carbon sequestration via aqueous olivine mineral carbonation: role of passivating layer formation.* Environmental science & technology, 2006. **40**(15): p. 4802-4808.

260. Lazaro, A., et al., *The properties of amorphous nano-silica synthesized by the dissolution of olivine.* Chemical Engineering Journal, 2012. **211**: p. 112-121.

261. Béarat, H., et al., *Carbon sequestration via aqueous olivine mineral carbonation: role of passivating layer formation.* Environmental science & technology, 2006. **40**(15): p. 4802-4808.

262. Brindley, G. and R. Hayami, *Mechanism of formation of forsterite and enstatite from serpentine.* Mineralogical Magazine, 1965. **35**(269): p. 189-195.

263. Robie, R.A., B.S. Hemingway, and J.R. Fisher, *Thermodynamic properties of minerals and related substances at 298. 15 K and 1 bar (10/sup 5/pascals) pressure and at higher temperatures*. 1978, Geological Survey, Washington, DC (USA).

264. Grandstaff, D. *The dissolution of forsteritic olivine from Hawaiian beach sand*. in *Proc, 3rd Int. Symp. Water-Rock Interaction*. 1986.

265. Chen, Y. and S.L. Brantley, *Dissolution of forsteritic olivine at 65 C and 2< pH< 5.* Chemical Geology, 2000. **165**(3-4): p. 267-281.

266. Oelkers, E.H., *An experimental study of forsterite dissolution rates as a function of temperature and aqueous Mg and Si concentrations.* Chemical Geology, 2001. **175**(3-4): p. 485-494.

267. Hänchen, M., et al., *Dissolution kinetics of fosteritic olivine at 90-150°C including effects of the presence of CO2.* Geochimica et Cosmochimica Acta, 2006. **70**(17): p. 4403-4416.

268. Wogelius, R.A. and J.V. Walther, *Olivine dissolution at 25 °C: Effects of pH, CO2, and organic acids.* Chemical Geology, 1991. **55**: p. 943-954.

269. Brnmt, J., et al., *CRYSTAL STRUCTURES OF NATURAL OLIVINES.* THE AMERICAN MINERALOGISI, 1968. **53**.

270. Garcia, B., et al., *Experiments and geochemical modelling of CO2 sequestration by olivine: Potential, quantification.* Applied Geochemistry, 2010. **25**(9): p. 1383-1396.

271. Johnson, N.C., et al., *Olivine dissolution and carbonation under conditions relevant for in situ carbon storage.* Chemical Geology, 2014. **373**: p. 93-105.

272. Fasihnikoutalab, M.H., et al., *Utilization of carbonating olivine for soil stabilization.* Environmental Geotechnics, 2015(In press): p. 1-15.

273. Chatterji, S., *Mechanism of expansion of concrete due to the presence of dead-burnt CaO and MgO.* Cement and Concrete Research, 1995. **25**(1): p. 51-56.

274. Cao, F., M. Miao, and P. Yan, *Hydration characteristics and expansive mechanism of MgO expansive agents.* Construction and Building Materials, 2018. **183**: p. 234-242.

275. Mo, L., et al., *MgO expansive cement and concrete in China: Past, present and future.* Cement and Concrete Research, 2014. **57**: p. 1-12.

276. Mejias, J.A., et al., *The kinetics and mechanism of MgO dissolution.* Chemical Physics Letters, 1999. **314**(5-6): p. 558-563.

277. Szynkaruk, P., M. Wesolowski, and M. Samson-Rosa, *Principal component analysis of thermal decomposition of magnesium salts used as drugs.* Journal of Thermal Analysis and Calorimetry, 2010. **101**(2): p. 505-512.

278. Unluer, C. and A. Al-Tabbaa, *Characterization of light and heavy hydrated magnesium carbonates using thermal analysis.* Journal of Thermal Analysis and calorimetry, 2014. **115**(1): p. 595-607.

279. Anderson, P.J. and R.F. Horlock, *Thermal decomposition of magnesium hydroxide.* Transactions of the Faraday Society, 1962. **58**: p. 1993-2004.

280. Isa, K. and M. Nogawa, *Thermal decomposition of magnesium acetate tetrahydrate under self-generated atmosphere.* Thermochimica acta, 1984. **75**(1-2): p. 197-206.

281. Tran, H.M. and A. Scott, *Strength and workability of magnesium silicate hydrate binder systems.* Construction and Building Materials, 2017. **131**: p. 526-535.

282. Chiang, W.S., et al., *Multiscale structure of calcium-and magnesium-silicate-hydrate gels.* Journal of Materials Chemistry A, 2014. **2**(32): p. 12991-12998.

283. Bernard, E., et al., *Formation of magnesium silicate hydrates (MSH).* Physics and Chemistry of the Earth, Parts A/B/C, 2017. **99**: p. 142-157.

284. Petrosyan, M., *Thermal behavior of serpentine and kaolin.* Metals and Mining, Gerogian S.S.R. , 1951. **45**(3): p. 799-802.

285. Justnes, H., *Pozzolana from minerals – State of the art*, in *COIN P1 Advanced cementing materials and admixtures*. 2009, SINTEF Building and Infrastructure.

286. Brouwers, a.L. and H. H. J, *Nano-silica production by a sustainable process ; application in building materials.* 8th fib PhD Symposium in Kgs. Lyngby, Denmark, 2010(May): p. 1-6.

287. Lazaro, A., et al., *The kinetics of the olivine dissolution under the extreme conditions of nano-silica production.* Applied Geochemistry, 2015. **52**: p. 1-15.

288. Lázaro García, A., *Nano-silica production at low temperatures from the dissolution of olivine, PhD Thesis*. 2014. 252-252.

289. O'Connor, W., et al., *Aqueous Mineral Carbonation.* Doe/Arc-Tr-04-002, 2005.

290. Pietriková, A. and M. Búgel, *Silica gel procedure from serpentine.* 2005. **53**(4): p. 11-14.

291. Pietrikova, A., et al., *Preparation of SiO2 powder through leaching of serpentine.* Metalurgija, 2004. **43**(4): p. 299-304.

292. Fedoročková, A., et al., *Dissolution of magnesium from calcined serpentinite in hydrochloric acid.* Minerals Engineering, 2012. **32**: p. 1-4.

293. Payá, J., et al., *Enhanced conductivity measurement techniques for evaluation of fly ash pozzolanic activity.* Cement and Concrete Research, 2001. **31**(1): p. 41-49.

294. Diamond, S. and S. Sahu, *Densified silica fume: particle sizes and dispersion in concrete.* Materials and Structures, 2006. **39**(9): p. 849-859.

295. Thorstensen, R.T. and P. Fidjestol, *Inconsistencies in the pozzolanic strength activity index (SAI) for silica fume according to EN and ASTM.* Materials and Structures, 2015. **48**(12): p. 3979-3990.

296. Krauskopf, K.B., *Dissolution and precipitation of silica at low temperatures.* Geochimica et Cosmochimica Acta, 1956. **10**(1-2): p. 1-26.

297. Dove, P.M., et al., *Kinetics of amorphous silica dissolution and the paradox of the silica polymorphs.* Proceedings of the National Academy of Sciences, 2008. **105**(29): p. 9903-9908.

298. Icenhower, J.P. and P.M. Dove, *The dissolution kinetics of amorphous silica into sodium chloride solutions: effects of temperature and ionic strength.* Geochimica et Cosmochimica Acta, 2000. **64**(24): p. 4193-4203.

299. Denny, J., W. Robson, and D.A. Irwin, *The prevention of silicosis by metallic aluminum II.* Canadian Medical Association Journal, 1939. **40**(3): p. 213.

300. Jephcott, C. and J. Johnston, *Solubility of silica and alumina.* Arch. Indust. Hyg. & Occupational Med., 1950. **1**(3): p. 323-40.

301. Mitsyuk, B., *Mechanism of the reaction of silica with phosphoric acid in aqueous solutions.* Russian Journal of Inorganic Chem istry, 1972. **17**: p. 471.

302. Hast, N., *A REACTION BETWEEN SILICA AND SOME MAGNESIUM COMPOUNDS AT ROOM TEMPERATURE AND AT+ 37-DEGREES-C.* Arkiv for Kemi, 1956. **9**(4): p. 343-360.

303. Greenberg, S. and T. Chang, *The hydration of tricalcium silicate.* The Journal of Physical Chemistry, 1965. **69**(2): p. 553-561.

304. Zuhl, R.W. and Z. Amjad, *Solution Chemistry Impact on Silica Polymerization by Inhibitors.* Mineral Scales in Biological and Industrial Systems, 2013: p. 173.

305. Sheikholeslami, R. and J. Bright, *Silica and metals removal by pretreatment to prevent fouling of reverse osmosis membranes.* Desalination, 2002. **143**(3): p. 255-267.

306. Brew, D.R.M. and F.P. Glasser, *Synthesis and characterisation of magnesium silicate hydrate gels.* Cement and concrete research, 2005. **35**(1): p. 85-98.

307. Temuujin, J., K. Okada, and K.J.D.J.D. MacKenzie, *Role of Water in the Mechanochemical Reactions of MgO–SiO2Systems.* Journal of Solid State Chemistry, 1998. **138**(1): p. 169-177.

308. Mehta, P.K. and O.E. Gjørv, *Properties of portland cement concrete containing fly ash and condensed silica-fume.* Cement and Concrete Research, 1982. **12**(5): p. 587-595.

309. Cheng-Yi, H. and R.F. Feldman, *Hydration reactions in Portland cement-silica fume blends.* Cement and Concrete Research, 1985. **15**(4): p. 585-592.

310. Langan, B.W., K. Weng, and M.A. Ward, *Effect of silica fume and fly ash on heat of hydration of Portland cement.* Cement and Concrete research, 2002. **32**(7): p. 1045-1051.

311. Jin, F. and A. Al-Tabbaa, *Thermogravimetric study on the hydration of reactive magnesia and silica mixture at room temperature.* Thermochimica Acta, 2013. **566**: p. 162-168.

312. Tran, H.M., A. Scott, and R.P. Dhakal. *Strength development of mortars using a magnesium silicate hydrate binder system under different curing conditions*. in *Proceedings of the 2nd International RILEM Conference on Bio-based Building Materials*. 2017. ClermontFerrand, France.

313. Tran, H., *Developement of Magnesium Silicate Hydrate Binder System*. 2016.

314. Liska, M. and L.J. Vandeperre, *Influence of carbonation on the properties of reactive magnesia cement-based pressed masonry units.* 2008. **7605**(2): p. 53-64.

315. Song, K., et al., *Preparation of silica-alumina nanoparticles via blast-furnace slag dissolution in low-concentration acetic acid for carbonation.* Minerals, 2017. **7**(11): p. 206.

316. Song, K., et al., *Effects of experimental parameters on the extraction of silica and carbonation of blast furnace slag at atmospheric pressure in low-concentration acetic acid.* Metals, 2017. **7**(6): p. 199.

317. Sjöberg, S., *Silica in aqueous environments.* Journal of Non-Crystalline Solids, 1996. **196**: p. 51-57.

318. Plettinck, S., L. Chou, and R. Wollast, *Kinetics and mechanisms of dissolution of silica at room temperature and pressure.* Mineralogical Magazine, 1994. **58**: p. 728-729.

319. Theilig, G., G. Müller, and K. Bodenbenner, *Re‐Use and Disposal of Waste Acids.* Israel Journal of Chemistry, 1975. **14**(S1): p. 234-243.

320. Kalin, M., A. Fyson, and W.N. Wheeler, *The chemistry of conventional and alternative treatment systems for the neutralization of acid mine drainage.* Science of the Total Environment, 2006. **366**(2-3): p. 395-408.

321. Liu, F., et al., *Effect of neutralized solid waste generated in lime neutralization on the ferrous ion bio-oxidation process during acid mine drainage treatment.* Journal of hazardous materials, 2015. **299**: p. 404-411.

322. Glasser, F.P., *Progress in the immobilization of radioactive wastes in cement.* Cement and Concrete Research, 1992. **22**(2): p. 201-216.

323. Malviya, R. and R. Chaudhary, *Factors affecting hazardous waste solidification/stabilization: a review.* Journal of Hazardous Materials, 2006. **137**(1): p. 267-276.

324. Li, X.D., et al., *Heavy metal speciation and leaching behaviors in cement based solidified/stabilized waste materials.* Journal of Hazardous Materials, 2001. **82**(3): p. 215-230.

325. Beddoe, R.E. and H.W. Dorner, *Modelling acid attack on concrete: Part I. The essential mechanisms.* Cement and Concrete Research, 2005. **35**(12): p. 2333-2339.

326. Gutberlet, T., H. Hilbig, and R.E. Beddoe, *Acid attack on hydrated cement — Effect of mineral acids on the degradation process.* Cement and Concrete Research, 2015. **74**: p. 35-43.

327. Chandra, S., *Hydrochloric acid attack on cement mortar — An analytical study.* Cement and Concrete Research, 1988. **18**(2): p. 193-203.

328. Bart, F., et al., *Cement-based materials for nuclear waste storage*. 2012: Springer Science & Business Media.

329. Prosser, H.J. and A.D. Wilson, *Development of materials based on acid-base reaction cements.* Materials & Design, 1986. **7**(5): p. 262-266.

330. Wilson, A.D. and J.W. Nicholson, *Acid-Base Cements: Their Biomedical and Industrial Applications*. Chemistry of Solid State Materials. 1993, Cambridge: Cambridge University Press.

331. Wu, D., M. Fall, and S.J. Cai, *Coupling temperature, cement hydration and rheological behaviour of fresh cemented paste backfill.* Minerals Engineering, 2013. **42**: p. 76-87.

332. Zou, X., et al., *An experimental study on the concrete hydration process using Fabry–Perot fiber optic temperature sensors.* Measurement, 2012. **45**(5): p. 1077-1082.

333. Newman, E.S., *Preparation and heat of formation of a magnesium oxysulfate.* Journal of Research of the National Bureau of Standards. Section A, Physics and Chemistry, 1964. **68**(6): p. 645.

334. Demediuk, T., W.F. Cole, and H.V. Hueber, *Studies on magnesium and calcium oxychlorides.* Australian Journal of Chemistry, 1955. **8**(2): p. 215-233.

335. Dinnebier, R.E., et al., *2Mg (OH) 2· MgCl2· 2H2O and 2Mg (OH) 2· MgCl2· 4H2O, two high temperature phases of the magnesia cement system.* Zeitschrift für anorganische und allgemeine Chemie, 2012. **638**(3‐4): p. 628-633.

336. Dinnebier, R.E., et al., *9Mg (OH) 2· MgCl2· 4H2O, a high temperature phase of the magnesia binder system.* Inorganic chemistry, 2010. **49**(21): p. 9770-9776.

337. Vandeperre, L.J. and A. Al-Tabbaa, *Accelerated carbonation of reactive MgO cements.* Advances in Cement Research, 2007. **19**(2): p. 67-79.

338. Tooper, B. and L. Cartz, *Structure and formation of magnesium oxychloride sorel cements.* Nature, 1966. **211**(5044): p. 64-66.

339. MatkovlĆ, B., et al., *Reaction Products in Magnesium Oxychloride Cement Pastes. System MgO ‐ MgCl2 ‐ H2O.* Journal of the American Ceramic Society, 1977. **60**(11 ‐ 12): p. 504-507.

340. Lojka, M., et al., *Thermal Stability and Kinetics of Formation of Magnesium Oxychloride Phase 3Mg (OH) 2· MgCl2· 8H2O.* Materials, 2020. **13**(3): p. 767.

341. Hu, C., et al., *Micromechanical investigation of magnesium oxychloride cement paste.* Construction and Building Materials, 2016. **105**: p. 496-502.

342. Chau, C.K. and Z. Li, *Microstructures of magnesium oxychloride.* Materials and Structures, 2008. **41**(5): p. 853-862.